Localized Signaling and Communication during Yeast Mating

Christian Diener

Dissertation zur Erlangung des Grades
eines Doktors der Naturwissenschaften (Dr. rer. nat.)
am Fachbereich Mathematik und Informatik
der Freien Universität Berlin (2012)

1. Referent: Prof. Dr. Martin Vingron
2. Referent: Prof. Dr. Dr. h.c. Edda Klipp

Tag der Promotion: 12.12.2012

Preface

Acknowledgements

Together with this thesis also ends the most exciting part of my life so far and a new chapter begins. Many important persons have accompanied and supported me in this time, and I hope not to forget anybody here.
At first I would like to thank Prof. Dr. Edda Klipp for supervising me, and this thesis, with patience and support, despite my occasional stubbornness. I am also grateful to Prof Dr. Martin Vingron and the International Max Planck Research School for giving me the opportunity to investigate my Ph.D. project and supporting me throughout my doctorate. Particularly because my research topic was not exactly the scope of the research school, I am thankful that I could nevertheless develop it here. In this context I would like to acknowledge the immense help of Kirsten Kelleher and, especially Hannes Luz who sadly passed away last year. Hannes, you were truly a great person and you will be missed by us all.
Of course I would like to mention the entire Theoretical Biophysics group as big help to my investigation and me personally. My work would have been impossible to realize without the help of Wolfgang Giese and Gabriele Schreiber who have supported me with their immense experience in mathematics and molecular biology. I also want to particularly mention Thomas Spießer and Max Flöttmann which have contributed to this thesis with many fruitful discussions and to my personal well-being with uncounted burger nights.
Parts of this thesis have been discussed extensively with Gabriel del Rio Guerra. He has motivated me to enter the field of molecular biology and I am particularly looking forward to start the next chapter of my scientific development in his lab at the UNAM Mexico.
Some of the biggest support I have encountered, however, was not only found with my colleagues. This work would never have been possible without the steady believe of my parents Petra and Jörg-Uwe Diener in me and my work and their ongoing support even when times were hard for all of us. Last, but by no means least I would like to thank my girlfriend Erika Peláez for supporting me so many times, motivating me when I was doubting, and spoiling me me with amazing food when I needed it.

Collaborative work

Successful research can never be achieved by a single person alone. In the course of this thesis some parts were obtained in collaboration with fellow scientists. Here, the implementation of core algorithms for the finite element methods was done by Wolfgang Giese. The molecular biology in this thesis was performed together with Gabriele Schreiber, who was involved in all experiments found in chapter 3.
Additionally, even though not scope of this thesis, I also published work together with Thomas Spießer and Matteo Barberis in the field of yeast DNA replication and cell cycle [1, 2].

Structure of this thesis

I will begin this thesis with some general introductions to cellular signaling and System Biology in chapter 1. In the same chapter, I will also motivate the usage of yeast for molecular biology and introduce the biological system I investigate in this thesis, the pheromone response in the yeast *Saccharomyces cerevisiae*. Chapter 2 begins with an introduction into the experimental biology employed in this thesis. This is followed by the theory of reaction-diffusion systems. Even though stochastic and deterministic methods are usually treated as two different strategies to solve reaction-diffusion problems, I will rather derive the deterministic methods from the stochastic ones, showing under which conditions they converge to each other. Chapter 3 will present the performed investigation and results. This will not be done in chronological order, but rather in an order that allows for a better interpretation of the results. I will close the main part of this thesis with interpretations of the results and putting them into a larger context in chapter 4.

Zusammenfassung

Eine der grundlegenden Fähigkeiten, welche zelluläre Organismen im Laufe ihrer Evolution erworben haben, ist die Wahrnehmung von Informationen über ihre Umwelt und die Verwendung dieser zum eigenem Vorteil. Eigenschaften der Umwelt werden hier durch spezifische Rezeptoren an der Zelloberfläche wahrgenommen und an eine Signalkaskade weitergegeben, was in einer spezifischen Genexpression resultiert. Die korrekte Funktion dieser Signaltransduktion ist essentiell für alle Lebewesen und Fehler haben starke Auswirkungen auf die Vitalität des Organismus. Dies gilt insbesondere für die Kommunikation zwischen einzelnen Zellen wie sie in höheren Eukaryonten auftritt.
In dieser Arbeit untersuche ich die Fähigkeit eines prototypischen Signalsystems die mitunter unsicheren Informationen über die Umwelt optimal zu nutzen. Das studierte System ist die Pheromonantwort der Bäckerhefe *Saccharomyces cerevisiae*. Während dieser formen zwei haploide Hefezellen unterschiedlichen Typus, *MAT***a** oder *MAT*$\boldsymbol{\alpha}$, eine diploide Zelle. Dies wird durch die Sekretion von spezifischen Pheromonen realisiert, welche durch Zellen des jeweils anderen Typus wahrgenommen werden können und Informationen über die Lokalisation potentieller Konjugationspartner in der Population transmittiert. Die lokale Pheromonverteilung muss daher von den auch in der Präsenz ungünstiger Bedingungen, wie zum Beispiel starken Fluktuationen oder geringen Konzentrationen, von den Zellen genau wahrgenommen und interpretiert werden.
In dieser Arbeit präsentiere ich mehrere Mechanismen die dies realisieren. Mittels einer neu entwickelten Methode, welche mathematische Modellierung direkt mit Experimenten verbindet, quantifizieren wir die vorher nicht beobachtbare Verteilung von Pheromonen im extrazellulären Medium. Wir zeigen, dass diese Verteilung massiv durch die Aktivität der von *MAT***a**-Zellen sekretierten Aspartylprotease Bar1 reguliert wird. Dies erhöht den Informationsgehalt der Pheromonverteilung und koordiniert Wachstum mit Kommunikation in der Zellpopulation. Aufbauend darauf konstruieren wir ein detailliertes 3-D-Modell der Zelle welches genutzt wird um zu erklären wie Zellen auch winzige Pheromonverteilungen von nur ein paar Molekülen in eine genaue Antwort übersetzen und die Richtung der Partnerzelle identifizieren. Wir observieren dass *MAT***a**-Zellen Signalmoleküle über kurze Zeit an der Membran sammeln um Ungenauigkeiten zu minimieren. In einem letzten Schritt zeigen wir, mittels Analyse von partiellen Differentialgleichungen, dass die Bildung eines Multiproteinkomplexes an der Membran die Zellen in die Lage versetzt auch kleine Unterschiede im Raum in eine extreme Verdichtung an der Membran zu überführen.
Die identifizierten Mechanismen übersetzen spezifische Proteininteraktionen in deren Funktionen während der Wahrnehmung von extrazellulären Signalen und bieten einen neuen Einblick in das evolutionäre Design von Zell-Zell-Kommunikation.

Contents

1 Introduction **1**
1.1 Communication in cell populations . . . 1
1.2 How Systems Biology fixes your radio . . . 3
1.3 Why yeast? . . . 5
1.4 Yeast and pheromones . . . 7
1.4.1 The extracellular pheromone signal and its regulation . . . 7
1.4.2 The signaling pathway of *MAT***a** cells . . . 9
1.4.3 The path to gene expression . . . 12
1.4.4 The polarisome and induction of cell-cell fusion . . . 14
1.4.5 A blueprint for spatial signaling in human cells? . . . 16
1.5 The Systems Biology of yeast signaling . . . 17

2 Systems Biology of reaction-diffusion systems **21**
2.1 2012: Another Space Odyssey . . . 21
2.2 Experimental Techniques . . . 22
2.2.1 Fluorescence microscopy . . . 22
2.2.2 Assays for population studies . . . 30
2.2.3 Basics of yeast cloning . . . 32
2.3 Computational Techniques . . . 35
2.3.1 Stochastic Processes and the Master Equation . . . 36
2.3.2 Partial differential equations and finite element methods . . . 48
2.3.3 Nonlinear Optimization . . . 69

3 The yeast pheromone response as a complex communication system **75**
3.1 Introduction . . . 75
3.2 Bar1 regulates the extracellular signaling environment during mating . 76
3.2.1 An assay to quantify extracellular signaling molecules in yeast from *in vivo* microscopy images . . . 76
3.2.2 Bar1 induces $\boldsymbol{\alpha}$-factor hot-spots . . . 88
3.2.3 Bar1 coordinates growth along with mating in mixed haploid populations . . . 92
3.3 Signal accumulation and linear distance encoding in the yeast pheromone response . . . 95
3.3.1 A spatial stochastic model of the early pheromone response . . . 95
3.3.2 Linear distance encoding and global noise reduction . . . 99
3.3.3 Local noise reduction and depletion . . . 100
3.4 Multi-protein complexes and polarization . . . 102
3.4.1 The motifs promoting complex formation . . . 103
3.4.2 Complex formation enables increased polarization . . . 105
3.4.3 Gradient-response encoding . . . 107

3.4.4 Combination of the motifs leads to exponential polarization . . 108

4 Discussion **111**
4.1 Conclusions 111
4.2 The evolution of intercellular signaling: talking yeasts 113
4.3 Can we generalize from yeast? 115

5 Bibliography **117**

6 Appendix **133**
6.1 Derivations 133
6.2 Additional Data 139
6.3 Additional figures 144

List of Figures **147**

Curriculum vitae **151**

Ehrenwörtliche Erklärung **155**

1 Introduction

1.1 Communication in cell populations

One of the dogmas of Evolutionary Biology is that no living organism can exist completely independent of its environment. It is the capability to cope with a complex and possibly changing environment that will decide how successful a life form will be in surviving and passing its genes to the next generation. It is, therefore, of no surprise that one of the most ubiquitous features of life is the ability to sense information about the environment and to use it advantageously.
All cellular organisms employ specialized sets of proteins and protein interactions in order to sense various signals from their environment and convert them into an intracellular response. Those signals can be various and range from obvious choices, such as the availability of nutrients or the presence of harmful substances, to complex physiochemical properties of the environment, such as pressure, temperature, or osmotic properties. The ability to sense an extracellular signal and transmit it into the cell by a set of biochemical reactions is summarized in the term *signaling*, and the cascade of protein-protein interactions transmitting the signal is termed a *signaling pathway*. However, signaling pathways are far from being simple carriers of information that statically transmit any signal without modification. Signaling pathways rather serve the interpretation of the signal and may include an inherent ability to analyze it as well. For instance, a signaling pathway may employ a threshold where the signal is only transmitted when it is potentially large enough to be of use to the cell, or it may inherit feedback systems in order to diminish small signals but amplify large signals. In general, the more complex the organism, the more complex the signaling pathways and even simple organisms may include vast amounts of regulation in order to execute complex signaling. Additionally, cells may depend on very different properties of the extracellular signals such as concentrations, duration or even differences in space, called gradients[1].
Even though the name might imply otherwise, even single-cell organisms do not live alone, but rather share their environment with millions, and sometimes billions, of cells with the same or a different genotype. Those cell populations form a large part of the environment and it is one of the most interesting features of evolution that individuals of these populations can employ signaling in order to communicate with each other. Cell-cell communication can be observed from bacteria to human, however, the mechanics and complexity of this communication differs greatly between species.
Bacteria employ a very basic, yet elegant, communication. Here, every individual in the population produces an identical signaling molecule on a low concentration. Every

[1] The term gradient originates from the mathematical expression denoting a change relative to a reference variable. However, where gradient is often used to denote a change over time in mathematics, in the biology of signaling molecules it rather denotes the presence of inhomogeneities in the distribution of signaling molecules in space. The gradient, or strength of the gradient, thus, denotes the derivative of the signal in space.

cell in the population is at the same time capable of sensing the produced molecule by a distinct signaling pathway. The pathway entails a threshold which prohibits activation of the pathway by the low concentration of signaling molecules produced by a single cell. However, as the population grows very dense the concentration of signaling molecules produced jointly by all the individuals increases drastically, leading to an activation of the signaling pathway. As all individuals contribute to the signal equally this type of intercellular communication has been termed *quorum sensing* [3, 4]. This simple communication mechanism is made powerful by its cooperative nature. This is illustrated fatally in the capability of many bacteria to employ quorum sensing in order to initiate the production of individually small amounts of substances changing the extracellular environment into a favorable state for the entire population: a biofilm. The formed biofilm does not only provide optimal growth conditions, but also includes several substances that harm potential competitors and prohibit the entry of unfavorable substances, most importantly antibiotics. As a consequence, one of the most prominent causes of death from bacterial infections is the formation of biofilms [5, 6].

In single-cell eukaryotes we find a degree of communication that already hints to the complex communication between cells of multi-cellular organisms. Simple eukaryotes, like yeast, may employ pheromone-like proteins in order to signal complex properties of the cell population. Here, haploid cells of different genotypes, such as mating types[2], may employ chemically distinct signaling molecules. The underlying signaling pathways can sense complex information such as signaling gradients and, thus, the location of individual cells in the population. Those signaling pathways may control cell proliferation and fusion. We can also find first occurrences of proteins that act in the extracellular medium in order to modify the signaling environment of the pheromones in order to enable a more informative signal. This may be prototypical for the large amount of signal regulation in higher organisms such as organ segmentation or vessel systems, however, there is little research up to now concentrating on this hypothesis. Either way, the complex cell-cell signaling employed by populations of single-cell eukaryotes prepared the road for the formation of the first multi-cellular organisms that culminated in the tightly regulated cell population that constitutes the human body.

The dependence of a functioning organism on cell-cell communication was discovered in the sixties when there were first indications that cancer may be caused by a reduced level of communication between human cells [7]. This started a vast amount of research in signaling pathways but with the presence of more and more data it also became clear that the traditional methods were limited in explaining the function and inner workings of signaling pathways. Why is that? The problem lies within the inherent complexity of signaling. Signaling is realized by several interactions of proteins occurring in fast succession and often simultaneously. The pure study of the individual components can, however, not deliver essential information, for instance about how the signaling pathway actually modifies the signal. We could elucidate whether there is a feedback with classical experimental methods, but we can not answer the question what advantage this provides during signal sensing. This complexity is amplified even more when switching to cell populations, where communication between cells makes a clear functional explanation even more problematic. As such, the more data became available, the less likely it became to explain the actual function of a biological mech-

[2] A predecessor of what we know as genders.

anism. A fact that was also illustrated by the discontent following the sequencing of the human genome and the realization that knowledge of the genome alone was not sufficient to understand the resulting function.
A remedy to this paradox came along with the realization that an abstraction of the underlying principles was needed. The basic function of a signaling pathway is transmission and modification of the sensed signal. As such it resembles a mathematical function, where applying the function to a distinct input, the signal, would render a response, the phenotype of the cell. By combining methodology of mathematics, physics, engineering and, of course, molecular biology a new field of biology was born and termed Systems Biology, denoting the study of complex biological systems. But how did this new field aim at succeeding where others had failed?

1.2 How Systems Biology fixes your radio

The major complication in Systems Biology is that is inherently ambitious in its goals. Whereas large parts of Biology are mostly exploratory, observing something and interpreting it, Systems Biology asks for a functional characterization. This simply means that many project in this field will aim at answering a single question "How does it work?". It seems natural to assume that given the output of a system, so knowing "what it does", in combination with its ingredients, should lead to some idea of how its components interact in order to achieve the observed outcome. But this is by no means trivial. One of the most popular analogies illustrating this has been introduced by Yuri Lazebnik who compares the problem to understanding how a radio works using Biology [8]. Even though there is a clear outcome – the radio plays music – and a defined set of components it can be extremely difficult to unravel how all those components finally end up in the music playing, a problem that becomes even harder within a biological setting.
In Systems Biology we aim to understand how a biological system works by a bottom-up approach. This means that we try to decipher the system by tinkering with its components and/or observing its behavior in a variety of settings. In reaction-diffusion systems our components are oligopeptides, genes and, sometimes, small molecules. Unfortunately, none of those components are *per se* visible, so we have to modify the components even if we just want to visualize them. Owing to this fact, performing experiments on reaction-diffusion systems will always require some sort of interference, where we will usually treat components in the system by either tagging, deletion or substitution. Here, tagging is supposed to be the least invasive way and consists of adding a marker to the protein (or gene) which will allow tracking of the protein by some consecutive assay. In contrast, deletion is the most invasive way to interfere with a distinct protein since it means deleting the corresponding gene from the genome and, thus, abolishing the protein in the system. This may give very clear effects compared to the non-deleted case but may lead to only little information gain if the component is required for viability, since this will render the organism dead. For this reason, there is also an intermediate way, where the gene is substituted either with a version having an altered expression or with a version which carries some kind of mutation, modifying the function of the corresponding protein. Both ways, modification of expression or function, may then lead to an altered system outcome. The information we are gaining by the experiment is consecutively translated into a hypothesis about the

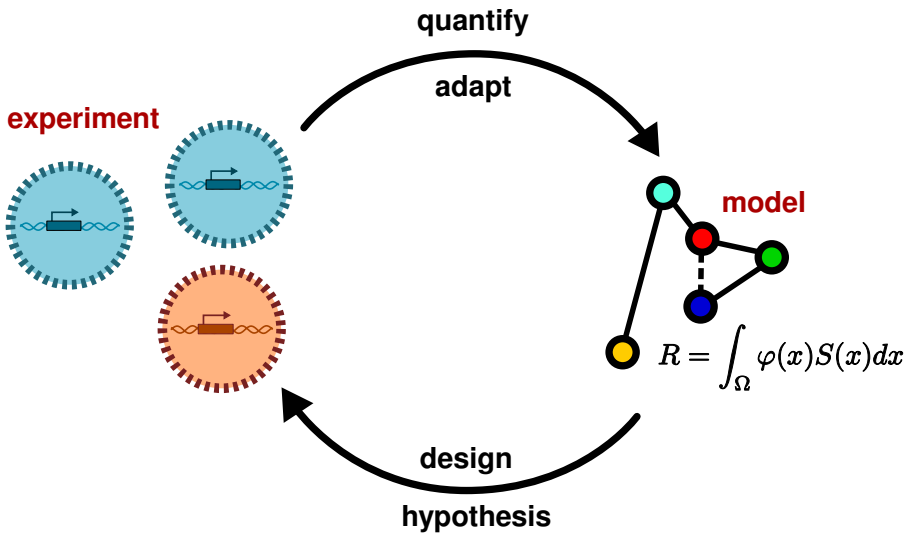

Figure 1.1: The life cycle of Systems Biology. Repeated modification and probing of the biological systems is used to unravel an abstract functional description of the system, the model, that is used in turn to generate hypotheses which are validated or falsified by experiments.

functionality of the system, the model. The model is supposed to be a clear concise and minimal description of the biological system which formulates how we think it works. By repeatedly generating predictions from the model we can design new experiments in order to falsify or validate our hypothesis [9, 10]. This "life cycle" forms the central paradigm of Systems Biology and may, given the right circumstances and luck, converge to an adequate understanding how the biological system works.
The challenge lies within coupling both parts of the cycle, because, even though they both belong to the Natural Sciences, Biology and Mathematics share only little common language that would facilitate an easy communication between the two. However, it is crucial for validation that we are able to couple experimental results to models and *vice versa*. The important part here is having a concise framework which lets us quantify how well a model agrees with the data and whether the outcome of an experiment significantly supports our current hypothesis. As a consequence Systems Biology will incorporate a variety of subfields, such as the "Omics" Sciences, Optimization, Statistics and Synthetic Biology, each covering a part of the required abilities.

However, as the name suggests the main interest of Systems Biology lies within the *system*. As such, we are limited to study biological systems which permit us to tinker with them in the way we need in order validate our hypothesis. This requires extensive experimentation, because the only way to do this is modifying the system itself and observing the new outcome. Naturally, we are mostly interested in biological systems which are important to ourselves, thus, the biology of the human. However, this imposes some problems. First of all, experimentation on humans to the extent which is required would impose quite a lot of ethical problems and many experiments are clearly out of question as they would harm human beings. As such we would be limited to study isolated cell lines which are in a completely artificial environment which has little to do with its natural state. Second, human cells have evolved quite elaborate measures to protect their genome from foreign modification. Because the genome is the blueprint

of the cell, even simple experiments turn out to be complicated. Thus, to understand the underlying principles it might be better to find a biological system which is easy to treat experimentally, but is sufficiently related in its own composition to allow extrapolation of the results to human. An organism fulfilling those requirements is called a *model organism*. But which eukaryotic organism is sufficiently close to human to have a similar biochemistry of signaling and communication without the ethical and experimental problems? Surprisingly, this "relative" has lived undiscovered among us for thousands of years.

1.3 Why yeast?

No other microorganism has been used as extensively by humans as the yeast *Saccharomyces cerevisiae*, which is one of the oldest domesticated organisms [11]. Without doubt yeast is, and has been, the most used microorganism in the history of man. Even though *Saccharomyces cerevisiae* was not discovered until 1680 by Van Leuuwenhook, it has already been employed for beer brewing in Sumeria and Babylonia, for wine production in Georgia, and dough leavening in Egypt around 6.000 B.C. With Van Leeuwenhook began the introduction of yeast into Science when he observed microscopically that beer included a small living organism. However, it took almost 200 years more before yeast was associated with alcoholic fermentation by Cagnaird-Latour in 1835 and it was mostly the work of Louis Pasteur in the 1850s which connected fermentation to the yeast metabolism. The importance of yeast for beer production was fortified in 1837 by Meyen who placed the found organism into a new genus, *Saccharomyces*, and termed the strain discovered in malt *cerevisiae*, for its usage in making beer. With the discovery that yeast alone was capable of producing alcoholic products from sugar began the industrial and scientific usage of yeast, not all of the developments positive as it was also used by Karl Neuberg in 1915 to produce glycerol. Glycerol was used to a large extent as a basis for trinitroglycerol, enabling the introduction of heavy explosives into modern warfare. Nevertheless, yeast led to the early discovery of fundamental biological processes and the realization that proteins within the yeast metabolism catalyze alcoholic fermentation. This is impressively mirrored in the name of these proteins: enzymes, stemming from the Greek expression *en zymi*, in yeast.
With the rise of genetics yeast was introduced as a biological model organism by H. Roman in the mid-1930s and was soon considered an ideal model organism for genetics. This was due to several reasons. First, yeast is an eukaryote, thus having a similar cell architecture and fundamental cellular mechanism as the cells in higher eukaryotes such as animals or human. Second, because in contrast to higher eukaryotes yeast is unicellular, it can be grown on defined media giving a complete control over environmental properties. Third, because yeast reproduces mitotically by budding (simple cell division) as well as meiotically (by sexual reproduction) it is tractable to many classic genetic techniques (compare Figure 1.2). As a consequence the first genetic map of yeast was published by Lindegren already in 1949 [12]. Additionally, yeast has played a large part in the development of reverse genetic engineering and molecular biology when it was discovered in 1978 that it could take up foreign DNA and recombine it into its own genome, a process termed *transformation* [13]. As such, prior to the Yeast Genome Project in 1989 (finalized in 1996) 1.200 genes (about 20% of all yeast genes) had already been mapped to the 16 yeast chromosomes or distinct phenotypes in yeast

[14].
It was not until the Human Genome Project was finished that scientists realized that this small simple organism inherited a huge hidden potential. In fact, yeast shares many similarities with human cells. 31% of the known yeast genes associated with a biological function have homologs in human [15]. Obviously, this is an underestimation as about 1.000 of the 6.000 genes in yeast are not associated with a function yet.

Nowadays, yeast as a model organism has helped to elucidate a large wealth of knowledge about the inner workings of the cell. This comprises biochemical processes – such as carbon, nitrogen and fatty acid metabolism as well as the underlying regulatory mechanisms – cytology studies – such as mechanisms in meiosis and mitosis, and biogenesis of organelles and cytoskeletal structure and function – and genetic regulation – such as mechanisms of recombination, control of cell cycle and gene expression, the involvement of chromatin structure, and the function of oncogenes [11, 15, 16].
However, research on yeast is still ongoing which is illustrated by the observation that in the last 11 years 3 Nobel prizes have been awarded to research performed in yeast (Lee Hartwell in 2001, Roger D. Kornberg in 2006 and Jack W. Szostak in 2009) a streak that has started already in 1907 by Eduard Buchner[3].

In this thesis we will use yeast as a model organisms for another biological process that is shared together with humans: the realization of cell-to-cell communication and its transduction into a directed cellular response. This process is present in yeast in a remarkable signaling mechanism: the yeast pheromone response.

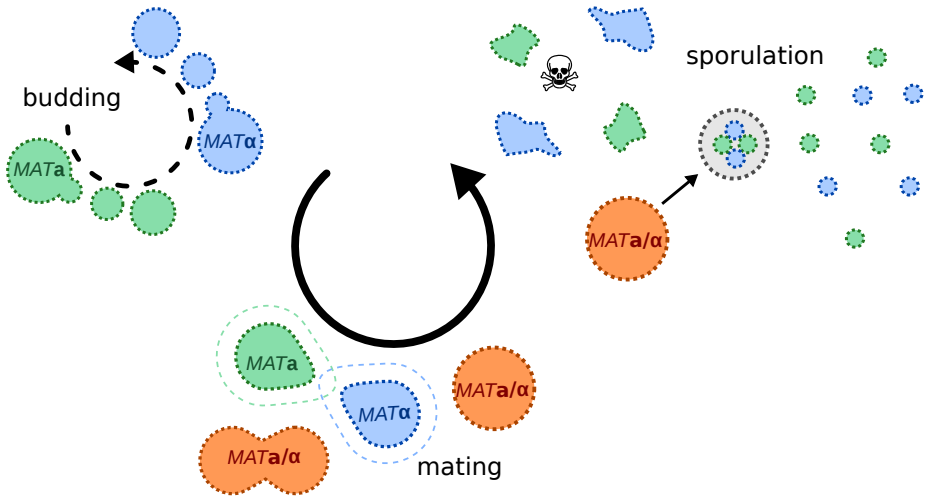

Figure 1.2: The life cycle of *Saccharomyces cerevisiae*. Haploid yeast cells can either reproduce asexually by budding or recombine into a new diploid cell by mating. Diploid cells can produce spores which again yield haploid cells. The transition of a haploid into a diploid population likely takes place in a newly awaken culture.

[3]The first Nobel prizes were awarded in 1901.

1.4 Yeast and pheromones

The most extensively studied signaling pathways in *Saccharomyces cerevisiae*, and probably one of the most studied signaling systems in molecular biology, is the pheromone signaling pathway of $MAT\mathbf{a}$ cells [11]. Budding yeast cells may exist in either the haploid cell state (single set of chromosomes) or the diploid state (double set of chromosomes) and the two states can be traversed by distinct developmental programs. Haploid yeast cells may occur in two mating types, $MAT\mathbf{a}$ and $MAT\boldsymbol{\alpha}$, and are formed from diploid $MAT\mathbf{a}/\boldsymbol{\alpha}$ cells via sporulation.
A diploid cell will always form two $MAT\mathbf{a}$ and two $MAT\boldsymbol{\alpha}$ spores. Spores are dormant haploid cells which can resist a wide variety of unfavorable environmental conditions, most importantly the depletion of nutrients. When the environment returns to a state which allows growth anew, the haploid spores return to the normal haploid cell state, which yields a haploid population again. In contrast $MAT\mathbf{a}/\boldsymbol{\alpha}$ diploids are formed by conjugation of a $MAT\mathbf{a}$ with a $MAT\boldsymbol{\alpha}$ cell. As yeast is not capable of chemotaxis, haploid yeast cells signal their location by the secretion of pheromones into the surrounding environment which will be picked up by nearby mating partners as a cue. Detection by an opposite mating partner then induces the pheromone response which culminates into expression of several mating-specific genes and a change of cell shape in the direction of the pheromone signal, forming a so called "shmoo"[4]. As soon as the $MAT\mathbf{a}$ and $MAT\boldsymbol{\alpha}$ cell touch, they will engage cell fusion, resulting in a diploid cell.
Considering this, the biological function of diploid formation in yeast is not trivial. The common view on diploid formation is that it is necessary since it underlies meiotic reproduction, however, *Saccharomyces cerevisiae* as any other yeast strain, can also reproduce asexually by mitotic division (budding). Consequently, yeast does not require the formation of diploids to reproduce. However, survival of starvation conditions is absolutely dependent on the formation of diploids. Each $MAT\mathbf{a}/\boldsymbol{\alpha}$ diploid will yield four spores which can survive extreme conditions, making it an efficient survival strategy during nutrient depletion. Therefore, diploid formation in yeast might provide a strategy to survive starvation conditions rather than sexual reproduction. This is supported by the observation that many other yeast strains explicitly link the ability to respond to pheromones to nutrient depletion, only triggering diploid formation in those conditions [17, 18]. Even though *Saccharomyces cerevisiae* does not require nutrient depletion in order to induce mating, diploid formation still might be interpreted as a survival strategy (also compare Figure 1.2). Furthermore, since haploid cells will only be present in newly formed yeast populations formed from progenitor spores, this process has to be coordinated with the growth of a new yeast population. As I will show later on, the pheromone response pathway has evolved specifically to achieve that and many parts of the signaling transduction are optimized to maintain population fitness despite the transition from the haploid to the diploid cell state.

1.4.1 The extracellular pheromone signal and its regulation

As mentioned above the signals haploid yeast cells employ in order to detect the presence of nearby mating partners are the pheromones secreted by both cell types. The

[4] A reference to a comic character by Al Capp with a similar body form.

pheromones are denoted *mating factors* and *MAT*$\boldsymbol{\alpha}$ cells secrete $\boldsymbol{\alpha}$-factor whereas *MAT***a** cells secrete **a**-factor. Presence of sufficiently high concentrations of the mating factors induce cell cycle arrest in order to maintain the integrity of the DNA and chromosomes, and induce shmoo formation. Even though both mating types have to react essentially the same, there is a significant level of asymmetry between the signaling in *MAT***a** and *MAT*$\boldsymbol{\alpha}$, which is mostly encountered on the level of the secreted pheromones and its extracellular regulation.
Both pheromones are small oligopeptides composed of 12 (**a**-factor) and 13 amino acids ($\boldsymbol{\alpha}$-factor), however, they differ greatly in export mechanisms and processing. $\boldsymbol{\alpha}$-factor is produced from a larger precursor protein which begins with a secretion signal, followed by four tandem copies of mature $\boldsymbol{\alpha}$-factor, separated by spacers which contain proteolytic sequences [19]. $\boldsymbol{\alpha}$-factor is produced on a low basal concentration from this precursor, and since it contains a secretion signal it is likely to be exported by the vesicular secretion pathway. There is a putative induction of $\boldsymbol{\alpha}$-factor secretion by about 3-fold during activation of the pheromone response in *MAT*$\boldsymbol{\alpha}$ cells, providing a regulated $\boldsymbol{\alpha}$-factor output [20, 21].
a-factor on the other hand is produced as two different molecules, each being present in two gene copies containing a single sequence of mature **a**-factor [22]. This is followed by various modification steps which are under active regulation and include several terminal modifications of the protein, attaching a N-terminal methyl ester and a farnesyl group, both being important for its biological function [23–26]. **a**-factor is not exported via the secretory pathway, but by an active ATP-dependent export catalyzed by the membrane-bound **a**-factor exporter Ste6 [27]. Ste6 is expressed by some basal gene expression but also induced by the activation of the pheromone response in *MAT***a** cells and newly produced Ste6 preferentially recruits to the shmoo tip [28, 29]. Similar to $\boldsymbol{\alpha}$-factor, the production of **a**-factor is up-regulated in response to $\boldsymbol{\alpha}$-factor [20]. However, many mechanisms might lead to the induction of high-level **a**-factor expression, such as gene expression of **a**-factor, regulation of protein modifications or a higher export rate due to larger Ste6 abundances. In any case, the induced expression of **a**-factor by *MAT***a** cells seems to be required in order to trigger the pheromone response in *MAT*$\boldsymbol{\alpha}$ cells, since they only induce mating in sufficiently high concentrations of **a**-factor [30].
As described before, *MAT***a** cells highly regulate the level of **a**-factor they secrete in quantity, by induction of **a**-factor secretion, as well as in location, by recruiting the **a**-factor transporter Ste6 selectively to the shmoo tip. However, this is not the only manner in which *MAT***a** cells regulate the distribution of extracellular pheromones. Interestingly, *MAT***a** also strongly regulate the extracellular distribution of $\boldsymbol{\alpha}$-factor, the pheromone that is not even secreted by them. They achieve that by secretion of the aspartyl protease Bar1 into the extracellular medium which cleaves and, therefore, inactivates $\boldsymbol{\alpha}$-factor. The name Bar1 stems from the ability of the protease to form a barrier for the freely diffusible $\boldsymbol{\alpha}$-factor and illustrates an elegant experiment performed by Hicks and Herskowitz in the seventies in order to demonstrate that Bar1 is indeed active in the extracellular environment (illustrated in Figure 1.3)[31].

The experiment performed by Hicks and Herskowitz included two parts: in the first a streak of *MAT*$\boldsymbol{\alpha}$ cells was placed on an agar plate to the left with a set of micromanipulated assay *MAT***a** cells to the right. Depending on the distance the assay cells would show a continued budding when exposed to low $\boldsymbol{\alpha}$-factor concentrations, or the shmoo phenotype when exposed to high $\boldsymbol{\alpha}$-factor concentrations. Putting a

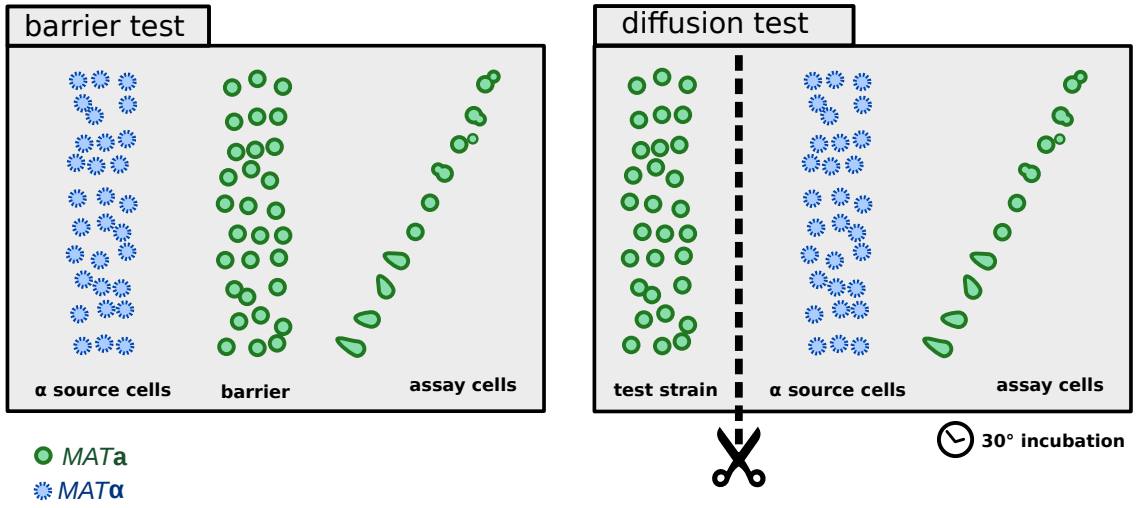

Figure 1.3: The barrier experiment performed by Hicks and Herskowitz demonstrating the presence of a $\boldsymbol{\alpha}$-factor-inhibiting protein in *MAT***a** and the presence of this protein in the extracellular medium.

streak of "barrier" *MAT***a** cells between the source and assay cells, they observed a switch of the assay strain phenotypes from shmooing to budding. Thus the *MAT***a** barrier lowered the perceived $\boldsymbol{\alpha}$-factor concentration. As such, *MAT***a** cells must have an intrinsic ability to lower the activity of $\boldsymbol{\alpha}$-factor.
In a second experiment the streak of *MAT***a** cells was now put to the left of the source cells incubated for a short period, cut away, and the source and assay strains observed under the microscope for up to 24 hours. When using wild type *MAT***a** cells this again led to a switch from the shmoo phenotype to budding, however, this was not the case for an empty lane or *MAT***a** mutants lacking the *BAR1* gene. Since the *MAT***a** test cells were cut away before measurement only substances secreted into the extracellular space would be able to influence the response of the assay *MAT***a** cells. They concluded that the gene *BAR1* must encode for a protein inhibiting $\boldsymbol{\alpha}$-factor which additionally is secreted into the extracellular medium.
Later, the activity of Bar1 in the extracellular medium of *MAT***a** cells was confirmed and it was also shown that Bar1 secretion by *MAT***a** cells increases by about 3 to 5-fold when stimulating the cells with $\boldsymbol{\alpha}$-factor [32]. Finally, Bar1 was identified as a aspartyl protease cleaving $\boldsymbol{\alpha}$-factor between Leu6 and Lys7 and thereby rendering it non-functional [33, 34].
Even though the activity of Bar1 is characterized, we still lack a distinct understanding, why *MAT***a** cells have an intrinsic activity to destroy the signal they need to sense ($\boldsymbol{\alpha}$-factor). The striking difference to many other negative regulators of signaling is that Bar1 is exported into the extracellular medium of cell populations where it remains active. I will introduce a possible explanation for this behavior in section 3.2.

1.4.2 The signaling pathway of MATa cells

Despite the fact that *MAT***a** and *MAT*$\boldsymbol{\alpha}$ cells differ in the way they secrete and regulate the extracellular pheromones, there are only little differences on the level of the intracellular signaling pathway. As a convention, genetic analyses have, thus,

concentrated on the signaling pathway in *MAT***a** cells.
As pointed out before, two processes have to coordinated during pheromone signaling:

1. induction of pheromone response-specific genes, in case there is a potential mating partner and if the external pheromone signal permits succesful mating, and [35]

2. recruitment of various proteins to the membrane site closest to the potential mating partner in order to induce shmoo formation and initiate cell-cell fusion by the formation of a large multi-protein complex (the "polarisome")[36].

Thus, *MAT***a** cells have to synchronize pheromone-dependent gene expression with cell polarization, a feat that is realized by a complex signaling cascade.

In *MAT***a** cells the pheromone response is initiated by binding of $\boldsymbol{\alpha}$-factor to the seven transmembrane-bound receptor Ste2. Binding of the $\boldsymbol{\alpha}$-factor to the third extracellular loop is a multi-step process which leads to a high affinity of Ste2 for $\boldsymbol{\alpha}$-factor and goes along with a conformational change of the receptor [37–39]. This activates the C-terminal end of the receptor which transmits the active state into the cell [40]. The C-terminal end of the receptor is also subject to various modifications which control its activity. The most important regulation takes place on the level of receptor turnover at the membrane. A single Ste2 molecule normally spends only little time on the yeast membrane since it is constantly phosphorylated by the kinases Yck1, Yck2 and Yck3. The phosphorylation then induces internalization of the receptor by the ubiquitination pathway with final destiny either being the vacuole or a return to the membrane [41–43].

The active C-terminal end of the receptor transmits the signal by interacting with a heterotrimeric G protein consisting of the proteins Gpa1 (G_α), Ste4 and Ste18 ($G_{\beta\gamma}$) [44]. The inactive G protein exists in a trimer state with a $G_\alpha^{GDP}G_{\beta\gamma}$ configuration. Interaction of the C terminus of Ste2 triggers exchange of the previously bound GDP with GTP which yields an unstable $G_\alpha^{GTP}G_{\beta\gamma}$ state where the $G_{\beta\gamma}$ dimer rapidly dissociates from the trimer and yields a free G_α^{GTP} subunit [45]. Different from many other organisms, further activation of the pathway is not promoted by the active G_α^{GTP} subunit but rather by the $G_{\beta\gamma}$ dimer.
In *Saccharomyces cerevisiae* G_α is instead used to regulate the activity of the G protein by various mechanisms. First of all, G_α has an intrinsic GTPase activity that may catalyze a spontaneous dephosphorylation of the bound GTP to GDP which returns G_α to its high affinity state for $G_{\beta\gamma}$, thus, again capturing it and resulting in the inactive trimer. Furthermore, the transient interaction of G_α with Ste2 keeps the the activated G_α close to its $G_{\beta\gamma}$ binding partners [46, 47]. This might promote a fast inactivation as the interaction partners remain close.
The intrinsic GTPase activity can be increased by two to three orders of magnitude due to interaction of the protein Sst2 with G_α [48]. Sst2 belongs to the family of RGS proteins (regulator of G protein signaling) and seems to be responsible for deactivation of the pathway by a fast hydrolyzation of G proteins. Absence of Sst2 leads to a hypersensitivity to $\boldsymbol{\alpha}$-factor as well as a prolonged inhibition of cell cycle progression. Sst2 itself is regulated on the transcriptional as well as on the posttranscriptional level [49]. Here, expression of Sst2 is induced by activation of pheromone-dependent gene

expression, which provides an increased level of Sst2 and, thus, a negative feedback on G protein activation as it accelerates deactivation of G protein subunits. Additionally, Sst2 is also phosphorylated by the active MAPK Fus3[5] which induces degradation of Sst2 by the ubiquitin pathway. This promotes a positive feedback on the pheromone pathway which acts on a small time scale and probably serves the regulation of the duration of pathway activation. Finally, Sst2 binds to the receptor Ste2 in the same region the Yck kinases do [50]. However, it is still unclear what function this might fulfill, though it has been argued that it might promote a close coupling of Sst2 with Ste2-bound Gpa1, promoting an efficient inhibition.

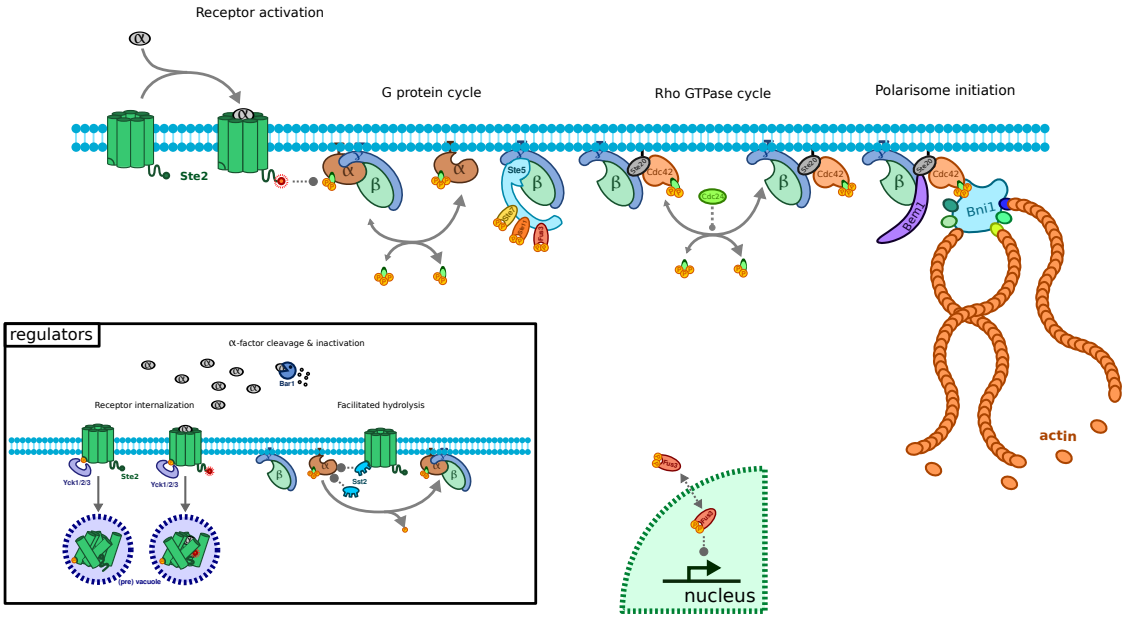

Figure 1.4: Overview of the pheromone response pathway in *MAT***a** cells of *Saccharomyces cerevisiae*.

As mentioned before, further signaling is driven by the $G_{\beta\gamma}$ subunit which recruits a variety of proteins to the membrane in order to drive all further pathway activation. The two subunits of the $G_{\beta\gamma}$ protein fulfill distinct functions. The γ-subunit Ste18 is responsible for the membrane binding of $G_{\beta\gamma}$. This is realized by a dual lipid modification consisting of a farnesylation and a palmitoylation which tether the γ-subunit to the membrane [51]. This is crucial for the function of $G_{\beta\gamma}$ and a deletion of the lipid binding domain leads to deficiencies in signaling. Additionally, a full deletion of Ste18 leads to a complete loss of the ability to mate [52–54]. The β-subunit Ste4 rather serves as a multiple adapter which sequestrates all the proteins binding $G_{\beta\gamma}$. A deletion of Ste4 also leads to an absence of pheromone sensitivity [55, 56]. As a consequence, the ability to sequester proteins as well as the ability to sequester those proteins specifically to the membrane is crucial to the activity of the pathway.

[5] a kinase activated later in the pheromone response

Two routes have to be completed downstream from the G protein: activation of gene expression and construction of the protein complex forming the shmoo. As the two use distinct sets of proteins and pathways I will start with the signaling route leading to the expression of the pheromone-specific genes and continue with the formation of the polarisome afterwards.

1.4.3 The path to gene expression

In order to relay the signal from the membrane to the nucleus *Saccharomyces cerevisiae* employs a conserved mitogen-activated kinase cascade (MAPK cascade) [57]. Here, a phosphorelay system consisting of three kinases, Ste11, Ste7 and Fus3, is used. Upon activation of the G protein double phosphorylated Ste11 phosphorylates and activates Ste7, yielding double phosphorylated Ste7^{PP}, which in turn phosphorylates and activates Fus3, yielding double phosphorylated Fus3^{PP}, the central effector protein within the pheromone response. Ste11 also phosphorylates Kss1, the central protein for the filamentous growth response [58]. Activated Fus3 induces transcriptional activation and cell cycle arrest by phosphorylation of a variety of downstream signaling components.

The kinases are not activated directly by interaction with the $G_{\beta\gamma}$ subunit of the G protein but require the prior binding to the scaffold protein Ste5 [59]. Ste5 tethers the three kinases into a close proximity and, upon pheromone induction, it is recruited to the membrane by binding the β-subunit of $G_{\beta\gamma}$ and also as connects directly to the membrane via an internal PM/NLS domain [60, 61]. The recruitment to the membrane as well as the binding to $G_{\beta\gamma}$ are required for a tight connection of Ste5 and promotion of MAPK activation [62].
Even though scaffold proteins are known to be important parts of signaling networks none has been as well studied as Ste5 [63, 64]. Ste5 strongly regulates the behavior of the signaling cascade by controlling the activation of the bound kinases. Major parts of the regulation and feedbacks in the pheromone response are exercised on Ste5. The most important being a negative feedback somehow related to Sst2 which limits the time Ste5 resides on the membrane as well as a competitive phosphorylation and dephosphorylation cycle of Ste5 by Fus3 and Ptc1. It has been shown that the negative feedback is required to align the activation of the pathway with the activation of the receptor Ste2 [65]. This enables a a pheromone response which efficiently incorporates the information of the occupied receptors. The phosphorylation cycle on Ste5 however is exercised directly by the kinase Fus3 and the phosphatase Ptc1 [66]. Here, Fus3 as well as Ptc1 bind to specific docking motives on Ste5 and then compete for the phosphorylation (by Fus3) and dephosphorylation (by Ptc1) of four residues on Ste5. A full phosphorylation is required for a fast dissociation of phosphorylated Fus3^{PP}, thus, providing a strong positive feedback which is thresholded by a fast dephosphorylation by Ptc1. As this process is tightly local to Ste5 this results in a tightly coupled feedback. As a result, the activation of Fus3 has a steep sigmoidal form where low pheromone concentrations result in low levels of Fus3 phosphorylation as it remains bound to Ste5. A high pheromone concentration, however, results in a rapid release of activated Fus3^{PP} and a stable high concentration of Fus3^{PP}. Consequently, the activation of Fus3 shows a Hill-like kinetic with an unusually high Hill coefficient which is an order of magnitude higher than normaaly known for phosphorylation cycles. The

response encoded in Fus3 is therefore essentially switch-like, leading to a full activation of Fus3 when a threshold concentration is crossed. The decision to express pheromone-induced genes or not is an all-or-none commitment regulated by Ste5. On the contrary, activation of Kss1 is independent of Ste5 and does only require active Ste7.
As mentioned before, membrane recruitment of Ste5 is required for activation of the MAPK cascade. Initiation of this cascade requires an initial phosphorylation for the activation of Ste11 taking place at one the membrane. This reaction is catalyzed by the protein Ste20 a member of a large family of kinases, the p21-activated kinases. Ste20 resides on the membrane and activates Ste11 after it has been recruited along with Ste5 [67, 68]. The activity of Ste20 strongly depends on binding to active $G_{\beta\gamma}$ as well as binding to proteins involved in formation of the polarisome, such as Cdc42 and Bem1 [69–72]. This results in a co-localization of Ste20 with the sites of active polarisome formation, thus, explicitly coupling the activation of Fus3 to the correct formation of the polarisome [73].

Activation of Fus3 strongly depends on membrane recruitment of Ste5. However, as Ste5 also binds the membrane with a low affinity in absence of $G_{\beta\gamma}$, there is a low basal activity of Fus3 in the in the absence of pheromone [74]. Activation of gene expression induced by this basal activity is prevented by the switch-like response of Fus3 on Ste5 but also by unspecific phosphorylation of Fus3 in the cytosol. Because the regulation of gene expression of Fus3 takes place in the nucleus, this dephosphorylation results in a gradient of Fus3 phosphorylation emanating from the membrane and declining as it approaches the nucleus [75]. It has been speculated that the basal activity allows for a high signaling fidelity and enables a fast response which can deal with extracellular signals that change rapidly [74].

As soon as $Fus3^{PP}$ reaches the nucleus, it associates with a protein complex containing the transcription factor Ste12 [76]. Ste12 controls the expression of two distinct set of proteins: proteins required for the pheromone response and proteins required for a filamentous growth response induced by nutrient depletion [77]. The complex required for the activation of pheromone-specific genes consists of Ste12 bound to the two repressors Dig1 and Dig2 [78]. $Fus3^{PP}$phosphorylates all of the three proteins which relieves the repression of Dig1 and Dig2 and enables binding of Ste12 to the pheromone response elements (PRE) that encode loci for pheromone specific genes [79, 80]. Binding of liberated Ste12 finally induces the gene expression of pheromone-specific genes.
Apart from expressing pheromone-specific genes, Ste12 also participates in the expression of genes specific to the filamentous growth response. This response is activated in conditions with diminishing nutrients and results in the formation of long connected cells in order to invade a new environment [11]. During filamentous growth, Kss1 is phosphorylated by the same MAPK cascade employed in the pheromone response in a Ste5-independent manner. Double phosphorylated $Kss1^{PP}$ also interacts with Ste12 complexes. However, the complex responsible for induction of the filamentous growth response consists of Ste12, Dig1 and Tec1 [77]. Kss1 phosphorylates all three proteins in the same manner as Fus3 but its phosphorylation leads to a derepression of Dig1 and a stabilization of Tec1. The liberated Ste12-Tec1 complex than binds to several loci encoding for filamentous response-specific genes ($FREs$). But how do cells avoid an unwanted activation of the filamentous growth response by activation of the

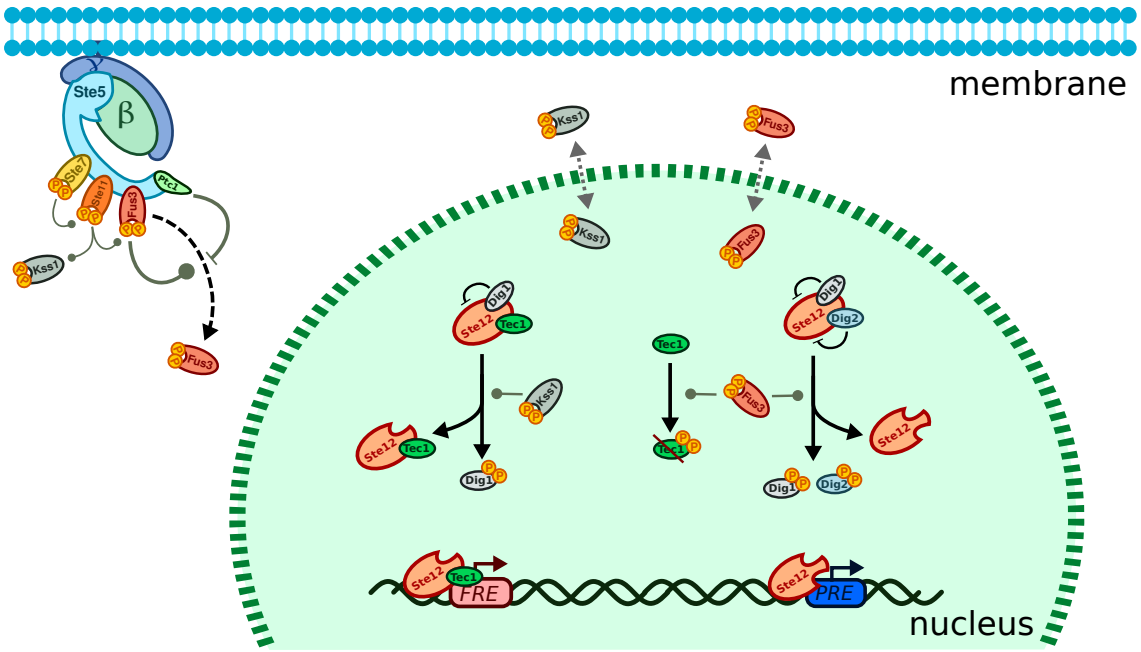

Figure 1.5: The activation of Fus3 on Ste5 and its effect on the gene expression. Fus3 blocks activation of the filamentous growth response by inducing the degradation of Tec1, a component of the filamentous transcription factor complex. The small P indicates phosphorylation events.

pheromone response? This is also achieved by $Fus3^{PP}$ which phosphorylates Tec1 and therefore targets it for ubiquitin-dependent degradation [81, 82]. Kss1 on the other hand is incapable of phosphorylating Dig2 and, thus, the Ste12-Dig1-Dig2 complex can not be derepressed by Kss1, which blocks expression of pheromone-specific genes by Kss1 (also illustrated in Figure 1.5). Cell cycle progression is blocked in both pathways (filamentous growth and pheromone response) by inducing the expression of the protein Far1, which binds and inhibits the cell cycle regulator Cdc28 [83, 84]. This results in an arrest of the *MAT***a** cell in a cell cycle stage prior to DNA replication, the *G1 phase*. In all other phases of the cell cycle, the yeast pheromone response can not be initiated due to deactivation of Ste5 by proteins involved in cell cycle progression [85]. This ensures that signaling may take place exclusively in the G1 phase.

1.4.4 The polarisome and induction of cell-cell fusion

Apart from inducing pheromone-specific genes, *MAT***a** cells also need to prepare cell fusion by forming the shmoo. This is achieved by a large protein complex which is mainly preformed at the membrane, but whose final activation depends on the pheromone-induced gene expression. The formation of this complex is restricted to the sites of the highest extracellular pheromone signal, thus, involving a spontaneous symmetry breaking in the spatial distribution of those complexes on the membrane. This specialized localization is driven by two major steps [86]:

1. initial spontaneous binding of a Rho-GTPase cycle which is stabilized by a positive feedback, and

2. recruitment of various proteins which promote the reorganization of the actin cytoskeleton, transport of new cell wall material and proteins involved in cell-cell fusion as well as membrane rearrangements.

The involvement of Rho proteins in the formation of localized protein complexes within the cell is highly conserved in eukaryotes and is used in various processes, for instance mitotic division, cell migration, dendrite formation, embryonic development, and neutrophil polarity [87–92]. The name Rho stems from its close homology to the small G protein Ras (Ras HOmolog) and all Rho proteins are small G proteins with an intrinsic GTPase activity, thus, having an active GTP-bound form as well as an inactive GDP-bound form.
In *Saccharomyces cerevisiae*, as well as in many other eukaryotes, the principal Rho protein promoting cell polarization is Cdc42. Cdc42 is capable of inducing spontaneous symmetry breaking and is required for the formation of the mating projection during the pheromone response [93, 94]. Activation of Cdc42 by a GTP-GDP exchange on the inactive GDP-bound Cdc42 is catalyzed by the guanosine exchange factor (GEF) Cdc24 [95, 96]. During the pheromone response Cdc42 is recruited to the membrane sites with high extracellular pheromone concentrations by interaction with Ste20, which links it to the active $G_{\beta\gamma}$ subunit [97–99]. Activation of the pheromone response leads to expression of the nuclear export receptor Msn5 which catalyzes the export of a Far1-Cdc24 complex [100]. Cytosolic Far1 then links Cdc24 to $G_{\beta\gamma}$ by binding directly to $G_{\beta\gamma}$ [101, 102].

As the Ste20-Cdc42 complex is also linked to $G_{\beta\gamma}$, this promotes initial activation of Cdc42. However, membrane-bound Cdc24 also recruits the protein Bem1 which binds $G_{\beta\gamma}$, Ste5 and Ste20 [103]. This double recruitment allows the activation of nearby Cdc42 molecules by forming clusters, thus, enabling a positive feedback where single active Cdc42-Cdc24 complexes promote the recruitment of further Cdc42 and Cdc24 molecules. This positive feedback is sufficient to induce a strong polarization of active Cdc42 where activation of Cdc42 is enhanced on membrane-sites with high levels of Cdc42 but quickly drops at sites where only few active Cdc42 molecules are present [104, 105].
Stably activated Cdc42 then targets the recruitment of various proteins to the site of polarization and induces a reorganization of the actin cytoskeleton. This is achieved by the recruitment of the proteins Bni1, Pea2 and Bud6. Bni1 is a formin which is capable of recruiting actin and initiating the formation of actin cables at the site of polarization in a Cdc42-dependent manner [106]. The formation of actin cables at the recruited Bni1 is initiated by Bud6 which is regulated by the recruited Pea2 [107, 108]. This leads to the formation of actin cables which originate at the site of polarization and promote the active transport of new cell wall material and several proteins required for pheromone signaling and cell-cell fusion.

The polarisome also recruits several regulators of cell-cell fusion. This includes Bem3, a negative regulator of Cdc42 which controls the termination of mating projection formation, and proteins required for membrane fusion of the mating *MAT***a** and *MAT*$\boldsymbol{\alpha}$ cell such as Fus1, Fus2 and Por1 [36, 86]. The formation of an intact mating projection with a stable membrane is further promoted by the recruitment of the protein Spa2 which forms a scaffold for the the sensors of the cell wall integrity pathway, Mkk1 and Mpk1 [109–112].

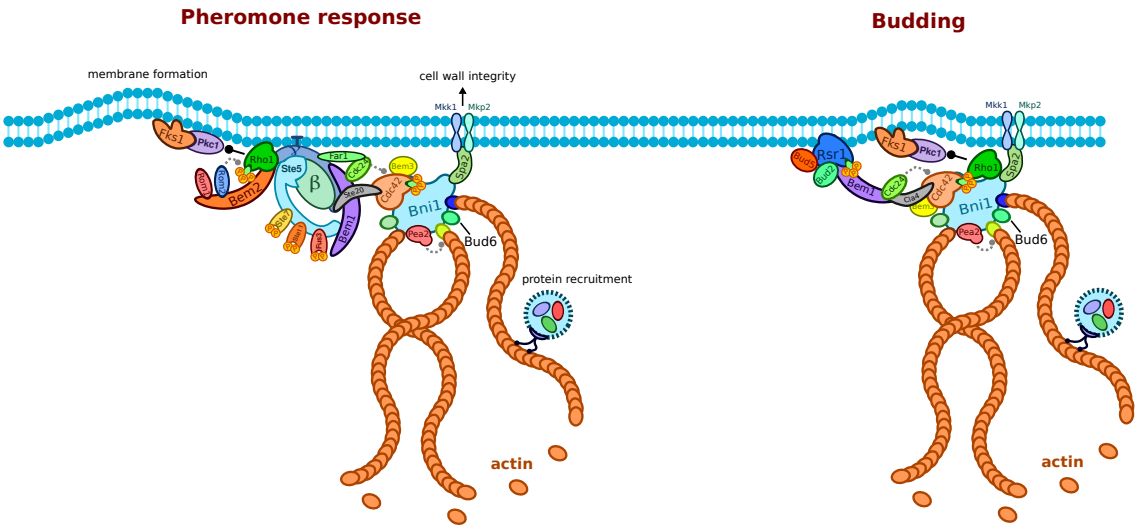

Figure 1.6: Components involved in the formation of the polarisome and budding of *Saccharomyces cerevisiae*.

Formation of new cell wall is catalyzed by recycling several proteins that are also involved in the mitotic division of *Saccharomyces cerevisiae*, more specifically: in bud formation. This includes another Rho-GTPase cycle consisting of the Rho protein Rho1 and its regulators Rom1, Rom2 and Bem2 [113–115]. Rho1 directly binds to $G_{\beta\gamma}$ and induces the recruitment and activation of protein kinase C (Pkc1) and Fks1, which directly results in the formation of new membrane on the sites of active Rho1 [116, 117].

Interestingly, the spontaneous selection of the bud site itself uses the same mechanism as the polarization in the pheromone response. During mitotic division the bud site is not marked by active $G_{\beta\gamma}$, but by yet another Rho-GTPase cycle consisting of the proteins Rsr1, Bud2 and Bud5 which are constitutively active on the membrane during G1 phase [118]. Rsr1 also recruits Bem1, thus, inducing two negative feedback loops by Cdc42-Cdc24 and Rsr1-Bud2-Bud5. This induces strong symmetry breaking and creates the clue for the new bud site [119]. As a result, *MAT***a** cells subject to a uniform pheromone concentration and, thus, a uniform $G_{\beta\gamma}$ profile will form mating projections that coincide with the former bud site which further illustrates the strong connection between mitotic division and the formation of the mating projection [120, 121].

1.4.5 A blueprint for spatial signaling in human cells?

I have argued before that *Saccharomyces cerevisiae* is an excellent modeling organism for human cell lines, but what can we gain from studying only one specific signaling pathway in yeast? Despite the fact that *Homo sapiens* has several different pathways controlling cellular shape and spatially directed responses, virtually all of them show the same mechanisms as the yeast pheromone response. Of course, we find a much more complicated picture as in yeast. However, this is mostly due to a higher level of regulation, as most human cells are highly specialized in function. Nevertheless, not only the mechanisms are conserved but also the individual participating proteins.

What is the reason for that? The answer lies in the importance of those signaling pathways. Spatial segregation is essential for the organization and correct functioning of higher eukaryotes. Important processes where cells have to respond to signals in space and initiate directed responses include developmental programs, neural growth, the immune response and intracellular organization of the spindle bodies during cell division [122–131]. Mutations in key components, thus, have vile consequences and lead to inviable cells, which is why many mutations in those proteins are disease-associated [132]. As a consequence, those proteins are strictly conserved in human.
Many proteins involved in the pheromone response can be found in humans in the same configuration as in yeast with remarkable homology. Transmembrane receptors as Ste2 are involved in a vast majority of human signaling pathway, the *GPA1* gene encoding for the G_α subunit in yeast has a homolog in almost all higher eukaryotes, (*GNAI2*). The same holds for *FUS3* which is encoded by *MAPK3* in higher eukaryotes and *STE20* which is encoded by *SLK*. Many components of the polarisome are conserved as well and the essential Cdc42-dependent mechanism is conserved to such a degree, that a deletion of Cdc42 in *Saccharomyces cerevisiae* can be complemented by its human counter-part, the Cdc42 of *Homo sapiens*. Particularly the studies with Cdc42 have shown that cell polarization in human is governed by the same principles as in the pheromone response of yeast and takes place in processes such as dendrite formation, immune responses, epithelial morphogenesis and the formation of filopodia [133–135, 92]. Additionally, the Wiskott-Aldrich syndrome an X-chromosomal immuno-deficiency is directly connected to a malfunctioning Cdc42 [136].

Given that tight relation between signaling in yeast and the signaling pathways occurring during cell polarization in human, we can probably extrapolate results from yeast to human. The pheromone response in yeast serves the search for nearby cells of opposing mating type and a dependent gene expression as well as polarization of the cell in the direction of the potential mating partner. However, the important question here is why the pheromone response in yeast, as well as many other pathways, is composed the way it is. The question how the proteins and their interactions in the pheromone response deliver the required functionality will therefore be our scope from hereon.

1.5 The Systems Biology of yeast signaling

The ease of experimental manipulation and the wealth of already existing knowledge have made signaling in yeast one of the principal objects of study in Systems Biology. This is also due to a good timing. In the mid nineties, many favorable circumstances came together in order to secure the entry of yeast into Systems Biology. The Human Genome Project was finished, the analyses had begun, and it became more and more obvious that many proteins in human were homologes of yeast proteins, particularly in signaling. At the same time, computers started to become cheap and more powerful and the mathematical methods applying to dynamic systems could finally employed on a large scale in order to simulate the behavior of complex biological systems. Last, but not least, the molecular biology of yeast was well established at this point and many questions concerning dynamic behavior had arisen already. As such the time was right to establish the first successful cycles of Systems Biology in this field.

Two pathways in *Saccharomyces cerevisiae* were extensively studied employing the methodology of Systems Biology: the osmotic shock response and the pheromone response. The first, because it existed in the same form in all higher eukaryotes and was thought to be prototypical for the way cells dealt with stress, and the latter because it employed intercellular communication and a complex transcriptional program.
It was the introduction of mathematical methods that could predict the behavior of the systems in time, that made Systems Biology so prominent here, since data could be generated by experimentation in the same manner. Starting from initial coarse models that could reproduce the system at least qualitative in the mid nineties the Systems Biology practice rapidly took over the research of those pathways, delivering more and more complex and quantitative models by 2010 which could be validated experimentally [66, 75, 137–139].

For the pheromone response in yeast the methodology of Systems Biology has developed to be the prominent strategy in investigating the function of the pathway. Most research has concentrated on modeling and understanding the path from receptor binding to gene expression. The first full model of those processes was developed by Kofahl and Klipp in 2004 and could already explain the various mutants and reproduce the dynamics of the pathway [140]. A reduced model was used in 2005 in a combined model of several signaling cascades in yeast in order to predict several new features during the osmotic stress response, which could be validated experimentally [141]. Further research concentrated on the scaffold Ste5 and its regulatory ability during the pheromone response. It was mainly Systems Biology that elucidated Ste5's function in regulating the signal transduction and its essential ability to convert a continuous input in an ultrasensitive switch [64, 66, 142, 143]. As such, the function of Ste5 was identified to enable the cells to execute an all-or-none response, an essential feature as yeast cells have to commit to forming a diploid or continuing budding, but can not execute an intermediate of those two processes.
Recently, there have also been attempts to model the process of polarization in *Saccharomyces cerevisiae* in order to investigate how yeast cells can maintain a strict polarization. It was discovered that yeast employs a mechanisms which is in perfect agreement with the requirements Turing proposed in 1952 in order to promote formation of patterns, and that polarization is mainly promoted by the Cdc42 activation cycle[105, 144, 145].

However, there are still basic question remaining about the signaling and communication between yeast cells. As mentioned earlier, the research of the pheromone response began with the observation that yeast cells secrete specific pheromones in order to signal their location to potential mating partners. From early on it was assumed that this would create complex gradients in mating yeast populations. However, this part was skipped in further research and virtually all further studies would study the response of the pathway to artificially added concentrations of pheromone or to gradients which were introduced artificially as well. Today, we still have no idea how the distribution of pheromone looks *in vivo*. However, from higher eukaryotes we know that the control of signaling molecules is crucial for the functioning of cell populations. In humans the availability of growth factors, for instance, is highly controlled and restricted to small spatial areas in order to promote regulated growth. For this we have developed several mechanisms which include local dispersal of signaling components,

negative regulation of their presence and spatial segregation which is provided by organelles and the vessel system. Studying *Saccharomyces cerevisiae* in this context is interesting as it seems to be a system in transition from a simple single cell organism to an entity which entails cell-cell communication. Additionally, yeast is one of the first eukaryotic organisms where an extracellular control of the signaling components in form of a negative regulation by Bar1 has been shown. This makes Bar1 secretion a prime example for the regulation of signaling components in a cell population. As such, I will place large emphasis on introducing a combined experimental and theoretical assay in order to visualize and quantify the distribution of pheromones in mating yeast populations and present a cooperative mechanism of Bar1-induced regulation of the pheromone signal in chapter 3.2.
Other open questions regard the the response of the cells to a shallow or noisy signal. Even with very high secretion rates of $\boldsymbol{\alpha}$-factor the fast diffusion of this small peptide will result in very shallow signals where often only a few $\boldsymbol{\alpha}$-factor molecules are present on any given *MAT***a** cell. Still, we can observe a reliable activation of the pathway, even with a very high noise level in the order of magnitude of the actual pheromone concentration. How can yeast cells reliably detect the distance to a nearby mating partner in the presence of those noise levels? Using an *in silico* system which can be used to study the complete pathway activation in time and space, we will describe a possible mechanism in chapter 3.3.
Following the sensing of extracellular signals all pathways inducing polarization are capable of condensing even shallow differences of activated receptors on the membrane to a single dense point of active polarisomes. This condensation is so extreme that even *MAT***a** cells exposed to an artificially homogeneous $\boldsymbol{\alpha}$-factor concentration will form single polarisome structures on a random position on the membrane.
Even though the Turing mechanism explains how this asymmetry is maintained stably, it remains an open question how this strong amplification of spatial differences occurs and how it is condensed into a single point-like structure on the membrane. We will treat this problem in chapter 3.4 and show that the formation of a multi-protein complex, as given by the polarisome, has the potential of providing a single strong polarization as a emergent property by controlling the location and quantity of polarisome complexes in a gradient-dependent manner.

However, in order to study all of those effects we will first have to dive deeper into the experimental and theoretical methodology which is available to study a signaling process taking place in time as well as space.

2 Systems Biology of reaction-diffusion systems

2.1 2012: Another Space Odyssey

A reaction-diffusion system is a biological system whose behavior is, as the name suggests, governed by two processes: biochemical reactions and passive or active diffusion. The biological entities which can be considered here are numerous and stretch over several space scales, the most popular being small molecules, proteins, multi-protein structures and cellular organisms. Both processes, reactions and diffusion, are assumed to have an influence on the behavior of the system, where reactions change the system in a temporal manner and diffusion does so in a spatial manner. As a consequence, one crucial part is to track the system in time as well as space.
Even in a standard setting, recovering the functionality of a biological system will result in performing many experiments and model modifications. This complicates even more in reaction-diffusion systems, because we treat space as an explicit variable. This can be illustrated easily when looking at the functionality that has to be recovered. In general our system behaves according to a multidimensional function $\mathbf{F}$ depending on some parameters $\boldsymbol{\theta}$[1] and the independent variables $\boldsymbol{\nu}$[2]. If we assume this relationship, the state of the system $\mathbf{S}$ is given as

$$\mathbf{S} = \mathbf{F}(\boldsymbol{\theta}, \boldsymbol{\nu}) \tag{2.1}$$

Obviously, the complexity of finding $\mathbf{F}$, possibly along with $\boldsymbol{\theta}$, depends on the complexity of $\boldsymbol{\nu}$. In "classical" Systems Biology the only considered independent variable is the time ($\boldsymbol{\nu} = t$). So one typical way to enter the Systems Biology cycle would be by measuring some biological quantity for a set of time points and relating this to some quantity of the modeled state $\mathbf{S}$. For this we will need one data point per time point, so the complexity equals the number of time points. However, as argued before, reaction-diffusion system require that space is explicitly treated as an independent variable. This transfers the problem from a univariate to a multivariate problem with $\boldsymbol{\nu} = \{t, \mathbf{x}\}$. Additionally, space is usually multidimensional by itself, for instance being composed as $\mathbf{x} = \{x_x, x_y\}$ in a 2-D system. The resulting rise in complexity can be seen by a simple example. A typical resolution for a fluorescence microscopy picture is 512×512 pixels. Thus, where we had one data point per time point in a "classical" model, every pixel will now have a different location in space, which results in more than 250,000 data points per time point in a reaction-diffusion system.

[1] From hereon all bold variables will denote vectors and all cursive variables scalars. The same holds for function, thus, bold functions return vectors.

[2] Independent variables denote quantities which are not governed by the system but rather drive the system such as time, pressure, etc.

This argument holds for the complexity of experimental as well as for the complexity of computational methods and creates the major obstacle when studying reaction-diffusion systems. Thus, it is not advisable to use this framework for biological systems where we expect the behavior to be homogeneous in space, since there is no apparent use in considering space if it does not influence the system. On the other hand, it might be crucial to treat space explicitly in biological systems which show strong spatial inhomogeneities. The biological system treated in this thesis clearly belongs to this second class, which is why we will now introduce the experimental methodology which is needed to treat those systems experimentally as well as computationally.

2.2 Experimental Techniques

Experimentally probing the studied biological system is crucial in a working Systems Biology study and is much too often neglected. This is due to the fact that often the model is confused to be an alternative to study the biological system, but as has been pointed out in section 1.2, it is just the representation of a hypothesis and does not describe the biological system *per se*. There is no way around testing the model, i.e. the hypothesis, against the biological system in order to neglect or accept it. As a consequence, the quality of our model, and with that also the quality of our functional understanding of the system, will depend on how rigorously we challenge it by experiments. This is why we will begin with the experimental techniques, since without them there would be little use in Systems Biology.
The major difference in treating a system as a reaction-diffusion system is the explicit treatment of space. This makes experimental techniques delivering spatial data the most important in studying reaction-diffusion systems. The obvious technique fulfilling that requirement is microscopy, which is certainly the most established experimental technique to study biological systems in space. Additional, since large parts of this thesis deal with population effects there is also a direct requirement to quantify cellular behavior on a population level. In principle, one could also use microscopy to do that, but this would only allow studying very small, and possibly unrepresentative, fraction of the population. Thus, we will also provide some techniques which allow us to use the same cell populations used for microscopy, but in combination with assays better-suited for populations studies. Finally, there will be a short overview concerning the basic ways one can genetically modify yeast (yeast transformation) in order to visualize and study the reaction-diffusion dynamics.

2.2.1 Fluorescence microscopy

Molecular Fluorescence

The discovery of fluorescence goes back to the Irish physicist George Gabriel Stokes. In a particularly elegant experiment in 1852 he moved a tube of quinine through the solar spectrum formed by means of a prism. As long as he would move the tube through the visible spectrum of light it would remain transparent but as soon as he passed the visible violet part of the spectrum into the ultraviolet the tube would start emitting a bright blue color [146]. Stokes concluded that the incoming non-visible light was somehow modified by the quinine and emitted as light of a longer wave length. He named this phenomenon *fluorescence*, coming from the mineral fluorite which showed

the same behavior. The apparent shift in wave lengths is hence called the *Stokes shift* and is the basis for any functional fluorophore [147]. During a Stokes shift some part of the incoming light is absorbed by the fluorescent molecules and leads to a shift in the internal energy of the molecules into a higher energy level, thus, electrons move to higher orbitals (excitation). A molecule in an excited state may spontaneously return to its ground state by emitting the remaining energy difference through light. However, some part of the energy of the incoming photon is lost due to changes in the rotational or vibrational state of the molecules.
Excited molecules may spontaneously return to their ground state by emitting photons with an energy which equals the difference in their current state and the ground state. The wave length λ of the emitted photon will be given by

$$\lambda = \frac{h \cdot c}{E} \tag{2.2}$$

and, thus, by the Planck constant h the speed of light c and the photons energy E [148]. Due to the internal loss of energy, this will result in emitted light with a longer wave length, however, it took almost 100 years after Stokes discovery before this was known. Excitation occurs rapidly within the order of femtoseconds and emission usually occurs within nanoseconds after excitation, which, by any human standard, makes fluorescence an instantaneous process. However, fluorescent molecules are limited to absorbing photons which correspond to possible energy transitions within the molecules. As a consequence, fluorophores will only absorb a small part of the spectrum, called the excitation spectrum. This also results in a specific emission spectrum which corresponds to the possible transitions the molecule may undergo from the excited to the ground state.
When studying biological systems *in vivo* one is mostly interested in using fluorophores which can be excited with relatively low energy light from the visual spectrum in order to minimize interference with the system. This property is usually provided in the presence of conjugated double-bonds, especially within aromatic rings, where the delocalization of π-orbitals assists passage into a higher energy state. Here, the most popular representative is certainly the enhanced green fluorescent protein (eGFP), a derivative of the original green fluorescent protein from the jellyfish *Aequorea victoria* [149]. It exhibits an excitation maximum at a wave length of 475 nm and shows a good absorption coefficient, quantum yield and slow bleaching [150]. Most importantly, since the DNA sequence is known, one can integrate it within the genome of living organisms and, thus, use it to visualize protein location or processes such as gene activation [151].

Most fluorophores used within cellular systems are derivatives of GFP, yielding a variety of different colors and enabling combinations of several fluorophores. Even though there are many individual criteria by which a fluorophore can be optimized, the major obstacle is usually resolution, since observing and quantifying fluorescence is needed on the level of individual cells whose sizes lie within the micrometer range [152].

Epifluorescence and confocal microscopy

Given the inherited physics of fluorescence, a general fluorescence microscope can be constructed from a few basic components. In principle, the only thing required is an

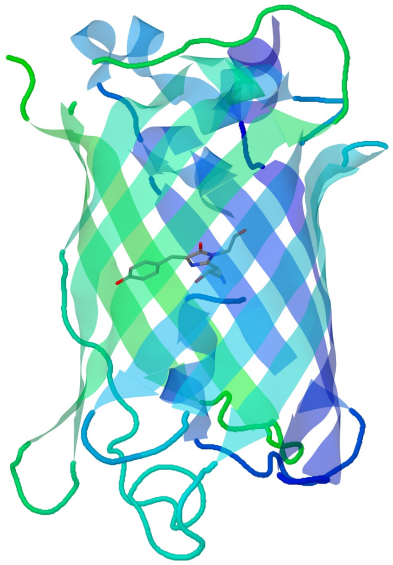

Figure 2.1: Structure of green fluorescent protein (GFP). GFP shows a barrel-like protein structure with an active core consisting of the amino acids Ser65–Tyr66–Gly67 which form the active chromophore by a stacking of the two aromatic rings.

excitation light source and a fluorescence detector. Nowadays, the most common setting for those components is the epifluorescence[3] microscope, where the light source and detector are both placed at the same side from the specimen. This has the advantage that only the light reflected from the specimen, and not the transmitted light, has to be measured, which strongly reduces the background illumination. However, this imposes the need for an additional component, which may separate the incoming excitation light from the emitted light coming from the specimen, a dichroic mirror or beam splitter. In the conventional epifluorescence setup depicted in figure 2.2 light is coming from an evenly illuminating light source such as a xenon or mercury arc lamp[4] which is passed through an excitation filter blocking all wave lengths except the excitation wave length and followed by a collimator to concentrate the light to a small area [153]. Light is consecutively transmitted onto the beam splitter which lets the excitation light pass onto the specimen but redirects the returning emission light towards a photon counter. The photon counter will consecutively transmit the signal to a computer where further analysis or visualization might take place.

Since the entire focal plane is illuminated during image acquisition epifluorescence is considered a *wide field method*. Thus, measuring fluorescence within the entire focal plane will take only a single stimulation and image acquisition, which makes it rapid compared to *local scanning* techniques where each pixel is mapped to a point in the focal plane which are illuminated and measured individually. Even though the even illumination in the xy-plane[5] is beneficial to image acquisition, it also accumulates fluorescence over the z-axis[6]. This is due to the fact that the excitation light will be

[3] Coming from the Greek word *epi*, meaning above.

[4] In very recent setups you may also find LEDs. Alternatively, the light may also come from a laser which abolishes the need for a wave length filter.

[5] the plane perpendicular to the direction of the excitation

[6] the axis parallel to the excitation direction

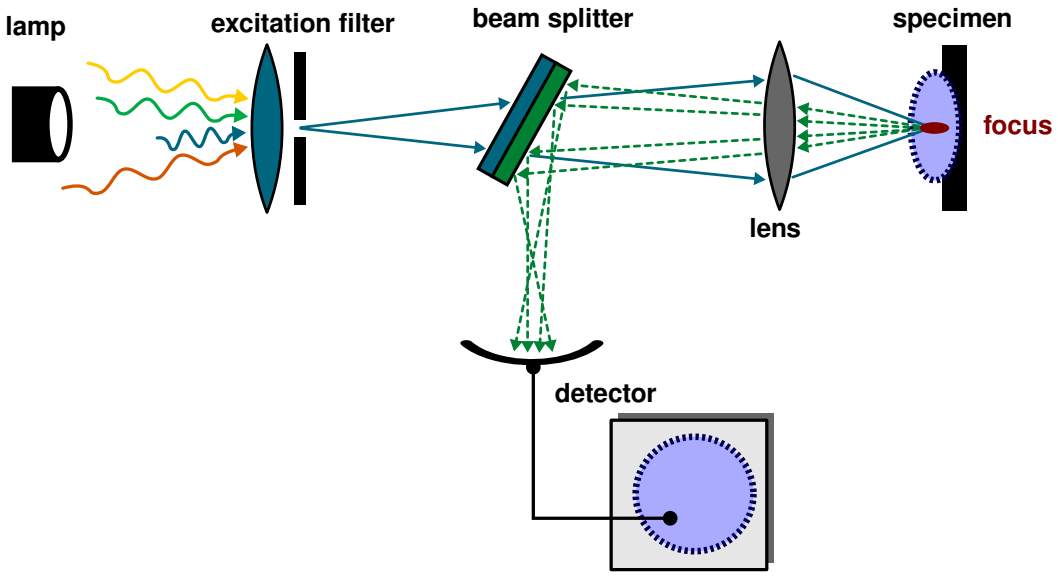

Figure 2.2: Schematic view of the main components of an epifluorescence microscope.

capable of passing the specimen to a certain depth. Since there is no filter discriminating the emission coming from different z-depths every pixel within the xy-plane will be the accumulated signal over the entire z-depth the excitation may pass. As such epifluorescence microscopes have a diminished resolution along the z-axis, up to two orders of magnitude larger than the xy-resolution [154]. As a consequence, the preferred application for epifluorescence microscopes is given in situations where one needs the integrated fluorescence over the z-axis combined with fast acquisition times (e.g. for gene expression time course data in individual cells).
Another popular microscope design is laser scanning confocal microscopy. The major difference between the confocal and epifluorescence design is the addition of a pinhole filter in front of the emission detector [154]. The pinhole is adjusted in a way that it will exclusively allow passage of light waves whose source coincides with the focal point (see Figure 2.3). This filtering immediately increases the resolution along the z-axis, as it prohibits light from points outside the focal plane to reach the detector. The resolution along the z-axis is now only limited by diffraction[7] which enables the visualization of slices of the specimen and enhances contrast [155]. However, blocking light from outside the focal point prevents confocal imaging to be used as a wide field technique and requires the specimen to be scanned focal point by focal point in order to compose an image of the entire focal plane. Thus, the excitation has to be localized to the focal points in order to prevent bleaching of nearby fluorophores, which is why the light sources for confocal microscopy are usually lasers which allow a strong condensation of the light at the focal point. Thus, most confocal microscopes using a pinhole usually belong to the class of *laser scanning confocal* microscopes. The scanning process makes image acquisition slower compared to wield field methods, but also introduces an additional level of information along the z-axis which is, for instance, required for the acquisition of three-dimensional data.
In an alternative setup the specimen is excited using a pulsed laser which stimulates

[7]Diffraction denotes the blurring of fluorescence due to the microscope.

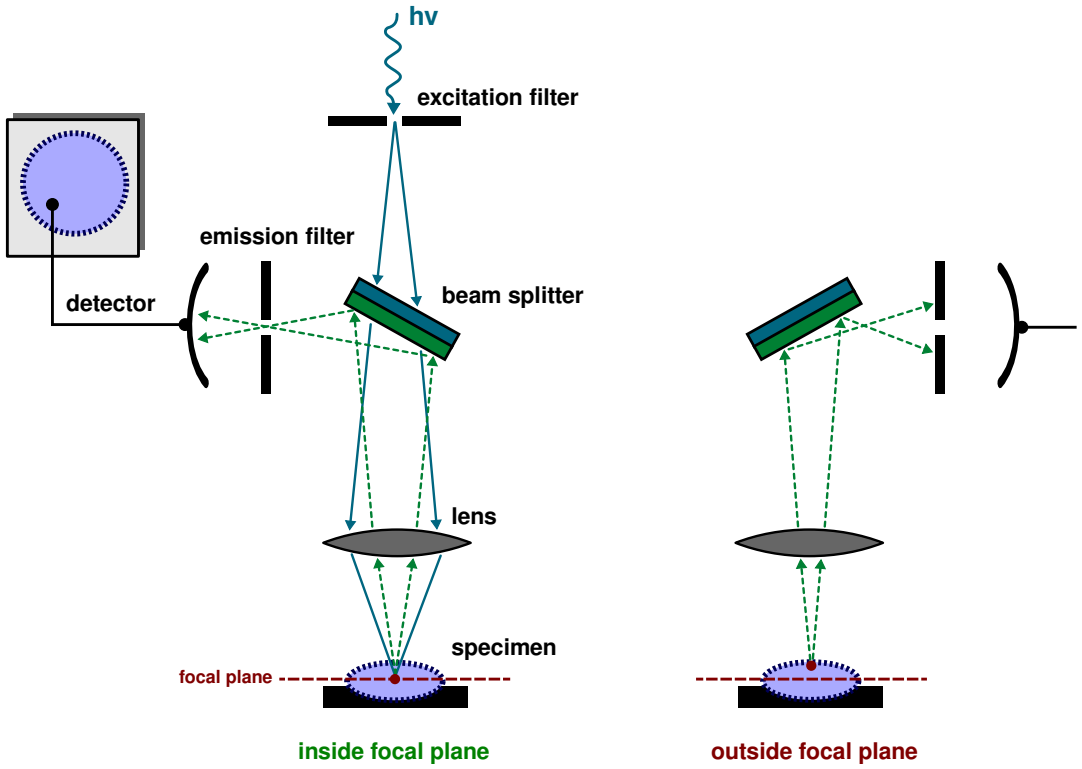

Figure 2.3: Schematic view of a confocal microscope and the obstruction of light from outside the focal point.

the specimen twice with light in the infrared spectrum whose energy corresponds to only half of the required excitation energy, the so-called two-photon laser scanning microscopy. Fluorophores will now need to absorb two photons in order to enter the excited state, the probability of that decreasing with the power of four along the distance from the focal point [156]. Due to this strongly localized excitation there is no need for a pinhole since all emission comes from the focal point. Additionally, light in the infrared spectrum is capable of passing even thick structures without interference which increases the maximum scanning depth on the z-axis compared to a conventional laser scanning confocal microscope. The two-photon setup is usually more complex and expensive but provides less bleaching and an increased z-depth during scanning and is, thus, especially useful when imaging living tissues.

Super-resolution microscopy

Even though the design of modern fluorescence microscopes is by far more complicated than that of conventional light microscopes, they both share a common limitation: their resolution is still constrained by diffraction. The first theoretical limitations for the resolution of optical microscopes were proposed by Helmholtz, but it was Ernst Abbe who should experimentally probe the resolution limit of microscopes [157]. He

found the resolution limit[8] on the xy-plane (Δr) and along the z-axis (Δz) to be

$$\Delta r = \frac{0.61\lambda}{\eta} \qquad \text{and} \qquad \Delta z = \frac{2\lambda n}{\eta^2}. \tag{2.3}$$

Here λ denotes the wave length of the used light and η the numerical aperture [155]. The numerical aperture quantifies how much light from the sample will be redirected onto the lens and is given by the refractive index n of the medium and the maximum half-angle θ at which light can still enter the lens through the relation

$$\eta = n \cdot \sin\theta. \tag{2.4}$$

Because θ quantifies the capability of the lens to capture light from a sample spot and n quantifies the additional amount of light redirected onto the lens at the interface of the sample and transmission medium, the numerical aperture counteracts diffraction to a certain amount, as it is reflected in the formula.
In a confocal microscope, the light beam hast to pass the lens during excitation and emission which leads to multiplication of the individual intensity functions of the individual beams which yields a slightly better resolution of

$$\Delta r_c = \frac{0.37\lambda}{\eta} \qquad \text{and} \qquad \Delta z_c = \frac{\sqrt{2}\lambda n}{\eta^2}. \tag{2.5}$$

Abbe's diffraction limit immediately imposes a fundamental problem in the microscopy of biological samples: as mentioned before it is necessary to use low energy light to minimize interference with the sample, but low energy light has relatively long wave lengths, which decreases the resolution. Using some oil objectives one can end up with a maximum numerical aperture of about 1.5, and since eGFP has an emission maximum at 509 nm this limits the resolution of a fluorescence microscope to a minimum of 200 nm in the xy-plane and 450 nm along the z-axis. However, the entities we would like to study are proteins, whose size ranges within 10 nm. Thus, the required accuracy is actually much lower than the diffraction limit [158]. A lot of effort was put in developing microscopes with a higher resolution while still using low-energy light, but it took almost 130 years after Abbe discovered the diffraction limit to break it. However, in order to understand how this was achieved, we first have to understand how diffraction influences the optics of a sample.
Even though diffraction will blur an emitting point source during detection, it will not do so randomly. Depending on the physical properties of the microscope the point source will be blurred in a deterministic manner, yielding a shape which often resembles as a Gaussian shape on the xy-plane and a hour-glass shape along the z-axis. The function describing the spatial intensity distribution of a point source after diffraction is called the *point spread function* (PSF). Early approaches to increase microscope resolution have mostly concentrated on trying to deconvolve the observed signal with a measured or theoretical point spread function of the microscope, however, since two Gaussian shapes are hard to distinguish below the level of their standard deviations, deconvolution will again not be able to distinguish point emitters which are close to each other. Nevertheless, the initial observation that the position of a single emitter

[8] This formula holds for an ideal optical system obeying the Fraunhofer diffraction. It does not include chromatic aberrations or transmission blur.

can be determined to arbitrary accuracy in the absence of other emitters in close vicinity, opened the door to break the limitation of Abbe's law during the beginning of the 20th century.
The methods to visualize structures beyond the diffraction limit using visible light are quite diverse, but all share a common approach. In order to use the determinism contained in the point spread function, stimulation of the fluorophores is executed in a manner that no two fluorophores in close vicinity to each other are ever excited at the same time. This will now enable to identify the location of the excited spot independently of the diffraction limit, thus overcoming Abbe's law. Since all those methods may depict entities beyond the normal resolution limit, they are collectively termed *super-resolution microscopy*. One of the first proposed strategies to overcome

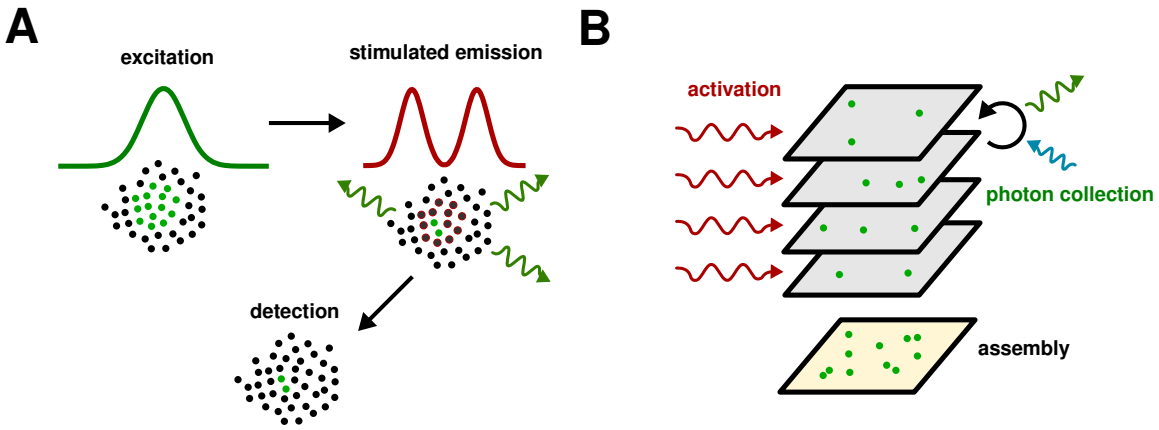

Figure 2.4: Super-resolution can either be achieved by (A) the RESOLFT principle (e.g. STED) or by (B) PALM/STORM.

the diffraction limit was *stimulated emission depletion* (STED) which was introduced by Stefan Hell as early as 1994 and has achieved some significant improvements and applications since then [159, 160]. During stimulated emission depletion microscopy the focal point is first excited as in conventional fluorescence microscopy, however the excitation is followed by a second laser beam, in the shape of a ring on the xy-plane with a confined zero intensity valley in the middle. This laser has a wave length which induces a stimulated emission, meaning that it pushes molecules towards emitting a photon with a rate faster than spontaneous emission. This will leave only molecules within a tiny spot within their excited state (also see figure 2.4). The resolution is now dependent on how effective the stimulated emission can deplete excitation of the fluorophores surrounding the valley. As such the resolution limit is given by the relation between the intensity used to stimulate the emission (I_E) and the minimum intensity required to outperform spontaneous emission I_S. This results in a new resolution limit

$$\Delta r = \frac{0.61\lambda}{\eta\sqrt{1 + I_E/I_S}}. \tag{2.6}$$

Increasing I_E the resolution can be arbitrarily enhanced, thus truly breaking the diffraction limit, however, the resulting light intensity might also harm the sample and increase bleaching, which again limits the resolution. A way to minimize those effects is not to use stimulated emission, but photoswitches, i.e. fluorophores which

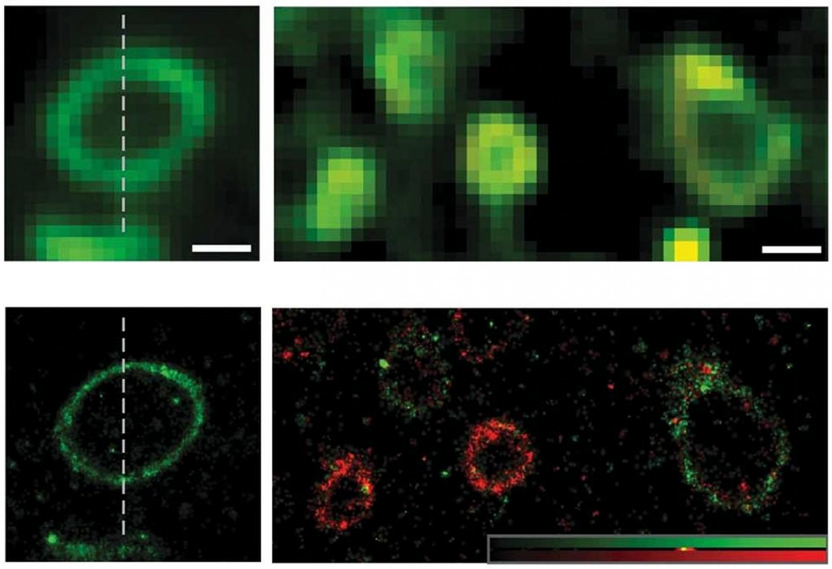

Figure 2.5: Example of the resolution gain using PALM. Shown are cryosections of *E. coli* stained with two membrane-anchored reversibly switchable fluorophores. The resolution of using conventional confocal imaging (upper) shows much less details than the PALM images (lower). Scale bars 500 nm, figure adapted from Andresen et. al [162].

can be brought into a non-excitable state using a specific light stimulus. Since those transitions are spontaneous this strongly lowers I_S and, thus, allows to use light with a low intensity again. Using this strategy STED has achieved lateral resolutions as small as 16 nm [161]. There exist several variations of the STED principle which usually only differ on how they induce de-excitation within the crest of the depletion spot. They are often referred to as *reversible saturable optical fluorescence transitions* (RESOLFT). Using switchable fluorophores the group of Hess proposed an alternative method called *photo-activated localization microscopy* (PALM) [163]. The same method was independently discovered in Zhouang's group where it was called *stochastic optical reconstruction microscopy* (STORM) [164]. Here the focal plane is first collectively brought into the non-excitable state by a non-specific laser pulse, followed by a laser pulse of weak intensity which reactivates the fluorophores. Due to the low intensity, activation is a stochastic event with low probability which will only switch a few scattered fluorophores. If few enough fluorophores are active the probability of two fluorophores being closer to each other than the diffraction limit drops to zero. Consecutive cycles of excitation and emission allow recording of the point spread function and thus calculation of the fluorophores centroids. The cycles are either continued until bleaching or terminated by a global deactivation and the stochastic activation is repeated until the entire image can be reconstructed. The resolution accuracy of PALM/STORM is, thus, given by how well the centroid can be identified by sampling from the point spread function. Due to the law of large numbers the resolution of PALM/STORM depends on the number of detected photons N_p per activated fluorophore with

$$\Delta r = \frac{0.61\lambda}{\eta\sqrt{N_p}}. \tag{2.7}$$

PALM/STORM needs less intensity light, but takes long to assemble the image and is vulnerable to background flourescence.

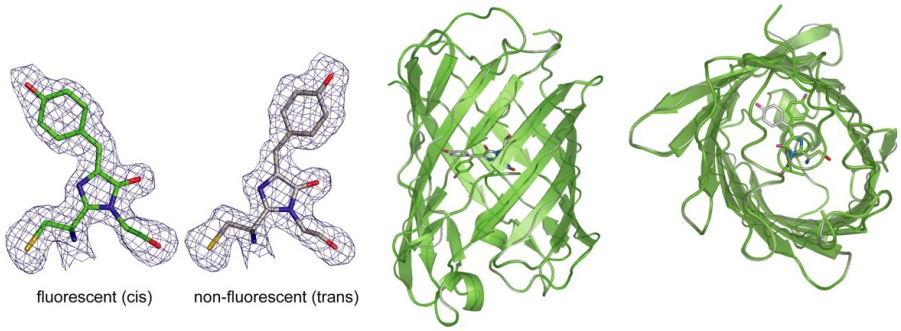

Figure 2.6: Structure of the reversibly switchable fluorescent protein Padron with its cis-trans chromophore center. Adapted from Brakemann et. al. [165].

There is a shift in priorities within super-resolution microscopy since resolution now depends on the quality of the fluorophore instead of the wave length of the light source. All super-resolution techniques require fluorophores with efficient switching characteristics and a high photon yield. All reversibly switchable fluorescent proteins (RSFPs) are derivatives of asFP595 which initially yielded a poor quantum yield, but has been optimized by mutation assays in order to yield a variety of efficient fluorophores such as rsFastLime, Padron or Dronpa. They all are capable of undergoing a stimulated rapid cis-trans-switch in their chromophore [158, 162, 165, 166]. Current limitations of super-resolution microscopy lie within the strong bleaching involved, since STED requires rather strong de-excitation intensities and PALM/STORM require a large number of excitation cycles. However, one can expect those problems to decline as better fluorophores become available.

2.2.2 Assays for population studies

Flow cytometry and fluorescence-activated cell sorting

Apart from analyzing molecular properties within single cells, we are also often interested how a certain property behaves within a population of cells. However, microscopy only gives access to the small fraction of the population contained in the focal volume, which may not be representative for the ensemble. Of course, one could assemble information on a population level by repeatedly analyzing different focal volumes, but this may turn out to be a rather lengthy task.
The pioneering work of extending the fluorescence principle to a high-throughput method was executed by Leonard A. Herzenberger, who extended the earlier works of Coulter in order to device a method to automatically analyze cells based on their fluorescence characteristics, flow cytometry [167]. In principle, the excitation and emission can be incorporated in the same manner as in an epifluorescence microscope, the difficulty is separating the individual cells while passing them through the scanning unit. Naively one could think that this could be achieved by a needle as thin as the cells, which may inject the cell solution into the scanning unit. However, liquids tend to interact with the surface of the needle interior, creating substantial force if the volume contained is small in comparison to the interior area. This is due to the relatively strong adhesion forces in this setting which counteracts gravity or advection

of the solution[9]. Due to this capillary effect, pushing the cell solution through the needle would require extremely high pressure and destroy the cells. This is overcome by injecting the cells into a liquid stream of a high density fluid (sheath fluid) which creates a stable hydrodynamic effect and results in the formation of a thin stream of cell solution within the liquid stream. This now enables the desired separation of cells into a line of single cells, which can be passed to the acquisition unit where the stream is constantly scanned by a one or several laser or diode units. During conventional

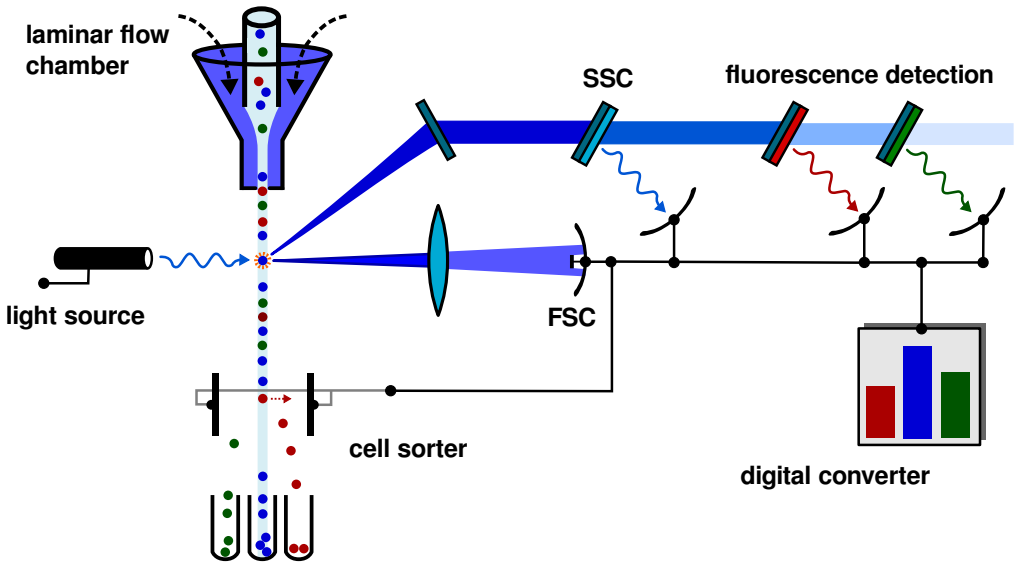

Figure 2.7: Components of a FACS system, including the liquid chamber generating the laminar flow, the acquisition unit and the optional cell sorting unit.

flow cytometry characterization of the particles itself is first performed by measuring the amount of scattering the particle produces when being stimulated with a laser. This is achieved by measuring two different scatter types, forward scatter (FSC) and side scatter (SSC). Forward scattering is observed by placing a detector directly in the line of the laser behind the particle stream. Directly transmitted light, not influenced by the particle, is blocked by an obscuration bar in front of the sample so that only scattered light might reach the detector. Thus, forward scatter is correlated with the amount of light hitting the specimen, since all matter will slightly scatter the light beam. This is mostly influenced by the volume of the scanned object, as a consequence FSC correlates with the volume of the individual particles or cells [168]. The side scatter is generated by redirection of the light beams along rather solid obstacles and, thus, indicates the composition and complexity of the cells. FSC in combination with SSC is usually sufficient for quite elaborate characterizations of cells via their morphology. Additionally, fluorescence tagging can be analyzed and allows the quantification and classification of cells via biochemical features. In a more advanced setting this can be employed to sort cells from a population by various fluorescence characteristics. Here, the carrying liquid is charged and passed through a set of conductor plates after detection. This can be used to pull the cells into specified collector tubes depending on the signal from the detection, which allows sorting of individual cells [169]. Combining flow cytometry with cell sorting is termed *Fluorescence-Activated Cell Sorting*,

[9] An effect most of us now from their childhood trying to drink fast through a thin straw.

commonly known as *FACS*.

Cell cycle synchronization and elutriation

A common complication when studying cell populations of budding yeast during signaling events is the large variety of responsiveness across the yeast cell cycle. As I have pointed out in chapter 1, this is especially true for the yeast pheromone response, as haploid yeast cells will only respond to pheromone during a short time frame of the cell cycle, the G1 phase (see section 1.4.3). As a consequence, studying responses to pheromone in an arbitrary culture is inherently problematic, as we can not tell *per se* whether a cell shows no response due to a low local pheromone concentration or due to being in a non-responsive cell cycle stage.
This can be overcome by treating the cell populations in a way that the majority of the cells are in the same cell cycle stage, a state called cell cycle synchronization. There is a variety of methods to synchronize yeast cells, however they all have their specific drawbacks. The first class of synchronization methods is formed by the so-called *block-and-release methods*, where yeast cells are treated with a chemical that inhibits further cell cycle progression but can be reversed by repeated washing of the culture. The most common chemicals used here are the mating pheromones, which, for obvious reasons, are not suited for our purposes. Other chemicals include Hydroxyurea or Nocodazole which may be used in the same manner. Unfortunately, apart from their ease of use, block-and-release methods induce a variety of stress responses which may strongly interfere when studying cellular signaling [170].
A less invasive method uses an indirect way to synchronize yeast cells: sorting them by size. This is a reasonable approach as cell size strongly correlates with cell cycle stage [171]. Size sorting is achieved by a physical method termed *elutriation*, which makes use of the balance between two distinct forces, centrifugal force and advection. During elutriation cells, as well as the medium, are pumped through a chamber arrested in a conventional centrifuge with a flow direction leading from the outside of the centrifuge to its center, thus, in the reversed direction of the centrifugal force. Advection affects small particles much stronger than large particles, which pushes them to the inside of the chamber, whereas the centrifugal force pushes all particles to the outside of the chamber. When correctly adjusted, this will lead to stationary state where newly arriving particles settle in an area of the chamber which corresponds to their specific equilibrium state of centrifugal and advection forces. Increasing the pump rate will push the smallest cells out of the chamber into a tube system which can be used to collect the cells [172]. Rotor speed and pump rate are usually kept low, so elutriation does not induce a stress response within the cells. As such, elutriation is one of the least invasive methods to synchronize yeast cells, but is limited by the low fraction of cells recovered from the entire population, its complicated adjustment and extraction protocol and the degree of correlation between cell size and cell cycle stage.

2.2.3 Basics of yeast cloning

We have seen that there is a variety of methods to study intracellular properties using fluorescence and population studies, however, none of them will provide exceptionally interesting insights when used with the wild type. To investigate any interesting property within the cells we will need to modify them genetically. Independent on whether

we want to tag a protein, delete, or substitute a gene, we need to be able to integrate a set of custom DNA into the genome of the yeast strain under investigation. This task can be split into two sub-tasks: the construction of the required DNA by PCR fusion techniques or by plasmid modification and introduction of the designed DNA fragment into the genome of the yeast strain. The most common approaches will be roughly outlined here, however, for detailed descriptions the reader shall be referred to a standard manual on yeast genetics [173, like].

Yeast transformation

One of the major reasons why is yeast is such a popular lab organism is because it is very easy to modify genetically. Under certain conditions yeast is capable of incorporating single stranded DNA as well as plasmids from the external environment. Cells that are capable of doing so are called *competent* and the process of taking up DNA from the environment is called *transformation* [174]. The most common way to transform yeast is by rendering the population chemically competent. This is achieved through mixing with polyethylene glycerol (PEG) and lithium acetate [175]. The efficiency of the transformation can furthermore be improved by adding a single-stranded carrier DNA in relatively high concentration [176]. Apart from its ability to take up plasmid vectors, one of the advantages of transforming yeast is its ability to integrate external DNA into is own genome by homologous recombination.
Under normal conditions homologous recombination serves the repair of double break strands during replication. The split DNA strand is first cut back along the its 5' ends during a resection step yielding two single-stranded 3' ends [177]. The protein Rpa now binds the loose 3' ends and, together with several other proteins, finds and invades another DNA template with the sequence homologous to the free 3' end [178]. The free 3' ends then serve as a primer for the synthesis of the repaired DNA strand. During that process the replication fork is often cleaved and ligated again to yield crossover events [179]. Homologous recombination can be used to integrate external DNA by constructing DNA strands with 3' ends homologous to some specific genomic entry points. This will yield *recombinant DNA* which can autonomously serve as a template during homologous recombination and will result in at least one daughter cell with the genomic insert. Depending on the genomic entry points chosen as a basis for the recombinant sites of the construct, one can achieve a variety of genomic modifications such as deleting genes or adding a marker to a protein under its native promoter (see figure 2.8). However, it turns out that the construction of the custom DNA is often much more time-consuming than the actual transformation, which can be done within a few hours plus 2-3 days for growth of the culture on the selective medium.

Building the DNA construct

Building up custom DNA constructs requires site-specific cutting as well as consecutive assembly of different DNA sequences. As such it is no surprise that molecular cloning was founded along with the discovery of restriction enzymes, proteins which are capable of cutting DNA strands at short specific palindromic sequences, and ligases, proteins which are consecutively capable of rejoining those separated DNA strands. These enzymes, for the first time, made it possible to cleave sets of DNA strands and reassemble a new DNA strand in a controlled manner via the use of ligases.

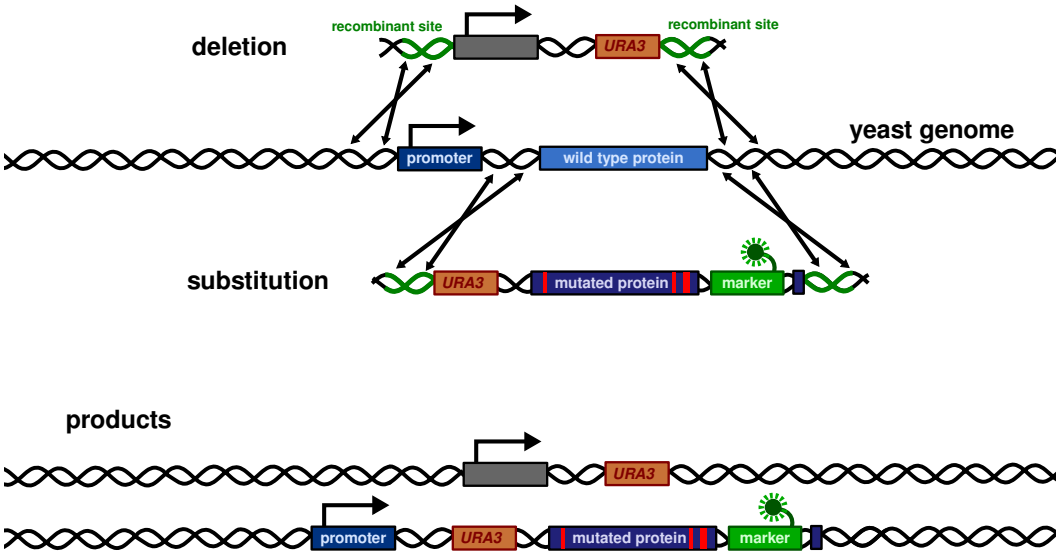

Figure 2.8: Examples for constructs achieving different kinds of mutations during a homologous recombination event.

This was soon used to build up distinct circular double-stranded DNA strands, called plasmid vectors, which included various potential cutting sites along with a set of genes for selection of the transformed cultures, termed auxotrophy markers. The choice of plasmids is due to historical reasons since the only method to artificially replicate a custom DNA construct was to introduce it as plasmid into bacteria like *E. coli*. The original plasmids contained an *E. coli* origin of replication along with a selective marker. The selective marker, a gene usually encoding an enzyme enabling synthesis of an essential amino acid not contained in the medium, would allow *E. coli* cells containing the plasmid to grow on a distinct selective medium, whereas cells not containing the plasmid would starve to death due to the lack of the amino acid. Thus, transforming an *E. coli* population with the plasmid induced its replication and multiplication in the culture.
Nowadays, this technique for DNA amplification has been superseded by the much faster *polymerase chain reaction* (PCR) in which repeated cycles of heating and cooling are used for DNA melting (separation of the double strand) and consecutive replication [180, 181]. During a PCR, a DNA template is mixed together with a set of primers flanking the sequence to be amplified at the 5' ends of the strands, a heat-stable DNA polymerase and the four deoxyribonucleotide triphosphates (dNTPs). A PCR cycle begins with a denaturation step during which the solution is heated to 94-98 °C to break the DNA double helix into its single strands. This is followed by an annealing step during which the temperature is dropped to 50-65 °C which allows the primers to bind the DNA templates and recruits the polymerase. In the elongation step the temperature is now again raised to 75-80 °C to induce efficient DNA synthesis by the polymerase. Since the newly synthesized DNA will serve as a new template for the next PCR cycle this results in an exponential amplification of the initial template, which enables rapid and exponential amplification of DNA fragments between custom positions. Still, plasmid vectors have asserted their position in Molecular Biology, as

they are easy to modify and can be used within most bacteria as well as yeast.
In order to integrate the construct into the yeast genome by homologous recombination it has to be flanked by two sequences homologous to the genomic entry points. This can be achieved conveniently by adding the homologous sites to the 5' ends of the primers as this will add them to the 3' ends of the synthesized strands. This yields recombinant DNA which can later be used for transformation. Building a functioning construct, however, will require to combine a variety of elements such as selective markers, fluorophores or modified versions of the proteins (also see figure 2.8). This assembly of different constructs can either be achieved by classical cutting and ligation or by newer PCR methods such as fusion PCR [182]. Fusion PCR utilizes two complete PCR runs where the first run uses primers with short 5' overhang regions fitting the end of the segment to be fused, yielding DNA strands with homologous overhangs. The DNA fragments containing the overhang are purified via gel extraction and undergo a second PCR run with the normal primers for the final product. During the annealing step this will induce recombination of the overhang strands yielding the assembled template for the fused product which can again be purified via gel extraction [183]. In principle, one can directly create the recombinant DNA for yeast transformation via fusion PCR, abolishing the need for plasmid vectors [184]. However, during large scale mutation projects it might still be beneficial to use plasmid vectors as they allow a highly modular design, well-suited for performing many similar mutations or marker assays [185].

2.3 Computational Techniques

What we are interested in is the function and mechanism of a given system. But how can we formulate this rather arbitrary question in an abstract way that allows us to study a biological system in a systematic way? I have stated earlier that in Systems Biology this question is resolved by applying some dogmas from statistics, more specific, hypothesis testing. We will formulate hypothesis about the biological system which we can either test experimentally or theoretically, employing computational methods. The core of Systems Biology is the model, which can either have a biological or mathematical interpretation, both describing the identical biological system. The property which is the most prominent and observable in Biology as well as Mathematics is the *state* of a system. The state describes the composition of the biological system in a fixed condition, thus, with fixed independent variables (e.g. at a fixed point in time and space). In an abstract sense the state is nothing else than a vector $\mathbf{S}$ of quantities which can denote a variety of biological entities, such as number of cells, number of molecules, concentrations, or volumes. Obviously, those properties can change in time t as well as space $\mathbf{x}$, thus, yielding the state as a function of those two independent variables, $\mathbf{S}(t, \mathbf{x})$. The dynamics of the system will be what changes the system in time as well as space and this can be done by a variety of processes such as chemical reactions, diffusion or spontaneous molecular rearrangements, all depending on a set of additional parameters, such as diffusion rates, kinetic constants, cell volumes, etc. Consequently, the system will dictate the state of the system by a distinct function $\mathbf{F}$, depending on the dependent variables t and $\mathbf{x}$ and the external parameters $\boldsymbol{\theta}$. This yields the basic equation of Systems Biology:

$$\mathbf{S} = \mathbf{F}(t, \mathbf{x}, \boldsymbol{\theta}). \tag{2.8}$$

The core belief of Systems Biology is, that **F** can be found repeating the life cycle of Systems Biology (see figure 1.1). As such, we look for a mathematical function which can fully predict the state of the system up to some limits. If we have found such a function the system has become transparent to us, allowing us a wide array of studies concerning system properties.
However, there are limits to this. The most strict limitation arises on the level of physics. The systems studied in Systems Biology are often very small making the state a vector of molecule numbers. Thus, the processes changing the state must not be deterministic, but may rather occur with some random variation. As such we can not identify a single state for a given time point in space, but will be limited to expressing probabilities to be in a certain state at a given time point in space.
Finding the function governing the evolution of the system state is not trivial. As such, I will start from basic principles here which initially might only treat a partial problem, such as finding the probabilities for a given state in time when space is no issue. We will use those simpler solutions to transit into more general solutions or extract properties of the state which are interesting to us, rather than the full state. The general strategy, however, will remain the same for all steps and will consist of the following: assuming we already now one initial state of the system, $\mathbf{S}_0(t_0, \mathbf{x})$, we will describe the change of the state by summing up all individual processes that may change the state of the system in time. However, which processes may this be and how do they interact with the system state?

2.3.1 Stochastic Processes and the Master Equation

The biological systems which we will investigate are usually biochemical pathways. As such, the state of the system is given by the individual numbers of molecules. Furthermore, we will initially assume that space has no influence on the sate any more, thus, that the fast movement of the molecules equilibrates their distribution in space. Even though this assumption might be correct for many processes, it is obvious that it is not holding in general. However, we will start from this assumption but drop it later on. The temporal evolution of system in a probabilistic setting will be driven by a process that is inherently random. In a mathematical setting those processes are called *stochastic processes* and will give us the methodology to study ways to observe the probability distribution of the system state.

Since there are no fractional numbers of molecules in the system our state space will consist of vectors of non-negative integers. Furthermore, in a probabilistic setting we can not assign a unique state to a certain time point anymore, but we can assign a probability to be in a certain state at some time t. If we do that for all the states we end up with a (possibly multidimensional) probability distribution for the states $\mathbb{P}(\mathbf{S}, t)$. In order to characterize this distribution we will have to make some basic assumptions about the nature of the stochastic process. The major assumption underlying the stochastic processes we will deal with is the *Markov property*. The assumption simply states that the system has no memory of its past. So after we once are in a certain state the system will not be able to remember in what state it was before; it is memory-less. Thus, if we knew the events that change the state, we could derive the probability for a specific state from the probability of another state and the probability of the event happening.

In biochemical reaction systems we know that the state can only be changed by reactions in the system (we will regard all in- and effluxes as reactions too). So what do we know about the reactions? The time, as we consider it, is continuous. Analogous to continuous probability distributions we will not be able to assign a probability for a reaction happening at a certain time t, but only for a very small interval $(t, t + \Delta t]$. If the minimum number of substrates required for the reaction is present, we know that we have a positive probability for the reaction happening in some interval $(t, t + \Delta t]$. If we also assume that the system is well-stirred, which means that we can ignore the movement of molecules as a contributing factor to the probabilities, we can derive those probabilities quite simple. By common sense we expect a reaction happening once every second to happen once if we wait one second and twice if we wait two seconds. So we would expect the probability for a reaction to scale with the length of the time interval. As such the probability for a reaction will be linear in Δt for very small intervals. So if we had the minimum number of substrates required for a single reaction the probability $\mathbb{P}(j, \Delta t)$ for a reaction of type j within some $(t, t + \Delta t]$ would be

$$\mathbb{P}(j, \Delta t) = k_j \cdot \Delta t, \tag{2.9}$$

with some constant k_j measured in s^{-1}. However, if we had more available molecules of one substrate than we need, we could have several possible reactions for any subset of molecules. So, for a reaction only taking a single molecule as a substrate but having, for instance, two possible molecules of the substrate available, we could have the first molecule reacting *or* the second, which leads to an addition of the two probabilities. Thus, the probability for a reaction also depends on the state $\mathbf{S}$ of the system and we have to multiply the probability shown above by the number of possibilities to choose the required molecules from the actual available molecules. Defining $\mathbf{a}_j = (a_k)_k$ as the vector of required molecules of type k to react in reaction j and $\mathbf{S} = (S_k)_k$ as the state (number of molecules of type k) of the system we can now derive the general probability by simple combinatorics:

$$\mathbb{P}(j, \mathbf{S}, \Delta t) = k_j \cdot \prod_k \binom{S_k}{a_k} \cdot \Delta t =: r_j(\mathbf{S}, t) \cdot \Delta t. \tag{2.10}$$

The terms $r_j(\mathbf{S}, t)$ are often called *propensities* or *infinitesimal characterization*.

Given the propensities, we can now construct the probability for being in a given state at a certain time point, if we know the initial time t_0 and the initial probability distribution of the state $\mathbb{P}(\mathbf{S}_0, t_0)$. There are only four basic ways to actually influence the probability for a state: (i) we stay in the state, (ii) a reaction within $(t, t + \Delta t]$ gets us into the state, (iii) we leave the state due to a reaction in $(t, t + \Delta t]$ or (iv) the state changes due to several reactions within $(t, t + \Delta t]$. Thus, the probability to be in a certain state after Δt, $\mathbb{P}(\mathbf{S}, t + \Delta t | \mathbf{S}_0, t_0)$, is the sum of the mentioned four probabilities.

The probability of (i) is the probability of being in a state exactly one reaction j away from entering the desired state *and* having that reaction actually happening within the next Δt. Defining $\boldsymbol{\phi}_j$ as the state change propagated by the reaction (denoting which which and how many molecules will be consumed or produced by the reaction), this is given by

$$\sum_j \mathbb{P}(\mathbf{S} - \boldsymbol{\phi}_j, t | \mathbf{S}_0, t_0) \cdot r_j(\mathbf{S} - \boldsymbol{\phi}_j, t) \cdot \Delta t, \tag{2.11}$$

with probabilities of negative states being equal to zero. Analogous the probability for leaving the state in Δt (ii) is given by

$$\sum_j \mathbb{P}(\mathbf{S}, t|\mathbf{S}_0, t_0) \cdot r_j(\mathbf{S}, t) \cdot \Delta t \tag{2.12}$$

The probability for being in the state simply is $\mathbb{P}(\mathbf{S}, t|\mathbf{S}_0, t_0)$ and since the probability for having more than one reaction within Δt will at some point include the term $(\Delta t)^k$ for $k > 1$, it will be a term in $o(\Delta t)$. That means that dividing it by Δt and having $\Delta t \to 0$ the entire probability for (iv) will become zero. Since either of the events can change the probability we have to sum them to get the joint probability (with probability contributions leaving the state being negative), leading to

$$\begin{aligned}\mathbb{P}(\mathbf{S}, t+\Delta t|\mathbf{S}_0, t_0) = \mathbb{P}(\mathbf{S}, t|\mathbf{S}_0, t_0) \\ + \sum_j \mathbb{P}(\mathbf{S}-\boldsymbol{\phi}_j, t|\mathbf{S}_0, t_0) \cdot r_j(\mathbf{S}-\boldsymbol{\phi}_j, t) \cdot \Delta t \\ - \sum_j \mathbb{P}(\mathbf{S}, t|\mathbf{S}_0, t_0) \cdot r_j(\mathbf{S}, t) \cdot \Delta t \\ + o(\Delta t)\end{aligned} \tag{2.13}$$

We still have the problem of the Δt. To actually fulfill the assumptions we have to eliminate all secondary effects on that equation which will only hold for a Δt smaller than the minimum time to the next reaction. Since there is a positive probability for all positive Δt we have to consider that equation in the limit of $\Delta t \to 0$. We will do that by first subtracting the $\mathbb{P}(\mathbf{S}, t|\mathbf{S}_0, t_0)$ from both sides of the equation, dividing by Δt and letting $\Delta t \to 0$ which leads to the definition of the derivative on the left side

$$\begin{aligned}&\lim_{\Delta t \to 0} \frac{\mathbb{P}(\mathbf{S}, t+\Delta t|\mathbf{S}_0, t_0) - \mathbb{P}(\mathbf{S}, t|\mathbf{S}_0, t_0)}{\Delta t} = \\ &\lim_{\Delta t \to 0} \sum_j \left[\mathbb{P}(\mathbf{S}-\boldsymbol{\phi}_j, t|\mathbf{S}_0, t_0) \cdot r_j(\mathbf{S}-\boldsymbol{\phi}_j, t) - \mathbb{P}(\mathbf{S}, t|\mathbf{S}_0, t_0) \cdot r_j(\mathbf{S}, t)\right] + \frac{o(\Delta t)}{\Delta t}.\end{aligned} \tag{2.14}$$

This gives us the so-called *chemical master equation*, with

$$\frac{d\,\mathbb{P}(\mathbf{S}, t|\mathbf{S}_0, t_0)}{dt} = \sum_j \left[\mathbb{P}(\mathbf{S}-\boldsymbol{\phi}_j, t|\mathbf{S}_0, t_0) \cdot r_j(\mathbf{S}-\boldsymbol{\phi}_j, t) - \mathbb{P}(\mathbf{S}, t|\mathbf{S}_0, t_0) \cdot r_j(\mathbf{S}, t)\right]. \tag{2.15}$$

As we can see, on the left side we have the probabilities for all possible states, which are in theory all vectors of non-negative integers. So solving the chemical master equations means solving an infinite and nonlinear set of differential equations. Thus, except for very simple systems, we can solve the chemical master equation neither analytically nor numerically.

This may seem quite an effort to formulate a problem we can not solve. However, in practice we do not need the entire probability distribution. We would be quite content with having some approximation for the mean and variance and to generate possible outcomes of the process. As we will see now, that is by far easier than dealing with the master equation.

Markov Jumping and Gillespie's Direct Method

If we go back to our basic assumptions we see that we have defined a process on a continuous time but with finite propensities. This means the "rate" by which reactions appear in our system might be stochastic but it is not unbounded. This makes sense as we would not expect an infinite number of reactions happening in real life either. So the process characterized by the chemical master equation takes a form where the state is only changed by reactions with a waiting time between consecutive reactions. Thus, the process waits for some random time before it suddenly jumps and changes the state. Because of that, processes defined as the one here are also referred to as *Markov jump processes*.
So can we say something about the waiting times? An entire derivation can be found in the appendix 6.1. We can find expressions for the probability of waiting some time τ till the next reaction happens and which reaction this will be. The probability $\mathbb{P}(\tau, 0)$ that we have to wait a time τ before the next reaction happens is

$$\mathbb{P}(\tau, 0) = r_0(\mathbf{S}, t) \exp\left(-r_0(\mathbf{S}, t)\tau\right), \text{ with } r_0(\mathbf{S}, t) := \sum_{j=1}^{n} r_j(\mathbf{S}, t). \tag{2.16}$$

The probability $\mathbb{P}(j|\tau)$ that the next reaction will be reaction j has the form

$$\mathbb{P}(j|\tau) = \frac{r_j(\mathbf{S}, t)}{r_0(\mathbf{S}, t)}. \tag{2.17}$$

Summarizing those two results we can now obtain the probability $\mathbb{P}(\tau, j|\mathbf{S}, t)$ of waiting time τ before the next reaction and that reaction being of type j, given we are in time t and in state $\mathbf{S}$, as

$$\mathbb{P}(\tau, j|\mathbf{S}, t) = \frac{r_j(\mathbf{S}, t)}{r_0(\mathbf{S}, t)} \cdot r_0(\mathbf{S}, t) \exp\left(-r_0(\mathbf{S}, t)\tau\right) = r_j(\mathbf{S}, t) \exp\left(-r_0(\mathbf{S}, t)\tau\right). \tag{2.18}$$

This concise solution regarding the jump characterization of the process was introduced to biochemical systems by Daniel T. Gillespie [reviewed in 186]. He is also responsible for almost all of the following theory and algorithms, the first of them being his *direct method*, which uses the results stated above to simulate a stochastic system and thus generate an exact sample.
The algorithm is straight forward and is shown in the following (also see Figure 2.9):

Data: $\mathbf{S}_0, t_0, t_{max}, r_j$
Result: $\mathbf{S}(t)$

Sample state $\mathbf{S}_0$ from $\mathbb{P}(\mathbf{S}_0)$;
$t = t_0$;
$\mathbf{S} = \mathbf{S}_0$;
while $t < t_{max}$ **do**
  $r_0 = \sum_j r_j(\mathbf{S}, t)$;
  draw a random τ from $\mathbb{P}(\tau, 0) = r_0(\mathbf{S}, t) \exp\left(-r_0(\mathbf{S}, t)\tau\right)$;
  draw a random reaction according to $\mathbb{P}(j|\tau) = \frac{r_j(\mathbf{S},t)}{r_0(\mathbf{S},t)}$;
  update $\mathbf{S}$;
  $t = t + \tau$;
end
return $\mathbf{S}$;

So we see that, even if the formulation of the probability distribution is quite complicated, we can derive a very simple exact procedure to generate samples from it. If we would now generate several samples we could simply calculate the population mean and variance and would get a good approximation for the expectation and variance of the distribution[10]. Additionally, we could also run a lot of samples and actually approximate the probability for being in a certain state at time t. Even though this only generates an exact solution to the chemical master equation if we run an infinite number of samples, it can be used to approximate the solution.

Gillespie's direct method is exact for arbitrary small or large numbers of molecules and the most accurate system sampling one can get. But it also has some drawbacks. The most obvious is the necessity of repeating the sampling quite often in order to get good approximations for the mean and variance. Additionally, the algorithm strongly depends on the reaction propensities. As we can see, the number of times we have to update is given by the relation between the time interval simulated and the frequency of the reactions taking place. For that reason the algorithm can be quite slow for systems that have either fast reactions or some molecules in high abundances. Therefore, we will now direct our attention towards finding some ways to speed up our sampling.

Tau-leaping

As we have seen in the previous section, the Gillespie method will update the system every time a single reaction takes place. This makes us quite dependent on the rates in the method, since we know that the mean of an exponential distribution is given by λ^{-1}, with λ as the rate parameter. So to simulate 100 seconds of a reaction which, in average, has 1 substrate available and happens with a rate of $1s^{-1}$ we would need in average 100 updates, whereas a reaction with 1000 substrates available and a rate of $10s^{-1}$ takes in average $10 \cdot 1000 \cdot 100 = 1.000.000$ updates. Thus, in particular if at least one substrate is highly abundant or the reaction rates are large, the Gillespie algorithm becomes unfeasibly slow. Even though there are many variations of the Gillespie method in order to deal with a high number of reactions[11], all of them essentially inherit the strong rate-dependence [187, 188].

However, in the unfortunate situation of constantly high substrate numbers and/or fast reactions it is easy to see that a single reaction may only slightly change the state of the system. In fact, since the state only changes slightly the reaction rates will also differ only slightly from the ones calculated in the previous step. This basically means that our reaction rates are now close to being constant. So instead of merely executing a single reaction, we could also execute several reactions at once. We can use the following "tactic": first we choose a small time step τ[12]. We now try to find out how many reactions of each type might happen in this time step. In the following step we execute those possible reactions and advance by the whole time step τ. If our requirements from above are met, this would allow us to execute many reactions at once without sacrificing too much accuracy. From the Gillespie method we already know the probability distribution of the waiting time for a single reaction, but how

[10] ...because population mean and variance are both unbiased estimators

[11] In fact, one can even design the algorithm completely independent of the *number* of different reactions in the system, but with a large constant.

[12] thus the name tau-leaping

do we get this distribution for several reactions? Since our rates are close to being constant, the Markov jump process now becomes a simple Poisson process, and the distribution of several occurrences of a reaction is Poisson distributed. Thus we can update our system state the following way[13]:

$$\begin{aligned} \mathbf{S}(t+\tau) &= \mathbf{S}(t) + \sum_j \rho_j \cdot \boldsymbol{\phi}_j, \\ \text{with } \mathbb{P}(\rho_j = k, \mathbf{S}, t) &= \exp(-r_j(\mathbf{S}, t) \cdot \tau) \cdot \frac{(r_j(\mathbf{S}, t)\tau)^k}{k!}. \end{aligned} \tag{2.19}$$

However, we are still left with one problem: choosing the τ. Up to now we just assumed that there is a τ so that the reaction rates stay constant. But for what τ do they actually do that? Our reaction rates can of course still be nonlinear so we can not expect to answer that question in general. Furthermore, the change of the system still depends on the realizations of the Poisson variables we are using. However, what we can do is linearize the *average* change in the reaction rates taking place in $(t, t+\tau]$. If we also do that for the variance of the change in the reaction rates we get safe boundaries for that change. After applying a Taylor expansion[14] we end up with the following results for the mean and variance of the rate changes[15]:

$$\left\langle \Delta r_j(\mathbf{S}, \tau) \right\rangle \approx \sum_k \frac{\partial r_j(\mathbf{S}, t)}{\partial S_k} \sum_l \phi_{kl} \cdot r_j(\mathbf{S}, t)\tau = \sum_l \mathcal{D}_{jl} \cdot r_j(\mathbf{S}, t)\tau \tag{2.20}$$

$$\mathbf{Var}\left(\Delta r_j(\mathbf{S}, \tau)\right) \approx \sum_k \left(\frac{\partial r_j(\mathbf{S}, t)}{\partial S_k}\right)^2 \sum_l \phi_{kl}^2 \cdot r_j(\mathbf{S}, t)\tau = \sum_l \mathcal{D}_{jl}^2 \cdot r_j(\mathbf{S}, t)\tau \tag{2.21}$$

$$\text{with } \mathcal{D}_{jl} := \sum_k \frac{\partial r_j(\mathbf{S}, t)}{\partial S_k} \cdot \phi_{kl}. \tag{2.22}$$

With that approximation we can now choose our τ in such a way that the reaction rates only slightly deviate from the overall reaction rate and as such stay close to constant. We will do that by requiring the τ to be small enough that individual reaction rates will in average not change by more than a fraction ϵ compared to the overall reaction rate r_0. We assume that this is is valid if neither the mean nor the standard deviation of the rate changes deviate by more than $\epsilon \cdot r_0(\mathbf{S}, t)$, therefore, fulfilling the so called leap condition

$$\forall j : \left\langle \Delta r_j(\mathbf{S}, \tau) \right\rangle \leq \epsilon \cdot r_0(\mathbf{S}, t) \text{ and } \mathbf{Var}(\Delta r_j(\mathbf{S}, \tau)) \leq \epsilon^2 \cdot r_0(\mathbf{S}, t)^2. \tag{2.23}$$

The maximum τ fulfilling that is now given by

$$\tau = \min_j \left\{ \frac{\epsilon \cdot r_j(\mathbf{S}, t)}{|\sum_l \mathcal{D}_{jl} \cdot r_j(\mathbf{S}, t)|}, \frac{\epsilon^2 \cdot r_j(\mathbf{S}, t)^2}{\sum_l \mathcal{D}_{jl}^2 \cdot r_j(\mathbf{S}, t)} \right\}. \tag{2.24}$$

[13] $\boldsymbol{\phi_j}$ is again the stoichiometry of reaction j

[14] The entire derivation can be found in appendix 6.1.

[15] $\langle X \rangle$ denotes the expectation, $\mathbf{Var}(X) = \left\langle \left(X - \langle X \rangle\right)^2 \right\rangle$ the variance and ϕ_{kl} denotes the k^{th} element of $\boldsymbol{\phi}_l$.

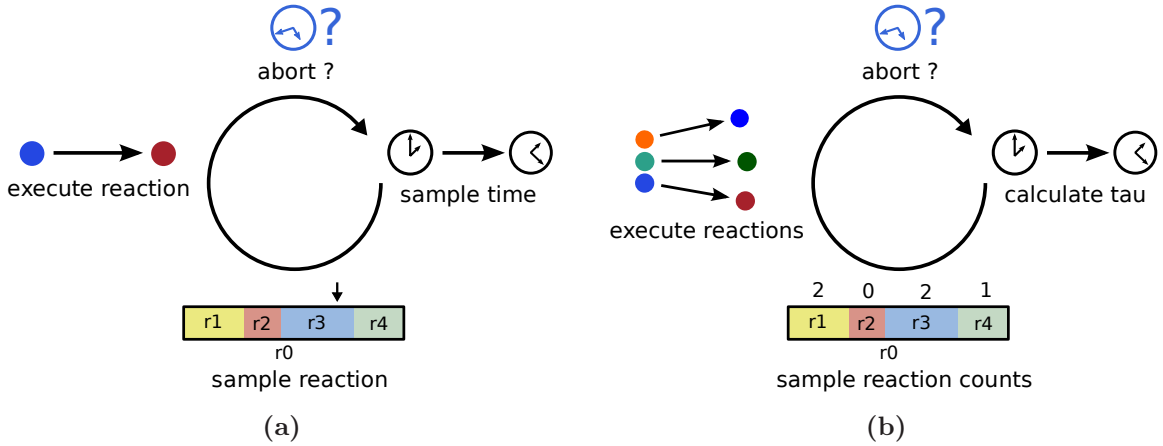

Figure 2.9: Comparison of the original Gillespie algorithm (a) to the Tau-leaping algorithms (b).

Notice here that $\mathcal{D}_{jl}$ can be computed *prior* to the simulation and will not change during the simulation. So the only thing left to do is calculating the updated reaction rates during the simulation which is more or less the same thing we had to do in the Gillespie method (compare 2.9). So for each individual step of the simulation we will need as much time as the Gillespie method, but we will need less simulation steps, which speeds up the simulation.

The Chemical Langevin Equation and transition to deterministic methods

If our molecule numbers are generally high we can simplify our previous results even more. The Poisson distribution can be well approximated by a Normal distribution $\mathcal{N}(\mu, \sigma^2)$ in that case. Let us now assume we would always be able to choose a τ that fulfills the leap condition and still allows for a high number of reactions within $(t, t+\tau]$. Then we can now formulate our tau-leaping update in the following way:

$$\begin{aligned} \mathbf{S}(t+\tau) &= \mathbf{S}(t) + \sum_j \rho_j \cdot \boldsymbol{\phi}_j, \\ \text{with } \mathbb{P}(\rho_j = k, \mathbf{S}, t) &\propto \mathcal{N}\big(r_j(\mathbf{S},t)\tau,\, r_j(\mathbf{S},t)\tau\big), \end{aligned} \tag{2.25}$$

with $\mathbf{S}(t)$ being the current state at time t.

If we now use the scaling properties of the Normal distribution[16] we can further decompose our distribution of reaction numbers by

$$\mathcal{N}\big(r_j(\mathbf{S},t)\tau,\, r_j(\mathbf{S},t)\tau\big) = r_j(\mathbf{S},t)\tau + \sqrt{r_j(\mathbf{S},t)\tau} \cdot \mathcal{N}\big(0,\, 1\big). \tag{2.26}$$

Plugging that into the update rule gives

$$\mathbf{S}(t+\tau) = \mathbf{S}(t) + \sum_j \left(r_j(\mathbf{S},t)\tau + \sqrt{r_j(\mathbf{S},t)\tau} \cdot \eta_j \right) \cdot \boldsymbol{\phi}_j \tag{2.27}$$

$$= \mathbf{S}(t) + \sum_j r_j(\mathbf{S},t)\tau \cdot \boldsymbol{\phi}_j + \sum_j \sqrt{r_j(\mathbf{S},t)\tau} \cdot \eta_j \cdot \boldsymbol{\phi}_j, \tag{2.28}$$

$$\tag{2.29}$$

[16] $\mathcal{N}(\mu, \sigma^2) = \mu + \sigma \cdot \mathcal{N}(0, 1)$

where η_j are standard normal i.i.d.[17] variables. This leaping formula is now a much faster version than the ones regarded above, since Normal distributed random variables can be generated much faster than Poisson variables. Due to our assumptions, we will also leap over several reactions in each step and can still use a large τ.

Subtracting $\mathbf{S}(t)$ and dividing both sides of the equation by τ now yields

$$\frac{\mathbf{S}(t+\tau)-\mathbf{S}(t)}{\tau} = \sum_j \boldsymbol{\phi}_j \cdot r_j(\mathbf{S},t) + \sum_j \boldsymbol{\phi}_j \cdot \sqrt{r_j(\mathbf{S},t)} \cdot \frac{\eta_j}{\sqrt{\tau}}. \tag{2.30}$$

After taking the limit for $\tau \to 0$ we end up with the *Chemical Langevin Equation*

$$\frac{d\mathbf{S}(t)}{dt} = \underbrace{\sum_j \boldsymbol{\phi}_j \cdot r_j(\mathbf{S},t)}_{\text{deterministic term}} + \underbrace{\sum_j \boldsymbol{\phi}_j \cdot \sqrt{r_j(\mathbf{S},t)} \cdot \Gamma_j(t)}_{\text{noise term}}. \tag{2.31}$$

The term $\Gamma_j(t)$ is the so-called *Gaussian White Noise* with

$$\Gamma_j(t) := \lim_{\tau \to 0^+} \frac{\eta_j}{\sqrt{\tau}} \propto \mathcal{N}(0, dt^{-1}). \tag{2.32}$$

It describes what would happen to a Normal distribution if the variance would scale inversely with the time step of the derivative. Furthermore, it is uncorrelated for all j. The important observation here is that the equation consists of two terms on the right hand side, where the first one does not include a stochastic variable, and is deterministic, and the second term drives all fluctuations in the system. There are two other important consequences which should be noted here:

1. When we defined the Langevin update we already approximated the number of reactions taking place by a normal distribution. A normal distribution, however, is defined on real numbers. As such the number of reactions as well as the state variables are now real numbers which somewhat opposes our interpretation of the variables as molecule numbers. One could transform the variables to concentrations to get rid of that problem but that would be nothing else than a dirty trick. In the end we are still approximating a discrete state space by a continuous one.

2. The Langevin equation also is a differential equation in time. As such the stochastic process we now define is continuous in time. This also contradicts our view of waiting certain time steps, since now the system is constantly changing.

The fundamental consequence is the following: we now describe a state- and time-continuous stochastic process, however one that still treats the same system generated from the same initial assumptions, with the difference that we also assumed that many reactions will occur constantly. This assumption however is not as arbitrary as it might seem. A cell is composed of millions of molecules and even simple biochemical pathways include several thousand molecules, making this assumption quite correct for many cases. Additionally, in this equation we can easily derive the mean value

[17] i.i.d. $\triangleq$ identically independently distributed

of the state for a given time point. Applying the expectation, $\langle\cdot\rangle$, to equation 2.31 immediately yields:

$$\left\langle \frac{d\mathbf{S}(t)}{dt} \right\rangle = \sum_j \boldsymbol{\phi}_j \cdot r_j(\mathbf{S}, t) + \sum_j \boldsymbol{\phi}_j \cdot \sqrt{r_j(\mathbf{S}, t)} \cdot \langle \Gamma_j(t) \rangle \tag{2.33}$$

$$\text{and with} \quad \langle \Gamma_j(t) \rangle = 0 \tag{2.34}$$

$$\text{follows} \quad \frac{d\langle \mathbf{S}(t) \rangle}{dt} = \sum_j \boldsymbol{\phi}_j \cdot r_j(\mathbf{S}, t). \tag{2.35}$$

Thus, the mean state is governed by a deterministic ordinary differential equation.

But what are the consequences regarding the stochastic character of the system? This question can be answered quite elegantly by visual inspection of equation 2.31. As we see the only term including a random variable is the second part of the sum. This "noise term" includes the square root of a reaction rate. As such, the randomness of the state change in time is governed by the relation of the reaction rate to its square root. As the reaction rates become very big the first term of the sum will take over the equation, making the random term negligible and leaving the state only few possibilities to deviate from its mean. Thus, under the condition of large molecule numbers and fast reactions in the system, the state is now *deterministic*, meaning it can be identified uniquely at each time point. This makes the treatment of the system and simulation of the model much simpler, a strategy which we employ later to solve reaction-diffusion systems.

The reaction-diffusion master equation

As we have seen before, we can express the probabilistic evolution of the state by expressing its change over time in a master equation. Up to know we have only dealt with problems homogeneous in space, such that the spatial dependence of $\mathbf{S}$ was abolished ($\mathbf{S}(t, \mathbf{x}) = \mathbf{S}(t)$). However, we have argued extensively before, that this might not be the case, in particular for the biological system we aim to treat with these methods. But how can we introduce space into the methodology we already derived?
The solution can be found in relaxing our initial requirements a little: even though there is no homogeneous distribution in space, there may be one in small parts of the entire space of the model. In fact, if we divide the entire space into many individually small subspaces, spatial homogeneity may be assumed for the small subspaces only. This is somehow equivalent by treating the entire spatial part of the system state by a sum of small very simple functions (constant functions). We will use the most simple subdivision one could think of for a complex, possibly three-dimensional, space: a partition into equally sized cubes. Because the subdivision is finer than the original tracking of quantities solemnly in the total volume (macroscopic), but rougher than treating molecules individually (microscopic), this treatment of a system is called *mesoscopic*. For each cube with index k out of n_c cubes we will now have an assigned state $\mathbf{S}_k(t)$ and the complete system state will have the form $mathbfS = \{\mathbf{S}_1, \ldots, \mathbf{S}_{n_c}\}$. Obviously the fact that we track the species numbers now for each cube will make our state vector much bigger, meaning that from an initial state vector with n_S entries we will go to a $n_S \cdot n_c$ state vector.
The partition now forces us to include diffusion as a way to change the system and,

thus, its state. Molecules can diffuse from each cube into a neighboring cube. The rate with which that may happen is related to the macroscopic diffusion rate D_i for the molecule type i. As all molecules in the current cube diffuse equally, the number of molecules leaving the cube is proportional to their diffusion rate and quantity. As macroscopic diffusion rates are formulated in area per time, we have to incorporate the size of the cube as well. As such the mesoscopic diffusion rate d_i, thus, the rate at which molecules leave the cube is given by:

$$d_i(\mathbf{S}_k, t)\Delta t = \frac{D_i}{l^2} \cdot S_{i,k}(t)\Delta t, \tag{2.36}$$

where D_i is the macroscopic diffusion rate, l the side length of the cube and $S_{i,k}(t)$ the number of molecules from species i in cube k at time t.
But how is the state changed by the diffusion? Molecules can either leave the cube k by diffusing out of it in any of the neighboring cubes, or enter the cube by diffusing into it from neighboring cubes. In order to express this in a mathematical term it, thus, helps to define the neighborhood of a cube with index k as the indices of cubes which are adjoint to it. We will denote the neighborhood of cube k as $\mathbf{N}(k)$ and a vector being one in position m and zero elsewhere will be denoted $\mathbf{1}_m$.
The state $\mathbf{S}(t, k)$ in cube k can be reached by diffusion of a molecule of any species i from a neighboring cube within Δt, if the previous state was the state with one molecule of this species less in cube k:

$$\sum_i \sum_{m \in \mathbf{N}(k)} \mathbb{P}(\mathbf{S} - \mathbf{1}_m, t, k) \cdot d_i(\mathbf{S}_m, t)\Delta t. \tag{2.37}$$

The state can be left within Δt by any of the molecules of a species i leaving the cube k and entering any of the $|\mathbf{N}(k)|$ cubes[18]:

$$\sum_i |\mathbf{N}(k)|\, \mathbb{P}(\mathbf{S}, t, k) \cdot d_i(\mathbf{S}_k, t). \tag{2.38}$$

This gives all the changes in probability due to diffusion and we can now construct the entire master equation analogously to section 2.3.1[19] by summing up all the changes due to reactions in a cube k and all the changes due to diffusion that may happen in an time step Δt, yielding the following expression for $\mathbb{P}(\mathbf{S}, t + \Delta t, k)$:

$$\begin{aligned}
\mathbb{P}(\mathbf{S}, t + \Delta t, k) = \mathbb{P}(\mathbf{S}, t, k) \\
&+ \sum_j \mathbb{P}(\mathbf{S}_k - \boldsymbol{\phi}_j, t, k) r_j(\mathbf{S}_k - \boldsymbol{\phi}_j, t)\Delta t \\
&- \sum_j \mathbb{P}(\mathbf{S}, t, k) r_j(\mathbf{S}_k, t)\Delta t \\
&+ \sum_i \sum_{m \in \mathbf{N}(k)} \mathbb{P}(\mathbf{S} - \mathbf{1}_m, t, k)\ d_i(\mathbf{S}_m, t)\Delta t \\
&- \sum_i |\mathbf{N}(k)|\, \mathbb{P}(\mathbf{S}, t, k) d_i(\mathbf{S}_k, t)\Delta t + o(\Delta t).
\end{aligned} \tag{2.39}$$

[18] The operator $|\cdot|$ applied to a vector will denote the number of elements in this vector from hereon, whereas $||\cdot||$ will denote a norm.

[19] To keep the notation concise we will drop the explicit dependence on the initial conditions here, even though it still applies, thus $\mathbb{P}(\mathbf{S}, t, k) = \mathbb{P}(\mathbf{S}, t, k|\mathbf{S}_0, t_0)$

Analogous to the chemical master equation (Eq. 2.15) we can convert this equation to a differential equation yielding the *reaction-diffusion master equation*

$$\begin{aligned}\forall k : \frac{d\,\mathbb{P}(\mathbf{S},t,k)}{dt} &= \sum_j \mathbb{P}(\mathbf{S}_k - \boldsymbol{\phi}_j, t, k) r_j(\mathbf{S}_k - \boldsymbol{\phi}_j, t) - \sum_j \mathbb{P}(\mathbf{S}, t, k) r_j(\mathbf{S}_k, t) \\ &+ \sum_i \sum_{m \in \mathbf{N}(k)} \mathbb{P}(\mathbf{S} - \mathbf{1}_m, t, k) d_i(\mathbf{S}_m, t) - \sum_i |\mathbf{N}(k)|\, \mathbb{P}(\mathbf{S}, t, k) d_i(\mathbf{S}_k, t)\end{aligned} \tag{2.40}$$

Why would it be helpful to us to formulate a master equation for a reaction-diffusion system if even the simpler chemical master equation can not be solved? This becomes obvious when comparing the reaction terms of the reaction-diffusion master equation with the diffusion terms. The diffusion events have a very similar form as the reaction terms. In fact, by defining a set of new propensity functions for each molecule capturing the diffusion of this molecule in one specific neighbor cube, the diffusion events can be treated exactly the same as reaction events. The difference will solemnly be found in the $\boldsymbol{\phi}_j$ vector. $\boldsymbol{\phi}_j$ will be non-zero only within one k-block for reaction events, which will not be the case for diffusion events.
As such the reaction-diffusion master equation is nothing else than a normal master equation as seen before, only with a large state space and additional propensities. Nevertheless, all the previous derivations immediately apply, including the sampling procedures we derived. This immediately gives us the Gillespie method however with a huge set of possible reactions and diffusions as every cube has its own set of reaction and diffusion events. The entire evolution, thus, can be sampled using Gillespie's method, but it would be very slow due to the many calculations we have to execute for every time step. However, we know that every event we execute, may it be diffusion or a reaction, will only involve a state update in at most two cubes, whereas all the other parts of the state vector $\mathbf{S}$ and the propensities for all other cubes will not change.

The next subvolume method

A more efficient algorithm was developed by Johan Elf which uses this property in order to speed up the sampling significantly [189, 190]. In the algorithm of Elf the state is stored in a $n_S \times n_c$ matrix which tracks the state for each cube. Additionally, the sum of reaction propensities, $r_{0,k}$, and diffusion propensities, $d_{0,k}$ are also stored for each cube k. The time until the next event, reaction or diffusion, occurs is sampled using Gillespie's formula for each individual cube initially and entered into a priority queue. The priority queue is a dynamic data structure which allows to find the cube with the smallest associated waiting time in at most $\log_2 n_c$ steps. In each simulation step the cube with the minimum waiting time is identified and the corresponding reaction or diffusion event executed (similar to a normal Gillespie step in that cube alone). As mentioned before, this will only involve update of at most two cubes. The sum of reaction and diffusion propensities for each cube are recalculated and new waiting times for the cubes are sampled. This results in the following algorithm:

Data: $\mathbf{S}_0(t,k), t_0, t_{max}, r_j, D_i$, geometry
Result: $\mathbf{S}(\mathbf{t},\mathbf{k})$

$t = t_0$;
initialize priority queue Q;
construct $\mathbf{N}(k)$ from geometry;
for $k = 1, \ldots, n_c$ **do**
  $\mathbf{S}_k = \mathbf{S}_{0,k}$;
  $r_{0,k} = \sum_j r_j(\mathbf{S}_k, t)$;
  $d_{0,k} = \sum_i |\mathbf{N}(k)| d_i(\mathbf{S}_k, t)$;
  draw a random τ_k from $\mathbb{P}(\tau_k, 0) = (r_{0,k} + d_{0,k}) \exp\left(-(r_{0,k} + d_{0,k})\tau_k\right)$;
  insert (τ_k, k) into Q;
end
while $t < t_{max}$ **do**
  get cube k with minimum τ_k from Q;
  sample random number r in $[0, 1]$;
  if $r < r_{0,k}/(r_{0,k} + d_{0,k})$ **then**
    draw a random reaction according to $\mathbb{P}(j|\tau_k) = \frac{r_j(\mathbf{S}_k,t)}{r_{0,k}}$;
    update $\mathbf{S}_k$;
    $r_{0,k} = \sum_j r_j(\mathbf{S}_k, t)$;
    $d_{0,k} = \sum_i |\mathbf{N}(k)| d_i(\mathbf{S}_k, t)$;
    draw new τ_k;
    update (τ_k, k) in Q;
  end
  else
    draw a random diffusion according to $\mathbb{P}(i|\tau_k) = \frac{d_i(\mathbf{S}_k,t)}{d_{0,k}}$;
    randomly select a neighbor m from $\mathbf{N}(k)$;
    update $\mathbf{S}_k$ and $\mathbf{S}_m$;
    recalculate $r_{0,k}, d_{0,k}, r_{0,m}, d_{0,m}$ draw new τ_k and τ_m;
    update (τ_k, k) and (τ_m, m) in Q;
  end
end
return $\mathbf{S}(t,k)$

Using the property that the remaining cubes have assigned waiting times that are still valid samples, Elf proved that this algorithm generates exact samples to the reaction-diffusion master equation. Because the core of his algorithm is to quickly find the "subvolume" with the smallest waiting time in each step, he termed his algorithm the *next subvolume method* (also summarized in Figure 2.10).

This gives us a clear idea how to sample solutions from the reaction-diffusion master equation, but until now we did not care about the subdivision into cubes at all. Is any subdivision with any cube size l permissible? The limitation for cube sizes are found within the approximation for reaction rates we have made before. The reaction constants k_j include the probability of encounter between two species in a reference volume, as such they scale with volume. In the case of the subdivision into cubes the reaction rates have to be rescaled by the cube volume. However, if the cube size

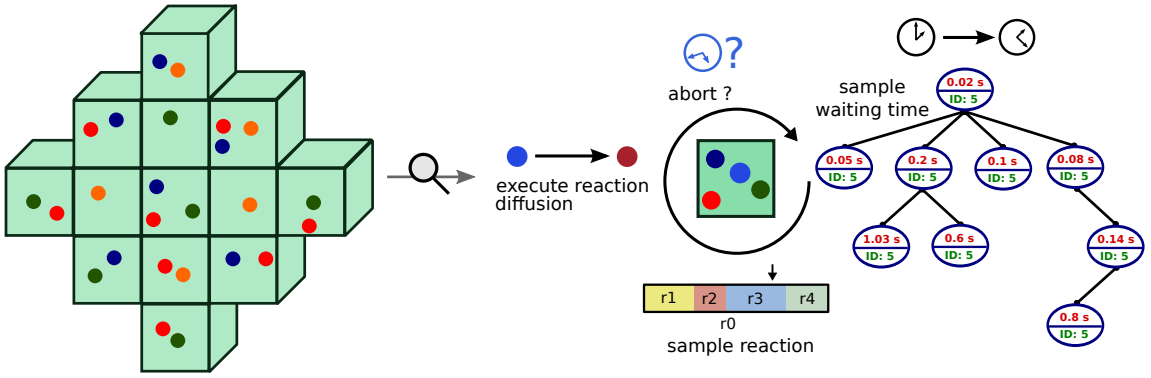

Figure 2.10: The next subvolume method as derived by Elf.

becomes close to molecule sizes this is not valid anymore as now other microscopic processes govern the reaction propensity. As thus, the cube size should be large enough so that the initial assumptions still hold but small enough to account for spatial inhomogeneities. As a general rule the minimum side length l of a cube should not be smaller than the mean reactive path p_r [191]. p_r denotes the average distance a molecule will pass before encountering a reaction and is given by:

$$p_r = \frac{\sqrt{\langle D_i \rangle}}{\langle r_j(\mathbf{S}, t) \rangle}. \tag{2.41}$$

It remains to mention that there have been recent advances in speeding up the sample generation from the reaction-diffusion master equation by employing massive parallelization. Here each thread will simulate a single cube and the strategy deviates a bit from the next subvolume method. In the parallelization it is first calculated what the minimum waiting time for any diffusion event will be, and the Gillespie algorithm is executed for all cubes at once in this time step. Employing hardware which enables a parallelization in such magnitudes, e.g. graphic processing units (GPUs), one can achieve significant speed-ups [192, 193]. However, those speed-ups are dependent on the minimum waiting time for a diffusion event. In the regime of very fast diffusion the waiting times for diffusion events will be very small, thus, only few reactions will take place and most of the advantage of parallelization will be lost. This is resolved by the implementations in rather using the mean waiting time for a diffusion event, however, this will introduce an approximation and the algorithm will not necessarily generate completely exact samples. In the biological system we will consider in this thesis fast diffusion of various molecules is present. As a consequence, for all stochastic models used in this thesis we will remain with the next subvolume method, as it guarantees exactness.

2.3.2 Partial differential equations and finite element methods

The reaction-diffusion equation

As we have seen in section 2.3.1 a master equation induces a corresponding Langevin equation which gives us a transition from a stochastic to a deterministic system. The

advantage of this transition is, that it also gives us some idea what conditions must hold in order that the system becomes deterministic. Free diffusion of molecules is usually fast compared to reaction rates. Consequently, we can expect many diffusion events to take place if our subdivision into cubes is sufficiently fine. As thus, the same assumptions as for the reaction events can be made for diffusion events and the number of diffusion events can be approximated by a Normal distribution. Analogous to equation 2.31 we can also formulate a Langevin equation for the reaction-diffusion master equation. Given an existent subdivision of the modeled volume into cubes with indices k and neighborhoods $\mathbf{N}(k)$ we can formulate the following update rule for the state change:

$$\begin{aligned} \mathbf{S}(t+\tau,k) &= \mathbf{S}(t,k) + \sum_j \rho_j \phi_j + \sum_i \left[\left(\sum_{m \in \mathbf{N}(k)} \zeta_i^m \mathbf{1}_m \right) - \zeta_i^k |\mathbf{N}(k)| \mathbf{1}_i \right] \\ \text{with } \mathbb{P}(\rho_j = x) &\propto \mathcal{N}\big(r_j(\mathbf{S},t)\tau,\, r_j(\mathbf{S},t)\tau\big) \\ \text{and } \mathbb{P}(\zeta_i^k = x) &\propto \mathcal{N}\big(d_i(\mathbf{S}_k,t)\tau,\, d_i(\mathbf{S}_k,t)\tau\big). \end{aligned} \tag{2.42}$$

Again we will use the scaling properties of the Normal distribution and take the limit case as $\tau \to 0$ which results in the Langevin equation

$$\begin{aligned} \frac{d\mathbf{S}(t,k)}{dt} = & \underbrace{\sum_j \phi_j r_j(\mathbf{S}_k,t) + \sum_i \left[\sum_{m \in \mathbf{N}(k)} \mathbf{1}_m d_i(\mathbf{S}_m,t) - |\mathbf{N}(k)| \mathbf{1}_i d_i(\mathbf{S}_k,t) \right]}_{\text{deterministic term}} \\ & \underbrace{+ \sum_j \phi_j \sqrt{r_j(\mathbf{S}_k,t)}\Gamma_j(t) + \sum_i \left[\sum_m \mathbf{1}_m \sqrt{d_i(\mathbf{S}_m,t)}\Lambda_i(t) - |\mathbf{N}(k)| \mathbf{1}_i \sqrt{d_i(\mathbf{S}_k,t)}\Xi_i(t) \right]}_{\text{noise term}}, \end{aligned} \tag{2.43}$$

where $\Gamma_j(t), \Lambda_i(t)$ and $\Xi_i(t)$ are Gaussian white noises. The equation behaves as for the non-spatial case, however it is interesting to see, that the diffusion part of the noise term uses two Gaussian white noise terms, one for the diffusive influx, $\Lambda_i(t)$, and one for the diffusive efflux, $\Xi_i(t)$. Because all of the noise terms behave the same, we see that the diffusive terms can contribute proportionally more to the noise than the reaction terms. As thus, diffusion might result in increased noise in the biological system.

As we have seen earlier the deterministic term of this Langevin equation are also the mean value of the state change, which gives us a deterministic ODE equation for the evolution of the state $\mathbf{S}$. Up to now we have considered a distinct discrete partition of the modeling volume into cubes. We will now attempt to drop this assumption in order to formulate a more general expression. We have seen that in the Langevin equation the state becomes continuous in time. Consistent with that we will, thus, also try to express the state continuous in space. How can we achieve that? We will first switch from expressing $\mathbf{S}$ in coordinates in space instead of cube indices k. This has been done implicitly with the cubes already as each cube had a position in space $\mathbf{x} = \{x, y, z\}$. Thus, we will now explicitly express $\mathbf{S}$ as function of $\mathbf{x}$. The neighborhood of a cube can still be expressed easily, for instance the neighbors of the state $\mathbf{S}(t, \{x, y, z\})$ on

the x-axis are given by $\mathbf{S}(t, \{x-l, y, z\})$ and $\mathbf{S}(t, \{x+l, y, z\})$, thus, the midpoints of the previous cubes. We will also keep the cube side length l as a variable now, thus explicitly including the propensity equation for d_i for species S_i as given in equation 2.36. This results in the following reformulation of the Langevin equation[20]:

$$\begin{aligned}\frac{d\langle \mathbf{S}(t,\mathbf{x})\rangle}{dt} &= \sum_j \phi_j r_j(\mathbf{S}, t, \mathbf{x}) \\ &\quad + \sum_i \frac{D_i}{l^2}\Big[S_i(t, \{x+l, y, z\}) + S_i(t, \{x-l, y, z\}) \\ &\quad + S_i(t, \{x, y+l, z\}) + S_i(t, \{x, y-l, z\}) \\ &\quad + S_i(t, \{x, y, z+l\}) + S_i(t, \{x, y, z-l\}) - |\mathbf{N}(k)| S_i(t, \{x, y, z\})\Big]\end{aligned} \tag{2.44}$$

We are now in continuous space. Thus our state $\mathbf{S}$ will be transformed to concentrations of molecules, with the variables continuous in time as well as space. This results in the following limit case for the propensities r_j derived in equation 2.10

$$r_j(\mathbf{S}, t, \mathbf{x}) = \tilde{k}_j \prod_k S_k(t, \mathbf{x})^{a_k}. \tag{2.45}$$

Also, l can now be fully varied. The sum over i is nothing else than multiplication of all the state vectors in the diffusion term by a diagonal matrix whose entries are given by the diffusion rates D_i. We will denote this matrix by $\mathbf{D}$. Furthermore, we will for now assume an unbounded space, so every cube has $|\mathbf{N}(k)| = 6$ neighbors[21]. As many reactions happen, the mean reaction path will be shorter and shorter and l will approach zero. Applying some rearrangements and letting $l \to 0$ this results in the following equation:

$$\begin{aligned}\frac{d\langle \mathbf{S}(t,\mathbf{x})\rangle}{dt} &= \sum_j \phi_j r_j(\mathbf{S}, t, \mathbf{x}) \\ &\quad + \lim_{l\to 0} \mathbf{D}\Big[\frac{\mathbf{S}(t, \{x+l, y, z\}) - 2\mathbf{S}(t,\mathbf{x}) + \mathbf{x}(t, \{x-l, y, z\})}{l^2} \\ &\quad + \frac{\mathbf{S}(t, \{x, y+l, z\}) - 2\mathbf{S}(t,\mathbf{x}) + \mathbf{x}(t, \{x, y-l, z\})}{l^2} \\ &\quad + \frac{\mathbf{S}(t, \{x, y, z+l\}) - 2\mathbf{S}(t,\mathbf{x}) + \mathbf{x}(t, \{x, y, z-l\})}{l^2}\Big].\end{aligned} \tag{2.46}$$

The expressions appearing in the diffusion term are second order central differences, as such the limit cases are the second-order partial derivatives in space and the sum is nothing else than the Laplace operator defined in 3-D space and for multivariate functions as[22]

$$\Delta_{\mathbf{x}} \mathbf{f}(\mathbf{x}) = \begin{pmatrix} \nabla_{\mathbf{x}} \cdot \nabla_{\mathbf{x}} f_1 \\ \vdots \\ \nabla_{\mathbf{x}} \cdot \nabla_{\mathbf{x}} f_n \end{pmatrix} = \frac{\partial \mathbf{f}}{\partial x} + \frac{\partial \mathbf{f}}{\partial y} + \frac{\partial \mathbf{f}}{\partial z} = \begin{pmatrix} \Delta_{\mathbf{x}} f_1 \\ \vdots \\ \Delta_{\mathbf{x}} f_n \end{pmatrix}. \tag{2.47}$$

[20] This is still the mean of the previous Langevin equation.

[21] Note, that all transformations can also be executed for a one- or two-dimensional space. In general every cube would then have $2 \cdot d$ neighbors with d being the dimension.

[22] f_i are the vector components of the multivariate function $\mathbf{f}$.

Assuming the absence of fluctuations, or explicitly modeling the mean state, this transforms in the reaction-diffusion equation given as

$$\frac{d\mathbf{S}(t,\mathbf{x})}{dt} = \sum_j \phi_j r_j(\mathbf{S},t,\mathbf{x}) + \mathbf{D}\Delta_{\mathbf{x}}\mathbf{S}(t,\mathbf{x}). \tag{2.48}$$

This equation now includes derivatives in space and time at the same time, thus, it is a *partial differential equation* (PDE). We will treat strategies to solve this equation later but before that we will make a short excursion to boundaries in space.

Boundary and initial conditions

In the previous section we defined an equation for the evolution of the system state in time and space. This reaction-diffusion equation defines the solution of the system, but is the equation sufficient to derive a unique solution for the state of the system? Even though we have not looked at the theory of solution strategies we can already say that the equation as we have defined it here imposes some problems.
In order to derive equation 2.48 we assumed an infinite space, however, this will not ever be the case in our modeling approaches. In most cases, our system will be modeled in a distinct volume Ω. The equation fully describes the system *within* that volume, but what happens at the boundary $\partial\Omega$? The boundary is also part of the solution, so for different boundary conditions we may expect different solutions. As a consequence, defining the system without boundary conditions prevents existence of a unique solution. As such the problem is already ill-posed and we need to provide boundary conditions.
Luckily, there are only few restrictions on the form of the boundary conditions. In fact, any unique function on $\partial\Omega$ is a suitable boundary condition, even though we will see later that some boundary conditions are more suitable than others. What are the most common boundary conditions when modeling biological systems? The most trivial choice would be to fix the value of the solution on the boundary. Thus, we get

$$\mathbf{S}(t,\mathbf{x}) = \mathbf{f}(t,\mathbf{x}) \quad \text{for} \quad \mathbf{x} \in \partial\Omega. \tag{2.49}$$

Boundary conditions of this type are called *Dirichlet boundary conditions*. This may look trivial, but if we do not know $\mathbf{S}$ we often will not know its values on $\partial\Omega$. It will be much more common, however, that we know some fluxes or conservation properties on the boundary. We will define this boundary condition via the normal $\mathbf{n}$ of the boundary. The normal is a vector which is perpendicular to the boundary, thus its scalar product $\langle\cdot,\cdot\rangle$ will evaluate to zero, $\langle\mathbf{n},\partial\Omega\rangle = 0$. With this definition the direction of the normal is not unique, thus, we will define it to always point outwards. This gives the *Neumann boundary condition*

$$\frac{d\mathbf{S}(t,\mathbf{x})}{d\mathbf{n}} = \mathbf{f}(t,\mathbf{x}) \quad \text{on} \quad \partial\Omega. \tag{2.50}$$

Having a Neumann boundary of zero would correspond to an isolated system, as it means that no substances are exchanged over the boundary. Consequently, a negative Neumann boundary describes an influx into the volume Ω over the boundary and a positive Neumann boundary an efflux. Neumann boundaries can be interpreted much easier biologically and are, thus, the preferred choice in Systems Biology.

Finally, the last boundary condition we will introduce is the *Robin boundary condition* which is a mixture of the Dirichlet and Neumann boundary condition and has the form

$$\alpha \mathbf{S}(t, \mathbf{x}) + \beta \frac{d\mathbf{S}(t, \mathbf{x})}{d\mathbf{n}} = \mathbf{f}(t, \mathbf{x}) \quad \text{on} \quad \partial\Omega, \tag{2.51}$$

with α and β being scalars. It can be seen as a coupling between the boundary value and its normal derivative, thus it acts like an equilibrium boundary condition.

Even with fully defined boundary conditions we still can not expect to find a solution to the problem formulated in equation 2.48. This is due to the fact that the equation describes the temporal and spatial evolution of the state, which will depend on the initial state $\mathbf{S}_0(\mathbf{x}) = \mathbf{S}(0, \mathbf{x})$. However, if we provide the initial state as well we finally end up with a fully defined *reaction-diffusion problem* which is given by:

1. its reaction-diffusion equation $d\mathbf{S}(t, \mathbf{x})/dt = \sum_j \phi_j r_j(\mathbf{S}, t, \mathbf{x}) + \mathbf{D}\Delta_{\mathbf{x}}\mathbf{S}(t, \mathbf{x})$,
2. its boundary conditions on $\partial\Omega$
3. and its initial condition $\mathbf{S}_0(\mathbf{x})$.

The central question is if, and how, we can solve this problem which, as we will see, will bring us to a large class of mathematical problems.

Weak formulations and bilinear forms

What we aim to find is a function $\mathbf{S}(t, \mathbf{x})$ which solves our reaction-diffusion problem. Classical algebra or calculus will not help us here, because were are not looking for a specific value, but the entire function. Additionally, we also want to find a unique solution. Because, some of the steps we will use may seem counterintuitive I will first exemplify them on a very simple problem and extend the solution strategy to the reaction-diffusion problem afterwards. The main strategy we will employ will be looking for a solution in a specific function space V of test functions. The test functions are chosen in a way that they form a basis of a large function space in which we aim to find our solution function u. Because the test functions v_i form a basis, a function u can be expressed by $u = \sum_i u_i v_i$, thus by a coefficient vector. We will apply this strategy to the following example problem of a linear system

$$\mathbf{A}\mathbf{u} = \mathbf{f} \quad \text{with} \quad \mathbf{u}, \mathbf{f} \in \mathbb{R}^n. \tag{2.52}$$

Our test functions v_i will be the unit vectors $\mathbf{e}_i$ which form a basis of $\mathbb{R}^n$. For each basis function we will now apply the scalar product on both sides of the equation, yielding

$$\forall i : \langle \mathbf{A}\mathbf{u}, \mathbf{e}_i \rangle = \langle \mathbf{f}, \mathbf{e}_i \rangle. \tag{2.53}$$

Applying the basis property to u results in

$$\langle \mathbf{A} \sum_j u_i \mathbf{e}_j, \mathbf{e}_i \rangle = \langle \mathbf{f}, \mathbf{e}_i \rangle \tag{2.54}$$

$$\sum_j u_j \langle \mathbf{A}\mathbf{e}_j, \mathbf{e}_i \rangle = \langle \mathbf{f}, \mathbf{e}_i \rangle \tag{2.55}$$

This is now an equation which only acts on the test functions in order to find u. As it is formulated on a finite subspace of functions which might be smaller than the original function space, it is called the *weak formulation* of the problem. But does that imply a unique solution to the problem. Letting $\mathbf{u} = u_i$ be the coefficient vector to v_i and $\mathbf{f} = \{f_i\} = \{\langle \mathbf{f}, \mathbf{e}_i \rangle\}$, one can see easily that the matrix formulation of this problem, $\mathbf{Au} = \mathbf{f}$, is equivalent to the original problem. The weak formulation also induces a bilinear form for all $v \in V$: $a(u, v) = \mathbf{v}^T \mathbf{Au}$. The problem can, thus, be formulated in the following standard form of the weak formulation: find $u \in V$ such that for any $v \in V$ it holds that $a(u, v) = f(v)$. In particular it seems to hold that the weak formulation implies existence and uniqueness of the solution.

The example makes it intriguing to ask whether this strategy always implies existence and uniqueness. Indeed, there is a large class of problems where this holds, the conditions being given by the following theorem [proof in 194].

Theorem 2.1 (Lax-Milgram Theorem)**.** *Let V be a Hilbert space, V' the dual of V and $a(u, v)$ a bilinear form on V. Then if $a(u, v)$ is*

1. *bounded: $||a(u, v)|| \leq c \cdot ||u|| \cdot ||v||$, $c \in \mathbb{R}$ and*
2. *coercive: $||a(u, u)|| \geq a \cdot ||u||^2$, $a \in \mathbb{R}, a > 0$*

it follows that for any $f \in V'$ there is a unique solution $u \in V$ to the equation

$$a(u, v) = f(v)$$

and that $||u|| \leq \frac{1}{c}||f||$.

We will now apply the same strategy to our reaction diffusion equation, thus, we aim to find a solution $\mathbf{u} = \mathbf{S}(t, \mathbf{x})$ fulfilling

$$\frac{d\mathbf{S}(t, \mathbf{x})}{dt} = \sum_j \phi_j r_j(\mathbf{S}, t, \mathbf{x}) + \mathbf{D}\Delta_{\mathbf{x}}\mathbf{S}(t, \mathbf{x}). \tag{2.56}$$

This formulates an equation for each component u_i of the solution $\mathbf{u}(\mathbf{x}) = \big(u_i(\mathbf{x})\big)_i$ as

$$\forall i : \frac{du_i}{dt} = \sum_j \phi_{i,j} r_j(\mathbf{u}) + D_i \Delta_{\mathbf{x}} u_i. \tag{2.57}$$

We will use the induced scalar product in the function spaces given by

$$\langle f, g \rangle = \int_{-\infty}^{\infty} f \cdot g \, dx, \text{ with } f, g \in V. \tag{2.58}$$

Multiplication with the test functions v and integration leads to the following formulation of our reaction-diffusion problem: find $u_i \in V$ such that for all $v \in V$

$$\int_\Omega \frac{du_i}{dt} v d\mathbf{s} = \sum_j \phi_{i,j} \int_\Omega r_j(\mathbf{u}) v d\mathbf{s} + D_i \int_\Omega (\Delta_{\mathbf{x}} u_i) v d\mathbf{s}. \tag{2.59}$$

In order to transform this into a more standardized weak formulation we have to separate terms which do not explicitly include the solution $\mathbf{u}$. This will be the case for all zero-order reactions, meaning reaction propensities which are solemnly composed by a constant k_j. We will collect those reaction terms in a vector $\mathbf{f}$ given by the set of all zero order reaction indices $\mathbf{R}_0$ in the following way

$$\mathbf{f} = \sum_{j \in \mathbf{R}_0} \phi_j r_j(\mathbf{u}) = \sum_{j \in \mathbf{R}_0} \phi_j k_j. \tag{2.60}$$

All the remaining reaction r_j should now be at least first order, yielding

$$\int_\Omega \frac{du_i}{dt} v d\mathbf{s} - \sum_j \phi_{i,j} \int_\Omega r_j(\mathbf{u}) v d\mathbf{s} - D_i \int_\Omega (\Delta_\mathbf{x} u_i) v d\mathbf{s} = \int_\Omega f_i v d\mathbf{s}. \tag{2.61}$$

Applying Green's identity furthermore results in

$$\int_\Omega \frac{du_i}{dt} v d\mathbf{s} - \sum_j \phi_{i,j} \int_\Omega r_j(\mathbf{u}) v d\mathbf{s} + D_i \int_\Omega \nabla_\mathbf{x} u_i \nabla_\mathbf{x} v d\mathbf{s} - D_i \int_{\partial\Omega} (\nabla_\mathbf{x} u_i \cdot \mathbf{n}) v d\mathbf{s} = \int_\Omega f_i v d\mathbf{s}. \tag{2.62}$$

Apart from reducing the order of the derivatives this has an important consequence: we now have a term defined on the boundaries of the volume Ω. In particular it already includes a spatial derivative of u_i. This allows us to insert the Neumann boundaries directly into the equation[23]. A similar strategy can be employed for Dirichlet and Robin boundaries. However, we will not treat Robin boundaries here. The strategy is similar, but since we will not use them further, they shall not be treated here.
Thus, we assume our volume boundary $\partial\Omega$ can be divided completely into a Neumann boundary Γ_N and a Dirichlet boundary Γ_D. Furthermore, let the Neumann boundary be given by

$$\frac{d\mathbf{u}}{d\mathbf{n}} = \left(\gamma_N^i(\mathbf{x})\right)_i = \boldsymbol{\gamma}_N(\mathbf{x}) \quad \text{on}\, \Gamma_N \tag{2.63}$$

and the Dirichlet boundary by

$$\mathbf{u} = \left(\gamma_D^i(\mathbf{x})\right)_i = \boldsymbol{\gamma}_D(\mathbf{x}) \quad \text{on}\, \Gamma_D, \tag{2.64}$$

thus, by a set of boundary conditions for each component of the solution u_i. Plugging this into equation 2.62 and sorting terms yields

$$\int_\Omega \frac{du_i}{dt} v d\mathbf{s} + \sum_j \phi_{i,j} \int_\Omega r_j(\mathbf{u}) v d\mathbf{s} - D_i \int_\Omega \nabla_\mathbf{x} u_i \nabla_\mathbf{x} v d\mathbf{s} = \int_\Omega f_i v d\mathbf{s} + D_i \int_{\Gamma_N} (\gamma_N^i \cdot \boldsymbol{n}) v d\mathbf{s} + D_i \int_{\Gamma_D} \frac{d\gamma_D^i}{d\mathbf{n}} v d\mathbf{s}. \tag{2.65}$$

However, even though this equation forces the derivative of the Dirichlet condition to be included it does not enforce the solution to have Dirichlet values on the boundary, which can be seen particularly easy when the Dirichlet boundary condition is a constant. The equation still implicitly induces a zero Dirichlet boundary. This can be

[23] This is why Neumann boundaries are often called *natural boundary conditions*.

fixed by substituting u_i by $u_i + \gamma_D^i$. Assuming we use a basis which vanishes on the boundary, this will result in the correct Dirichlet boundary values. Substituting this into equation 2.65, leads to

$$\int_\Omega \frac{du_i}{dt} v d\mathbf{s} + \sum_j \phi_{i,j} \int_\Omega r_j(\mathbf{u} + \boldsymbol{\gamma}_D) v d\mathbf{s} - D_i \int_\Omega \nabla_\mathbf{x} u_i \nabla_\mathbf{x} v d\mathbf{s} = \int_\Omega f_i v d\mathbf{s} + D_i \int_{\Gamma_N} (\gamma_N^i \cdot \boldsymbol{n}) v d\mathbf{s} + D_i \int_{\Gamma_D} \frac{d\gamma_D^i}{d\mathbf{n}} v d\mathbf{s} - D_i \int_\Omega \nabla_\mathbf{x} \gamma_D^i \nabla_\mathbf{x} v d\mathbf{s} - \int_\Omega \frac{d\gamma_D^i}{dt} v d\mathbf{s} \tag{2.66}$$

This equation now already has a standardized weak form. For now we can not reduce it further as we remain with the nonlinearities introduced by the reaction rate functions r_j and the derivative in t. We will treat strategies to solve nonlinear systems and ordinary differential equations later, but for that we first need a finite space for our test functions and solutions. The problem formulation for now is still for a Hilbert space and since the equations includes derivatives as well as the induced scalar product, this will be the Sobolev space $\mathbb{H}^0$, which is non-finite. So we we will now try to find a finite basis which gives good approximations of the solution.

The finite element method

We aim at finding the solution to our reaction-diffusion problem, $\mathbf{u}$, in a finite space which allows a good approximation of the real solution. There is a large theory of approximating functions by simpler functions spaces in mathematics and it is closely connected to interpolation. Taylor's theorem gives a way to approximate any function by a polynomial of possibly infinite degree:

Theorem 2.2 (Taylor's theorem)**.** *Let $f : \mathbb{R}^n \to \mathbb{R}$ be a k-times differentiable function at the point $\mathbf{a}$ then there exists a function $R_a : \mathbb{R}^n \to \mathbb{R}$ such that*

$$f(\mathbf{x}) = \sum_{|\mathbf{j}|=0}^{k} \frac{D^\mathbf{j} f(\mathbf{a})}{\mathbf{j}!} (\mathbf{x} - \mathbf{a})^\mathbf{j} + \sum_{|\mathbf{j}|=k} R_a(\mathbf{x}) (\mathbf{x} - \mathbf{a})^\mathbf{j}, \tag{2.67}$$

with $\lim_{\mathbf{x}\to\mathbf{a}} R_a(\mathbf{x}) = 0$.

As thus, it seems natural to choose a basis of polynomials up to some degree k as a basis to approximate our function $\mathbf{u}$. Another principle from interpolation theory is the approximation of higher order functions by piecewise polynomials of lower order. Thus, if we subdivide our volume Ω into a set $\Omega = \bigcup_h \Omega_h$ and choose a set of basis functions which is only non-zero on one element we can select a low-order polynomial basis in order to express the solution $\mathbf{u}$ within that basis. Because for this we will subdivide our volume into finite set of distinct elements those methods are called *finite element methods*. Thus, our basis will be given by the piecewise polynomial of degree k on each subvolume Ω_h

$$\{\mathbf{v}_h | \mathbf{v}_h \in \mathbb{P}^k, \mathbf{v}_h : \Omega_h \to \mathbb{R}^n\}. \tag{2.68}$$

We will concentrate on cases for two space dimensions in order to illustrate the construction of the basis functions as those are the ones we will use in our thesis. However, the derivation is completely equivalent for higher space dimensions. The subdivision of the volume $\bigcup_h \Omega_h$ is usually done by a triangulation, thus, by subdividing the area Ω into a set of triangles. The same can be done with rectangles or any other shape[24]. The coefficients of the basis functions are the quantities which we want to identify. However, we know that any polynomial of degree k in dimension d is also fully specified by $k \cdot d$ of its function values. As such the idea is to define a set of control points on the triangles or rectangles used and to express the function $\mathbf{v}_h$ by the values $\mathbf{u}_i$ on the control points. We will execute this for the univariate case only, as the basis for the multivariate case is just the same basis applied to every variable in the solution vector. First let us assume we have a triangular or rectangular element Ω_h with their respective corners $P_i = (x_i, y_i)$ each. In a first step we want to transform the finite elements into a coordinate system where every element is standardized. Thus if our original element was a function of x and y we want to map it to a α-β coordinate system where α and β are in $[0, 1]$ and the shapes are mapped as illustrated in figure 2.11. The transformation allowing that for the triangle shape is

$$x = x_1 + (x_2 - x_1)\alpha + (x_3 - x_1)\beta \tag{2.69}$$
$$y = y_1 + (y_2 - y_1)\alpha + (y_3 - y_1)\beta \tag{2.70}$$

and for the quadratic shape

$$x = x_1 + (x_2 - x_1)\alpha + (x_3 - x_1)\beta + (x_4 - x_1)\alpha\beta \tag{2.71}$$
$$y = y_1 + (y_2 - y_1)\alpha + (y_3 - y_1)\beta + (y_4 - y_1)\alpha\beta. \tag{2.72}$$

There are obviously several basis for the polynomials. The one we want to choose is defined by the control points, thus, if our control points have solutions u_i assigned to the control point P_i our basis functions $v_i = v_i(\alpha, \beta)$ should allow our solution s to be expressed as

$$s = \sum_i u_i v_i = \mathbf{uv}. \tag{2.73}$$

In order to derive this basis we start with an *Ansatz* based on the monomes m_i with coefficients c_i, thus the solution is given by

$$s = \mathbf{c} \cdot \mathbf{m} = \mathbf{u} \cdot \mathbf{v} \tag{2.74}$$

The trick is to find the vector $\mathbf{c}$. For this we identify the coefficients that lead to the correct values u_i at the control points $P_i = (\alpha_1, \beta_1)$. This condition is given by the following linear system:

$$\begin{pmatrix} m_1(\alpha_1, \beta_1) & \dots & m_n(\alpha_1, \beta_1) \\ \vdots & \ddots & \vdots \\ m_1(\alpha_n, \beta_n) & \dots & m_n(\alpha_n, \beta_n) \end{pmatrix} \cdot \begin{pmatrix} c_1 \\ \vdots \\ c_n \end{pmatrix} = \mathbf{A} \cdot \mathbf{c} = \mathbf{u} \tag{2.75}$$

Plugging this into equation 2.74 leads to

$$s = \mathbf{A}^{-1}\mathbf{u} \cdot \mathbf{m} = \mathbf{u} \cdot \mathbf{v} \tag{2.76}$$
$$\rightarrow s = \mathbf{u} \cdot (\mathbf{A}^{-1})^T \mathbf{m} = \mathbf{u} \cdot \mathbf{v} \tag{2.77}$$
$$\rightarrow \mathbf{v} = (\mathbf{A}^{-1})^T \mathbf{m}. \tag{2.78}$$

[24] In 3-D the most common shape is the tetrahedron.

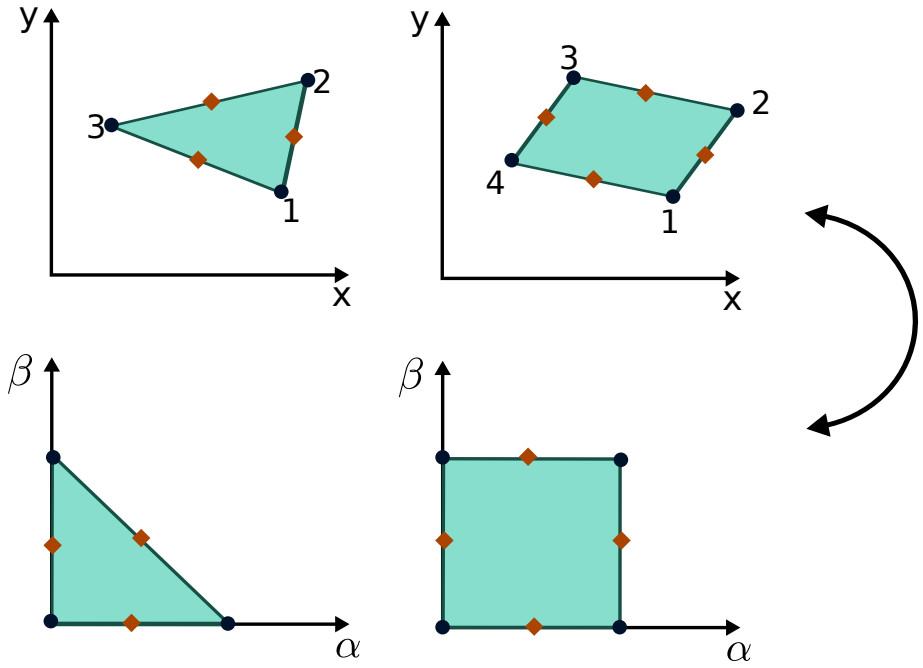

Figure 2.11: The shapes of the finite elements and their standardized mapping into a new coordinate system. Control points for the linear basis functions are shown as dark blue dots. The additional control points for the cubic basis functions are shown as red diamonds.

This gives us our basis functions v_i. One needs one control point for each initial monom basis function. Thus, for higher order polynomials, we have to add control points to the elements as illustrated in figure 2.11. If we keep the control points of lower order polynomials and only add new ones for higher order polynomials, this basis allows a quite simple transition between basis functions if the geometry of finite elements Ω_h remains unchanged. In particular, if we want to find a solution in the higher polynomial basis $\tilde{\mathbf{v}}$ we can easily map the solution of the lower polynomial basis $\mathbf{v}$ and use it as an initial guess for the new solution which allows a fast error reduction and fast computation of the new solution. Another advantage of those basis functions is that we can express our Dirichlet zero boundary by directly setting control points on the boundary to zero. This abolishes the need for the additional terms introduced in equation 2.66. However, one can see that only for linear basis functions this will result in a truly complete zero boundary. Consequently, if one wants to have good solutions at the boundaries, linear basis functions should be chosen for those elements.
The corresponding basis functions $\mathbf{v} = \{v_i(\alpha, \beta)\}$ for the linear and cubic case are given by:

$$\mathbf{v}^l = \begin{pmatrix} 1-\alpha-\beta \\ \alpha \\ \beta \end{pmatrix} \quad \text{and} \quad \mathbf{v}^c = \begin{pmatrix} (1-\alpha-\beta)(1-2\alpha-2\beta) \\ \alpha(2\alpha-1) \\ \beta(2\beta-1) \\ 4\alpha(1-\alpha-\beta) \\ 4\alpha\beta \\ 4\beta(1-\alpha-\beta) \end{pmatrix}. \tag{2.79}$$

With any of those basis functions $\mathbf{v}$ we can now express our solution u_i by the function values at the control points $p^h_{i,k}$ and over the finite element Ω_h with basis

functions $\mathbf{v}_i^h$. However, our solution is also a function of time. We can still use the same basis if we simply convert the *coefficients* into functions of time. Thus, let us assume we have a total of n_h finite elements, then the basis $\mathbf{v}_i$ can be defined as

$$\mathbf{v}_i = \begin{pmatrix} \mathbf{v}_i^1 \\ \vdots \\ \mathbf{v}_i^{n_h} \end{pmatrix} \tag{2.80}$$

with the coefficients $\mathbf{p}_i(t)$

$$\mathbf{p}_i = \begin{pmatrix} \mathbf{p}_i^1(t) \\ \vdots \\ \mathbf{p}_i^{n_h}(t) \end{pmatrix}. \tag{2.81}$$

Thus, the size of our basis will depend on the polynomial degrees as well as the number of finite elements n_h. With this basis we now can express our solution u_i simply by

$$u_i(t) = \sum_k p_{i,k}(t) \cdot v_{i,k}, \tag{2.82}$$

where k denotes an index running over the individual components of the basis functions $\mathbf{v}_i^h$. Plugging this into our weak formulation 2.65 now yields[25]

$$\forall l : \sum_k \frac{dp_{i,k}}{dt} \int_\Omega v_{i,k} v_{i,l} d\mathbf{s} + \sum_j \phi_{i,j} \int_\Omega r_j(\mathbf{u}) v_{i,l} d\mathbf{s} - D_i \sum_k p_{i,k} \int_\Omega \nabla_\mathbf{x} v_{i,k} \nabla_\mathbf{x} v_{i,l} d\mathbf{s} = \int_\Omega f_i v_{i,l} d\mathbf{s} + D_i \int_{\Gamma_N} (\gamma_N^i \cdot \boldsymbol{n}) v_{i,l} d\mathbf{s} + D_i \int_{\Gamma_D} \frac{d\gamma_D^i}{d\mathbf{n}} v_{i,l} d\mathbf{s} \tag{2.83}$$

The expression now defines our solution in terms of the coefficients $\mathbf{p}_i(t)$. All the other terms are already completely defined by our basis functions. In order to make this more apparent we will now define a set of matrices and functions.

We begin with defining the so called *mass matrix* $\mathbf{M}_i$ with

$$\mathbf{M}_i = \begin{pmatrix} \langle v_{i,1}, v_{i,1} \rangle & \dots & \langle v_{i,n_b^i}, v_{i,1} \rangle \\ \vdots & \ddots & \vdots \\ \langle v_{i,1}, v_{i,n_b^i} \rangle & \dots & \langle v_{i,n_b^i}, v_{i,n_b^i} \rangle \end{pmatrix} \tag{2.84}$$

using the induced scalar products

$$\langle \nabla_\mathbf{x} v_{i,k}, \nabla_\mathbf{x} v_{i,l} \rangle = \int_\Omega \nabla_\mathbf{x} v_{i,k} \cdot \nabla_\mathbf{x} v_{i,l} d\mathbf{s} \tag{2.85}$$

and n_b^i being the number of basis functions for u_i.

We also define the *stiffness matrix* $\mathbf{S}_i$ with

$$\mathbf{S}_i = \begin{pmatrix} \langle \nabla_\mathbf{x} v_{i,1}, \nabla_\mathbf{x} v_{i,1} \rangle & \dots & \langle \nabla_\mathbf{x} v_{i,n_b^i}, \nabla_\mathbf{x} v_{i,1} \rangle \\ \vdots & \ddots & \vdots \\ \langle \nabla_\mathbf{x} v_{i,1}, \nabla_\mathbf{x} v_{i,n_b^i} \rangle & \dots & \langle \nabla_\mathbf{x} v_{i,n_b^i}, \nabla_\mathbf{x} v_{i,n_b^i} \rangle \end{pmatrix}. \tag{2.86}$$

[25] Note that for the special case that we choose the same basis for all solution components it holds that $\forall k, i, j : v_{i,k} = v_{j,k}$.

The left hand side of the equation will be expressed in the linear form $\mathbf{L}_i = (l^i_j)_j$ with

$$l^i_j = \int_\Omega f_i v_{i,j} d\mathbf{s} + D_i \int_{\Gamma_N} (\gamma^i_N \cdot \boldsymbol{n}) v_{i,j} d\mathbf{s} + D_i \int_{\Gamma_D} \frac{d\gamma^i_D}{d\mathbf{n}} v_{i,j} d\mathbf{s} \tag{2.87}$$

Finally, the nonlinear terms are collected in $\mathbf{F}_i$ with

$$\mathbf{F}_i(\mathbf{p}) = \begin{pmatrix} \sum_j \phi_{i,j} \langle r_j(\mathbf{u}), v_{i,1} \rangle \\ \vdots \\ \sum_j \phi_{i,j} \langle r_j(\mathbf{u}), v_{i,n^i_b} \rangle \end{pmatrix}. \tag{2.88}$$

This now allows us to express the entire problem in a standard nonlinear ordinary differential equation (ODE) for each solution component u_i given by

$$\forall i : \mathbf{M}_i \frac{d\mathbf{p}_i}{dt} + \mathbf{F}_i(\mathbf{p}) + \mathbf{S}_i \mathbf{p}_i = \mathbf{L}_i. \tag{2.89}$$

Obviously, by defining matrices $\mathbf{M}, \mathbf{S}$ with the individual matrices for each u_i on their diagonal and appending all coefficients, nonlinear terms and left hand sides into vectors $\mathbf{F}, \mathbf{p}, \mathbf{L}$ the solution $\mathbf{u}$ is governed by the ODE system

$$\mathbf{M} \frac{d\mathbf{p}}{dt} + \mathbf{F}(\mathbf{p}) + \mathbf{S}\mathbf{p} = \mathbf{L}. \tag{2.90}$$

What do we gain with this formulation? We have started from a nonlinear ODE system for $\mathbf{u}$, however the original system contained several integrals which we could not determine as well as derivatives of the unknown solution in time as well as space. In equation 2.90 we find only derivatives and integrals over basis functions which we have defined ourselves. In fact, if we maintain the basis, all integrals and derivatives can be computed before solving the system once and used accordingly. Furthermore, the basis has small support, meaning that many of the products of the basis functions and their derivatives will evaluate to zero. Due to the definition of the basis this is the case for all scalar products involving basis functions from different finite elements. Because any finite element has a small bounded numbers of neighbors (three for triangles for instance), only a small fraction of the used matrices will be filled. Thus, the number of non-zero matrix entries is linear in the product of the numbers of basis functions and finite elements, making it very sparse.
Strategies how to solve this nonlinear ODE system will be introduced shortly in this section, however, before that we will introduce another method to formulate the problem over finite elements.
In order to reduce the complexity of our problem we have defined the solution u_i as a continuous function given by the finite element basis. This strategy is also known as the *Galerkin method*. However, this assumes that our solution will be continuous over the finite elements. This not only becomes problematic if our solutions is not continuous but also when the solution includes some extreme jumps in space. In order to express those jumps one would have to make the grid very fine, and thus, the finite elements extremely small. Thus, in those cases it would be advantageous to relax the condition of a continuous function and sometimes allow for jumps between neighboring finite elements (also illustrated in Figure 2.12). Thus, we are looking for

a stable method which would allow those jumps but still formulates a solution consistent with the weak formulation. Looking at equation 2.65 and 2.90 we see that we can add arbitrary functions to both sides of the equation or zero expressions to any side without loosing equivalence to the original system. This defines an infinite set of Galerkin methods to solve the system and we will aim at finding the class of methods which allows for the jumps. As we will allow for discontinuities in the solution those methods are called *discontinuous Galerkin methods* (dG-FEM).

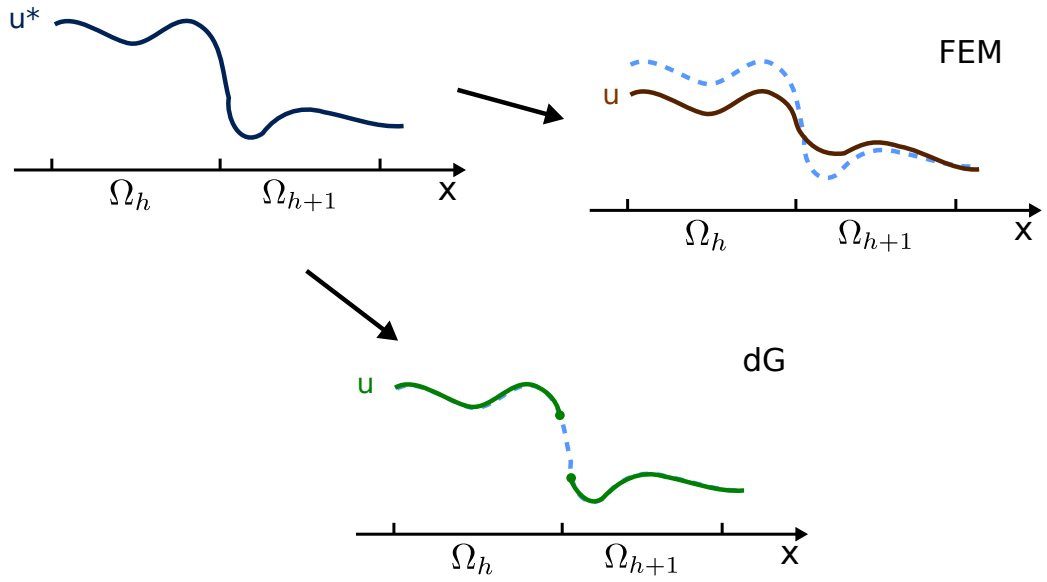

Figure 2.12: Allowing for discontinuities in space of the approximated solution u may sometimes be advantageous to a completely continuous solution as in FEM methods. Thus, the discontinuous Galerkin (dG) method may allow for discontinuities which improve the approximation even if the real solution u^* is continuous.

Discontinuous Galerkin methods

We will now construct a method to approximate the continuous solution $\mathbf{u}$ by piecewise discontinuous function. In order to maintain the equations concise we will use a simple example to introduce this discontinuous Galerkin method. For this, we will first define a few quantities to describe the jumps we will now allow between finite elements. On the boundary $\partial\Omega$ we already had an assigned normal pointing outwards of the boundary. We will extend this to all inner edges Ψ_j as well, thus the edges between finite elements. The normal will again point outwards of the finite element. Any function defined on the finite elements now may take two different values approaching the boundary depending on the direction it is coming from. We define the boundary value coming from the inside of the finite element as

$$f^i = \lim_{h \to 0^-} f(\boldsymbol{x} + h\boldsymbol{n}), \tag{2.91}$$

and the function value when approaching an edge point from the outside as

$$f^o = \lim_{h \to 0^+} f(\boldsymbol{x} + h\boldsymbol{n}). \tag{2.92}$$

We will furthermore define the average $\langle\cdot\rangle$ and the jump $[[\cdot]]$ as

$$\langle f \rangle = \frac{1}{2}(f^i + f^o) \qquad [[f]] = f^i - f^o. \tag{2.93}$$

The sample problem we will treat is the Poisson equation with mixed boundary conditions

$$\Delta u = 0 \tag{2.94}$$

$$\frac{du(\boldsymbol{x})}{d\boldsymbol{n}} = 0 \text{ on } \Gamma_N \tag{2.95}$$

$$u(\boldsymbol{x}) = C \text{ on } \Gamma_D \tag{2.96}$$

Again we will multiply the equation by the test functions v and apply Green's identity. However, since we now have interior boundaries and smooth functions only on the individual finite elements, we have to apply Green's identity to each finite element, which yields

$$\forall v: \quad \int_\Omega \nabla_{\boldsymbol{x}} u \nabla_{\boldsymbol{x}} v d\boldsymbol{s} = \int_{\partial\Omega} (\nabla_{\boldsymbol{x}} u \cdot \boldsymbol{n}) v d\boldsymbol{s} + \sum_j \int_{\Psi_j} (\nabla_{\boldsymbol{x}} u \cdot \boldsymbol{n})[[v]] d\boldsymbol{s}. \tag{2.97}$$

u is still a continuous functions, thus, at the boundaries we will have $u = \langle u \rangle$. Additionally, plugging in the boundary conditions the term for the outer boundaries disappears and we have

$$\int_\Omega \nabla_{\boldsymbol{x}} u \nabla_{\boldsymbol{x}} v d\boldsymbol{s} = \sum_j \int_{\Psi_j} (\nabla_{\boldsymbol{x}} \langle u \rangle \cdot \boldsymbol{n})[[v]] d\boldsymbol{s}. \tag{2.98}$$

We see that we now have a term that depends on the jumps of the basis functions, however no term that includes jumps in the solution u. We will make the equation more symmetric by adding a zero function to the left side which has a similar form as the term for the jumps in v, but now with the jumps in u

$$\sum_j \int_{\Psi_j} (\nabla_{\boldsymbol{x}} \langle v \rangle \cdot \boldsymbol{n})[[u]] d\boldsymbol{s} = 0. \tag{2.99}$$

This expression is zero due to the continuity of u, and for the sake of consistency this should also hold for the outer Dirichlet boundaries. Thus add the following expression to both sides of equation 2.98

$$\sum_j \int_{\Gamma_D} (\nabla_{\boldsymbol{x}} \langle v \rangle \cdot \boldsymbol{n})[[u]] d\boldsymbol{s}. \tag{2.100}$$

This yields the following discontinuous Galerkin equation

$$\int_\Omega \nabla_{\boldsymbol{x}} u \nabla_{\boldsymbol{x}} v d\boldsymbol{s} + \sum_j \int_{\Gamma_D} (\nabla_{\boldsymbol{x}} \langle v \rangle \cdot \boldsymbol{n})[[u]] d\boldsymbol{s} + \sum_j \int_{\Psi_j} (\nabla_{\boldsymbol{x}} \langle v \rangle \cdot \boldsymbol{n})[[u]] d\boldsymbol{s} = \sum_j \int_{\Psi_j} (\nabla_{\boldsymbol{x}} \langle u \rangle \cdot \boldsymbol{n})[[v]] d\boldsymbol{s} + \sum_j \int_{\Gamma_D} (\nabla_{\boldsymbol{x}} \langle v \rangle \cdot \boldsymbol{n})[[u]] d\boldsymbol{s}. \tag{2.101}$$

Due to the addition of the terms (and not subtraction) the resulting bilinear form will not be completely symmetric, which is why this discontinuous Galerkin method is called *non-symmetric interior penalty Galerkin* method (NIPG). The advantage of this method over other interior penalty methods for us is that it fulfills a conservation law, meaning that integrals over the real solution u are conserved in the solution of the NIPG method. The importance for this will become more apparent in section 3.2. The method as formulated in equation 2.101 is still very unstable. This is due to the fact that we allow jumps and do not restrict them, which gives a lot of freedom to either approximate the solution by the polynomials or the jumps. As such there are many different solutions which "almost" fulfill the equation. However, if we can approximate the solution very well without the jumps we would like to have a fully continuous solution. As such, it would be beneficial to penalize large jumps. Due to this, we can stabilize the method significantly by adding a *jump penalty* to the left side

$$-\sum_j \int_{\Psi_j} \sigma_j [[u]] \cdot [[v]] d\boldsymbol{s} = 0. \tag{2.102}$$

This finally yields the stabilized NIPG method for the Poisson equation given by

$$\begin{aligned} &\int_\Omega \nabla_{\boldsymbol{x}} u \nabla_{\boldsymbol{x}} v d\boldsymbol{s} + \sum_j \int_{\Gamma_D} (\nabla_{\boldsymbol{x}} \langle v \rangle \cdot \boldsymbol{n})[[u]] d\boldsymbol{s} + \sum_j \int_{\Psi_j} (\nabla_{\boldsymbol{x}} \langle v \rangle \cdot \boldsymbol{n})[[u]] d\boldsymbol{s} \\ &\quad - \sum_j \int_{\Psi_j} \sigma_j [[u]] \cdot [[v]] d\boldsymbol{s} = \sum_j \int_{\Psi_j} (\nabla_{\boldsymbol{x}} \langle u \rangle \cdot \boldsymbol{n})[[v]] d\boldsymbol{s} + \sum_j \int_{\Gamma_D} (\nabla_{\boldsymbol{x}} \langle v \rangle \cdot \boldsymbol{n})[[u]] d\boldsymbol{s}. \end{aligned} \tag{2.103}$$

The parameter σ_j must only be larger than zero to assure convergence. However, one can improve the performance by normalizing the penalties, so that jumps are penalized the same independent of edge properties. This can be achieved by scaling σ_j with the edge length l_j, thus

$$\sigma_j = \frac{A}{l_j}, \quad A > 0 \in \mathbb{R}. \tag{2.104}$$

We see that any normal FEM formulation can be transformed easily into a NIPG method by adding the interior integrals of Green's identity, the symmetry terms and the jump penalty. The jumps are defined on the basis functions only and can be pre-computed again. Thus, we result in a nonlinear ODE as in equation 2.90.

We can now ask ourselves how we can solve the resulting nonlinear ODE system. The main strategy one employs when solving such systems is to discretize the system in time and solve nonlinear equations systems for each time-step. Thus, we will begin to introduce strategies to solve nonlinear systems and continue with time discretization techniques.

Nonlinear root finding

The Newton-Raphson method

Nonlinear systems also arise when looking for steady state solution, thus, solutions where the system state is in equilibrium. In our framework, this means that the solution

components u_i are constant in time. Thus their coefficients for the basis functions must be as well[26] and equation 2.90 reduces to

$$\mathbf{F}(\mathbf{p}) + \mathbf{S}\mathbf{p} = \mathbf{L}. \tag{2.105}$$

This is the steady state equation and it is obviously a nonlinear equation system. Furthermore, if we define a function $\mathbf{G}(\mathbf{p}) = \mathbf{F}(\mathbf{p}) + \mathbf{S}\mathbf{p} - \mathbf{L}$ we can formulate the problem into the usual form of nonlinear systems, given by

$$\mathbf{G}(\mathbf{p}) = 0. \tag{2.106}$$

Thus, in the general case we aim to solve the nonlinear system

$$\mathbf{F}(\mathbf{x}) = 0. \tag{2.107}$$

In order to identify the vector $\mathbf{x}^*$ which fulfills this property we will use a succession of linear approximations of the function $\mathbf{F}$. From the Taylor theorem 2.2 we know that we can approximate $\mathbf{F}$ linearly by

$$\mathbf{F}(\mathbf{x}) = \mathbf{F}(\mathbf{x}_0) + \mathcal{D}_\mathbf{F}(\mathbf{x}_0)(\mathbf{x} - \mathbf{x}_0), \tag{2.108}$$

where $\mathcal{D}_\mathbf{F}$ is the Jacobian matrix of $\mathbf{F}$ given by

$$\mathcal{D}_\mathbf{F} = \begin{pmatrix} \frac{dF_1}{dx_1} & \cdots & \frac{dF_1}{dx_n} \\ \vdots & \ddots & \vdots \\ \frac{dF_n}{dx_1} & \cdots & \frac{dF_n}{dx_n} \end{pmatrix}. \tag{2.109}$$

Applying this to our nonlinear system we derive

$$\mathbf{F}(\mathbf{x}) = 0 \tag{2.110}$$
$$\mathbf{F}(\mathbf{x}_0) + \mathcal{D}_\mathbf{F}(\mathbf{x}_0)(\mathbf{x} - \mathbf{x}_0) = 0 \tag{2.111}$$
$$\mathcal{D}_\mathbf{F}(\mathbf{x}_0)(\mathbf{x} - \mathbf{x}_0) = -\mathbf{F}(\mathbf{x}_0) \tag{2.112}$$
$$\mathcal{D}_\mathbf{F}(\mathbf{x}_0)\Delta\mathbf{x} = -\mathbf{F}(\mathbf{x}_0) \tag{2.113}$$

This defines an iterative rule to approximate the optimal coefficients $\mathbf{x}^*$ by starting from an arbitrary initial set $\mathbf{x}_0$ and applying the method repetitively yielding $\mathbf{x}_{k+1}$ in each iteration. If $\mathbf{x}_k$ is sufficiently close to $\mathbf{x}^*$ the iteration will converge with the order two, meaning that the difference between approximation and real coefficients will decline by a power of two in each iteration [195]. This is essentially a consequence of the Taylor theorem as the linear approximation describes linear functions, thus, functions of order one, exactly. Consequently, the update rule given by the linear system

$$\mathcal{D}_\mathbf{F}(\mathbf{x}_k)\Delta\mathbf{x}_k = -\mathbf{F}(\mathbf{x}_k) \tag{2.114}$$

defines an iterative method to derive better approximations $\mathbf{x}_{k+1}$ for $\mathbf{x}^*$, with $\mathbf{x}_{k+1} = \mathbf{x}_k + \Delta\mathbf{x}_k$. The method is known as the *Newton-Raphson method*.
One of the major obstacles is finding an initial candidate solution which is close enough

[26] $\frac{d\mathbf{p}}{dt} = 0$

to the real solution in order to assure convergence. If our initial guess is to far away we run into the danger of *overshoot*, meaning that we chose a too large $\Delta\mathbf{x}_k$ and actually increase the distance to the real solution. This local convergence can be transformed into global convergence by a *damping* strategy. Here the step size $\Delta\mathbf{x}_k$ is multiplied by a damping factor λ_k chosen in a way to assure convergence of the method. A strategy to choose λ_k is based on the natural monotonicity test, where we first test with the old Jacobian whether the step $\lambda_k\mathbf{x}_k$ will bring us closer to the solution [196]. The resulting globally converging algorithm looks the following:

Data: $\mathbf{x}_0, \mathbf{F}, \mathcal{D}_\mathbf{F}, \epsilon_{res}, \epsilon_{red}$
Result: $\mathbf{x}_k \approx \mathbf{x}^*$

$\mathbf{x}_k = \mathbf{x}_0$;
repeat
  $\lambda_k = 1$;
  solve $\mathcal{D}_\mathbf{F}(\mathbf{x}_k)\Delta\mathbf{x}_k = -\mathbf{F}(\mathbf{x}_k)$;
  solve $\mathcal{D}_\mathbf{F}(\mathbf{x}_k)\overline{\Delta\mathbf{x}_k} = -\mathbf{F}(\mathbf{x}_k + \lambda_k\Delta\mathbf{x}_k)$;
  while $\overline{\Delta\mathbf{x}_k} \leq (1 - \lambda_k/2)\Delta\mathbf{x}_k$ *is not fulfilled* **do**
    $\lambda_k = \lambda_k/2$;
    solve $\mathcal{D}_\mathbf{F}(\mathbf{x}_k)\overline{\Delta\mathbf{x}_k} = -\mathbf{F}(\mathbf{x}_k + \lambda_k\Delta\mathbf{x}_k)$;
  end
  $\mathbf{x}_{k+1} = \mathbf{x}_k + \lambda_k\Delta\mathbf{x}_k$;
until $||\lambda_k\Delta\mathbf{x}_k|| < \epsilon_{red}$ *and* $||\mathbf{F}(\mathbf{x}_{k+1})|| < \epsilon_{res}$;
return $\mathbf{x}_{k+1}$

Here ϵ_{red} and ϵ_{res} denote stopping criteria for the step size and residual, respectively. One should note that one can implement the damping efficiently by calculating a LU-decomposition of the Jacobian matrix, as this allows for fast solution with varying right hand sides as it is the case here.

Applying the Newton-Raphson method to our weak formulation requires the function $\mathbf{G}$ but also $\mathcal{D}_\mathbf{G}$ which is given by

$$\mathcal{D}_{\mathbf{G}_i} = \mathcal{D}_{\mathbf{F}_i} + \mathbf{S}_i = \left(\sum_k \phi_{i,k}\langle\frac{dr_k(\mathbf{u})}{dp_j}, v_i\rangle\right)_{i,j} + \mathbf{S}_i. \tag{2.115}$$

It is important here to mention that the Jacobian defined in this way will exist for all coefficients, as long as our reaction propensities are differentiable for all coefficients[27]. In this case all the linear systems arising in the Newton-Raphson method exist and have a unique solution.
The linear system arising in the Newton-Raphson iteration with the form

$$\mathcal{D}_\mathbf{F}(\mathbf{x}_k)\Delta\mathbf{x}_k = -\mathbf{F}(\mathbf{x}_k) \tag{2.116}$$

can be solved using standard algorithms for solving linear system, most prominently the Gauss algorithm, which yields a LU-decomposition of the matrix. However, given

[27] When using our initial definition of reaction propensities from equation 2.10 this will always be the case

the sparse structure and instabilities in the original system the most efficient methods are the ones reordering the original system. Let us assume we start from an initial system $\mathbf{Ax} = \mathbf{b}$, then we can multiply this system by a row ordering matrix $\mathbf{P}$, a column ordering matrix $\mathbf{Q}^T$ and a diagonal scaling matrix $\mathbf{R}$ yielding

$$\mathbf{PRAxQ}^T = \mathbf{PRbQ}^T \tag{2.117}$$
$$\mathbf{PRAQx} = \mathbf{PRQb}. \tag{2.118}$$

The matrices used $\mathbf{P}, \mathbf{R}$ and $\mathbf{Q}$ are chosen in a way that they maximize stability and sparsity and allow for rapid calculation of the LU-decomposition. Two of the fastest implementations of this kind are *SuperLU* and *UMFPACK* [197, 198].

Picard iteration

Next to Newton methods there exists another simpler method for some special cases. Let us assume our nonlinear part of the ODE system $\mathbf{F}(\mathbf{u}) = \mathbf{F}(\mathbf{p})$ can be decomposed into the following form

$$\mathbf{F}(\mathbf{u}) = \boldsymbol{\lambda}(\mathbf{u})\mathbf{u} + \mathbf{g}(\mathbf{u}). \tag{2.119}$$

In this case there is already an implied linearization of the system, and we can construct a simple iteration scheme by delaying the nonlinearities in the following manner:

$$\mathbf{F}(\mathbf{u}_{k+1}) = \boldsymbol{\lambda}(\mathbf{u}_k)\mathbf{u}_{k+1} + \mathbf{g}(\mathbf{u}_k),\ k = 0, 1, 2, \ldots \tag{2.120}$$

This iterative scheme can be shown to converge to the real solution as well [199]. Additionally, it has the advantage of not requiring the Jacobian, thus, it is fully defined by the weak formulation alone. In this thesis we will introduce an additional speed-up of the Picard method in the following manner.
Let us assume that $\mathbf{F}_i(\mathbf{u})$ does not depend on all functions contained in $\mathbf{u}$ but rather a subset denoted by a dependence $\mathbf{d} = \big\{i | i \in \{1, \ldots, n_s\}, \mathbf{F} = \mathbf{F}(u_i)\big\}$. Then we can order the system such that the equations for the u_i with the fewest dependencies $|\mathbf{d}|$ are solved first, giving better approximations for the delayed nonlinearities. Thus, given a new ordering of u_i beginning with the smallest dependencies and ending with the largest dependency, we now derive the following equations for u_i:

$$\boldsymbol{\lambda}_i(u_{j\geq i,k}, u_{j<i,k+1})u_{i,k+1} + \mathbf{g}(u_{j\geq i,k}, u_{j<i,k+1}) + \mathbf{S}_i\mathbf{p}_{k+1} = \mathbf{L}_i \tag{2.121}$$
$$\forall l: \boldsymbol{\lambda}_i(\mathbf{p}_{j\geq i,k}, \mathbf{p}_{j<i,k+1}) \sum_j p^j_{i,k+1} v_{j,l} v_{i,l} + \mathbf{g}_i(\mathbf{p}_{j\geq i,k}, \mathbf{p}_{j<i,k+1}) + \mathbf{S}_i\mathbf{p}_{k+1} = \mathbf{L}_i \tag{2.122}$$
$$\mathbf{diag}(\boldsymbol{\lambda}_i(\mathbf{p}_{j\geq i,k}, \mathbf{p}_{j<i,k+1}))\mathbf{M}\mathbf{p}_{k+1} + \mathbf{S}\mathbf{p}_{k+1} = \mathbf{L}_i - \mathbf{g}_i(\mathbf{p}_{j\geq i,k}, \mathbf{p}_{j<i,k+1}). \tag{2.123}$$

Here $\mathbf{diag}(\mathbf{x})$ denotes a diagonal matrix with the entries being $\mathbf{x}$. All those systems are linear, if the dependency is completely resolved. Thus, if one equation is linear, another equation nonlinear only in one solution etc., this method solves the system in one iteration. For any other case intermediate approximations are incorporated in the solution of the equations providing better convergence within a single iteration.

This gives us an efficient methods to solve nonlinear systems. Thus, we will now look at methods to achieve the time discretization for our ODE system.

Runge-Kutta methods for large sparse systems

Analogous to our spatial discretization by the finite elements, we will also discretize our solution in time. For this we will advance in time by a distinct step size h. Thus in each time step we will advance from a time point t_i to a time point $t_i + h$.
We will begin by bringing our system into a standard form for an ODE system in the following manner

$$\mathbf{M}\frac{d\mathbf{p}}{dt} + \mathbf{F}(\mathbf{p}) + \mathbf{S}\mathbf{p} = \mathbf{L} \tag{2.124}$$

$$\rightarrow \frac{d\mathbf{M}\mathbf{p}}{dt} = \mathbf{L} - \mathbf{F}(\mathbf{p}) - \mathbf{S}\mathbf{p} \tag{2.125}$$

$$\rightarrow \frac{d\mathbf{p}}{dt} = \mathbf{M}^{-1}\mathbf{f}(\mathbf{p}) \text{ with } \mathbf{f}(\mathbf{p}) = \mathbf{L} - \mathbf{F}(\mathbf{p}) - \mathbf{S}\mathbf{p}. \tag{2.126}$$

Thus, the general form of this ODE system is

$$\frac{d\mathbf{y}(t)}{dt} = \mathbf{f}(\mathbf{y}, t). \tag{2.127}$$

Using our time stepping scheme and applying the fundamental theorem of calculus, we can write down the solution to this problem directly as

$$\mathbf{y}(t_k + h) = \mathbf{y}(t_k) + \int_{t_k}^{t_k+h} \mathbf{f}(\mathbf{y}, t)dt. \tag{2.128}$$

However, this integral is usually not solvable analytically so we will approximate it by a quadrature formula with s stages yielding [200]

$$\mathbf{y}(t_k + h) \approx \mathbf{y}(t_k) + h\sum_{i}^{s} b_i \mathbf{f}(\mathbf{y}, t_k + c_i h). \tag{2.129}$$

However, we do not know $\mathbf{y}$ and as such neither $\mathbf{y}(t_k + c_i h)$. Thus, we will have to substitute $\mathbf{y}(t_k + c_i h)$ by another quadrature formula as well yielding

$$\mathbf{f}(\mathbf{y}, t_k + c_i h) \approx k_i = \mathbf{f}(\mathbf{y}_k + h\sum_{j} a_{ij}k_j, t_k + c_i h). \tag{2.130}$$

This yields the general form of the *Runge-Kutta methods*, which are defined by its coefficients $\mathbf{b}, \mathbf{c}$ and the coefficient matrix $\mathbf{A} = (a_{ij})_{ij}$. As such an s stage Runge-Kutta method is represented by its Butcher array given by

$$\begin{array}{c|c} \mathbf{c} & \mathbf{A} \\ \hline & \mathbf{b} \end{array} \tag{2.131}$$

As one can see, if $\mathbf{A}$ is lower triangular with a zero diagonal all quantities can be directly computed by forward substitution, yielding the approximation explicitly. This class of Runge-Kutta methods is called *explicit methods* whereas all other methods are called *implicit methods*. Explicit Runge-Kutta methods with s stages can employ error reduction in the order of $\mathcal{O}(h^s)$. Additionally, there are embedded Runge-Kutta schemes were an s stage method and an $s + 1$ stage method share s of their stages,

which can be used for error control and adaptive step size selection.
Given this information, one might think that explicit methods might me a good general choice for most problems given their simple computation, good error properties and adaptivity. However, it turns out that there is a large class of problem where explicit methods perform very bad and require extreme step size reduction on smooth parts of the solution to uphold a given error constraint. Equations of this kind are called *stiff*. Integration methods which can deal efficiently with stiffness are generally called *stable*. There is a large theory concerning stability of ODE solvers which we will not recapitulate here as we will treat ODE systems only marginally in this thesis. For more information on stability and the underlying mathematics we refer to some standard books in this area [201, 200, 202]. For us it will be sufficient to know that no explicit method is stable. This is unfortunate as many reaction as well as reaction-diffusion systems employ a high degree of stiffness. This is due to the different time scales at which diffusion and reactions can take place.
Whereas no explicit method is stable, there is a large class of implicit methods that are stable. For instance, a class of implicit Runge-Kutta methods, the Gauss collocations methods [202]. An s stage Gauss collocation method assures error reduction in $\mathcal{O}(h^{2s})$, however due to its completely filled coefficient matrix $\mathbf{A}$ it also needs more computation as we will see now.
An s stage Gauss collocation method is again defined by its Butcher array $\mathbf{A}, \mathbf{b}, \mathbf{c}$ with the Runge-Kutta equations

$$\mathbf{y}(t_k + h) = \mathbf{y}(t_k) + h \sum_{i=1}^{s} b_i \mathbf{f}(k_i, t_k + c_i h), \tag{2.132}$$

$$\text{where } k_i = \mathbf{y}(t_k) + h \sum_{j=1}^{s} a_{ij} \mathbf{f}(k_j, t_k + c_j h). \tag{2.133}$$

The quadrature rules for the intermediate solutions k_i formulate a nonlinear equation system with

$$\forall i : \mathbf{F}_i(\mathbf{k}) = \mathbf{k}_i - \mathbf{y}_i(t_k) - h \sum_{j=1}^{s} a_{ij} \mathbf{f}(k_j, t_k + c_j h) = 0 \tag{2.134}$$

We can solve this method using the Newton-Raphson method which will require us to calculate the LU decomposition of the Jacobian $\mathcal{D}_{\mathbf{F}_i}$ to obtain

$$\mathcal{D}_{\mathcal{F}_i}(k_{i,n}) \Delta k_{i,n+1} = \begin{pmatrix} \mathbf{I} - h a_{11} \mathbf{J}_1 & -h a_{12} \mathbf{J}_2 & \dots & -h a_{1s} \mathbf{J}_s \\ -h a_{21} \mathbf{J}_1 & \mathbf{I} - h a_{22} \mathbf{J}_2 & \dots & -h a_{2s} \mathbf{J}_s \\ \vdots & \vdots & \ddots & \vdots \\ -h a_{s1} \mathbf{J}_1 & -h a_{s2} \mathbf{J}_2 & \dots & \mathbf{I} - h a_{ss} \mathbf{J}_s \end{pmatrix} \Delta k_{i,n+1} = -\mathbf{F}_i(k_{i,n}) \tag{2.135}$$

with $\mathbf{J}_i = \mathcal{D}_{\mathbf{f}}(k_{i,n}, t_k + c_i h)$. Defining $\mathbf{k} = (k_i)_i, \mathbf{J} = \mathcal{D}_{\mathbf{f}}(\mathbf{k}_n)$ and $\mathbf{F} = (\mathbf{F}_i)_i$ we can write the entire system compactly as

$$\mathcal{D}_{\mathcal{F}}(\mathbf{k}_n) \Delta \mathbf{k}_{n+1} = \begin{pmatrix} \mathbf{I} - h a_{11} \mathbf{J} & -h a_{12} \mathbf{J} & \dots & -h a_{1s} \mathbf{J} \\ -h a_{21} \mathbf{J} & \mathbf{I} - h a_{22} \mathbf{J} & \dots & -h a_{2s} \mathbf{J} \\ \vdots & \vdots & \ddots & \vdots \\ -h a_{s1} \mathbf{J} & -h a_{s2} \mathbf{J} & \dots & \mathbf{I} - h a_{ss} \mathbf{J} \end{pmatrix} \Delta \mathbf{k}_{n+1} = -\mathbf{F}(\mathbf{k}_n) \tag{2.136}$$

$$= (\mathbf{I} - h \mathbf{A} \otimes \mathbf{J}) \Delta \mathbf{k}_{n+1} = -\mathbf{F}(\mathbf{k}_n), \tag{2.137}$$

where $\otimes$ defines the Kronecker product. As we see in each step we have to decompose a matrix with dimensions $ms \times ms$, where m is a product of the polynomial degree of the basis functions the number of solution components and number of finite elements. The resulting LU factorization becomes computationally expensive which makes a fully implicit method unfeasible for solving reaction-diffusion equations[28]. As thus we will look at a special case of implicit Runge-Kutta methods.
We will use an implicit Runge-Kutta method with a lower triangular matrix $\mathbf{A}$ and a diagonal where all the entries are equal. Those methods are called *singly diagonally implicit Runge-Kutta methods* (SDIRK). Due to the special structure ($a_{ii} = \alpha$) this results in a Jacobian matrix

$$\mathcal{D}_{\mathbf{F}}(\mathbf{k}_n) = \begin{pmatrix} \mathbf{I} - h\alpha\mathbf{J} & 0 & \dots & 0 \\ -ha_{21}\mathbf{J} & \mathbf{I} - h\alpha\mathbf{J} & \dots & 0 \\ \vdots & \vdots & \ddots & \vdots \\ -ha_{s1}\mathbf{J} & -ha_{s2}\mathbf{J} & \dots & \mathbf{I} - h\alpha\mathbf{J} \end{pmatrix}. \tag{2.138}$$

Here $\mathbf{J}$ has to be factorized only once and the rest of the system can be solved with forward substitutions, which lowers the computational effort considerably. Additionally, SDIRK methods are still stable up to 3 stages and have a error reduction of at least order $\mathcal{O}(h^s)$, which make them an appropriate method to solve ODE systems arising from the weak formulation of reaction-diffusion systems. Those methods were introduced by Roger Alexander which is why they are also often called *Alexander s-parameter method* [203]. The Butcher arrays for Alexander's methods of order 1 to 3 are given by the following schemes.

$$\begin{array}{c|cc} \frac{1}{2} & \frac{1}{2} \\ \hline & 1 \end{array} \qquad \begin{array}{c|cc} \alpha & \alpha & 0 \\ 1 & 1-\alpha & \alpha \\ \hline & 1-\alpha & \alpha \end{array} \qquad \begin{array}{c|ccc} \alpha & \alpha & 0 & 0 \\ \frac{1+\alpha}{2} & \frac{1+\alpha}{2} - \alpha & \alpha & 0 \\ 1 & b_1 & b_2 & \alpha \\ \hline & b_1 & b_2 & \alpha \end{array}$$

$$\alpha = 1 \pm \frac{1}{2}\sqrt{2} \qquad \alpha^3 - 3\alpha^2 + \frac{3}{2}\alpha - \frac{1}{6} = 0 \tag{2.139}$$

$$b_1 = -\frac{(6\alpha^2 - 16\alpha + 1)}{4}$$

$$b_2 = \frac{6\alpha^2 - 20\alpha + 5}{4}$$

This gives us three different options to solve the temporal component of our system stably and with error reduction in different orders.

Some final observations

We have derived a general strategy to solve reaction-diffusion equations based on weak formulations and finite element basis functions. This scheme has many advantages over naive methods such as finite differences or line methods. The most important being clear existence of solutions and stability. Additionally, we have seen that many subclasses such as steady state approximations result in large, but simple linear systems

[28] Typical examples are solved on 20.000 finite elements with 2-5 solution components and polynomial order 2. Using a 2 stage method we have to factorize a matrix of size 400.000×400.000.

which can be solved efficiently. The major complication with defining weak formulations for any partial differential equation is the derivation of an appropriate weak formulation. Additionally, if the system is nonlinear one either needs a linearization for Picard iteration or the Jacobian for the nonlinear parts of the Galerkin scheme. Those parts can not be automatized. Consequently, the implemented libraries for finite element methods rather concentrate on managing the grid, standardizations of finite elements and the basis functions. For the Newton-Raphson method it is not necessary that the user actually specifies the derivatives in the coefficient vector, which would be inefficient if one wants to use different basis functions. Rather one only provides the derivative in u_i. Application of the chain rule then results in:

$$\frac{d\mathbf{F}}{d\mathbf{p}} = \frac{d\mathbf{F}}{du_i}\frac{du_i}{d\mathbf{p}}. \tag{2.140}$$

Because $\frac{du_i}{d\mathbf{p}}$ is a property of the basis, this can be managed by the library easily.
Consequently, the user usually specifies the weak formulation, the grid, boundary, and initial condition whereas assembly of the nonlinear systems and their solution is handled by the libraries. Some of the most powerful implementation in this field are *DUNE* (`www.dune-project.org`) and *Hermes* (`www.hpfem.org`).

2.3.3 Nonlinear Optimization

A crucial part of Systems Biology is connecting the model with experimental data in a consistent manner. In an abstract sense we have seen that any reaction-diffusion system inherits some freedom due to the arbitrary parameters of the reaction propensities and the initial conditions. Given some experimental data, we want to choose the model that is most consistent with the data. To achieve that, we will choose a quantity $\mathbf{M}(\mathbf{S}, t, \mathbf{x}, \boldsymbol{\theta})$ depending on the parameters $\boldsymbol{\theta}$ and relate it to the data $\mathbf{D}$. For this we choose some quality function $Q : \boldsymbol{\theta} \times \mathbf{D} \to \mathbb{R}$ which measures the agreement of the model with the data, or differently said, how good or bad the data agrees with the model. We aim to optimize the quality, thus, enforcing

$$Q(\boldsymbol{\theta}, \mathbf{D}) \overset{!}{\to} \min_{\boldsymbol{\theta}} / \max_{\boldsymbol{\theta}}, \tag{2.141}$$

where the type of optimization depends on the form of Q. I will introduce a combination of methods to solve this problem efficiently and we will derive two different forms of Q depending on the type of data we have available.
We will require that Q is strictly monotonous in all θ_i and thus lower or upper unbounded. Then a sufficient condition for the existence of a minimum or maximum at $\boldsymbol{\theta}^*$ is

$$\nabla_{\boldsymbol{\theta}} Q(\boldsymbol{\theta}^*, \mathbf{D}) = 0. \tag{2.142}$$

This requires the differentiability of Q. If Q is even twice differentiable we can employ the Newton-Raphson method we have introduced in section 2.3.2. However, in practice this turns out to be very slow as any evaluation of the function Q usually requires solving the reaction-diffusion problem before extracting $\mathbf{M}$. As thus we will introduce some methods which orientate on Newton-Raphson methods but are much faster, the *quasi Newton-Raphson methods*.

The BFGS method

Applying the Newton-Raphson method to equation 2.142 yields the following iteration scheme for $\boldsymbol{\theta}_k$:

$$\mathcal{H}_Q(\boldsymbol{\theta}_k)\Delta\boldsymbol{\theta}_{k+1} = -\nabla_{\boldsymbol{\theta}} Q(\boldsymbol{\theta}_k, \mathbf{D}) = -\nabla_{\boldsymbol{\theta}} Q(\boldsymbol{\theta}_k). \tag{2.143}$$

Here $\mathcal{H}_Q$ is the *Hessian matrix* of Q given by

$$\mathcal{H}_Q = \nabla_{\boldsymbol{\theta}}\nabla_{\boldsymbol{\theta}}^T Q = \begin{pmatrix} \frac{d^2Q}{d\theta_1^2} & \frac{d^2Q}{d\theta_1\theta_2} & \cdots & \frac{d^2Q}{d\theta_1\theta_n} \\ \frac{d^2Q}{d\theta_2\theta_1} & \frac{d^2Q}{d\theta_2^2} & \cdots & \frac{d^2Q}{d\theta_2\theta_n} \\ \vdots & \vdots & \ddots & \vdots \\ \frac{d^2Q}{d\theta_n\theta_1} & \frac{d^2Q}{d\theta_n\theta_2} & \cdots & \frac{d^2Q}{d\theta_n^2} \end{pmatrix}. \tag{2.144}$$

The costly part of the calculation is the evaluation of the Hessian matrix for Q and its LU decomposition. As such we try to substitute $\mathcal{H}_Q$ by an approximation $\mathcal{H}_Q^k$ which is sufficiently close. We will define an update scheme for $\mathcal{H}_Q^k$ which is easy to compute as it uses only matrix additions of easily constructable matrices $\mathbf{U}_k, \mathbf{V}_k$

$$\mathcal{H}_Q^{k+1} = \mathcal{H}_Q^k + \mathbf{U}_k + \mathbf{V}_k. \tag{2.145}$$

The two matrices are symmetric rank-one matrices, which means they can be expressed as a product of two vectors

$$\mathbf{A} = \mathbf{a}\mathbf{b}^T. \tag{2.146}$$

In order to derive a condition for the update of $\mathcal{H}_Q^k$ we will use a linear approximation of $\nabla_{\boldsymbol{\theta}}$ which yields the following derivation

$$\nabla_{\boldsymbol{\theta}} Q(\boldsymbol{\theta}_{k+1}) = \nabla_{\boldsymbol{\theta}} Q(\boldsymbol{\theta}_k + \Delta\boldsymbol{\theta}_k) \tag{2.147}$$

$$\nabla_{\boldsymbol{\theta}} Q(\boldsymbol{\theta}_k + \Delta\boldsymbol{\theta}_k) \approx \nabla_{\boldsymbol{\theta}} Q(\boldsymbol{\theta}_k) + \mathcal{H}_Q^{k+1}(\boldsymbol{\theta}_k)\Delta\boldsymbol{\theta}_k \tag{2.148}$$

$$\mathcal{H}_Q^{k+1}(\boldsymbol{\theta}_k)\Delta\boldsymbol{\theta}_k = \nabla_{\boldsymbol{\theta}} Q(\boldsymbol{\theta}_{k+1}) - \nabla_{\boldsymbol{\theta}} Q(\boldsymbol{\theta}_k). \tag{2.149}$$

We define $\Delta_k = \nabla_{\boldsymbol{\theta}} Q(\boldsymbol{\theta}_{k+1}) - \nabla_{\boldsymbol{\theta}} Q(\boldsymbol{\theta}_k)$ and solve for the matrices $\mathbf{U}_k$ and $\mathbf{V}_k$ fulfilling the condition. Again we will allow a dampening, thus, our step size may be given by $\lambda_k\boldsymbol{\theta}_k$. This yields an update rule for the Hessian, with

$$\mathcal{H}_Q^{k+1} = \mathcal{H}_Q^{k+1} + \frac{\Delta_k\Delta_k^T}{\Delta_k^T\lambda_k\Delta\boldsymbol{\theta}_k} - \frac{\mathcal{H}_Q^k\lambda_k\Delta\boldsymbol{\theta}_k(\lambda_k\Delta\boldsymbol{\theta}_k)^T\mathcal{H}_Q^k}{(\lambda_k\Delta\boldsymbol{\theta}_k)^T\mathcal{H}_Q^k\lambda_k\Delta\boldsymbol{\theta}_k}. \tag{2.150}$$

This provides a strategy to calculate the Hessian for each step using only evaluations of $\nabla_{\boldsymbol{\theta}} Q$, which was already calculated before. Moreover, in this methods we do not even have to factorize $\mathcal{H}_Q^{k+1}$ as the inverse is directly given by the Sherman-Morrison formula

$$\mathcal{H}_{k+1}^{-1} = \mathcal{H}_k^{-1} + \frac{(\lambda_k\Delta\boldsymbol{\theta}_k)^T\Delta_k + \Delta_k^T\mathcal{H}_k^{-1}\Delta_k)(\lambda_k\Delta\boldsymbol{\theta}_k(\lambda_k\Delta\boldsymbol{\theta}_k)^T)}{((\lambda_k\Delta\boldsymbol{\theta}_k)^T\Delta_k)^2} - \frac{\mathcal{H}_k^{-1}\Delta_k(\lambda_k\Delta\boldsymbol{\theta}_k)^T + \lambda_k\Delta\boldsymbol{\theta}_k\Delta_k^T\mathcal{H}_k^{-1}}{(\lambda_k\Delta\boldsymbol{\theta}_k)^T\Delta_k}. \tag{2.151}$$

Substituting the approximated Hessian and update rules into a dampened Newton-Raphson scheme yields the *Broyden-Fletcher-Goldfarb-Shanno method*[29] (BFGS). A simple initialization for the Hessian $\mathcal{H}_Q^0$ is the identity matrix $\mathbf{I}$, which corresponds to an initial gradient descent step.

Simulated Annealing

The BFGS method provides fast convergence and clear mathematical frameworks for the existence of an optimum, but it has some severe limitations. The first is the necessity of a continuously differentiable function Q. This does not have to be the case in general. Additionally, the BFGS method will only find local optima, and in the existence of multiple optima it will find the one closest to the initial value, but not necessarily the global optimum.
Another optimization strategy not bounded by this limitations is inspired by the process used in hardening steel (annealing). Here, the steel is heated and cooled down slowly. In high temperatures iron atoms will move and may even exit favorable energy states, but as the temperature diminishes those molecules are forced more and more to reside in efficient energy states. As a result, this process converges to an annealed configuration of atoms, which is more stable than the initial one.
This strategy, can be adapted to build up an optimization strategy. Starting from an initial temperature T_0, randomly new vectors $\boldsymbol{\theta}$ are sampled from a large neighborhood and the new parameters are accepted randomly, allowing acceptance of parameters even if the new approximation is not better than the previous one, but still favoring better parameter sets. As the temperature drops, new solutions are sampled from smaller and smaller neighborhoods to ensure convergence. Due to their inspiration in metallurgy those optimization strategies are called *Simulated Annealing*. As Simulated Annealing only finds minima the problem hast to be transformed to a minimization problem first. If Q is to be maximized this can be done simply by redefining $Q = -Q$. The choice of the cooling schedule for the temperature T, as well as the function generating new candidates, can be chosen freely and will influence the convergence of the Simulated Annealing method. The acceptance of new candidate solutions $\boldsymbol{\theta}_{k+1}$ coming from $\boldsymbol{\theta}_k$ is inspired by thermodynamics and Markov theory. It is chosen by the Gibbs distribution which coincides to be a Metropolis-Hastings acceptance probability

$$\mathbb{P}(\boldsymbol{\theta}_k \to \boldsymbol{\theta}_{k+1}) = \max\left\{1, \exp\left(-\frac{Q(\boldsymbol{\theta}_{k+1}, \mathbf{D}) - Q(\boldsymbol{\theta}_k, \mathbf{D}}{T}\right)\right\}. \tag{2.152}$$

The candidate generation will be governed by a Gaussian kernel with a scale parameter proportional to the temperature T. The cooling schedule will be chosen in a way to optimize convergence properties given the the current total iteration k [204]

$$T_{k+1} = \frac{T_k}{\log\left(k - 1 - exp(1)\right)}. \tag{2.153}$$

For each temperature the sampling is repeated n_R times which results in the following optimization algorithm:

[29] In some implementations the choice of the dampening factor is not the natural monotonicity test as we have employed it in this thesis, however, all of them belong to the larger class of linesearch strategies.

Data: $Q, \mathbf{D}, \boldsymbol{\theta}_0, T_0, n_R, i_{max}$
Result: $\boldsymbol{\theta}^*$

$T = T_0, i = 0, \boldsymbol{\theta} = \boldsymbol{\theta}_0, \sigma = T_0^{-1}$;
$\boldsymbol{\theta}_{opt} = \boldsymbol{\theta}$;
while $i < i_{max}$ **do**
  for $j = 1, \ldots, n_R$ **do**
    $i = i + 1$;
    $T = \frac{T}{\log(k-1-exp(1))}$;
    Generate new candidate with $\forall i : \overline{\theta_i} \propto \mathcal{N}(\theta_i, (\sigma \cdot T)^2)$;
    Accept new candidate with $\mathbb{P}(\boldsymbol{\theta} \to \overline{\boldsymbol{\theta}}) = \max\left\{1, \exp\left(-\frac{Q(\overline{\boldsymbol{\theta}},\mathbf{D}) - Q(\boldsymbol{\theta},\mathbf{D}}{T}\right)\right\}$;
    if $Q(\boldsymbol{\theta}, \mathbf{D}) < Q(\boldsymbol{\theta}_{opt}, \mathbf{D})$ **then**
      $\boldsymbol{\theta}_{opt} = \boldsymbol{\theta}$
    end
  end
end
return $\boldsymbol{\theta}_{opt}$

This Simulated Annealing algorithm will find global minima because it is allowed to jump out local ones in order to find a new global optimum. Furthermore, it will converge to the optimum in probability and uses only the function itself and no derivatives [204]. However, in practice Simulated Annealing is very efficient in finding minima coarsely, but converges slowly when very close to the minimum. As such, a good strategy for general optimization is to start of with a few iterations of Simulated Annealing to come close to the global optimum and continue with the BFGS method which will converge rapidly to the optimum (due to its quasi-quadratic error reduction in this area).
This provides a global optimization strategy and we will now take a look at the form of the function Q.

Residual sum of squares and log-likelihood

Our conditions for the function Q were strict monotonicity and differentiability, as well as boundedness in one direction. Clearly, there is a large class of functions that can be found to comply with those conditions. We will introduce the two most popular ones. We begin with functions that can be used if our data is represented by a simple vector of individual data points, each corresponding to a different value of independent variables[30]. The corresponding model quantity to the data will be denoted as $\mathbf{M}_{\boldsymbol{\theta}} = \mathbf{M}(\mathbf{S}, t, \mathbf{x}, \boldsymbol{\theta})$. Then, a feasible function Q is given by

$$Q(\boldsymbol{\theta}, \mathbf{D}) = \sum_i (M^i_{\boldsymbol{\theta}} - D_i)^2 = (\mathbf{M}_{\boldsymbol{\theta}} - \mathbf{D})^2. \tag{2.154}$$

Q has a lower bound of zero and is strictly monotonous and differentiable if $\mathbf{M}$ is strictly monotonous and differentiable. Due to its definition it is called *Residual Sum of Squares* (RSSQ). If the residuals $\mathbf{M}_{\boldsymbol{\theta}} - \mathbf{D}$ are approximately Normal distributed,

[30] for instance different time points

statistical significance of the optimization can be tested with the F-test. Here the, RSSQ is compared to the RSSQ of a reference model (for instance the zero model for a no-intercept model or the mean value of the data for an intercept model). The resulting test statistic F for two models where model 1 is nested within model 2 and for n data points is given by

$$F = \frac{(n - p_2)(RSSQ_1 - RSSQ_2)}{(p_2 - p_1)(RSSQ_2)}. \tag{2.155}$$

p_1 and p_2 denote the number of parameters for each model and the value F is tested against an F-distribution with $p_2 - p_1$ and $n - p_2$) degrees of freedom.

However, we may obtain more information experimentally. Thus, we will now describe a function Q if we can not only measure $\mathbf{D}$ but actually obtain a statistic of $\mathbf{D}$ for a given set of independent variables. In this case we aim to identify the model which has the largest probability under the obtained data. $\mathbf{D}$ defines a vector of random variables D_i, each inducing a continuous probability density

$$\varphi(D_i, x) = \varphi_i(x) \text{ where } \mathbb{P}(D_i \leq x) = \int_{-\infty}^{x} \varphi_i(s)ds. \tag{2.156}$$

This can either be a distribution assumed to hold (often the Normal distribution) or a non-parametric approximation given by a density approximation (for instance by a sum of Gaussian kernels). The joint probability of the model quantity $\mathbf{M}_{\boldsymbol{\theta}}$ is then given by the likelihood $\mathcal{L}_{\boldsymbol{\theta}}$ with

$$\mathcal{L}_{\boldsymbol{\theta}} = \prod_i \varphi_i(M^i_{\boldsymbol{\theta}}). \tag{2.157}$$

The likelihood has an upper bound of 1 and is continuous and differentiable. However, it is rarely used due to instable numerics arising from the multiplication of many quantities smaller than one. A stable transformation is the log-likelihood which is has an upper bound of zero and is given by

$$\log \mathcal{L}_{\boldsymbol{\theta}} = \log \prod_i \varphi_i(M^i_{\boldsymbol{\theta}}) = \sum_i \log \varphi_i(M^i_{\boldsymbol{\theta}}). \tag{2.158}$$

Maximization of the log-likelihood employs information over the entire statistics of the data. The implied statistical test is the χ^2-test with test statistic R. Again we will assume we have a nested models 1 and 2 with respective log-likelihoods and degrees of freedom $df1$ and $df2$[31]. Then we can define the likelihood ratio as

$$R = 2 \log \mathcal{L}^2_{\boldsymbol{\theta}} - 2 \log \mathcal{L}^1_{\boldsymbol{\theta}}. \tag{2.159}$$

The likelihood ratio is tested against a χ^2-distribution with $df2 - df1$ degrees of freedom.

[31] A feasible reference model is that the entire set of data points is just governed by a single normal distribution, even when coming from different independent variables.

This now provides us with methods to couple the model to our data and to identify the underlying parameters globally. Furthermore, we are equipped with statistics to quantify the significance of our model to the experimental data. This brings us back to the life cycle of Systems Biology where we aim to connect the hypothesis formulated by our model with the data obtained by experiments. We now have a consistent framework to do that with our models, composed of reaction-diffusion master equations or deterministic reaction-diffusion equations, and our experimental data, coming from microscopy and populations studies as well as mutants. This framework has been applied to study the biological system we have started with in chapter 1, the communication of yeast via pheromones, as we will see in the following chapters.

3 The yeast pheromone response as a complex communication system

3.1 Introduction

In the preceding chapters we have introduced the molecular biology of the yeast pheromone response and the Systems Biology of reaction-diffusion equations. As such, we have all the methodology and biology at hand which was needed to obtain the results I will present now. We have seen in section 1.5 that significant knowledge has been obtained already concerning the functioning of the yeast pheromone response. For a biologically edible interpretation of a signaling pathway it is necessary to connect biological pathways with distinct functions. In order to do this we will treat the pheromone signaling occurring in yeast as an abstract signal sensing mechanism that has evolved specifically to create, sense and interpret information about the surrounding cell population. In order to do this three main goals have to be achieved by the yeast population:

1. An informative signal has to be created using as few resources as possible.

2. The signal has to be detected reliably with a minimum loss of information.

3. Detection of the signal has to induce a complex all-or-none response which is aimed in the direction of the gradient.

Those three main points formed the road map for the investigations I performed on this pathway and which will be presented in the following. In the first part I will introduce a non-invasive method to visualize and quantify the signaling environment produced by yeast populations *in vivo*. In particular I studied the effect of Bar1 on shaping and modifying this environment. We have discovered that an active regulation of the extracellular signaling components is crucial for the correct formation of diploids and that its absence leads to severely altered phenotypes and abolishment of cell growth. Those results will be provided in section 3.2 in this chapter. In section 3.3 we will take a look at the ability of the pathway to detect even small differences in extracellular pheromone concentration and propose a mechanism where cells accumulate signal in order to reduce noise levels dramatically. Furthermore, we will see in section 3.4 that the downstream formation of large multi-protein complexes such as the polarisome can transform shallow gradients in point-like distribution patterns of the membrane while at the same time making the number of formed polarisomes dependent on the extracellular gradient.

3.2 Bar1 regulates the extracellular signaling environment during mating

I have argued in section 1.4.1 that in particular *MAT***a** cells of yeast employ a variety of mechanisms in order to control the extracellular signaling environment provided by the pheromones. Apart from regulating the secretion of **a**-factor, one important feature of this regulation is the secretion of Bar1, an aspartyl protease, which degrades $\boldsymbol{\alpha}$-factor [33, 34]. Bar1 was found in the periplasmic space of *MAT***a** cells as well as in the growth medium. Additionally, basal Bar1 activity can be stimulated by exposure of *MAT***a** cells to $\boldsymbol{\alpha}$-factor [31, 32]. It has been argued about the beneficial effect for *MAT***a** cells to destroy the signal they need to sense. Previous work indicated that secretion of a negative regulator provides an increased ability to distinguish the direction of the gradient, gives benefit due to its negative regulation, or might help *MAT***a** cells to avoid each other during shmoo formation [205–208]. However, secreting a small molecule into the extracellular space strongly dilutes it, reducing the possibility to benefit the secreting cell.

Secretion of molecules into the culture medium, however, is often associated with cooperative behavior, quorum sensing, communication, and social behavior in microbial communities including yeast [209–214]. This raised the question how Bar1 influences the distribution of $\boldsymbol{\alpha}$-factor in a population of mixed haploid yeast cells, particularly since extracellular Bar1 is shared across the mating cell population. Unfortunately, studying the extracellular distribution of $\boldsymbol{\alpha}$-factor is strongly limited by the fast diffusion, low concentration, and small size of the pheromone, which prevents it from being visualized by purely experimental approaches. Furthermore, due to its small size, tagging $\boldsymbol{\alpha}$-factor alters its mass and, consequently, its diffusion rate. Furthermore, at least C-terminal modification of $\boldsymbol{\alpha}$-factor was also shown to influence its affinity for the Ste2 receptor [38].

Physical principles, however, capture diffusion of small particles and their interaction in fluids and allow for calculation of spatial distributions from a few parameters [215, 216]. We used such an inference method here to identify the most likely $\boldsymbol{\alpha}$-factor distribution within mixed haploid yeast populations directly from confocal microscopic images with fluorescently tagged marker proteins. We coupled physical reaction-diffusion models with experimental imaging in order to quantify the spatial distribution of extracellular proteins. The use of simple marker constructs, that altered neither $\boldsymbol{\alpha}$-factor nor Bar1, served for minimal interference with the biological system. We used this approach to directly estimate the influence of Bar1 on the distribution of $\boldsymbol{\alpha}$-factor in a mixed yeast population and to explain its influence on the coordination of growth and signaling.

3.2.1 An assay to quantify extracellular signaling molecules in yeast from in vivo microscopy images

We combined image analysis with spatiotemporal mathematical modeling to determine spatial concentration distributions of Bar1 and of $\boldsymbol{\alpha}$-factor. The general concept of the approach is the following:

1. Take images, detect cell location and mating type, and quantify pheromone stim-

ulation of *MAT***a** cells with a fluorescent marker.

2. Use a mathematical model based on real cell location and activation to calculate the distribution of Bar1 and $\boldsymbol{\alpha}$-factor in the extracellular space.

3. Predict effects on population growth and mating efficiency, confirmed by further experiments.

In mathematical terms the problem is described as a purely extracellular reaction-diffusion process for $\boldsymbol{\alpha}$-factor and Bar1 with distinct boundary conditions.

How do we connect the model to the experimental data? As mentioned above, there is no way of obtaining the $\boldsymbol{\alpha}$-factor concentration directly by experimentation. However, there is an indirect method to quantify the amount of $\boldsymbol{\alpha}$-factor a *MAT***a** cell is exposed to. As described in chapter 1, there are a variety of proteins which are expressed upon stimulation with pheromone. By taking one of those proteins and adding a fluorescent marker we can read the pathway output for individual *MAT***a** cells. If we now construct a calibration curve of this pathway output in a strain lacking Bar1 with various artificially added uniform $\boldsymbol{\alpha}$-factor concentrations, we can associate the fluorescence of the marker with the extracellular concentration of $\boldsymbol{\alpha}$-factor the cells are exposed to. This gives us information about the extracellular concentration of $\boldsymbol{\alpha}$-factor at the cell membrane, a quantity which is explicitly contained in the model. However, this requires us to modify the system first in order to obtain the desired output.

Used strains and constructs

In this study, we used the wild type *MAT***a** reporter strains Fus1-GFP and Rpl9a-GFP, based on BY4741 (*MAT***a** *his3Δ1 leu2Δ0 met15Δ0 ura3Δ0*) and part of the yeast GFP collection [217]. Additionally, we also employed a *MAT*$\boldsymbol{\alpha}$ reporter strain expressing mCherry under control of the constantly active TDH3 promoter. This strain, *MAT*$\boldsymbol{\alpha}$ *can1Δ::STE2pr-SpHIS5 lyp1Δ::STE3pr-LEU2 his3Δ1 leu2Δ0 ura3Δ0 met15Δ ho Δ0::TDH3pr-mCherry-NATMX4*) was a friendly gift of Alexander DeLuna [218]. Yeast strains were cultivated at 30 °C in synthetic medium[1]. In all the *MAT***a** reporters strains we inserted Bar1 deletions by homologous integration of a *URA3* cassette in the *BAR1* locus (*bar1Δ0::URA3*). Here, we used the methodology described in section 2.2.3. PCR amplification of the *URA3* cassette from plasmid template pESC-Ura (Stratagene) was done by sequential amplification with the primer pairs, which are provided in table 3.1.

This was followed by transformation and selection on agar plates with synthetic medium lacking uracil. Verification of the Bar1 deletion was done with a physiological assay based on growth inhibition by $\boldsymbol{\alpha}$-factor pheromone [32]. This gave us the required strains to construct the calibration curves.

[1]Synthetic medium: 0.17 % yeast nitrogen base without amino acids; 0,5% ammonium sulfate, 2% glucose, 55mg/l adenine, 55 mg/l L-thyrosine, 55 mg/l uracil, 20 mg/l L-arginine, 10 mg/l L-histidine, 60 mg/l L-isoleucine, 60 mg/l L-leucine, 40 mg/l L-lysine, 10 mg/l L-methionine, 60 mg/l L-phenylalanine, 50 mg/l L-threonine and 40 mg/l L-tryptophane

Name	Sequence	Use
Primer 1	5'-GAAGGGTCATATAATGTCGCGCGTTTCGGTGATG-3'	PCR1
Primer 2	5'-CTCCAGATTTCTTAGTTTTGCTGGCCGC-3'	PCR2
Primer 3	5-GGTTCGTATCGCCTAAAATCATACCAAAATAAAAAGAGT GTCTAGAAGGGTCATATAATG-3'	PCR3
Primer 4	5'-GACTATATATTTGATATTTATATGCTATAAAGAAATTGTA CTCCAGATTTCTTA-3'	PCR4

Table 3.1: The primers used for sequential amplification of PCR products in order to obtain the *BAR1*Δ strains.

Confocal microscopy and calibration curves

Microscopic images were acquired with an inverted FluoView 1000 microscope (Olympus, Tokio, Japan) equipped with a 60x (1.2 N.A) water-immersion objective and a climate chamber (Tokai Hit, Japan). GFP was excited with a 488 nm argon laser and fluorescence emission was detected in the range of 500-545 nm. Image acquisition for $\boldsymbol{\alpha}$-factor calibration curves was done with synchronized cultures of Fus1-GFP in wild type or *BAR1*Δ background. Cultures were synchronized in G1 phase by elutriation with a Beckman Coulter JE-5.0 elutriation system. Synchronized cells were incubated with $\boldsymbol{\alpha}$-factor pheromone for 3 hours at 30 °C.
Normally, microscopic inspection requires cells to be fixed on the culture dish in order to avoid sedimentation during image acquisition. This is usually achieved by coating the dish with Concanavalin A, a chemical which interacts with the surface sugars of the yeast cell wall. However, we observed that this abolishes pheromone signaling, probably by inhibiting the diffusion of pheromones. Thus, we constructed insets for a conventional centrifuge to hold the culture dishes. This way we could create low forces pushing the cells onto the culture dish, which abolished sedimentation and fixed the majority of the cells on the bottom of the dish. Using this "forced sedimentation", cells were spinned down on the glass surface of the culture dish (MatTek Corporation, Ashland, US) by centrifugation at $100g$. Clearly, cells in a non-moving medium would also sink to the bottom of the culture dish just by gravitation. However, since this takes time synchrony of the population would be lost. Thus, the method we employ can be seen as an acceleration of the sedimentation taking place in any cell culture put in a non-moving medium.
For the calibration curve with Fus1-GFP constructs carrying *BAR1*Δ we used $\boldsymbol{\alpha}$-factor concentrations in the range of $0.1nM - 1\mu M$. The cultures where then observed under the confocal microscope and several z-stacks (images at different depth positions) were obtained for the bright field[2] and the fluorescence channel. In order to prepare them for analysis, all z positions in the bright field starting from the focal plane to the most extreme out-of-focus coordinate (thus, the upper half of the z-stack) were projected over the z-axis via an average intensity projection. This was done in order to obtain out-of-focus images with low noise levels. Since far out-of-focus images in the fluorescent channels generally showed a strong autofluorescence, only the three slices closest to the focus were used for an average intensity z-projection here.

[2] a general laser with no specific excitation which will result in black and white images of the cells by contrast.

The generated projections were consecutively analyzed using programs which allow automatic segmentation and tracking of cells by identifying cell boundaries from out-of-focus images (see figure 3.1). The programs we employed were VCellID and a modified version of CellID [219]. Here, the modification of CellID led to additional text file output containing the individual boundaries for each detected cell along with a list of all interior pixels and by-pixel fluorescence values contained within an area extending the cell boundary by 3 pixels. Parameters for CellID were chosen within VCellID to maximize the fraction of detected cells. The output was further analyzed with the statistical scripting environment *R* [220].

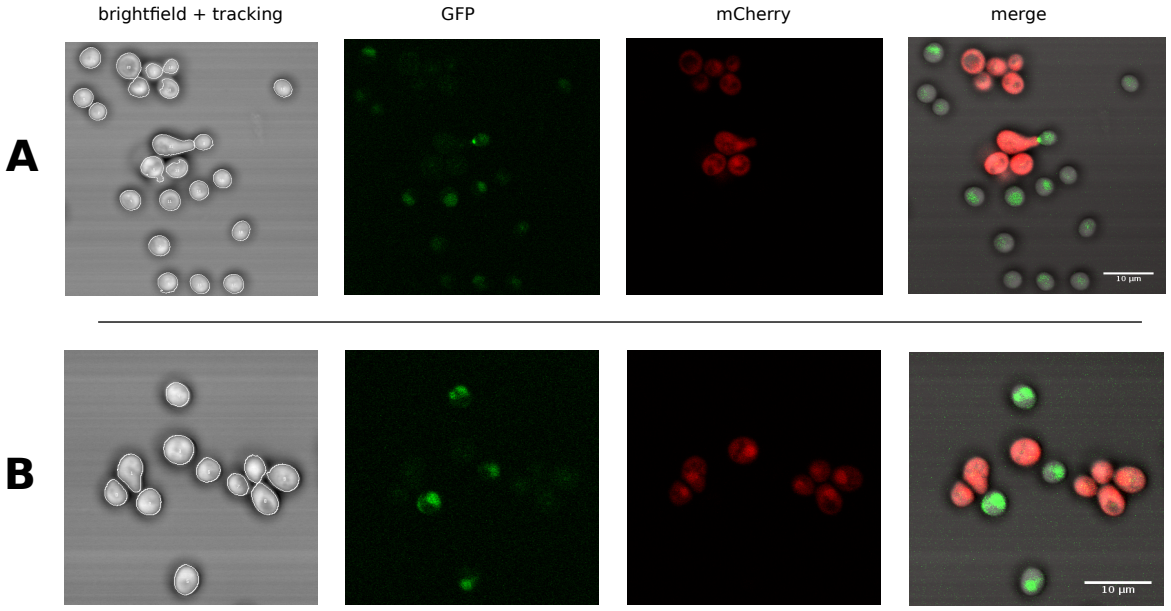

Figure 3.1: Confocal microscopy images of mixed cell populations with different fluorescent markers in (A) Bar1 wild type and (B) *BAR1*Δ.

Using CellID output, we first transformed the x and y locations to micrometers. For each cell i the fluorescence level (mCherry for $MAT\boldsymbol{\alpha}$ and GFP for $MAT\mathbf{a}$) was translated to the average fluorescence per pixel F_i with

$$F_i = \frac{F^i_{tot}}{n^i_{pix}} - F_{bg}. \tag{3.1}$$

Here, F^i_{tot} denotes the total fluorescence for a given cell with index i, n^i_{pix} the number of contained pixels and F_{bg} is the background fluorescence, which is calculated from the intensities of the pixels not contained in cells.

Since it has been reported that the response behavior of the pathway follows a Hill curve, we fitted the fluorescence values to that functional form [65, 66]. This yielded a functional relationship between Fus1-GFP expression F_{obs} and local $\boldsymbol{\alpha}$-factor concentrations α, given the saturated fluorescence F_{max}, the Hill coefficient H, the half maximum concentration EC_{50}, and the background flourescence F_{base}:

$$F_{obs} = F_{max} \cdot \frac{\alpha^H}{\alpha^H + EC^H_{50}} + F_{base}. \tag{3.2}$$

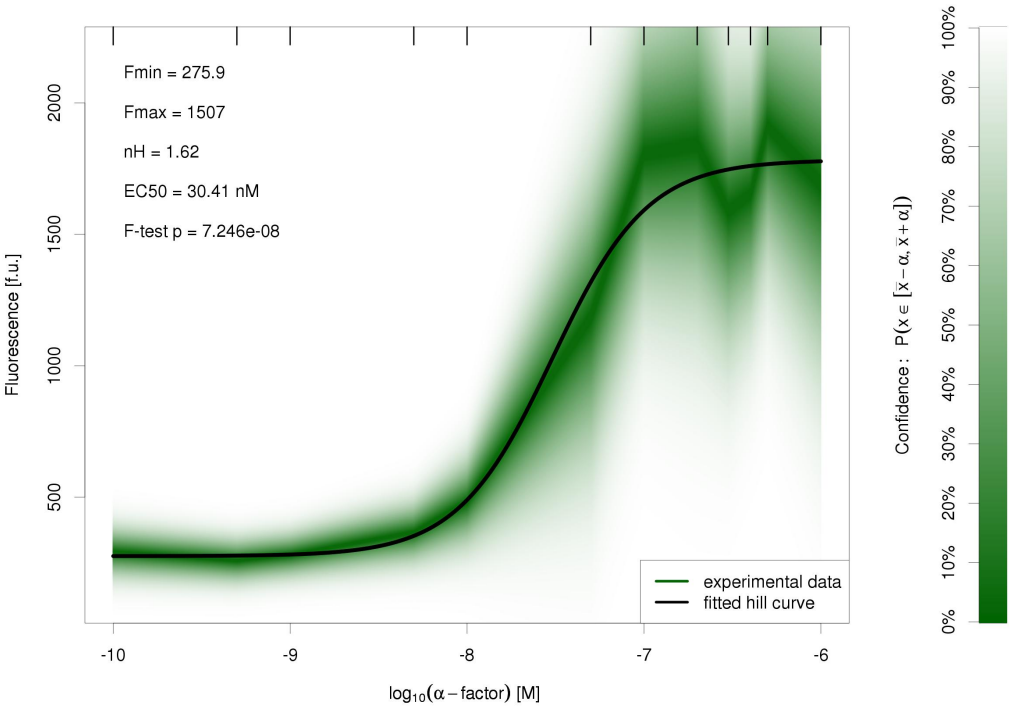

Figure 3.2: The calibration curve obtained from Fus1-GFP-*BAR1*Δ strains. The confidence for each data set is shown in green. Tick marks at the upper border indicate the $\boldsymbol{\alpha}$-factor concentrations used for the experiments. The fitted hill curve is shown in black along with parameter values and statistics.

For a given $\boldsymbol{\alpha}$-factor concentration the distribution of fluorescence values showed a normal distribution (105-588 cells for each concentration, see appendix figure 6.4). The fitting of the Hill curve was, thus, performed by optimizing the log-likelihood of the calculated curve under the data by iteratively using a Simulated Annealing run followed by a BFGS optimization as described in section 2.3.3. Significance was assessed using the F-test[3]. The resulting calibration curve along with confidences obtained from the data is shown in figure 3.2.

For any given local $\boldsymbol{\alpha}$-factor concentration equation 3.2 provides a unique relationship between the concentration and the steady state Fus1-GFP fluorescence. As a consequence, for a given observed Fus1-GFP expression we can derive the local $\boldsymbol{\alpha}$-factor concentration α_i in direct vicinity of the *MAT***a** cell i from the observed Fus1-GFP fluorescence F_i in steady state as

$$\alpha_i = EC_{50} \cdot \left(\frac{F_i}{F_{max} + F_{base} - F_i} \right)^{\frac{1}{H}} . \tag{3.3}$$

This gives us a way to couple the data to a reaction-diffusion model only describing the extracellular diffusion of $\boldsymbol{\alpha}$-factor and its degradation by Bar1. This model can be formulated by the deterministic reaction-diffusion equation 2.48 due to the large volume and the large number of cells jointly secreting $\boldsymbol{\alpha}$-factor.

[3]We used the F-test here, because it is more conservative. The χ^2-test resulted in even smaller p-values since we optimized the test statistic. This was not the case for the F-test.

The reaction-diffusion equations for the extracellular signaling environment

Due to the calibration, we only needed to describe the extracellular events, given by the diffusion of $\boldsymbol{\alpha}$-factor and Bar1 and the degradation of $\boldsymbol{\alpha}$-factor by Bar1. This resulted in a simple reaction-diffusion system given by

$$\frac{\partial \alpha(\boldsymbol{x},t)}{\partial t} = D_\alpha \Delta \alpha(\boldsymbol{x},t) - k \cdot Bar1(\boldsymbol{x},t) \cdot \alpha(\boldsymbol{x},t) \qquad \text{in } \Omega \times (0,T) \tag{3.4}$$

$$\frac{\partial Bar1(\boldsymbol{x},t)}{\partial t} = D_B \Delta Bar1(\boldsymbol{x},t) \qquad \text{in } \Omega \times (0,T). \tag{3.5}$$

However, this model is quite badly defined due to the product $k \cdot Bar1$. One can easily see that one could choose any combination of values resulting in the same product here. As we were not interested in the concentration of Bar1, but rather the distribution of $\boldsymbol{\alpha}$-factor, we substituted this term by a degradation activity $B(\boldsymbol{x},t) = k \cdot Bar1(\boldsymbol{x},t)$. This activity now comprises spontaneous degradation of $\boldsymbol{\alpha}$-factor as well as its degradation by Bar1 in an identifiable term. The former system then immediately implies the new system

$$\frac{\partial \alpha(\boldsymbol{x},t)}{\partial t} = D_\alpha \Delta \alpha(\boldsymbol{x},t) - B(\boldsymbol{x},t) \cdot \alpha(\boldsymbol{x},t) \qquad \text{in } \Omega \times (0,T) \tag{3.6}$$

$$\frac{\partial B(\boldsymbol{x},t)}{\partial t} = D_B \Delta B(\boldsymbol{x},t) \qquad \text{in } \Omega \times (0,T). \tag{3.7}$$

An important question remaining is the dimensionality of the considered space. The biological system acts in three dimensions as such should our model. However, in any non-moving liquid cells will sink to the bottom of the culture dish which arranges them on a plane. Furthermore, we do not know how gravity might affect $\boldsymbol{\alpha}$-factor diffusion in the z-axis. The way microscopy visualizes fluorescence is by a projection over the z-axis resulting in 2-D images. We aimed at reproducing those images. Furthermore, we aimed at reproducing a visualization from a microscope in the hypothetical case that $\boldsymbol{\alpha}$-factor and Bar1 could be visualized without modification. Thus, the appropriate transformation for our model would be the integration over the z-axis, yielding a model which still describes a process in 3-D, but is effectively a 2-D model.

This model is still not very well defined as it is lacking several parts. The first is the computational domain, thus the area on which we solved the equations. We treated the domain as a circular disc corresponding roughly to the area of the microscope image. As we only modeled processes between, but not in the cells, all cells were cut out of the disc. This resulted in several boundaries: one for the disc, termed Γ_{sur} and individual boundaries for all the $MAT\mathbf{a}$ cells, Γ_{a_i}, and $MAT\boldsymbol{\alpha}$ cells, Γ_{α_i}, respectively. The entire space Ω is also depicted in figure 3.3.

Furthermore, we still lacked parts of the biological and mathematical description. From the view of biology, we still miss the secretion kinetics of Bar1 and $\boldsymbol{\alpha}$-factor. In terms of mathematics we still miss parts to make the problem well-posed, most importantly, the boundary conditions. Thus, we had to describe the secretion characteristics somehow by the boundary conditions. For this we chose to use the most simple descriptions available in order to express the biological knowledge with the least unknown parameters possible. For the outer boundary Γ_{sur} we assumed an equilibrium with the environment, thus no substances enter of leave the system. This resulted in

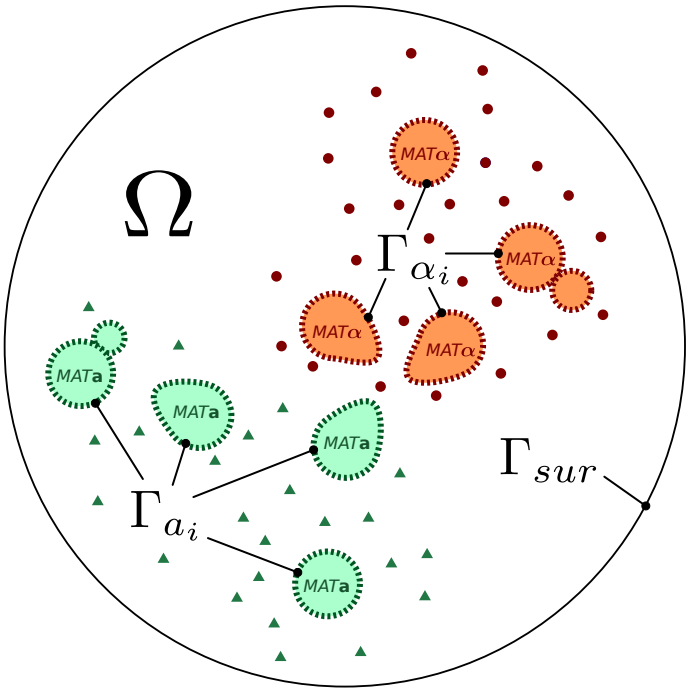

Figure 3.3: The subdivision and boundaries of the space Ω used for the model.

a zero Neumann condition with

$$\frac{d\alpha}{d\boldsymbol{n}} = 0 = \frac{dB}{d\boldsymbol{n}} \qquad \text{on } \Gamma_{sur}. \tag{3.8}$$

The $\boldsymbol{\alpha}$-factor secretion rate is a consequence of the induction by **a**-factor, which is not included in our model. However, the spatial distribution of **a**-factor is not regulated in the extracellular medium. Thus, we can assume that its large diffusion rate effectively results in a uniform distribution in the small volume that is captured by the image. Consequently, we assume that for one image all $MAT\boldsymbol{\alpha}$ cells have the same $\boldsymbol{\alpha}$-factor secretion rate, but those might be different for different images. This effectively results in a constant secretion rate J_α for each image, corresponding to the average flux of $\boldsymbol{\alpha}$-factor per second at each point on the cell boundary. This yields a Neumann boundary with

$$\frac{d\alpha}{d\boldsymbol{n}} = J_\alpha \qquad \text{on } \Gamma_{\alpha_i}. \tag{3.9}$$

The most complex boundary condition has to be employed for the degradation activity B on $MAT\mathbf{a}$ cells. We have a basal degradation activity in the medium due to Bar1 and spontaneous degradation but there is also the induction of Bar1 due to the response to $\boldsymbol{\alpha}$-factor. In the case that there are no $MAT\boldsymbol{\alpha}$ cells this should result in a steady state where the basal activity is homogeneously distributed over the entire space. This can be achieved with a Dirichlet boundary condition for each $MAT\mathbf{a}$ cell corresponding to the basal degradation activity and Neumann zero boundary condition at Γ_{sur}[4]. In the case of induction of Bar1 in $MAT\mathbf{a}$ cells a similar argumentation holds, only that now each $MAT\mathbf{a}$ cell has a Dirichlet condition corresponding to the *induced* activity,

[4]This implies a solution who has the value of the Dirichlet condition at the cell and a derivative of zero at the boundary, thus a constant function in steady state.

which gives differences in distribution even with diffusion. Thus, we can still use the Dirichlet boundary for the $MAT\mathbf{a}$ cell i, but it will now depend on the average extracellular pheromone concentration at the cell given by:

$$\mu_{\alpha,i} = \frac{1}{C} \int_{\Gamma_{a_i}} \alpha(\boldsymbol{x}, t) d\boldsymbol{s}, \tag{3.10}$$

where C denotes the circumference of the cells and, thus, the length of the boundary Γ_{α_i}. Since there is only one promoter present for the expression of pheromone induced genes, we assumed that the induction of Bar1 expression is governed by the same kinetics as Fus1, thus, we can use the obtained parameters of the Hill curve. However, the expression of Bar1 will take some time, resulting in a delay τ until secretion of Bar1 occurs. This results in the following boundary conditions for B

$$B(\boldsymbol{x}, t) = g_D(i, \alpha, t) = k_0 + k_1 \frac{\mu_{\alpha,i}(\boldsymbol{x}, t-\tau)^H}{\mu_{\alpha,i}(\boldsymbol{x}, t-\tau)^H + EC50^H} \qquad \text{on } \Gamma_{a_i}. \tag{3.11}$$

All other boundary conditions on the cell borders were zero Neumann. For the initial state of the model we chose a zero distribution for $\boldsymbol{\alpha}$-factor and k_0 for the degradation activity B. This resulted in a fully specified model, which was fully non-linear due to the coupling induced in the Dirichlet boundary for B which depends on α. Due to the stacked dependencies, we resolved nonlinearities by the Picard iteration as introduced in section 2.3.2. This was particularly simple for this problem, as the equation without the boundary conditions defined one linear equation for B and a nonlinear equation for α depending only on B. Thus, without the Dirichlet boundary one could simply solve for B first and plug the solution into the equation for α now yielding two successive linear systems. Thus, in the Picard iteration we only needed to linearize the boundary condition g_D. However, since the reaction-diffusion equation for B is just the Poisson equation introduced in section 2.3.2, this could be achieved by fixing the values for the Dirichlet boundaries in the coefficient vector according to $g_D^i(\alpha_k, t)$ when calculating B_{k+1}. Using this property, we could now construct the initial weak form for the discontinuous case as

$$\forall v: \quad \int_\Omega \frac{dB}{dt} v d\boldsymbol{s} + D_B \int_\Omega \nabla_{\boldsymbol{x}} B \nabla_{\boldsymbol{x}} v d\boldsymbol{s} - D_B \sum_j \int_{\Psi_j} (\nabla_{\boldsymbol{x}} \langle B \rangle \cdot \boldsymbol{n})[[v]] d\boldsymbol{s} = 0 \tag{3.12}$$

$$\int_\Omega \frac{d\alpha}{dt} v d\boldsymbol{s} + D_\alpha \int_\Omega \nabla_{\boldsymbol{x}} \alpha \nabla_{\boldsymbol{x}} v d\boldsymbol{s} + \int_\Omega B \cdot \alpha d\boldsymbol{s} \tag{3.13}$$

$$- D_\alpha \sum_j \int_{\Psi_j} (\nabla_{\boldsymbol{x}} \langle \alpha \rangle)[[v]] d\boldsymbol{s} = D_\alpha \sum_i \int_{\Gamma_{\alpha_i}} (J_\alpha \boldsymbol{n}) v d\boldsymbol{s}$$

$$\text{with } B_{k+1} = g_D^i(\alpha_k, t) \text{ on } \Gamma_{\alpha_i}. \tag{3.14}$$

This scheme is easy to implement. For each iteration one only has to update the Dirichlet boundary conditions for B using the previous solution for α. In order to obtain the NIPG method we, furthermore, added the corresponding symmetry terms and jump stabilization as described in section 2.3.2. As basis functions we used the linear and cubic basis functions as defined in equation 2.79. This defined our model and the corresponding NIPG method to solve it. Thus, we now concentrated on identifying the parameters of the model from microscope images.

Model parameterization based on microscope images

The unknown parameters are given by $J_\alpha, k_0, k_1, \tau, D_\alpha$ and D_B. Not all of the parameters had to be obtained by optimization. The diffusion rates can be derived from simple physical principles due to the fact that diffusion here takes place in an aqueous solution. In this condition the diffusion rate can be obtained from the Einstein-Stokes equation

$$D = \frac{k_B T}{6\pi \cdot \eta \cdot r}, \tag{3.15}$$

where k_B denotes the Boltzmann constant, T the temperature of the medium, η the viscosity of the medium and r the protein radius. The radius r is approximated from the density derived via the protein mass and applying the correction of Fischer et. al. [221] to approximate the density of the protein from its mass:

$$\rho(M) = 1.41 + 0.145 \cdot \exp\left(\frac{M[kDa]}{13}\right)[g \cdot cm^{-3}]. \tag{3.16}$$

Converting that to $[kg \cdot cm^{-3}]$ and assuming a globular shape for the protein within the aqueous medium M with viscosity η_M the diffusion rate of a protein P is given by

$$D(P) = \frac{k_B T}{6\pi \cdot \eta_M} \cdot \left(\frac{750 \cdot M_P}{\pi \cdot \rho(M_P)}\right)^{-1/3}. \tag{3.17}$$

Substituting the masses by the ones known for $\boldsymbol{\alpha}$-factor and Bar1 results in effective diffusion rates of $361.48\,\mu m^2 s^{-1}$ and $104.63\,\mu m^2 s^{-1}$, respectively. The relevant temperature was 30 °C.
Thus, we remained with quantifying J_α, k_0, k_1 and τ. One can see that in the case of broad spatial distributions, the degradation activity and $\boldsymbol{\alpha}$-factor are highly connected so that a high α distribution can be counteracted by a high B activity. Thus, optimizing all parameters at once is highly unstable due to the correlation. We tried to overcome this limitation in a setting where we can identify the set of parameters for only B first. This was achieved by stimulating wild type *MAT***a** cells carrying the Fus1-GFP marker with controlled concentrations of $\boldsymbol{\alpha}$-factor and observing their response after some time point $t_{obs} = 3h$. As these cells secrete Bar1 and there are no *MAT*$\boldsymbol{\alpha}$ cells, the observed fluorescence is a consequence of the remaining $\boldsymbol{\alpha}$-factor concentration *after* degradation. Furthermore, if $\boldsymbol{\alpha}$-factor is added to the cells in a spatially homogeneous distribution with concentration α_0, this results in a homogeneous Bar1 degradation activity and we can reduce the equations system to an ODE. This depended crucially on the conservation law of the NIPG method as it allowed for integration over Ω yielding

$$\frac{d}{dt}\alpha_{tot}(t) = -\alpha_{tot}(t)\left(k_0 + k_1 \frac{\mu(\alpha_{tot}, t-\tau)^H}{\mu(\alpha_{tot}, t-\tau)^H + (EC_{50})^H}\right) \tag{3.18}$$

$$\alpha_{tot}(0) = \alpha_0. \tag{3.19}$$

The experimental data was obtained in the same way as the former calibration curve, only this time with the Fus1-GFP strain carrying the wild type *BAR1* gene and a concentration range of $0.1\mu M - 10\mu M$ (147-746 cells for each concentration, 2458 cells in total). The observed flourescence values $F_i(t_{obs})$ were then fitted to the predicted

fluorescence values $F(t_{obs})$ given by equation 3.2. This resulted in the following log-likelihood optimization problem

$$\text{Find } k_0, k_1, \tau \text{ such that for}$$
$$\mathbf{F}(t) = \{F_i(t_{obs})\} : \sum_{i=1}^{N_c} \ln f_i(F_i(t_{obs}), \mu_i, \sigma_i) \to \max . \tag{3.20}$$

Here, f_i are again the Normal distributions given by the data. The results are shown in figure 3.4.

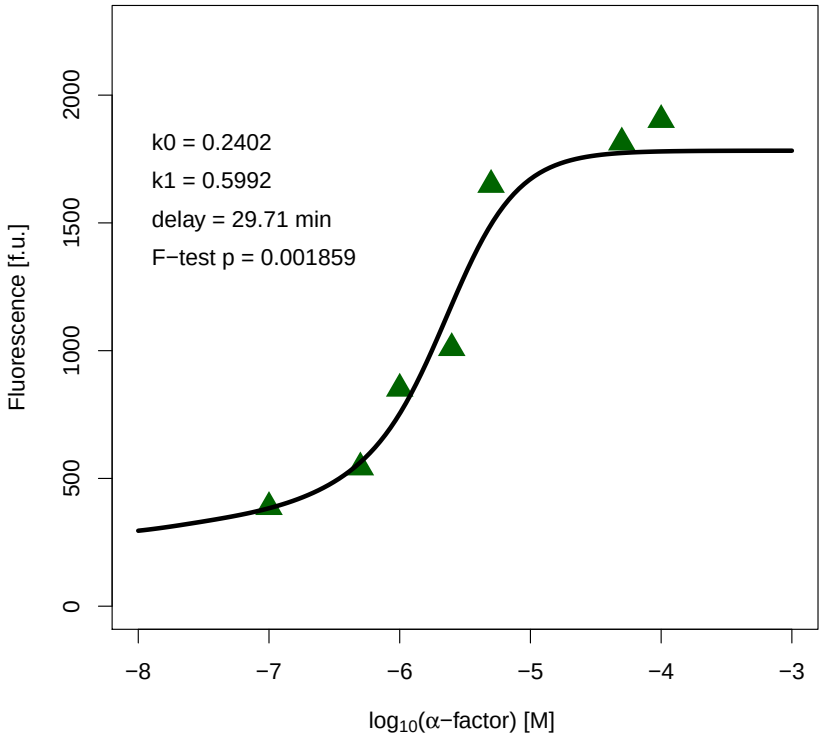

Figure 3.4: Results of the parameter optimization for the degradation activity by Bar1. Shown are the mean values of the fluorescence measurements and the resulting parameters.

The ODE was solved by the fully adaptive implicit LSODA method and used during the optimization by again iterating Simulated Annealing and BFGS runs. Significance was assessed again using an F-test. The fitted parameters were the steady state (stimulated) Bar1 activities and the delay time τ under the given number of cells in the population and the given volume.
The delay time τ was optimized here as well since this was the only time course optimization we performed ($\boldsymbol{\alpha}$-factor secretion parameter is fitted later to the steady state). The activation of the Ste12 transcription factor takes at least 5 minutes [65]. Considering that Bar1 also has to be transcribed, translated, modified and exported, we do expect that cells will need more time to adequately react with an increased Bar1 secretion. The fitted value of $\tau \approx 30\,min$ is in good agreement with this consideration

and our own observations that expression of Fus1 started roughly half an hour after mixing of cultures.
However, since all cells secrete Bar1, the steady state Bar1 activity is dependent on the number, and possibly, size of the cells in the population. Since the overall Bar1 activity will scale linearly with the total amount of Bar1 secreted, we normalized the obtained parameters by the fraction of the image area occupied by the total area of the $MAT\mathbf{a}$ cells. For any given cell configuration on an image we calculated the corresponding Bar1 activity parameters. The fitted parameters are in volume units ($nMs^{-1}\mu m^{-3}$), however the model was expressed in integrated quantities over the z-axis ($nMs^{-1}\mu m^{-2}$), so we still had to integrate the Bar1 activity over the z-axis. Because in the experimental setting Bar1 was uniformly distributed, the integration was simply a multiplication by the height of the liquid film. This height h is given by the surface tension γ of the medium (aqueous solution), the gravitational acceleration g and the liquid density ρ via

$$h = 2\sqrt{\frac{\gamma}{g\rho}}. \tag{3.21}$$

This finally yielded the Bar1 activity with and without stimulation, which was plugged into the reaction-diffusion equations (also see figure 3.4). The fitted Bar1 activity indicated a pheromone-dependent induction of about 3-fold which was in good agreement with previous measurements after 3 hours of incubation (3.4 ± 1.1 [32]). The approximated Bar1 activity in a typical liquid film ($h \approx 170\mu m$) where the bottom is covered completely with cells (due to the normalization) was derived as 0.24 nM/s without $\boldsymbol{\alpha}$-factor induction and could rise to 0.6 nM/s when induced by $\boldsymbol{\alpha}$-factor. Consequently, if the entire volume would be filled by cells, the cooperative secretion could lead to a maximum Bar1 activity of $60nM/s$ within the medium (assuming that approximately 100 cells can fit above each other in the liquid film). Thus, the Bar1 activity is strongly coupled to the cell mass in the medium and can reach a substantial value in high density cultures.

We were only left with one parameter, the flux of $\boldsymbol{\alpha}$-factor J_α. We optimized this parameter from the steady state equations by data generated from mixed $MAT\mathbf{a}$-$MAT\boldsymbol{\alpha}$ cell populations. Here the $MAT\mathbf{a}$-Fus1-GFP cells were elutriated, mixed to a 1:1 relation with $MAT\boldsymbol{\alpha}$-mCherry cells and sedimented by centrifugation as described before. Following that, cells were placed in a climate chamber for 3h under the confocal microscope and time course data as well as several images after 3 hours were obtained. The images were analyzed with VCellID and our own modified version of CellID. $MAT\boldsymbol{\alpha}$ cells were identified by having no significant GFP signal and a mCherry signal which was at least 4 times higher than the average background fluorescence in the mCherry channel. Further analysis was performed in R.

For each $MAT\mathbf{a}$ cell we obtained the $\boldsymbol{\alpha}$-factor concentration at the membrane by the calibration curve for Fus1-GFP-$BAR1\Delta$. The grid for the NIPG-FEM method was obtained by first reading all boundary pixels for each individual cell from CellID output. For each cell pixel, values were transformed into μm and expressed in polar coordinates. A smoothing spline was calculated in order to convert the border into a smooth functions for each cell. Overlaps between cells were resolved using a heuristic algorithm where parts of the smoothing spline were iteratively diminished until there were no more overlapping pixels of the two cells. The entire space was then transformed

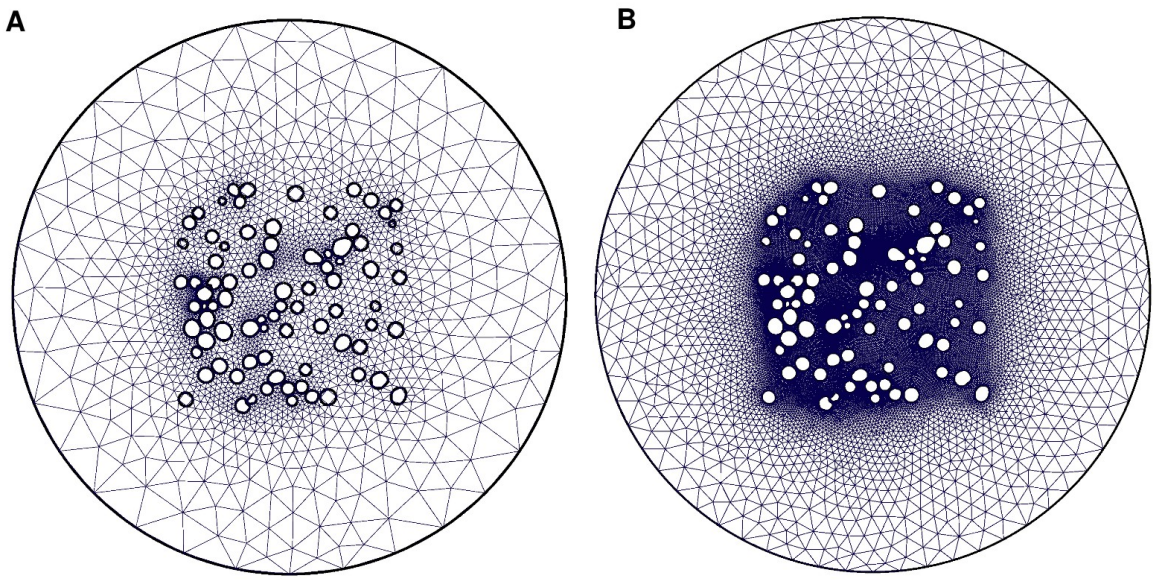

Figure 3.5: Meshes generated from microscope images with different degrees of coarseness.

into a Gmsh file by creating a disc with a radius equal to the image width and height and cutting out the smooth cell shapes [222, 223]. In order to obtain a triangulation that performed well, particularly at points where the solution would change a lot, we assigned each point at the cell surface a target triangle size. This size was chosen to be very small at points where cell density was highest and increased exponentially while approaching the boundary of the disk. Thus, the target size s was assigned to each point used in the geometry of the grid via the relation

$$s = \max\{\lambda_s \cdot \exp(-\gamma D(x, y)), \lambda_M\}, \tag{3.22}$$

where $D(x, y)$ is the local density of the point and γ, λ_S and λ_M were scaling parameters controlling the minimum and maximum target size. The local density D was obtained from the binned densities of all original boundary points returned by CellID with 128 bins in the x and y direction. The target size was used consecutively by the Frontal algorithm implemented in Gmsh in order to construct the triangulation [224]. Additionally, each cell boundary was assigned a unique ID associated with the mating type and, if $MAT\mathbf{a}$ the unique local $\boldsymbol{\alpha}$-factor distribution α_i.

The steady state was solved by implementing the NIPG method[5] as described in section 2.3.2 for equation 3.7 in DUNE using the UG grid library and PDElab [225–228]. The integrals required by $\mu(\alpha)$ were computed using a quadrature over the cell edges of $MAT\mathbf{a}$ cells and used to update the Picard iteration with the acceleration described in section 2.3.2. Here the iteration was considered converged when the summed difference of coefficients from the previous solution was smaller than 10^{-5}. Convergence was usually rapid with less than 10 iterations necessary to obtain the required accuracy. The occurring linear systems were solved with SuperLU.
Given the local alpha concentration α_i observed via Fus1-GFP fluorescence we could

[5] σ_j was chosen as $\sigma_j = 4/l_j$.

estimate J_α for several images by solving the following RSSQ optimization problem:

$$\text{Find } J_\alpha \text{ such that for } \boldsymbol{\alpha} = \{\alpha_i\} : \sum_{i=1}^{N_a} \left(\mu(\alpha)|\Gamma_{a_i} - \alpha_i\right)^2 \to \min\,. \tag{3.23}$$

Due to the strict monotonicity for $J_\alpha > J_\alpha^{*}$[6] a local optimizer was sufficient. Here we employed the BFGS method as described in section 2.3.3 with a stable numeric approximation of the derivative. The results were cross-checked with another optimizer, the Nelder-Mead optimization, which yielded the same results. We fitted the secretion rate of $\boldsymbol{\alpha}$-factor to 10 images obtained on 2 different days. Only the 9 fits with a significant F-test were used to obtain J_α (a total of 52 $MAT\boldsymbol{\alpha}$ and 90 $MAT\mathbf{a}$ cells). The fitted J_α for the nine images showed a distribution with several peaks, where the largest group contained 5 images with J_α values clustered around 5 $nM \cdot s^{-1}$ which corresponded to an average secretion rate of about 2300 molecules per cell and second (see appendix figure 6.5). Because this was measured after 3 hours of incubation with accumulated **a**-factor secreted by the $MAT\mathbf{a}$ cells, this likely describes the induced $\boldsymbol{\alpha}$-factor secretion. The obtained value was in good agreement with recent experimental results obtaining a secretion rate of around 2000 molecules per second and cell. The remaining 4 images showed significantly higher $\boldsymbol{\alpha}$-factor fluxes than the first group up to 40 $nM \cdot s^{-1}$. This is likely a consequence of the boundary condition for $\boldsymbol{\alpha}$-factor on Γ_{sur} because additional $MAT\boldsymbol{\alpha}$ cell in the vicinity of the image increase the $\boldsymbol{\alpha}$-factor level which is compensated by the optimization by a higher J_α.
Significance was assessed for all fits using the F-test for a zero-intercept-one-parameter model. Additionally, we also tested whether the obtained mean secretion flux obtained from all 9 significant fits could reliably predict the fluorescence values from an independent image not used in the optimization, which it did (F-test p-value $< 2.2 \cdot 10^{-6}$, 67 $MAT\boldsymbol{\alpha}$ cells and 78 $MAT\mathbf{a}$ cells). This was a validation for the model and also proved that the approximation of the 3-D process by a 2-D model was capable to correctly predict $\boldsymbol{\alpha}$-factor distributions. The resulting mean flux J_α was estimated as $15.11 nM/s$.
This fully characterized the model which could now be used to quantify the extracellular signaling environment during mating. The full assay along with some representative results is given in figure 3.6.

3.2.2 Bar1 induces α-factor hot-spots

With the parameterized model we could now start to analyze the distribution of $\boldsymbol{\alpha}$-factor in the presence or absence of Bar1. From steady state distributions of $\boldsymbol{\alpha}$-factor we observed that the wild type had much more restricted pheromone distributions coinciding with higher gradients (compare figure 3.6B). Additionally, approximating the temporal evolution of $\boldsymbol{\alpha}$-factor distributions in time by using the parameterized model on time course data, we observed that the pheromone distribution initially rises to a high concentration with little gradients which is quickly counteracted in time by the high-level secretion of Bar1 and declines to the steady state afterwards (see figure 3.7). The pheromone distribution in time was obtained by implementing the reaction-diffusion system by a 2-stage Alexander method. Interestingly, the formation

[6] Increasing J_α results in higher and higher distributions which means the RSSQ grows.

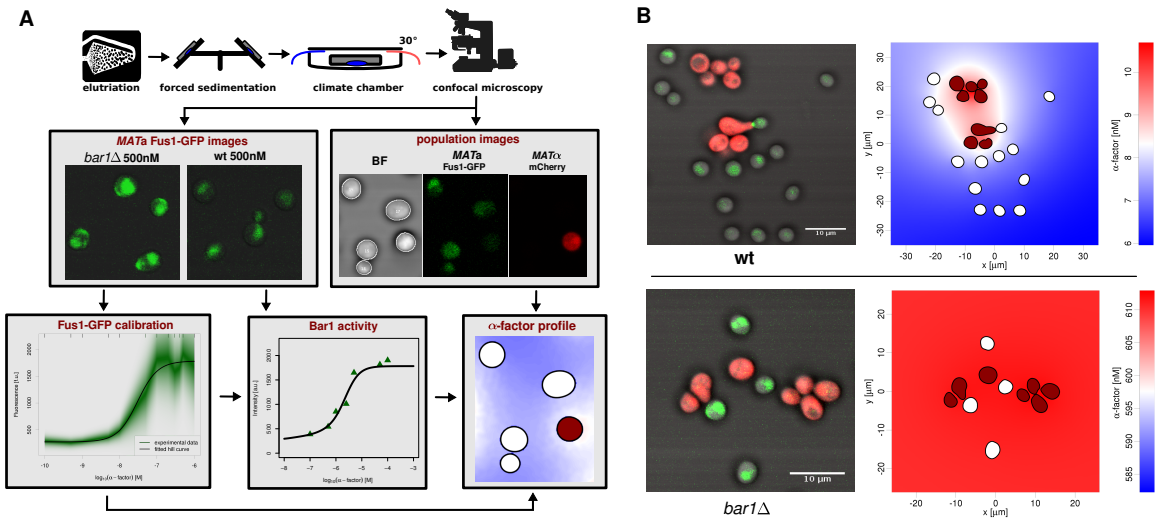

Figure 3.6: (A) The full assay to quantify the extracellular signaling environment. (B) Obtained $\boldsymbol{\alpha}$-factor distributions for the wild type and $BAR1\Delta$.

of shmoos coincided with the stabilization of the gradient, indicating that yeast cells wait for a stable $\boldsymbol{\alpha}$-factor distribution before committing to mating.

In general, we observed large differences in the estimated local $\boldsymbol{\alpha}$-factor concentrations between wild type cell populations and cell populations with a $BAR1\Delta$ background. Wild type cell populations showed a strongly localized $\boldsymbol{\alpha}$-factor distribution at sites of high $MAT\boldsymbol{\alpha}$ cell density, with $\boldsymbol{\alpha}$-factor concentration quickly declining with distance. Consequently, $MAT\mathbf{a}$ cells farther away from a $MAT\boldsymbol{\alpha}$ cell than what could normally be bridged by shmooing experienced significantly lower local $\boldsymbol{\alpha}$-factor concentrations that were often non-permissive for induction of the pheromone response. In populations with $BAR1\Delta$ background the $\boldsymbol{\alpha}$-factor showed an almost uniform distribution of very high pheromone concentrations, resulting in global pathway activation as evidenced by high Fus1-GFP expression.

We wanted to see whether this behavior arises in general and independently of the exact spatial composition of the culture. Thus, we performed a systematic computational study using randomly generated cell populations mimicking the ones observed microscopically with varying cell densities. For that we generated cell populations *in silico* with varying total numbers of 1:1 mixed haploid cells. The cells here were circular with radii sampled from a Normal distribution obtained from the zero samples of the calibration curve ($n = 730$, $\mu = 1.98\mu m$, $\sigma = 0.25\mu m$). This was done for populations sizes of 2 up to 700 cells, roughly corresponding to a range of 20 up to 10,000 cells per mm^2. Each virtual population was simulated both with wild type Bar1 secretion and in $BAR1\Delta$ background and for each fixed number of $MAT\mathbf{a}$ and $MAT\boldsymbol{\alpha}$ cells we simulated 16 randomly sampled cell configurations. The $\boldsymbol{\alpha}$-factor flux J_α was chosen as the mean value obtained from the 9 significant fits. This allowed to track key components of the $\boldsymbol{\alpha}$-factor distribution without the influence of the exact spatial composition. Furthermore, in this cultures we could directly compare the $\boldsymbol{\alpha}$-factor distributions within the same exact cell configuration in wild type and $BAR1\Delta$

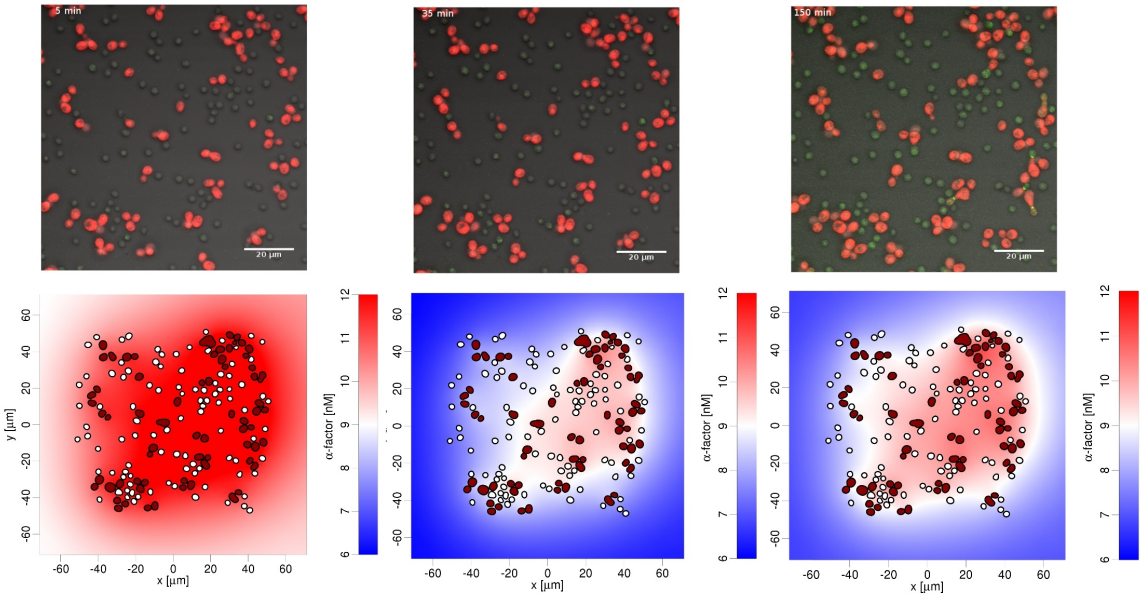

Figure 3.7: Time course data of mixed haploid yeast populations consisting of wild type *MAT***a**-Fus1-GFP and *MAT*$\boldsymbol{\alpha}$-mCherry and the resulting pheromone gradients.

conditions.

So, how can we quantify the influence of Bar1 on the information provided by the $\boldsymbol{\alpha}$-factor distribution? In an abstract sense the maximum information I_{max} that can be provided by the distribution of $\boldsymbol{\alpha}$-factor is given by the entropy of the $\boldsymbol{\alpha}$-factor distribution. In order to obtain this quantity, we started by taking the overall $\boldsymbol{\alpha}$-factor distribution from all pixels of the simulated image ($N = 512 \times 512$ points). The observed $\boldsymbol{\alpha}$-factor concentrations were subdivided into N_{bins} bins and the number of bins chosen by Sturges' law

$$N_{bins} = \lceil \log_2 N + 1 \rceil. \tag{3.24}$$

This was used to obtain a discrete distribution from which the bin probabilities p_i ($i = 1, \ldots, N_{bins}$) were approximated using a shrinkage estimator [229]. The entropy H, and thus the maximum information content I_{max}, was finally computed as

$$I_{max} = H = -\sum_{i=1}^{N_{bins}} p_i \ln p_i \tag{3.25}$$

For each population density the entropy was averaged over the 16 replicates.

Another important property of the $\boldsymbol{\alpha}$-factor distribution are the resulting gradients which are perceived by the individual *MAT***a** cells as those mark the location of nearby mating partners. In order to do that, we implemented an additional output in DUNE that would return the boundary values for all edges forming the boundary of any *MAT***a** cell. For each *MAT***a** cell we then computed the front-back ratio of $\boldsymbol{\alpha}$-factor, defined as the relative difference between the point with the highest and the points with the lowest $\boldsymbol{\alpha}$-factor concentration on the cell surface, given by

$$d_i = \frac{\max\limits_{\mathbf{x} \in \Gamma_{a_i}} \alpha(\mathbf{x}, t) - \min\limits_{\mathbf{x} \in \Gamma_{a_i}} \alpha(\mathbf{x}, t)}{\min\limits_{\mathbf{x} \in \Gamma_{a_i}} \alpha(\mathbf{x}, t)} \tag{3.26}$$

. This quantity was averaged over all *MAT***a** cells in the 16 replicates for a distinct cell density.

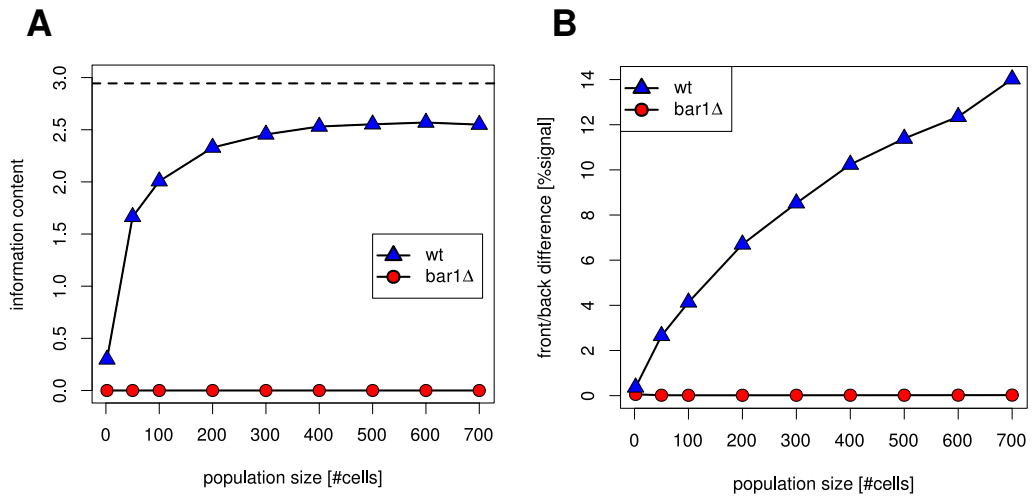

Figure 3.8: (A) Maximum information content and (B) relative front-back ratios (gradients) produced by the $\boldsymbol{\alpha}$-factor distribution in wild type and *BAR1*Δ conditions. The theoretical maximum information content of any distribution with the same binning is given as a dashed line.

Virtual wild type populations exhibited a strong gain of the information content of the $\boldsymbol{\alpha}$-factor distribution for growing population size (figure 3.8A), which was accompanied by increasing gradients across *MAT***a** cells (figure 3.8B). In contrast, populations not secreting Bar1 showed information contents close to zero as well as insignificant pheromone gradients, both independently of population density (figure 3.8, red symbols). We noted that the overall pheromone concentration remained constrained in wild type, but in the mutant linearly increased with population density (see appendix figure 6.6). Altogether, the results indicate that particularly in high cell densities the gradients and, thus, the direction of nearby mating partners can only be detected faithfully in cell populations secreting Bar1.

Additionally, we simulated various scenarios where a high-density subpopulation was placed next to a low-density subpopulation (figure 3.9). Here, the wild type is capable of limiting the $\boldsymbol{\alpha}$-factor distribution to the corresponding subpopulation, leaving the low-density subpopulation unaffected by the high local $\boldsymbol{\alpha}$-factor concentration of the high-density sub-population. This creates $\boldsymbol{\alpha}$-factor hot-spots where only locally dense sub-populations are exposed to $\boldsymbol{\alpha}$-factor concentrations permissive for mating. Again, this behavior was not observed in the absence of Bar1, showing that Bar1 activity restricts the distribution of $\boldsymbol{\alpha}$-factor.

The obtained results created two important hypotheses concerning mating yeast populations. First, we observed that the activity of Bar1 greatly improves the information contained in the $\boldsymbol{\alpha}$-factor signal, resulting in steep gradients in the presence of Bar1. This should make it easier for *MAT***a** cells to find a *MAT*$\boldsymbol{\alpha}$ cell for conjugation and should result in a more efficient formation of diploids in the presence of Bar1.

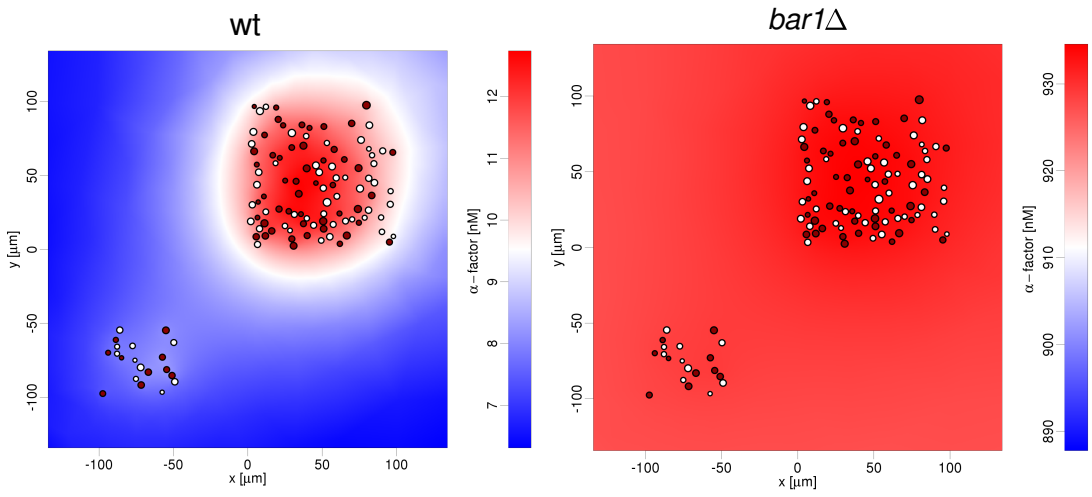

Figure 3.9: In the presence of Bar1 activity high $\boldsymbol{\alpha}$-factor concentrations are kept within high density mating sub-populations. This creates hot-spots of $\boldsymbol{\alpha}$-factor activity. This effect is absent in *BAR1*Δ conditions.

Second, the lack of Bar1 induces a globally high $\boldsymbol{\alpha}$-factor concentration which should induce activation of the mating pathway in all *MAT***a** cells and result in a global growth arrest of the culture, because *MAT***a** as well as *MAT*$\boldsymbol{\alpha}$ do not have an extracellular protease activity in this setting. In the wild type, however, mating is concentrated to the $\boldsymbol{\alpha}$-factor hot-spots which should result in a recovered growth compared with *BAR1*Δ cultures. We now set out to investigate the validity of these hypotheses.

3.2.3 Bar1 coordinates growth along with mating in mixed haploid populations

In order to test the validity of this prediction we observed mating between *MAT***a** cells (here marked with the constitutively expressed RPL9a-GFP) and *MAT*$\boldsymbol{\alpha}$ cells (marked with mCherry) and quantified their growth rates with FACS analysis and cell counting in wild type and in *BAR1*Δ populations during 5 hours of incubation.
To measure the diploid formation rate independently of the population density and without destroying extracellular gradients, we used flow cytometry (see 2.2.2) for mixed populations of *MAT***a** and *MAT*$\boldsymbol{\alpha}$ to quantify the fractions of *MAT***a**, *MAT*$\boldsymbol{\alpha}$ and *MAT***a**/$\boldsymbol{\alpha}$ diploids over time for a fixed number of cell counts.
Growth of equally mixed *MAT***a** and *MAT*$\boldsymbol{\alpha}$ reporter strains, as well as a haploid control strain was analyzed by measuring optical density at 600nm with a Photometer (Eppendorf BioPhotometer plus) and in parallel by analysis of cell number and cell size distribution with a cell counter (Casy Counter TTC, Schärfe System). Yeast cells were incubated in a water bath at 30 °C without shaking. In time steps of 15 minutes samples were removed from the water bath, vortexed, appropriately diluted, and analyzed in duplicate.

We measured fluorescence intensities for GFP and mCherry of 10.000 living cells of each sample by FACS analysis taking advantage of the fluorescence of *MAT***a**-RPL9a-GFP and *MAT*$\boldsymbol{\alpha}$-mCherry in a BD FACS AriaII cell sorter (Becton Dickinson,

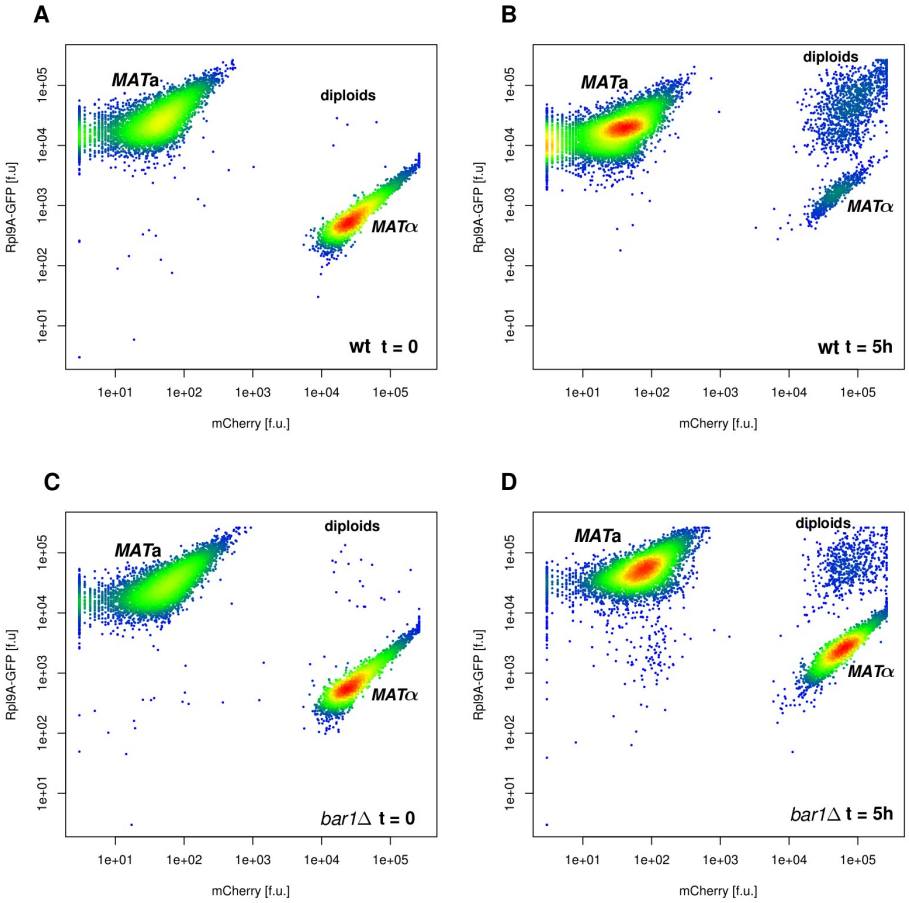

Figure 3.10: Flourescence obtained by flow cytometry of mixed haploid cultures in wild type (A,B) and *BAR1*Δ conditions (C,D). Points are colored by local density from blue to red.

Franklin Lakes, NJ), equipped with a 488 nm and a 561 nm Laser with filter sets for GFP (525/50 BP, 505LP) and for mCherry (610/20BP, 600LB). Cultures were incubated in a water bath at 30 °C without shaking. In 20 min time steps, duplicate samples were removed from the water bath, mixed vigorously, diluted in PBS and FACS analysed. Gates for *MAT***a**, *MAT*$\boldsymbol{\alpha}$ and diploids were set by hand identifying the cell types as shown in figure 3.10.

We found no difference in the rate of diploid formation between wild type and *BAR1*Δ cultures before completion of the first cell cycle (<120 min). This observation is in agreement with our results that positive effects on the perceived pheromone gradients require higher cell densities. However, after approximately passing the first cell cycle, the relative fraction of diploids is clearly larger in the wild type cultures than in the mutant (see figure 3.11A). This is consistent with the general view that Bar1 activity helps to recover the position of mating partners [205–207].

When looking at population growth during mating we found strong differences between wild type and *BAR1*Δ cultures (figure 3.11B). For *BAR1*Δ cultures, the global activation of the pheromone response in effectively all *MAT***a** cells of the population led to an almost complete loss of population growth (figure 3.11B,C). This also caused a characteristic population phenotype with many pheromone-stimulated *MAT***a** cells being significantly larger than normal *MAT***a** cells and showing multiple mating pro-

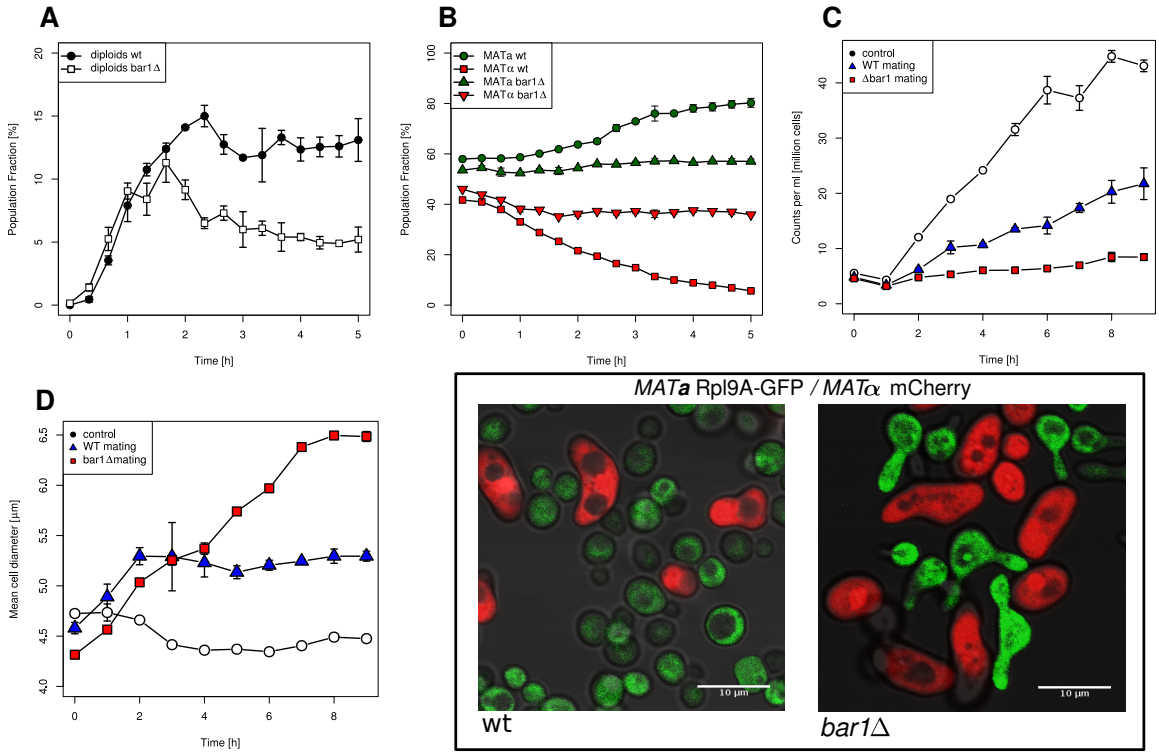

Figure 3.11: (A-B) Results of the FACS experiment. Each point denotes fractions obtained from 2×10.000 living cells. Error bars denote differences of the two biological samples in order indicate reproducibility of the experiment. (C-D) Cell numbers and and sizes (error bars denote standard deviation, n=6). The box indicates phenotypes in mixed cultures.

jections (figure 3.11E). This phenotype was never encountered in unperturbed wild type mixtures of *MAT***a** and *MAT*$\boldsymbol{\alpha}$ cells, but could be induced by swirling them rapidly to inhibit cell fusion. Thus, this phenotype appears associated with induction of pheromone response *in vivo* under conditions where a cell cycle arrest has been induced but successful mating is inhibited.

Wild type cultures exhibited significant growth on the population level despite the higher rate of diploid formation and a normal phenotype of *MAT***a** cells (figure 3.11B,D). The effect of Bar1 secretion on haploid growth rates was even more prominent when looking at the *MAT***a**/*MAT*$\boldsymbol{\alpha}$ ratio in the population (figure 3.11C). There is no secretion of an extracellular protease described for *MAT*$\boldsymbol{\alpha}$ cells. Co-cultured wild type *MAT***a** cells strongly outperform *MAT*$\boldsymbol{\alpha}$ cells in growth during mating to an extent that within 5 hours *MAT***a** is the predominant haploid cell type in the population. This cannot be observed in *BAR1*Δ background where the *MAT***a**/*MAT*$\boldsymbol{\alpha}$ ratio remains constant, presumably because both haploid cell types are equally inhibited in growth.

In summary, secretion of Bar1 enables a high mating rate on a population level, but also strongly optimizes the population growth rate by avoiding unnecessary cell cycle arrest when successful mating is improbable.

3.3 Signal accumulation and linear distance encoding in the yeast pheromone response

We saw that the extracellular pheromone signal is highly regulated in mating yeast populations. However, we also observed that the resulting concentrations of $\boldsymbol{\alpha}$-factor are quite low ($\approx 10nM$). Even though the *average* $\boldsymbol{\alpha}$-factor distribution is highly informative, how is this information sensed by the cells in the presence of high noise due to the fast diffusion and small abundance of $\boldsymbol{\alpha}$-factor? As we have seen in section 2.3.2, small abundance together with fast diffusion can introduce significant noise into a system. This can indeed be observed to be true when looking at the response of $MAT\mathbf{a}$ cells secreting Bar1 incubated with defined initial concentrations of $\boldsymbol{\alpha}$-factor in figure 3.12.

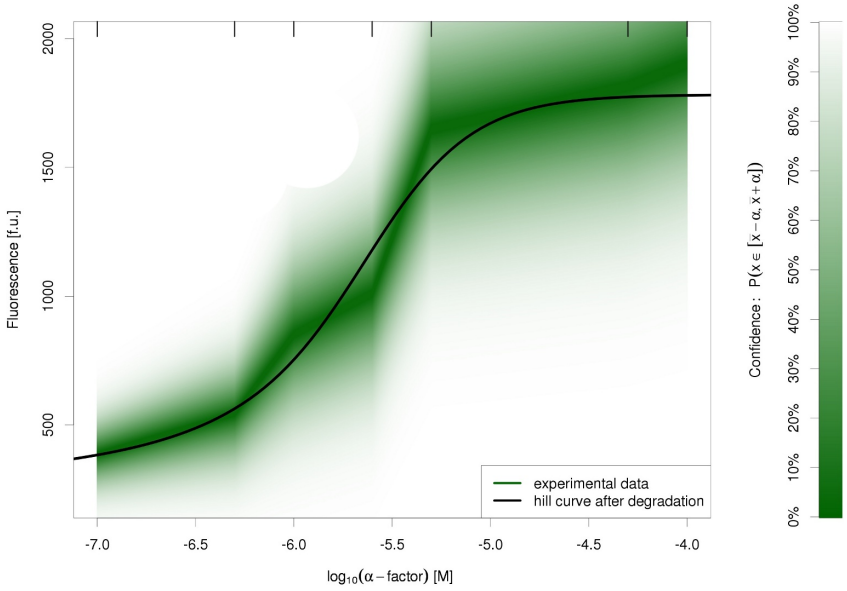

Figure 3.12: The presence of Bar1 also induces higher noise levels in the response. Compare to figure 3.2.

The increased noise levels impose a challenge to the sensing cell, particularly when only few secreting $MAT\boldsymbol{\alpha}$ cells and thus little pheromone is available to sense. Additionally, $MAT\mathbf{a}$ cells do not only have to recover the abundance of $\boldsymbol{\alpha}$-factor but also its distribution in space as it marks the site of the future polarisome. Thus we set out to study the early response to pheromones in detail considering a modeling which would allow us to quantify the stochastic properties as well as spatial arrangements.

3.3.1 A spatial stochastic model of the early pheromone response

Even though the volume of the entire cell population is high and the overall number of $\boldsymbol{\alpha}$-factor molecules as well, this does not necessarily hold for an individual $MAT\mathbf{a}$ cell in the population. Due to this we used a characterization by the reaction diffusion master equation described in section 2.3.1. In particular we used the next subvolume

method implemented in the program MesoRD (`http://mesord.sourceforge.net`) to obtain the spatial dynamics of the system [189]. As we were interested in the parts of the system participating in noise reduction, we constructed a much more detailed model containing 18 different types of molecules influenced by 24 unique reactions. The system included the entire early onset activation of the yeast pheromone response as described in section 1.4.2, including secretion of $\boldsymbol{\alpha}$-factor and Bar1, receptor regulation, G protein activation and Ste5 recruitment. Those processes were implemented in a $MAT\mathbf{a}$ cell with a single nearby $MAT\boldsymbol{\alpha}$ cell. The model could be parameterized completely by values obtained from published measurements or direct derivation. Here, the entire derivation of kinetic parameters can be found in the appendix 6.2. Diffusion rates for individual molecules were again calculated from the Einstein-Stokes relation as described earlier in section 3.2.1 (also see appendix 6.2). The volume in which the cells were immersed was modeled as an outer "world" compartment having a ellipsoid shape and containing a single $MAT\mathbf{a}$ and $MAT\boldsymbol{\alpha}$ cell with variable distance to each other. Both cells were assumed to be large haploid cells with ellipsoid shapes having a radius of 2.5 μm over the xy-plane and a height of 1.5 μm over the z-plane. The entire computational domain is illustrated in figure 3.13. Apart from the nucleus indicated in

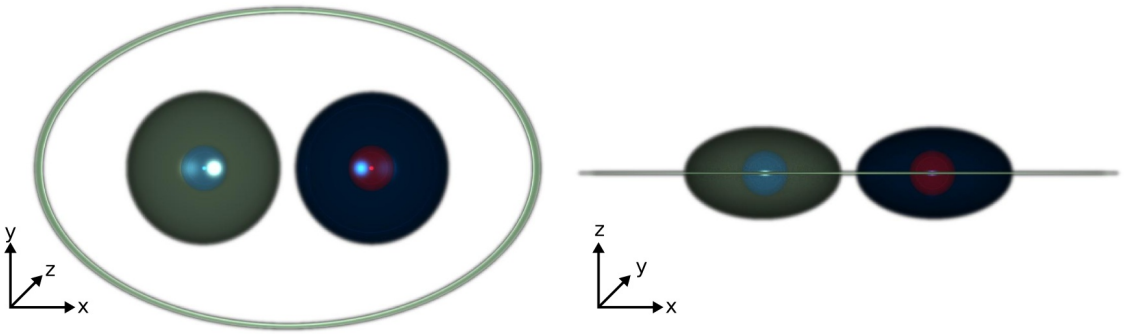

Figure 3.13: The geometry of the used model. The $MAT\mathbf{a}$ cell is shown in green with blue nucleus and the $MAT\boldsymbol{\alpha}$ cell in blue with red nucleus. The outer boundary of the simulated volume is indicated with the lightgreen ellipsis.

the images, the $MAT\mathbf{a}$ cell is subdivided into several biological compartments. Here, the most important is the membrane/cell wall, which is the space protruding 100 nm from the cell boundary into the $MAT\mathbf{a}$ cell volume. Furthermore, we define the cytosol as the cell volume which is neither part of the membrane nor of the nucleus. Diffusion rates and reactions are automatically adapted depending in which compartment the molecules reside. Furthermore, a 100 nm space protruding from the outer boundary of the world compartment is reserved as a unique compartment "end of world" in order to enforce various boundary conditions. Boundary conditions are much more different to enforce than in the PDE model as they have to be expressed in the formalism of "events" as used by the next subvolume method.
The expression of $\boldsymbol{\alpha}$-factor was modeled by having it produced with a constant rate of $4000 molecs/s$ with an almost instantaneous export due to very high diffusion rates within the $MAT\boldsymbol{\alpha}$ cell. This corresponds to an unstimulated secretion of $\boldsymbol{\alpha}$-factor. In

order to obtain significant gradients of Bar1 and $\boldsymbol{\alpha}$-factor the viscosity of the volume between the cells (in the "world") was chosen as to be the same as in the yeast cytosol. Furthermore, we wanted to model the cells as being immersed into much larger empty volume than explicitly treated by the system. In order to do this we made the "end of world" compartment absorbing, meaning that any molecule entering it will not exit it anymore. We then created a reaction destroying any molecule x from this volume with a constant rate ($\mathbb{P}(destroy) = c \cdot x$). The constant was finally chosen to reproduce the $\boldsymbol{\alpha}$-factor and Bar1 profiles obtained from an analytical solution of constant secretion from a spherical volume into an infinite space. Any point with the distance d_C from the center of the emitting volume than has a local concentration $C(d_C)$ with

$$C(d_C) = \int_0^T \left[\frac{k_E}{2} \cdot \left(\operatorname{erf}\left(\frac{a - d_C}{2\sqrt{D \cdot t}} \right) + \operatorname{erf}\left(\frac{a + d_C}{2\sqrt{D \cdot t}} \right) \right) - \frac{k_E}{a} \sqrt{\frac{D \cdot t}{\pi}} \left(\exp\left(-\frac{(a - d_C)^2}{4D \cdot t} \right) - \exp\left(-\frac{(a + d_C)^2}{4D \cdot t} \right) \right) \right] dt, \tag{3.27}$$

where k_E is the secretion rate, D is the diffusion rate, a the radius of the emitting spheroid and T the time point at which the profile is taken [230]. The function erf denotes the Gaussian error function given by

$$\operatorname{erf}(x) = \frac{2}{\sqrt{\pi}} \int_0^x \exp(-t^2) dt. \tag{3.28}$$

Obviously the relation can be calculated independent of the actual secretion rate as it only enters the equation by a constant factor. We simulated the profiles with MesoRD and chose the constants which would reproduce the infinite profile obtained by the approximate analytical solution (F-test p-value $< 2 \cdot 10^{-16}$). With the model and the

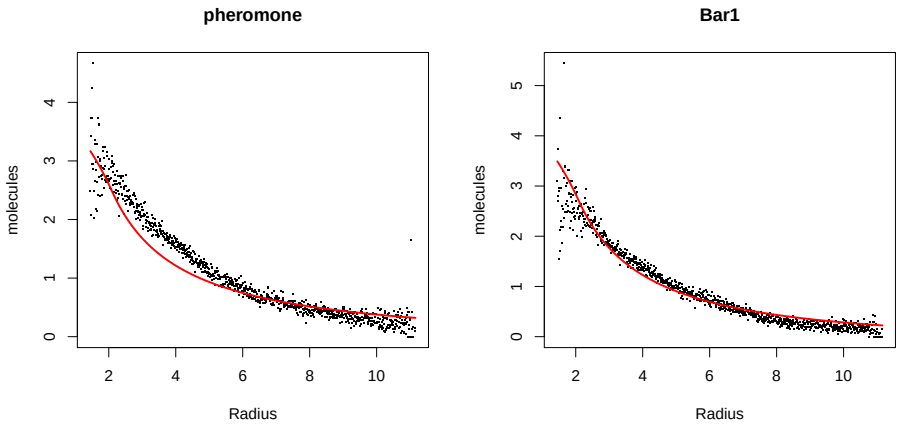

Figure 3.14: The approximation of the analytical solution by the outer boundary condition.

boundary condition defined we lacked only the initial condition for simulation. Overall molecule numbers were obtained from literature and are summarized in the appendix 6.2. The spatial distribution was obtained by an initial run were the molecules were

placed in arbitrary compartments without any reactions. This model was simulated until a steady state was reached. Continuing the simulation after the steady state, statistics for the abundance of each molecule in each compartment were obtained and used as initial state for all further simulations.
Simulation trajectories were generated for 6 different distances between the cells ranging from 0.5 to 6 μm and for a simulation time of 10 minutes. Each trajectory was obtained in 10 independent replicates. Those replicates were computed in parallel on a cluster since a single simulation would take almost a week to simulate. Output parsing was performed in Python (`http://www.python.org`) and statistical analysis in *R*. Visualization of the molecules in 3-D was obtained by parsing the MesoRD output via custom scripts in Python into ray shading scenes which were rendered in PovRay (`http://www.povray.org`).

Even with the model formulated, the question remained how well it would connect to real data. We employed a big amount of parameters and, even though we could derive them directly, it gives some insecurity how well the model connects to experimental data. Thus, we used an experimental data set, not included in our model construction to see how well the model performed. The data set employed was previously published and was particularly adapted to our model as it used a kinase-dead Fus3 mutant, thus, corresponding to our model which did not consider the MAPK cascade [231]. In order to account for the constant $\boldsymbol{\alpha}$-factor concentration used in the experiment we added $\boldsymbol{\alpha}$-factor which was not depleted by binding to the receptor[7], in the same concentration in the membrane compartment. It can be seen in figure 3.15 that the data corresponded well to the model simulation. Additionally, the noise of the measured data seems to be reconstructed by the model as well, as the measurement points lie within the confidence area of around 95%. As such we could now employ the model to study the dynamics

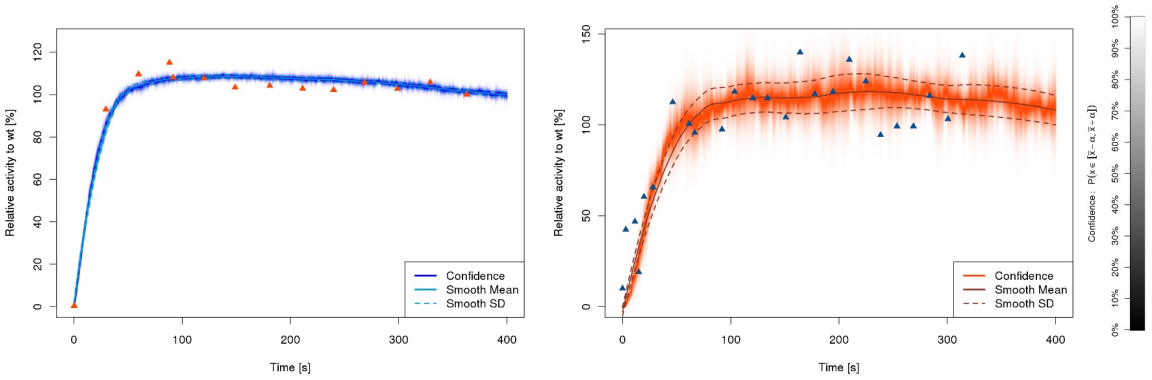

Figure 3.15: Validation of the model simulations using and independent data set from Yu et. al. (triangles, [231]). The dynamics and noise levels are correctly predicted by the model.

of the pheromone detection under varying distances of the $MAT\mathbf{a}$ and $MAT\boldsymbol{\alpha}$ cell.

[7]More precisely, the concentration of $\boldsymbol{\alpha}$-factor remained constant in the cell wall/membrane, which mimicked the constant concentration kept in the experiment.

3.3.2 Linear distance encoding and global noise reduction

In contrast to the constant external $\boldsymbol{\alpha}$-factor distribution (as in figure 3.15) where a plateau phase was reached within a minute, we observed that the small secreted gradients led to a different temporal behavior of the global activation. Here, the activation of receptors was gradually accumulating until reaching the plateau phase at the end of 10 minutes. This behavior was mirrored by the number of active $G_{\beta\gamma}$ molecules at the membrane and by the number of recruited Ste5 molecules. As observable in

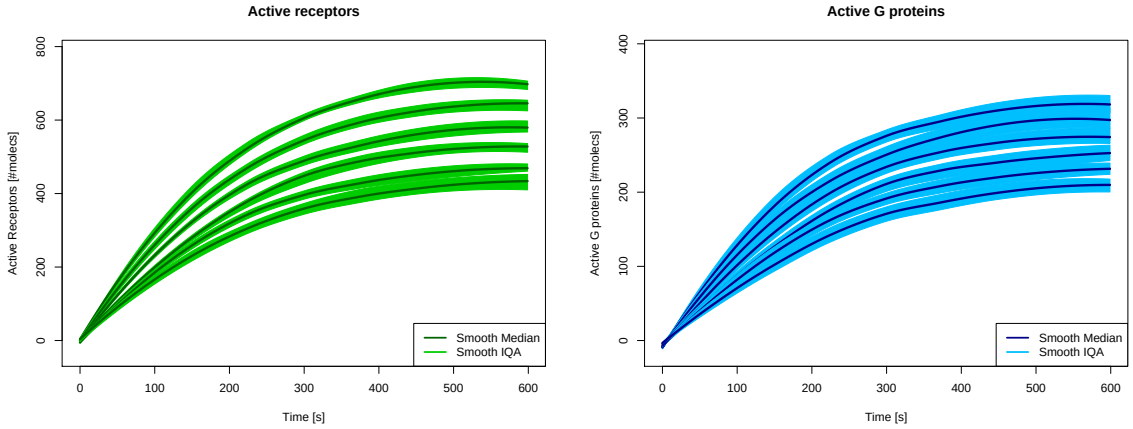

Figure 3.16: Activation profiles of key components in the pheromone detection. The six curves correspond to increasing cell distances from bottom (0.5 μm) to top (3 μm). Means and quartiles were smoothed by a sliding mean approach over the 10 replicates.

figure 3.16, the slower response seems to go along with a significant amplification of the signal. The different distances resulted in an average 5-20 $\boldsymbol{\alpha}$-factor molecules on the cell membrane at each time point, however, this lead to an activation of up to 750 receptors and 350 G proteins. It seemed that the signal was well separated in abundance, thus the activation curves of Ste2 could be distinguished between different distances. The question was now how this relates to the distances of the cells and the noise of the $\boldsymbol{\alpha}$-factor profile. For this we studied the statistics of the $\boldsymbol{\alpha}$-factor abundance on the membrane along with the abundances of the last 10 seconds of the plateau phase for Ste2, $G_{\beta\gamma}$, and Ste5. Figure 3.17 shows the results. We observed that on the level of $\boldsymbol{\alpha}$-factor it almost seemed as if any distance would lead to the same $\boldsymbol{\alpha}$-factor abundance at the cell membrane, in mean varying only by 5-10 molecules and having high noise levels. Global noise levels were strongly reduced on the level of the activated receptors. Here, the response was almost perfectly linear in the distances showing significant separation of the number of activated receptors by distance (see figure 3.17). This was also the case for the G proteins.
Thus, we concluded that the strong fluctuations in the number of $\boldsymbol{\alpha}$-factor molecules at the membrane are efficiently reduced by the receptors. This is achieved by accumulating the signal over time. The quality improvement acquired that way is passed on to the G protein, however not to the number of recruited Ste5 molecules. However, the activation of the MAPK cascade also depends on Ste20, whose activation depends again on $G_{\beta\gamma}$.
That indicated that $MAT\mathbf{a}$ cells collect signal over time in order to improve the reliability, a process that seems particularly helpful in shallow concentrations of $\boldsymbol{\alpha}$-factor.

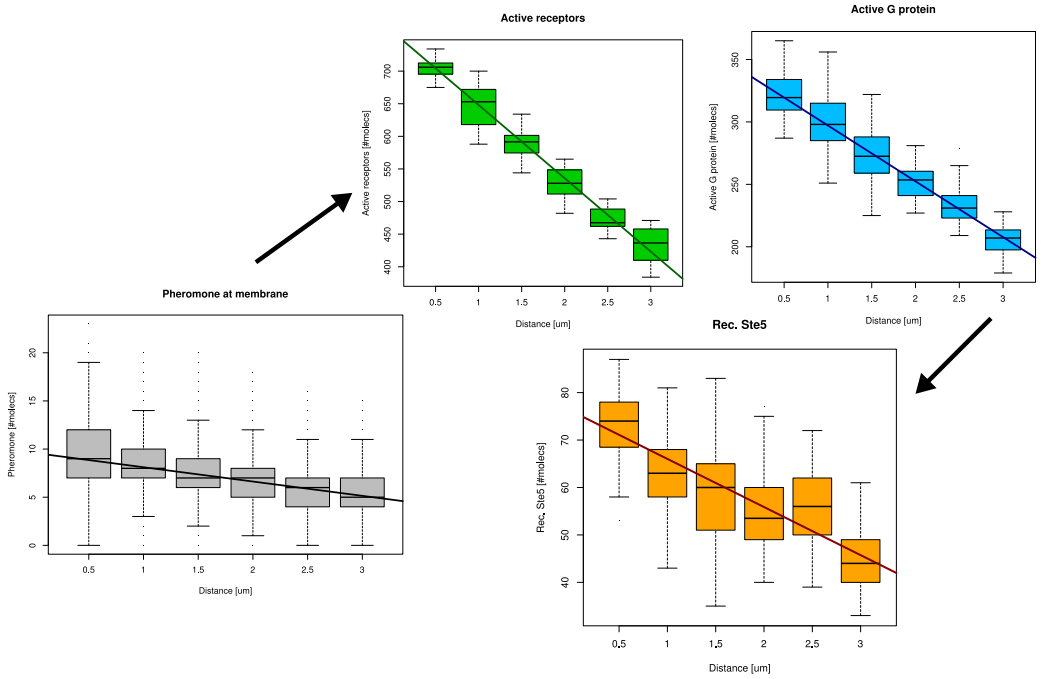

Figure 3.17: The distance is linearly encoded in the molecule abundances as shown by the regression lines. However, good separation is only achieved on the level of receptors and G proteins, whereas $\boldsymbol{\alpha}$-factor itself and G proteins show very high noise levels.

Thus, *MAT***a** cells employ a simple but effective noise reduction strategy, temporal signal accumulation on the level of the receptor, that allows for a linear encoding of the distance between mating partners in activated pathway components and enables reliable detection of cell distances smaller than 500 nm.

3.3.3 Local noise reduction and depletion

The observation that cell distances are encoded in the overall concentrations of signaling molecules raises the question why *MAT***a** cells do not employ the spatial distribution of $\boldsymbol{\alpha}$-factor in order to do this, but rather its total abundance over time. In order to investigate the reason for this, we studied the arising distributions of signaling molecules (gradients) at the membrane. Initial visualization lead to disperse distributions which seemed to vary only little with distance, which raised the question whether the spatial distributions were indeed the same (figure 3.18). In order to quantify the resulting gradients, we reduced the complexity by switching to a polar coordinate system. This was done by taking the imaginary line connecting the centers of the two cells as an "optimum" and calculating the angles between the vector emanating from the cell center of *MAT***a** cells to any molecule on its membrane and the optimum line. The gradient could than be quantified by the angular distribution of molecules, where a single peak at the zero angle would indicate complete polarization on the point closest to the *MAT*$\boldsymbol{\alpha}$ cell. Analogously, a uniform distribution would indicate a completely dispersed distribution over the cell membrane and, thus, the absence of polarization. Gradients were then visualized by binning the angles and calculating the average number of molecules in the cubes corresponding to a single bin over all replicates. Finally,

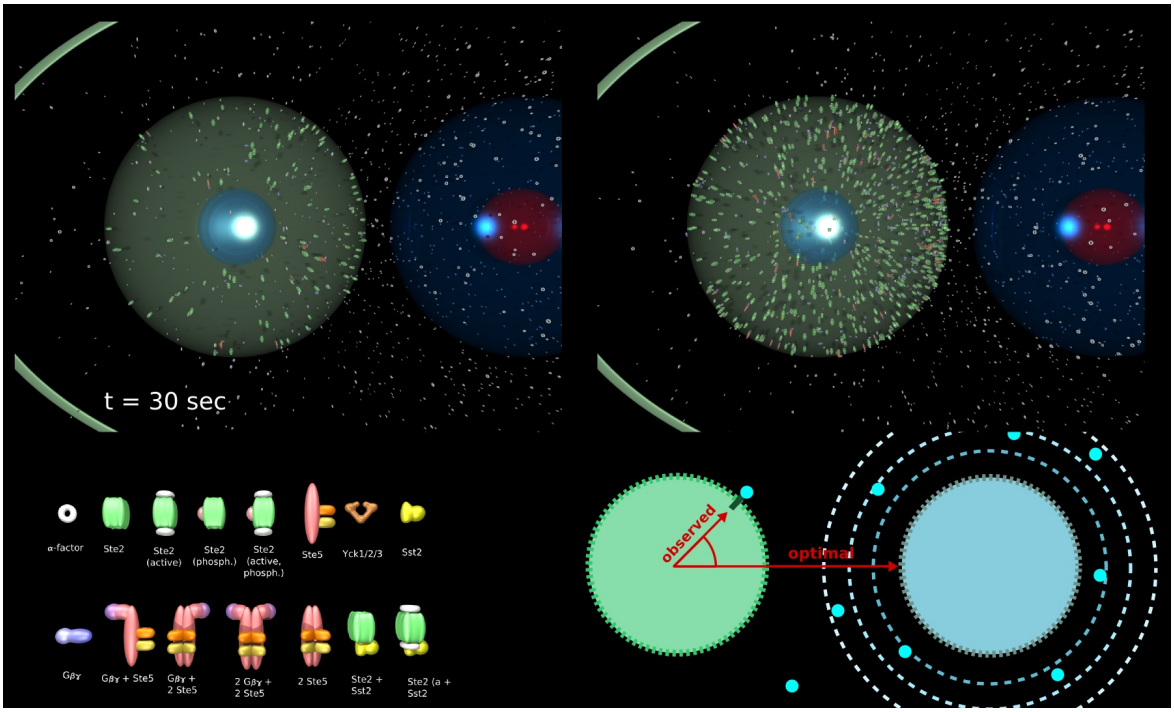

Figure 3.18: Three dimensional rendering of simulation output. Setup shown here is for a cell distance of 0.5 μm, but the spatial distribution varied only little with distance. The illustration in the lower right shows the calculation of angles used to quantify the gradients.

in order to make the angular distribution comparable between different molecules, we divided those numbers by its integral to obtain distributions. The angular distribution of $\boldsymbol{\alpha}$-factor was non-discernible in different distances. This was also true for active receptors, G proteins and recruited Ste5 molecules. Why does the accumulation of signal on the level of Ste2 receptors not increase the detection of gradients? We observed that the effect of accumulation on a local level in space was counteracted by the local depletion of non-active receptors. As such, locations on the yeast membrane of $MAT\mathbf{a}$ cells were quickly running out of remaining non-activated Ste2 receptors (see appendix figure 6.7). Local depletion, thus, seemed to be the reason that gradients are only a poor indicator of the distance to the $MAT\boldsymbol{\alpha}$ cell, which makes it more efficient to use total concentrations.
Even though, the mean angular distribution did not vary over different distances we observed a strong local noise reduction. This was quantified by calculating the angular distribution as before but now calculating the noise level η_M for a molecule M in each cube c given by

$$\eta_M = \frac{\sqrt{\mathbf{Var}(M_c)}}{\langle M_c \rangle}. \tag{3.29}$$

Normally, one desires a noise level where the standard deviation is significantly smaller than the mean, thus $\eta < 1$.

We observed a noise level bigger than one for $\boldsymbol{\alpha}$-factor which dropped strongly as the signal was passed to the receptors and G proteins, stabilizing the gradient (figure 3.20). Interestingly, noise levels were not constant in space but rather varied with location.

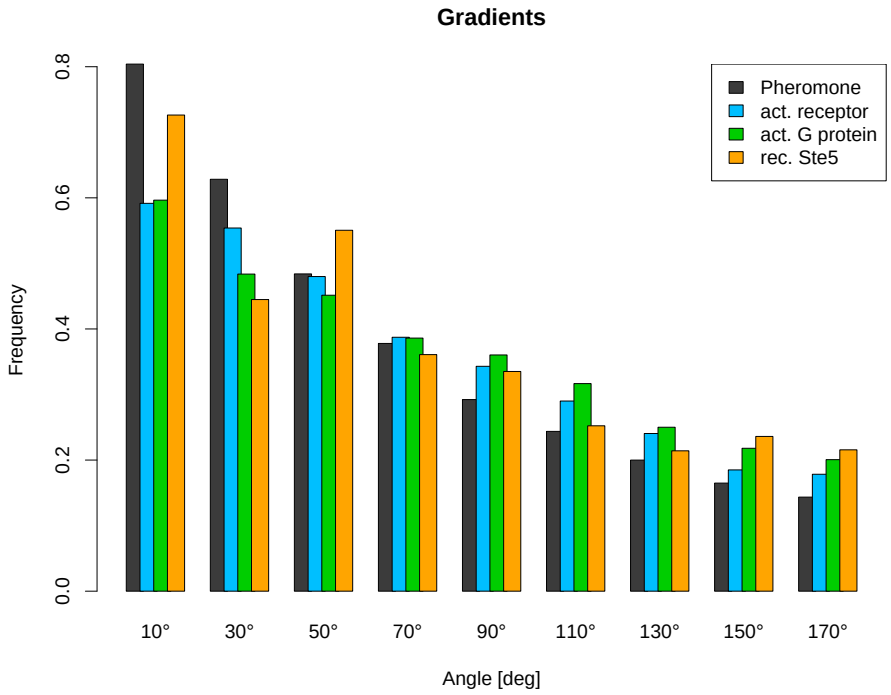

Figure 3.19: Angular distributions of key components in the pheromone detection system at a cell-to-cell distance of 0.5 μm.

3.4 Multi-protein complexes and polarization

As we have observed in the previous section, gradients are transmitted accurately from the extracellular environment into the distribution of active receptors and $G_{\beta\gamma}$ on the cell membrane. However, this transmission is preserving and shallow gradients will result in shallow differences in the membrane distributions of those compounds. When looking at markers for the distribution of polarisome complexes, however, we observe a quite different picture. Here even uniform $\boldsymbol{\alpha}$-factor distributions can induce a massive condensation of the membrane distribution as indicated in figure 3.21A. It is known that positive feedback loops in polarization can induce stable symmetry breaking (see section 1.4.4). But what induces the strong polarization? In order to study this phenomenon we did not construct a detailed model. Rather, we reduced our research to the basic principles that form the polarisome.
We have introduced the processes forming the polarisome in yeast in section 1.4.4. The polarisome is mostly formed by the recruitment and activation of proteins to precursor components. Those proteins can either be membrane-bound before recruitment or tethered to the membrane upon presence of the signal, as it is the case for key components like Far1, Cdc24 or Cdc42. The recruited components then interact to induce further activation and formation of the polarisome. Thus, the basic motif used here is the activation of proteins during presence of an extracellular signal and their posterior interaction. The most basic structure of such a system is shown in figure 3.21B. It consists of a model that considers only the activation and interaction of effector proteins. Here, proteins are either pre-bound to the membrane and activated directly (direct model), or are recruited from the cytosol to the membrane, which induces activation

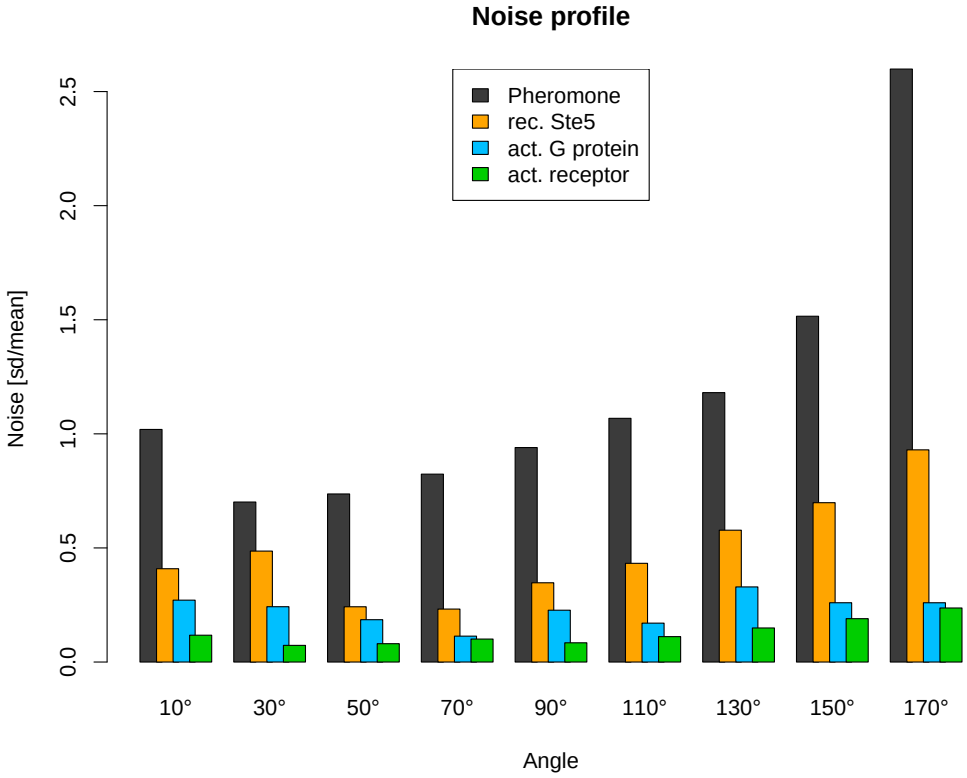

Figure 3.20: Local noise levels for the key components of the pheromone detection.

(recruited model).

3.4.1 The motifs promoting complex formation

We have seen that complexes can be formed by direct or recruited activation. The most simple motifs are the ones where only two components interact. We will denote those two components as A and B, and the extracellular signal the cell is exposed to as $S(x,t)$[8]. For the direct model this leads to the following set of reactions

$$A \underset{k_2}{\overset{k_1 S}{\rightleftarrows}} A^{on} \qquad B \underset{k_4}{\overset{k_3 S}{\rightleftarrows}} B^{on} \qquad A^{on} + B^{on} \underset{k_6}{\overset{k_5}{\rightleftarrows}} AB^{on}, \tag{3.30}$$

where the "on" state denotes the active state of the molecules. As we are interested in the basic processes, we will treat those reactions on a crude representation of a cell membrane/cell wall, represented by a circular shape in the xy-plane. This corresponds, for instance, to a cut through a cell in the xy-plane. We assigned a cell a constant radius r which allows us to reduce the dimensionality to a 1-D problem by switching to polar coordinates. This allows the space to be treated as a line with circular boundaries as illustrated in figure 3.22. This now implies the following set of reaction-diffusion

[8] As before the extracellular signal is a function of time t and space x.

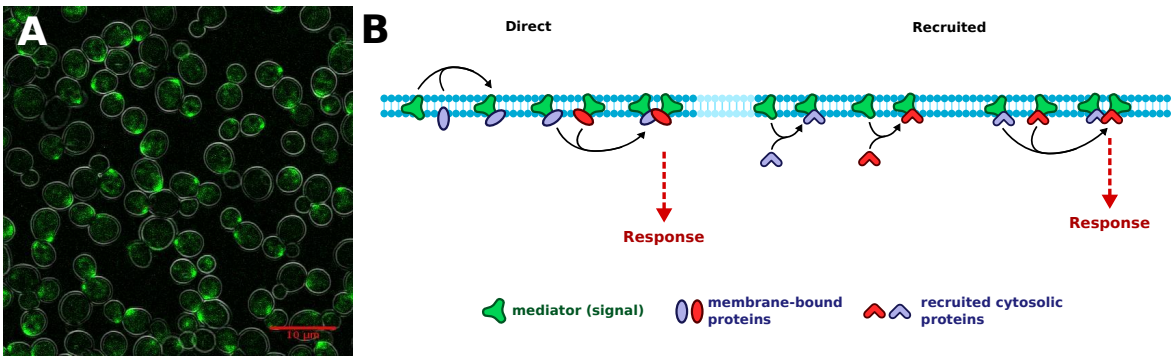

Figure 3.21: (A) Wild type *MAT***a** carrying a Fus1-GFP marker. Fus1 is recruited to the polarisome before conjugation. The cells were subjected to a uniform concentration of 25 μM of $\boldsymbol{\alpha}$-factor for 1 hour. (B) The basic processes governing the construction of the polarisome.

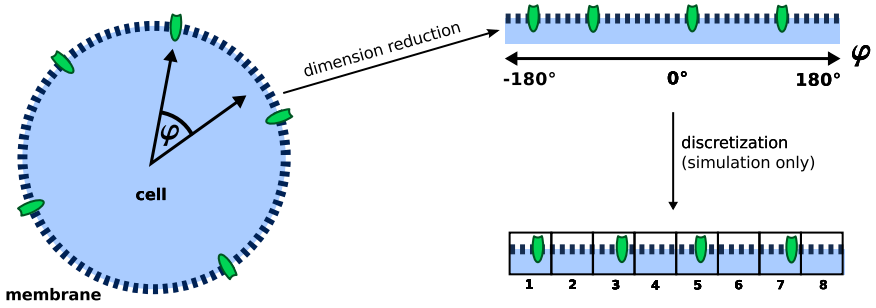

Figure 3.22: The simplifications applied to reduce the dimensionality of the space.

equations for the direct model [9]:

$$\frac{\partial A(x,t)}{\partial t} = k_2 A^{on}(x,t) - k_1 A(x,t) S(x) + D_A \Delta A(x,t) \tag{3.31}$$

$$\frac{\partial A^{on}(x,t)}{\partial t} = k_1 A(x,t) S(x) + k_6 A B^{on}(x,t) - k_2 A^{on}(x,t) - k_5 A^{on}(x,t) B^{on}(x,t) + D_A \Delta A^{on}(x,t) \tag{3.32}$$

$$\frac{\partial B(x,t)}{\partial t} = k_4 B^{on}(x,t) - k_3 B(x,t) S(x) + D_B \Delta B(x,t) \tag{3.33}$$

$$\frac{\partial A^{on}(x,t)}{\partial t} = k_3 B(x,t) S(x) + k_6 A B^{on}(x,t) - k_4 B^{on}(x,t) - k_5 A^{on}(x,t) B^{on}(x,t) + D_B \Delta B^{on}(x,t) \tag{3.34}$$

$$\frac{\partial A B^{on}(x,t)}{\partial t} = k_5 A^{on}(x,t) B^{on}(x,t) - k_6 A B^{on}(x,t) + D_{AB} \Delta A B^{on}(x,t) \tag{3.35}$$

[9] Since we only consider a single angular dimension, the Laplace operator is given by: $\Delta f(x,t) = \partial^2 f(x,t)/\partial x^2$.

with the boundary conditions

$$A(-\pi r, t) = A(\pi r, t) \qquad B(-\pi r, t) = B(\pi r, t) \qquad A^{on}(-\pi r, t) = A^{on}(\pi r, t) \tag{3.36}$$

$$B^{on}(-\pi r, t) = B^{on}(\pi r, t) \quad AB^{on}(-\pi r, t) = AB^{on}(\pi r, t) \tag{3.37}$$

and initial conditions

$$A(x, 0) = A_0 \qquad B(x, 0) = B_0 \qquad A^{on}(x, 0) = B^{on}(x, 0) = AB^{on}(x, 0) = 0 \tag{3.38}$$

for some arbitrary $S(x)$. The reactions of the recruitment model are essentially the same as the in the direct model with the difference that the proteins A and B are cytosolic and are recruited to the membrane in a signal-dependent manner. Recruitment to the membrane than enables formation of the AB^m heteromer.

$$A \underset{k_2}{\overset{k_1 S}{\rightleftarrows}} A^m \qquad B \underset{k_4}{\overset{k_3 S}{\rightleftarrows}} B^m \qquad A^m + B^m \underset{k_6}{\overset{k_5}{\rightleftarrows}} AB^m$$

The resulting reaction-diffusion equations are exactly same as in the direct model except that the diffusion rates of the free A and B proteins are now cytosolic diffusion rates D_A^c and D_B^c. The boundary and initial conditions are equivalent to the direct model. As such the major difference between the two mechanisms is given by the differences between the cytosolic and membrane diffusion rates of the free proteins. However, this difference may have large impacts, since those diffusion rates usually differ by two orders of magnitude [as measured in 232].

The resulting system was mostly treated by analyzing the steady state solution which could be derived analytically for the simple model (see appendix 6.1). We preferred this strategy, because the parameters were mostly unknown and by solving the steady state analytically one could observe how they influence the response. Additionally, we also simulated the model for some particular sets of parameters in order to validate the results obtained by the analytical solution. To this end we first discretized the space by decomposing it into $n = 100$ intervals with respective lengths $h = 2\pi r/n$. For each interval i we treated the system state as a vector of constants $\mathbf{Y}$. The Laplace operator was approximated by central differences which yielded

$$\Delta \mathbf{Y}_i \approx \frac{1}{h^2}(\mathbf{Y}_{i-1} - 2\mathbf{Y}_i + \mathbf{Y}_{i+1}).$$

The resulting ODEs were solved numerically with the *deSolve* package within the scripting language *R*. We applied the *lsode* method with a rearranged system yielding a banded Jacobian [233, 220]. As input signals we used triangular, rectangular, cubic and Gaussian shapes with varying width parameters w. The detailed descriptions of those shapes can be found in appendix 6.1.

3.4.2 Complex formation enables increased polarization

Analytically solving the steady state for the reaction-diffusion model provided expressions for the spatial distribution of the downstream effectors upon activation of the motif. Here, the monomers showed a spatial distribution according to

$$A^{on}(x) = \frac{a \cdot S(x)}{b + c \cdot \frac{D_A}{D_A^*} \cdot S(x)} \tag{3.39}$$

where a, b, c are constants composed of the kinetic rates and initial conditions and $\frac{D_A}{D_A^*}$ is the ratio of diffusion rates for the active (or recruited) protein and the inactive (or free) protein (again a detailed derivation can be found in appendix 6.1). An equivalent formula holds for the B^{on} monomer. Relationship (3.39) describes a hyperbola depending on the local value of $S(x)$. Its behavior will be greatly influenced by its parametrization and can be divided into two general classes.
In the presence of high local signal concentrations $S(x)$, it will show a saturation effect. Mechanistically, this can again be explained by the local depletion of of non-active proteins, since most proteins in the vicinity of a strong signal concentration will be in their active state. In that case the steady state expression for the concentration of active protein complexes takes a rather complicated form with

$$AB^{on}(x) = \frac{1}{2}p(S, x, \mathbf{k}) - \sqrt{\frac{1}{4}p(S, x, \mathbf{k})^2 - q(\mathbf{k})}. \tag{3.40}$$

$p(S, x, \mathbf{k})$ is a non-trivial function, composed of the signal function $S(x)$ and the parameters $\mathbf{k}$, and $q(\mathbf{k})$ is a constant function depending on the parameters $\mathbf{k}$.

In case the signal concentration is globally low, saturation of the curve is not achieved and local depletion will not occur, since only a small fraction of the proteins will be in the active state. The expression for the active protein complexes now simplifies to

$$AB^{on} = d \cdot S(x)^2, \tag{3.41}$$

with a constant d composed of the kinetic rates and initial conditions. This resembles a high-pass filter since the quadratic term will suppress the signal at positions x with a low signal concentration and amplify it at positions x with a high signal concentration.

It can be seen from equation (3.39) that the sensitivity to local depletion is strongly influenced by the ratio of diffusion rates. In case the proteins are also membrane-bound in their inactive forms the diffusion ratio will be close to one, enabling strong local depletion. However, in case the proteins are cytosolic and recruited to the membrane during activation, the ratio of diffusion rates will become negligible. Thus, recruitment of cytosolic proteins to the membrane upon activation will abolish the effect of local depletion due to their fast diffusion rates.
This effect is also confirmed by numerical simulations of the models. In the direct model the analytical steady state approximations agree with the simulation results, showing a strong local depletion of free monomers during complex formation of membrane-bound proteins, which leads to a less defined distribution of active monomers. On the level of active complexes, however, the effect of local depletion is counteracted and the spatial distribution resembles that of the initial signal (see figure 3.23). This is also reflected in the activated membrane area. 95% of the signal covers 67% of the membrane, whereas 95% of the active monomers cover 75% of the membrane and the active complexes cover only 59% of the membrane.
As predicted, simulations of the recruitment model, where complexes are formed from recruited cytosolic proteins, abolishes local depletion. Due to the linear relationship this leads to a distribution of active monomers which resembles the distribution of the signal, whereas the active complexes show a sharper spatial distribution than the signal. Thus, the active monomers, as well as the signal, cover 67% of the membrane,

whereas the active complexes cover only 49%. This effect presents a sharpening in the local distribution from monomers to complexes.

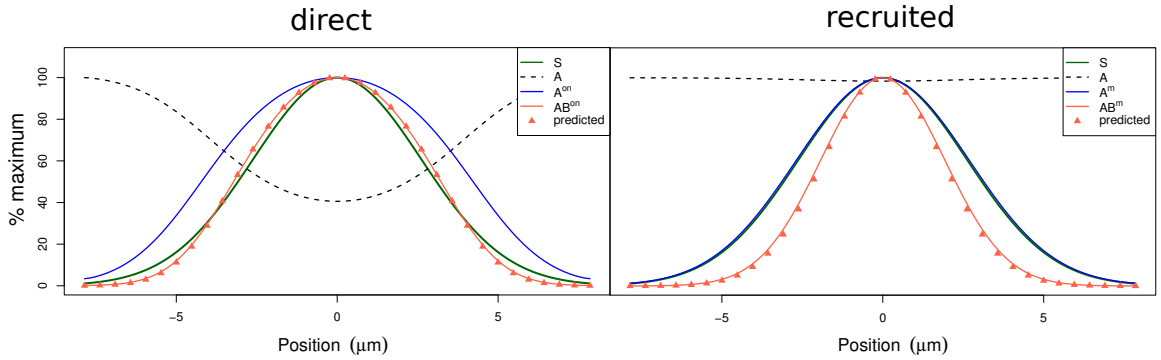

Figure 3.23: Simulation of the reaction-diffusion systems. The steady state approximation is shown in triangles. Chosen parameters: $r = 2.5\mu m, w = \pi r/3, A(x,0) = B(x,0) = 1, A^{on}(x,0) = B^{on}(x,0) = AB^{on}(x,0) = 0, k_1 = 8, k_2 = 1, k_3 = 0.5, k_4 = 1, k_5 = 10, k_6 = 1, k_7 = 1, k_8 = 1$. Diffusion rates are $0.05\mu m^2 s^{-1}$ in the direct model and $5\mu m^2 s^{-1}$ for cytosolic proteins in the recruited model.

3.4.3 Gradient-response encoding

The nonlinearity introduced by the complex formation also has another consequence for the formation of the complexes. For any linear kinetic the total response $\mathcal{R}_{tot}$ in steady state will depend on the signal S_{tot} in a linear form, thus, the overall response $\mathcal{R}_{tot}(S, x)$ is given by

$$\mathcal{R}_{tot}(S) = \int_{-\pi \cdot r}^{\pi \cdot r} a \cdot S(x) dx = a \cdot S_{tot}. \tag{3.42}$$

Thus, it is independent of the signal width w and, in consequence, also independent of the gradient. However, in the case of complex formation, this does not hold. For the recruited model, we found that the responses of the active complexes AB^{on} are inversely proportional to the signal width w for all three signal shapes with

$$\mathcal{R}_{tot}(S) = k_P \cdot k_S \cdot \frac{1}{w}, \tag{3.43}$$

where k_P is a constant which arises from the kinetic parameters and initial concentrations of the model and k_S is a constant determined by the type (shape) of the signal $S(x)$ (the mathematical derivation can be found in the appendix 6.1). Since w^{-1} is monotonously decreasing in w, a decrease in the signal width leads to an increase in the response facilitated by the complexes (see figure 3.24). In the direct model one can again observe that local depletion counteracts this effect on the sites of large signal S again, which leads to a peak-and-decline behavior. Here the expressions could not be calculated analytically, but were obtained by integrating the steady state solution numerically. One should note that this form is exactly the same found for the receptor and G protein complexes in the previous section (compare figure 3.19), indicating that this relation between gradient and response is ubiquitous for local depletion. In gen-

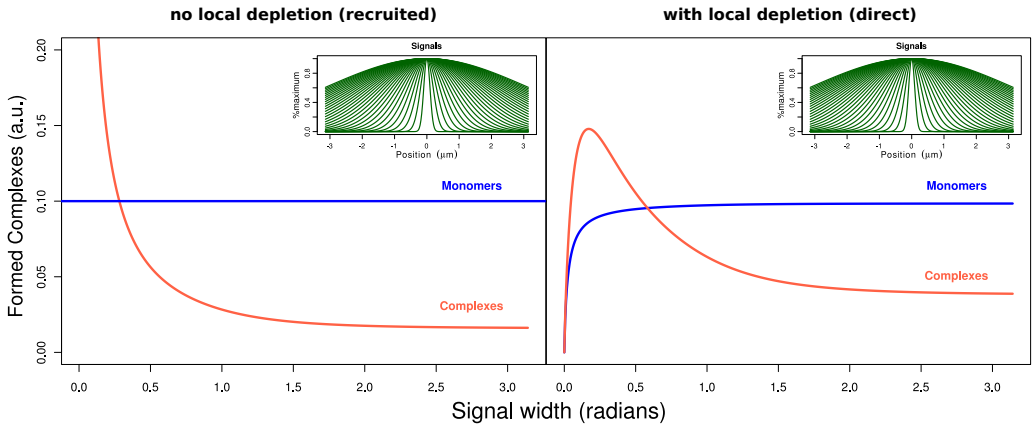

Figure 3.24: The relation between signal widths and the amount of formed complexes. Numbers represent the fraction of of initial A and B molecules bound in complexes.

eral, we found that for any complex formation, the response will scale inversely with the signal width, thus encoding the shape of the response and steepness of the signal gradient into the number of formed complexes. I will denote this property *gradient-response encoding*. We found gradient-response encoding with the same form for all three signal shapes analyzed here (see appendix figure 6.1).

3.4.4 Combination of the motifs leads to exponential polarization

We have observed that a single complex formation is capable of inducing an enhanced polarization. Thus, we now investigated the question whether combination of this motifs can induce the point-like polarization observed in the yeast cells as in figure 3.21. We considered two general forms of motif combination, summarized in figure 3.25. In the first mechanism, called *stacking*, formed complexes serve as enzymes for the formation of a different complex, for instance by a phosphorylation or acting as an activator for a GTP exchange. Alternatively, the complexes can also participate in the formation of a multi-protein complex by directly forming a large complex from several heteromers. We call this *coupling*.
Stacking of the motifs means that already formed complexes form even higher order complexes. Considering, for instance, two complexes AB^{on} and XY^{on} with steady state responses (according to the appendix 6.1)

$$AB^{on} = k_1 \cdot A_0 B_0 S(x)^2 \tag{3.44}$$
$$XY^{on} = k_2 \cdot X_0 Y_0 S(x)^2, \tag{3.45}$$

formation of a higher order complex $ABXY^{on}$ leads to a response

$$ABXY^{on} = k_3 \cdot AB^{on} XY^{on} = k_3 A_0 B_0 X_0 Y_0 \cdot S(x)^4. \tag{3.46}$$

Repeated stacking of responses will lead to a general response $\mathcal{R}(x)$ with

$$\mathcal{R}(x) = \alpha \cdot S(x)^K, \tag{3.47}$$

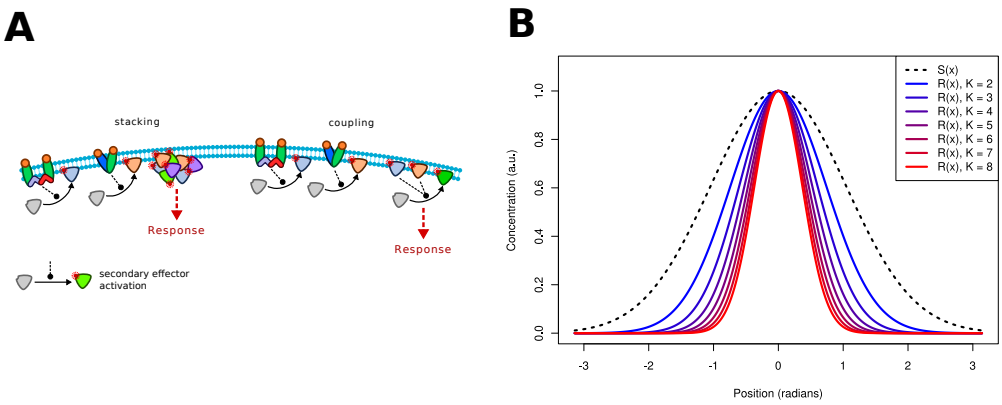

Figure 3.25: (A) the considered mechanisms of motif combination. (B) The resulting amplified polarization, due to the exponential dependence on the signal S, here exemplified for a Gaussian signal.

with a constant α, which comprises the kinetic parameters and initial concentrations, and a response degree K which denotes the number of individual proteins bound in the complex.

During coupling several different effectors E_i are activated by independent complex formation motifs each having a specific response $\mathcal{R}_i$ according to equation 3.47 with

$$\mathcal{R}_i = \alpha_i \cdot S^{K_i}. \tag{3.48}$$

If all those different effectors participate in a joint reaction producing a substance C, thus

$$E_1 + E_2 \ldots + E_N \underset{k_8}{\overset{k_7}{\rightleftarrows}} C, \tag{3.49}$$

this leads to the following reaction-diffusion equation for C:

$$\frac{\partial C(x,t)}{\partial t} = k_7 \prod_{i=1}^{N} E_i - k_8 A + D_C \Delta C(x,t). \tag{3.50}$$

This system has the steady state

$$C(x) = \frac{k_7}{k_8} \prod_{i=1}^{N} E_i + \frac{D_C}{k_2} \Delta C(x) \tag{3.51}$$

$$\rightarrow C(x) = \frac{k_7}{k_8} \left(\prod_{i=1}^{N} \alpha_i \right) \cdot S^{\sum_{i=1}^{N} K_i} + \frac{D_C}{k_8} \Delta C(x) \tag{3.52}$$

As such the degree of the response will be the sum of degrees of the individual effectors with the same form as in stacking the motifs.

Consequently both mechanisms to combine the motifs lead to an exponential dependence on the signal S. This results in a strong amplification at locations where the signal is high, but a diminishing response at sites with low signal, resulting in a strong

polarization which may become point-like. However, the strong amplification will also result in a spontaneous amplification of random fluctuations of the signal, which explains the observed spontaneous polarization occurring in *MAT***a** cells exposed to uniform $\boldsymbol{\alpha}$-factor concentrations. As our motifs do not inherit a intrinsic ability to unite individual polarisome complexes, however, we can not explain why only a single polarisome is formed. To some extent this is controlled by the low number of formed polarisome complexes, due to the gradient-response encoding. However, additional mechanisms are necessary to assure convergence to a single polarisome. This was not scope of our work, but we will briefly mention this topic again in the discussion.
The central result of this section is that the formation of multi-protein complexes does inherit a strong polarization of those complexes on the membrane and, furthermore, induces a higher number of formed polarisomes specifically in the presence of strong signal gradients. This effect may be counter-acted by local depletion of membrane-bound complexes, which is avoided by rather recruiting key components from the cytosol, where the fast diffusion assures availability.

4 Discussion

4.1 Conclusions

In the beginning of this thesis I motivated the use of Systems Biology as a way to to gain some new understanding of a prototypical signaling pathway. So what have we learned about the signaling in yeast? In a first part we looked at the very basic prerequisite of signaling itself, the signal. To that extent we studied the phenomenon that *MAT***a** cells of budding yeast actively alter their extracellular signaling environment through the secretion of a protease that acts in the extracellular space by destroying $\boldsymbol{\alpha}$-factor. As we have seen, this strongly alters the characteristic of the signal, resulting in an apparent quality gain. Not only does the information content of the signal increase, but regulated signal degradation also allows for the coordination of signaling with growth. This is achieved by restricting $\boldsymbol{\alpha}$-factor to distinct local regions in space, corresponding to locations with high local cell densities. As we have shown, this strategy is very beneficial because the diploid formation is particularly efficient in those regions as the cells are very close. The remainder of the population is left to continued growth, probably a good decision as those cells are to far apart to conjugate. This is done on the cost of a lower abundance of signaling molecules in the extracellular medium, resulting in a small range $\boldsymbol{\alpha}$-factor levels spanning approximately 15 nM.

$\boldsymbol{\alpha}$-factor efficiently encodes spatial information about the cell culture which is realized by restricting it in space. The degradation by an additionally secreted protease is a metabolically cheap strategy to achieve that. This becomes clear when looking at the alternative mechanisms to achieve the same outcome. In the original work of Turing, spatial inhomogeneities were created by differences in diffusion rates [144]. In fact, a restricted distribution of $\boldsymbol{\alpha}$-factor can be achieved by slow diffusion. However, the diffusion rate is governed by the viscosity of the medium and the size of the protein. Thus, lowering the diffusion rate to the necessary value, the $\boldsymbol{\alpha}$-factor oligopeptide would have to be substituted by a much larger protein which would be very costly for *MAT***a** cells. The secretion of Bar1 is a much efficient mechanism mainly due to two reasons. First, a single Bar1 molecule may degrade many $\boldsymbol{\alpha}$-factor molecules consecutively. Second, because Bar1 is a quickly diffusing molecules it is shared between all the *MAT***a** cells in the cell population, which essentially results in an accumulation of the individually secreted Bar1 concentrations. As thus, the *MAT***a** populations may jointly create Bar1 concentrations which are by a factor of 1000 higher than what could be produced by a single cell, resulting in a mutual benefit.

However, the low concentration of $\boldsymbol{\alpha}$-factor molecules resulting from its degradation by Bar1 also has a negative consequence: the introduction of noise. The presence of few $\boldsymbol{\alpha}$-factor molecules on the *MAT***a** cell membrane together with its fast diffusion converts it into a highly fluctuating signal. Consequently, yeast cells had to adapt

to make reliable decisions based on this noisy signal. I have demonstrated that this is achieved by very simple mechanism where the $\boldsymbol{\alpha}$-factor signal is collected by the Ste2 receptors over a short time interval. As this, results in many activated receptors, even in the presence of few $\boldsymbol{\alpha}$-factor molecules, the noise decreases. This leads to a linear relation between the number of activated receptors and G proteins between and the distance between the perceiving *MAT***a** cell and a potential *MAT*$\boldsymbol{\alpha}$ partner cell. This relation is very exact and leads to distinguishable differences in activation for distances differing by less than 500 nm. The spatial distribution of $\boldsymbol{\alpha}$-factor molecules, and consequently also of active receptors and G proteins, does only differ mildly with the distance between the cells. As such, it seems as yeast cells have adapted to rather use the concentration of $\boldsymbol{\alpha}$-factor as a measure of the distance to the nearest mating partner. As described by others, and also observed by us, the activation of pheromone-dependent gene expression has a sigmoidal dependence on the logarithm of the extracellular $\boldsymbol{\alpha}$-factor concentration (compare [231, 66] and section 3.2). This gives a switch-like dependence of pathway activation on the distance of the cells, where the pheromone response is induced by passing a threshold distance to the nearest *MAT*$\boldsymbol{\alpha}$ cell. This is also due to the fact that gradients can not be recovered with complete accuracy from the environment, a consequence of the local depletion of sensing molecules such as the Ste2 receptor and G proteins.

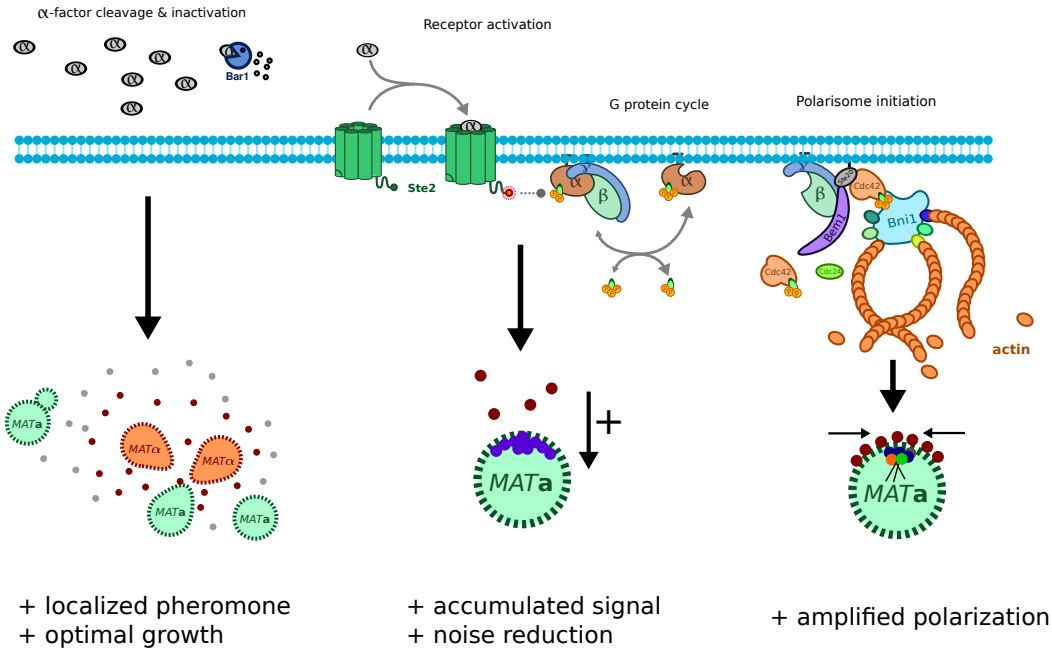

Figure 4.1: The functional interpretation of different parts of the pheromone response as obtained in this thesis.

Detection of the extracellular signal is followed by a strong polarization on the membrane even in the presence of shallow gradients. Our results indicate that this is a consequence of the formation of multi-protein complexes at the membrane, the polarisomes. The positive feedbacks intrinsic to this process can concentrate polarisomes to a small region corresponding to the direction of the mating partner. Local depletion can be avoided here by recruiting polarisome components from the cytosol rather than the membrane because the fast cytosolic diffusion enables availability of

the entire pool of recruitable molecules. The formation of those polarized structures also takes place preferentially in the presence of signal gradients where the number of formed complexes is anti-proportional to the signal width. During microscopy we have observed that this strong polarization is indeed observed *in vivo* and results in a single polarisome. The convergence of individual polarisome to a single structure was not investigated, but seems to be a consequence of components which we have not considered here. Probable suspects converging the polarisome into a single super-structure are actin cables formed from the individual polarisome and protruding into the cell (recall section 1.4.4). This creates directed transport of polarisome components along the cables. Molecular transporters can jump between actin cables, but this jump might have higher probability of success when actin cables are parallel. Thus, the transport will be preferential into directions where already several polarisomes cluster. Another mechanism could be given by the resulting forces. The actin cables formed from the individual polarisomes can be compared to individual ropes connected to a metal ring. As the polarisome start to integrate new membrane into the cell wall, the cell begins to grow due to the shmoo formation. This corresponds to pulling the ropes connected to the metal ring all at once, which will result in convergence to a single point.

4.2 The evolution of intercellular signaling: talking yeasts

In this thesis I have spent a large amount of time on the communication taking place in cell populations of yeast. In the field it is still accepted almost dogmatically that the extracellular signaling environment is basically passive. That means it is believed that *MAT***a** cells secrete the pheromone $\boldsymbol{\alpha}$-factor, providing the signal, and *MAT*$\boldsymbol{\alpha}$ react to this constant and basically unchanged signal, and *vice versa*. In this thesis, we have seen that this is not the case. In an initial state *MAT***a** cells and *MAT*$\boldsymbol{\alpha}$ cells do secrete basal levels of $\boldsymbol{\alpha}$-factor and **a**-factor, but this is by no means the end of the story. Both cells will induce a higher secretion level in the presence of pheromone of the opposing mating partner and particularly *MAT***a** cells highly regulate the extracellular signaling environment by secreting Bar1. This makes signaling in yeast different from bacteria, where signaling is usually governed by basal secretion and a global detection of signaling molecules. Thus, we can observe an evolutionary leap in the complexity of the signaling environment formed by the cells from bacteria to the simple eukaryote yeast. This leap was probably enforced by the necessity to coordinate responses in a spatial manner in a population. An argument for this is found in the bacterium *Dictyostelium discoideum*. *Dictyostelium* is a bacterium which is capable of forming a super-organism from many identical cells. The formation of this multicellular structure is coordinated by the secretion and detection of cAMP. Similar to yeast, *Dictyostelium* regulates this signal through degradation by several phophodiesterases (PDEs), which can be found in membrane-bound and secreted forms [234, 235]. As thus, it might be that Bar1 has evolved from an initially membrane-bound form to a secreted form. The benefit of this behavior is the cooperative accumulation of Bar1 in the medium which allows the cells to save resources and to secrete individually small amounts of Bar1. Additionally, since yeast in nature can switch its mating type spontaneously during budding mixed haploid populations probably consist of equal fractions of *MAT***a** and

MAT$\boldsymbol{\alpha}$ cells. As a consequence, due to the cooperative secretion of Bar1, the level of Bar1 activity will scale with the number of *MAT*$\boldsymbol{\alpha}$ cells. Bar1 is also regulated by the activity of the pheromone response in *MAT***a** cells and, thus, adapts depending on the perceived concentration of $\boldsymbol{\alpha}$-factor.
But how can the cooperative secretion of Bar1 prevail in evolution, even though it can be exploited easily by "cheater" cells which do not secrete Bar1 but benefit from the Bar1 secreted by other cells? This can be explained from the nature of yeast mating. In the beginning of this thesis we have introduced the life cycle of *Saccharomyces cerevisiae* (see figure 1.2). Haploid cells do normally occur only in populations awakening from spores. As thus, few spores form local populations of *MAT***a** and *MAT***a** cells, and because yeast does not employ chemotaxis, populations arising from budding of a single haploid progenitor will remain close. As a consequence, cells sharing Bar1 are likely to be genetically related. On the other hand, offspring from a "cheater" progenitor will also be cheaters and, therefore, there will be no Bar1 activity, resulting in loss of growth and a clear evolutionary disadvantage[1]. This process is commonly known as *kin-selection* and is indeed a condition in which cooperative behavior can arise stably [236, 237].

However, *Saccharomyces cerevisiae* also takes a special place in the kingdom of yeasts, since it forms diploids independent of the presence of starvation conditions. As such, *Saccharomyces cerevisiae* already adapts to a potential future lack of nutrients, even though this condition may never arrive. Thus, budding yeast cells *anticipate* a future lack of nutrients by already converting part of the culture into a protected state. Probably for that reason it is so important to perform this transition without drawing resources from normal cell growth or metabolism. This gives a possible explanation why *Saccharomyces cerevisiae* invests intricate mechanisms to ensure growth during the formation of diploids.

Given the entire knowledge we have about the formation of the extracellular signaling environment in budding yeast, we can derive the following sequence of events. In a newly formed haploid culture both haploid cell types initially secrete small amount of pheromones and *MAT***a** cells also a basal amount of Bar1. Because **a**-factor is not degraded by an extracellular protease like Bar1, it will accumulate rapidly. This leads to an initial induction of the pheromone response in *MAT*$\boldsymbol{\alpha}$ cells and results in an increased secretion of $\boldsymbol{\alpha}$-factor. This induces the pheromone response in *MAT***a** cells and is followed by a strong secretion of Bar1 again decreasing the $\boldsymbol{\alpha}$-factor signal. This creates a negative feedback which leads to a diminished Bar1 secretion and a resulting steady state distribution of $\boldsymbol{\alpha}$-factor which coincides with the induction of shmooing in both cell types. Thus, both haploid cell types do repeatedly adapt their behavior in response to changes in the extracellular environment.
This describes a complex communication going on back and forth between cooperating *MAT***a** and *MAT*$\boldsymbol{\alpha}$ cells in order to optimize information flow in the extracellular environment and to assure future survival under starvation without sacrificing growth. This communication uses information about the signaling pathway activation of other

[1] This would not work if *Saccharomyces cerevisiae* was capable of chemotaxis, since it would allow cheaters to invade non- cheater populations, thus, the absence of chemotaxis favors the evolution of cooperative behavior here.

cells as it is encoded by the quantity of available pheromones. One could see this as a rudimentary mechanism to adapt the cellular response to the behavior of other cells in the population. Communication in such complexity between individuals of a cell population is not observed in bacteria and is often believed to require at least multicellular organisms. Thus, *Saccharomyces cerevisiae* seems to be an exemplary organism for the study of cell-cell communication.

4.3 Can we generalize from yeast?

Of course, it will also be important to discuss the results in the light of other organisms than yeast. The results obtained on the level of the intracellular pheromone response have direct implications for signaling in higher eukaryotes as well, since the results can be extrapolated to their homologes. I have discussed this in length already in section 1.4.5. The accurate detection of noisy extracellular signals is a general requirement for many signaling pathways and accumulation on the receptor level to reduce noise might a strategy used by many cells. The study of polarization employed in this thesis was constructed from the start not to be restricted to a particular pathway. The fact that many eukaryotes employ polarisome-like structures indicates that they may use the same mechanisms in yeast in order to achieve polarization.
The regulation of the extracellular signaling environment in yeast does not have a direct relation to other cells, however the used methods do. In particular the developed assay in order to quantify extracellular signaling environments can be applied to any cell population and might be applied to various purposes. A particular example is found in the formation of biofilms. Biofilms are formed by many bacteria and are a leading cause of death in bacterial infection [5, 238]. The obtained results about communication in cell populations and application of our methodology might help to study potential ways to disrupt the formation of biofilms.

5 Bibliography

[1] Thomas W Spiesser, Christian Diener, Matteo Barberis, and Edda Klipp. What influences DNA replication rate in budding yeast? *PloS one*, 5(4):e10203, January 2010.

[2] Matteo Barberis, Claudia Beck, Aouefa Amoussouvi, Gabriele Schreiber, Christian Diener, Andreas Herrmann, and Edda Klipp. A low number of SIC1 mRNA molecules ensures a low noise level in cell cycle progression of budding yeast. *Molecular bioSystems*, 7(10):2804–12, October 2011.

[3] Andrew Camilli and Bonnie L Bassler. Bacterial small-molecule signaling pathways. *Science (New York, N.Y.)*, 311(5764):1113–6, February 2006.

[4] Ann M Stevens, Martin Schuster, and Kendra P Rumbaugh. Working together for the common good: cell-cell communication in bacteria. *Journal of bacteriology*, 194(9):2131–41, May 2012.

[5] Carey D Nadell, Joao B Xavier, Simon A Levin, and Kevin R Foster. The evolution of quorum sensing in bacterial biofilms. *PLoS biology*, 6(1):e14, January 2008.

[6] J. W. Costerton. Bacterial Biofilms: A Common Cause of Persistent Infections. *Science*, 284(5418):1318–1322, May 1999.

[7] W R Loewenstein and Y Kanno. Intercellular communication and the control of tissue growth: lack of communication between cancer cells. *Nature*, 209(5029):1248–9, March 1966.

[8] Yuri Lazebnik. Can a biologist fix a radio?–Or, what I learned while studying apoptosis. *Cancer cell*, 2(3):179–82, September 2002.

[9] Hiroaki Kitano. Systems biology: a brief overview. *Science (New York, N.Y.)*, 295(5560):1662–4, March 2002.

[10] Kendall Powell. All systems go. *The Journal of cell biology*, 165(3):299–303, May 2004.

[11] H Feldmann. *Yeast: Molecular and Cell Biology*. John Wiley & Sons, Weinheim, 1 edition, 2010.

[12] C C Lindegren. *The yeast cell: its genetics and cytology*. Educational Publishers, 1949.

[13] J D Beggs. Transformation of yeast by a replicating hybrid plasmid. *Nature*, 275(5676):104–9, September 1978.

[14] A Goffeau, B G Barrell, H Bussey, R W Davis, B Dujon, H Feldmann, F Galibert, J D Hoheisel, C Jacq, M Johnston, E J Louis, H W Mewes, Y Murakami, P Philippsen, H Tettelin, and S G Oliver. Life with 6000 genes. *Science (New York, N.Y.)*, 274(5287):546, 563–7, October 1996.

[15] D Botstein, S A Chervitz, and J M Cherry. Yeast as a model organism. *Science (New York, N.Y.)*, 277(5330):1259–60, August 1997.

[16] James A Barnett. Beginnings of microbiology and biochemistry: the contribution of yeast research. *Microbiology (Reading, England)*, 149(Pt 3):557–67, March 2003.

[17] Olaf Nielsen. Signal transduction during mating and meiosis in S. pombe. *Trends in Cell Biology*, 3(2):60–65, February 1993.

[18] Lauren N Booth, Brian B Tuch, and Alexander D Johnson. Intercalation of a new tier of transcription regulation into an ancient circuit. *Nature*, 468(7326):959–63, December 2010.

[19] Janet Kurjan and Ira Herskowitz. Structure of a yeast pheromone gene (MFα): A putative α-factor precursor contains four tandem copies of mature α-factor. *Cell*, 30(3):933–943, October 1982.

[20] J R Strazdis and V L MacKay. Induction of yeast mating pheromone a-factor by alpha cells. *Nature*, 305(5934):543–545, 1983.

[21] David W Rogers, Ellen McConnell, and Duncan Greig. Molecular quantification of Saccharomyces cerevisiae α-pheromone secretion. *FEMS yeast research*, 12(6):668–74, September 2012.

[22] R Betz, J W Crabb, H E Meyer, R Wittig, and W Duntze. Amino acid sequences of a-factor mating peptides from Saccharomyces cerevisiae. *The Journal of biological chemistry*, 262(2):546–8, January 1987.

[23] R J Anderegg, R Betz, S a Carr, J W Crabb, and W Duntze. Structure of Saccharomyces cerevisiae mating hormone a-factor. Identification of S-farnesyl cysteine as a structural component. *The Journal of biological chemistry*, 263(34):18236–40, December 1988.

[24] P Chen, J D Choi, R Wang, R J Cotter, and S Michaelis. A novel a-factor-related peptide of Saccharomyces cerevisiae that exits the cell by a Ste6p-independent mechanism. *Mol Biol Cell*, 8(7):1273–1291, July 1997.

[25] K Fujimura-Kamada, F J Nouvet, and S Michaelis. A novel membrane-associated metalloprotease, Ste24p, is required for the first step of NH2-terminal processing of the yeast a-factor precursor. *J Cell Biol*, 136(2):271–285, January 1997.

[26] Gregory Huyer, Amy Kistler, Franklin J Nouvet, Carolyn M George, Meredith L Boyle, and Susan Michaelis. Saccharomyces cerevisiae a-factor mutants reveal residues critical for processing, activity, and export. *Eukaryotic cell*, 5(9):1560–70, September 2006.

[27] C J Ketchum, W K Schmidt, G V Rajendrakumar, S Michaelis, and P C Maloney. The yeast a-factor transporter Ste6p, a member of the ABC superfamily, couples ATP hydrolysis to pheromone export. *J Biol Chem*, 276(31):29007–29011, August 2001.

[28] K Kuchler, H G Dohlman, and J Thorner. The a-factor transporter (STE6 gene product) and cell polarity in the yeast Saccharomyces cerevisiae. *The Journal of cell biology*, 120(5):1203–15, March 1993.

[29] R Kölling and C P Hollenberg. The ABC-transporter Ste6 accumulates in the plasma membrane in a ubiquitinated form in endocytosis mutants. *The EMBO journal*, 13(14):3261–71, July 1994.

[30] V Brizzio, A E Gammie, G Nijbroek, S Michaelis, and M D Rose. Cell fusion during yeast mating requires high levels of a-factor mating pheromone. *The Journal of cell biology*, 135(6 Pt 2):1727–39, December 1996.

[31] James B. Hicks and Ira Herskowitz. Evidence for a new diffusible element of mating pheromones in yeast. *Nature*, 260(5548):246–248, March 1976.

[32] T R Manney. Expression of the BAR1 gene in Saccharomyces cerevisiae: induction by the alpha mating pheromone of an activity associated with a secreted protein. *J Bacteriol*, 155(1):291–301, July 1983.

[33] V L MacKay, S K Welch, M Y Insley, T R Manney, J Holly, G C Saari, and M L Parker. The Saccharomyces cerevisiae BAR1 gene encodes an exported protein with homology to pepsin. *Proceedings of the National Academy of Sciences of the United States of America*, 85(1):55–9, January 1988.

[34] W Ballensiefen and H D Schmitt. Periplasmic Bar1 protease of Saccharomyces cerevisiae is active before reaching its extracellular destination. *European journal of biochemistry / FEBS*, 247(1):142–7, July 1997.

[35] Lee Bardwell. A walk-through of the yeast mating pheromone response pathway. *Peptides*, 26(2):339–350, February 2005.

[36] Robert A Arkowitz. Chemical gradients and chemotropism in yeast. *Cold Spring Harbor perspectives in biology*, 1(2):a001958, August 2009.

[37] Anshika Bajaj, Andjelka Celic, Fa-Xiang Ding, Fred Naider, Jeffrey M Becker, and Mark E Dumont. A fluorescent alpha-factor analogue exhibits multiple steps on binding to its G protein coupled receptor in yeast. *Biochemistry*, 43(42):13564–13578, October 2004.

[38] Anshika Bajaj, Sara M Connelly, Austin U Gehret, Fred Naider, and Mark E Dumont. Role of extracellular charged amino acids in the yeast alpha-factor receptor. *Biochimica et biophysica acta*, 1773(6):707–17, June 2007.

[39] Melinda Hauser, Sarah Kauffman, Byung-Kwon Lee, Fred Naider, and Jeffrey M Becker. The first extracellular loop of the Saccharomyces cerevisiae G protein-coupled receptor Ste2p undergoes a conformational change upon ligand binding. *The Journal of biological chemistry*, 282(14):10387–97, April 2007.

[40] Kyeong-Man Kim, Yong-Hun Lee, Ayca Akal-Strader, M Seraj Uddin, Melinda Hauser, Fred Naider, and Jeffrey M Becker. Multiple regulatory roles of the carboxy terminus of Ste2p a yeast GPCR. *Pharmacological research : the official journal of the Italian Pharmacological Society*, 65(1):31–40, January 2012.

[41] D D Jenness and P Spatrick. Down regulation of the alpha-factor pheromone receptor in S. cerevisiae. *Cell*, 46(3):345–353, August 1986.

[42] L Hicke, B Zanolari, and H Riezman. Cytoplasmic tail phosphorylation of the alpha-factor receptor is required for its ubiquitination and internalization. *J Cell Biol*, 141(2):349–358, April 1998.

[43] J Mulholland, J Konopka, B Singer-Kruger, M Zerial, and D Botstein. Visualization of receptor-mediated endocytosis in yeast. *Molecular biology of the cell*, 10(3):799–817, March 1999.

[44] Chunhua Shi, Susan Kaminskyj, Sarah Caldwell, and Mich?le C Loewen. A role for a complex between activated G protein-coupled receptors in yeast cellular mating. *Proceedings of the National Academy of Sciences of the United States of America*, 104(13):5395–5400, March 2007.

[45] H Dohlman. G Proteins and pheromone signaling. *Annual Review of Physiology*, 64:129–152, 2002.

[46] M Dosil, K A Schandel, E Gupta, D D Jenness, and J B Konopka. The C terminus of the Saccharomyces cerevisiae alpha-factor receptor contributes to the formation of preactivation complexes with its cognate G protein. *Molecular and cellular biology*, 20(14):5321–9, July 2000.

[47] M J Durán-Avelar, L Ongay-Larios, A Zentella-Dehesa, and R Coria. The carboxy-terminal tail of the Ste2 receptor is involved in activation of the G protein in the Saccharomyces cerevisiae alpha-pheromone response pathway. *FEMS microbiology letters*, 197(1):65–71, April 2001.

[48] H G Dohlman, J Song, D Ma, W E Courchesne, and J Thorner. Sst2, a negative regulator of pheromone signaling in the yeast Saccharomyces cerevisiae: expression, localization, and genetic interaction and physical association with Gpa1 (the G-protein alpha subunit). *Molecular and cellular biology*, 16(9):5194–209, September 1996.

[49] Nan Hao, Necmettin Yildirim, Yuqi Wang, Timothy C Elston, and Henrik G Dohlman. Regulators of G protein signaling and transient activation of signaling: experimental and computational analysis reveals negative and positive feedback controls on G protein activity. *J Biol Chem*, 278(47):46506–46515, November 2003.

[50] Daniel R Ballon, Paul L Flanary, Douglas P Gladue, James B Konopka, Henrik G Dohlman, and Jeremy Thorner. DEP-domain-mediated regulation of GPCR signaling responses. *Cell*, 126(6):1079–1093, September 2006.

[51] J E Hirschman and D D Jenness. Dual lipid modification of the yeast ggamma subunit Ste18p determines membrane localization of Gbetagamma. *Molecular and cellular biology*, 19(11):7705–11, November 1999.

[52] C L Manahan, M Patnana, K J Blumer, and M E Linder. Dual lipid modification motifs in G(alpha) and G(gamma) subunits are required for full activity of the pheromone response pathway in Saccharomyces cerevisiae. *Molecular biology of the cell*, 11(3):957–68, March 2000.

[53] M Whiteway, L Hougan, D Dignard, D Y Thomas, L Bell, G C Saari, F J Grant, P O'Hara, and V L MacKay. The STE4 and STE18 genes of yeast encode potential beta and gamma subunits of the mating factor receptor-coupled G protein. *Cell*, 56(3):467–77, March 1989.

[54] M Whiteway, D Dignard, and D Y Thomas. Mutagenesis of Ste18, a putative G gamma subunit in the Saccharomyces cerevisiae pheromone response pathway. *Biochemistry and cell biology / Biochimie et biologie cellulaire*, 70(10-11):1230–7, 1992.

[55] L H Hartwell. Mutants of Saccharomyces cerevisiae unresponsive to cell division control by polypeptide mating hormone. *The Journal of cell biology*, 85(3):811–22, June 1980.

[56] Scott A Chasse, Paul Flanary, Stephen C Parnell, Nan Hao, Jiyoung Y Cha, David P Siderovski, and Henrik G Dohlman. Genome-scale analysis reveals Sst2 as the principal regulator of mating pheromone signaling in the yeast Saccharomyces cerevisiae. *Eukaryotic cell*, 5(2):330–46, March 2006.

[57] Z G Goldsmith and D N Dhanasekaran. G protein regulation of MAPK networks. *Oncogene*, 26(22):3122–3142, May 2007.

[58] Raymond E Chen and Jeremy Thorner. Function and regulation in MAPK signaling pathways: lessons learned from the yeast Saccharomyces cerevisiae. *Biochim Biophys Acta*, 1773(8):1311–1340, August 2007.

[59] P M Pryciak and F A Huntress. Membrane recruitment of the kinase cascade scaffold protein Ste5 by the Gbetagamma complex underlies activation of the yeast pheromone response pathway. *Genes & development*, 12(17):2684–97, September 1998.

[60] Y Feng, L Y Song, E Kincaid, S K Mahanty, and E A Elion. Functional binding between Gbeta and the LIM domain of Ste5 is required to activate the MEKK Ste11. *Curr Biol*, 8(5):267–278, February 1998.

[61] Lindsay S Garrenton, Susan L Young, and Jeremy Thorner. Function of the MAPK scaffold protein, Ste5, requires a cryptic PH domain. *Genes Dev*, 20(14):1946–1958, July 2006.

[62] Matthew J Winters, Rachel E Lamson, Hideki Nakanishi, Aaron M Neiman, and Peter M Pryciak. A membrane binding domain in the ste5 scaffold synergizes with gbetagamma binding to control localization and signaling in pheromone response. *Molecular cell*, 20(1):21–32, October 2005.

[63] D N Dhanasekaran, K Kashef, C M Lee, H Xu, and E P Reddy. Scaffold proteins of MAP-kinase modules. *Oncogene*, 26(22):3185–3202, May 2007.

[64] E A Elion. The Ste5p scaffold. *Journal of cell science*, 114(Pt 22):3967–78, November 2001.

[65] Lu Yu, Maosong Qi, Mark A Sheff, and Elaine A Elion. Counteractive control of polarized morphogenesis during mating by mitogen-activated protein kinase Fus3 and G1 cyclin-dependent kinase. *Mol Biol Cell*, 19(4):1739–1752, April 2008.

[66] Mohan K Malleshaiah, Vahid Shahrezaei, Peter S Swain, and Stephen W Michnick. The scaffold protein Ste5 directly controls a switch-like mating decision in yeast. *Nature*, 465(7294):101–5, May 2010.

[67] F Drogen, S M O'Rourke, V M Stucke, M Jaquenoud, A M Neiman, and M Peter. Phosphorylation of the MEKK Ste11p by the PAK-like kinase Ste20p is required for MAP kinase signaling in vivo. *Current biology : CB*, 10(11):630–9, June 2000.

[68] Rachel E Lamson, Matthew J Winters, and Peter M Pryciak. Cdc42 regulation of kinase activity and signaling by the yeast p21-activated kinase Ste20. *Molecular and cellular biology*, 22(9):2939–51, May 2002.

[69] E Leberer, D Dignard, D Harcus, D Y Thomas, and M Whiteway. The protein kinase homologue Ste20p is required to link the yeast pheromone response G-protein beta gamma subunits to downstream signalling components. *The EMBO journal*, 11(13):4815–24, December 1992.

[70] M Peter, A M Neiman, H O Park, M van Lohuizen, and I Herskowitz. Functional analysis of the interaction between the small GTP binding protein Cdc42 and the Ste20 protein kinase in yeast. *The EMBO journal*, 15(24):7046–59, December 1996.

[71] T Leeuw, C Wu, J D Schrag, M Whiteway, D Y Thomas, and E Leberer. Interaction of a G-protein beta-subunit with a conserved sequence in Ste20/PAK family protein kinases. *Nature*, 391(6663):191–5, January 1998.

[72] Matthew J Winters and Peter M Pryciak. Interaction with the SH3 domain protein Bem1 regulates signaling by the Saccharomyces cerevisiae p21-activated kinase Ste20. *Molecular and cellular biology*, 25(6):2177–90, March 2005.

[73] April S Goehring, David A Mitchell, Amy Hin Yan Tong, Megan E Keniry, Charles Boone, and George F Sprague. Synthetic lethal analysis implicates Ste20p, a p21-activated potein kinase, in polarisome activation. *Molecular biology of the cell*, 14(4):1501–16, April 2003.

[74] Javier Macia, Sergi Regot, Tom Peeters, Núria Conde, Ricard Solé, and Francesc Posas. Dynamic signaling in the Hog1 MAPK pathway relies on high basal signal transduction. *Science signaling*, 2(63):ra13, January 2009.

[75] Celine I Maeder, Mark A Hink, Ali Kinkhabwala, Reinhard Mayr, Philippe I H Bastiaens, and Michael Knop. Spatial regulation of Fus3 MAP kinase activity through a reaction-diffusion mechanism in yeast pheromone signalling. *Nat Cell Biol*, 9(11):1319–1326, November 2007.

[76] Kerry Tedford, Sammy Kim, Danne Sa, Ken Stevens, and Mike Tyers. Regulation of the mating pheromone and invasive growth responses in yeast by two MAP kinase substrates. *Current Biology*, 7(4):228–238, April 1997.

[77] Julia Zeitlinger, Itamar Simon, Christopher T Harbison, Nancy M Hannett, Thomas L Volkert, Gerald R Fink, and Richard A Young. Program-specific distribution of a transcription factor dependent on partner transcription factor and MAPK signaling. *Cell*, 113(3):395–404, May 2003.

[78] K A Olson, C Nelson, G Tai, W Hung, C Yong, C Astell, and I Sadowski. Two regulators of Ste12p inhibit pheromone-responsive transcription by separate mechanisms. *Molecular and cellular biology*, 20(12):4199–209, June 2000.

[79] Anasua B Kusari, Douglas M Molina, Walid Sabbagh, Chang S Lau, and Lee Bardwell. A conserved protein interaction network involving the yeast MAP kinases Fus3 and Kss1. *The Journal of cell biology*, 164(2):267–77, January 2004.

[80] Ernest Blackwell, Hye-Jin N Kim, and David E Stone. The pheromone-induced nuclear accumulation of the Fus3 MAPK in yeast depends on its phosphorylation state and on Dig1 and Dig2. *BMC cell biology*, 8:44, January 2007.

[81] Marie Z Bao, Monica A Schwartz, Greg T Cantin, John R Yates, and Hiten D Madhani. Pheromone-dependent destruction of the Tec1 transcription factor is required for MAP kinase signaling specificity in yeast. *Cell*, 119(7):991–1000, December 2004.

[82] Ching-Shan Chou, Qing Nie, and Tau-Mu Yi. Modeling Robustness Tradeoffs in Yeast Cell Polarization Induced by Spatial Gradients. *PLoS ONE*, 3(9):e3103, 2008.

[83] M Peter and I Herskowitz. Direct inhibition of the yeast cyclin-dependent kinase Cdc28-Cln by Far1. *Science (New York, N.Y.)*, 265(5176):1228–31, August 1994.

[84] M D Mendenhall. Cyclin-dependent kinase inhibitors of Saccharomyces cerevisiae and Schizosaccharomyces pombe. *Current topics in microbiology and immunology*, 227:1–24, January 1998.

[85] Shelly C Strickfaden, Matthew J Winters, Giora Ben-Ari, Rachel E Lamson, Mike Tyers, and Peter M Pryciak. A mechanism for cell-cycle regulation of MAP kinase signaling in a yeast differentiation pathway. *Cell*, 128(3):519–531, February 2007.

[86] K Madden and M Snyder. Cell polarity and morphogenesis in budding yeast. *Annu Rev Microbiol*, 52:687–744, 1998.

[87] Aron B Jaffe and Alan Hall. Rho GTPases: biochemistry and biology. *Annual review of cell and developmental biology*, 21:247–69, January 2005.

[88] Orion D Weiner, Paul O Neilsen, Glenn D Prestwich, Marc W Kirschner, Lewis C Cantley, and Henry R Bourne. A PtdInsP(3)- and Rho GTPase-mediated positive feedback loop regulates neutrophil polarity. *Nature cell biology*, 4(7):509–13, July 2002.

[89] G. Servant. Polarization of Chemoattractant Receptor Signaling During Neutrophil Chemotaxis. *Science*, 287(5455):1037–1040, February 2000.

[90] Myrto Raftopoulou and Alan Hall. Cell migration: Rho GTPases lead the way. *Developmental Biology*, 265(1):23–32, January 2004.

[91] Maitreyi Das, Tyler Drake, David J Wiley, Peter Buchwald, Dimitrios Vavylonis, and Fulvia Verde. Oscillatory Dynamics of Cdc42 GTPase in the Control of Polarized Growth. *Science (New York, N.Y.)*, May 2012.

[92] Julian Pulecio, Jelena Petrovic, Francesca Prete, Giulia Chiaruttini, Ana-Maria Lennon-Dumenil, Chantal Desdouets, Stephane Gasman, Oscar R Burrone, and Federica Benvenuti. Cdc42-mediated MTOC polarization in dendritic cells controls targeted delivery of cytokines at the immune synapse. *The Journal of experimental medicine*, 207(12):2719–32, November 2010.

[93] Roland Wedlich-Soldner, Steve Altschuler, Lani Wu, and Rong Li. Spontaneous cell polarization through actomyosin-based delivery of the Cdc42 GTPase. *Science (New York, N.Y.)*, 299(5610):1231–5, February 2003.

[94] M Ziman, D Preuss, J Mulholland, J M O'Brien, D Botstein, and D I Johnson. Subcellular localization of Cdc42p, a Saccharomyces cerevisiae GTP-binding protein involved in the control of cell polarity. *Molecular biology of the cell*, 4(12):1307–16, December 1993.

[95] A Nern and R A Arkowitz. A GTP-exchange factor required for cell orientation. *Nature*, 391(6663):195–8, January 1998.

[96] Sophie Barale, Derek McCusker, and Robert A Arkowitz. The exchange factor Cdc24 is required for cell fusion during yeast mating. *Eukaryotic cell*, 3(4):1049–61, August 2004.

[97] E Leberer, C Wu, T Leeuw, A Fourest-Lieuvin, J E Segall, and D Y Thomas. Functional characterization of the Cdc42p binding domain of yeast Ste20p protein kinase. *The EMBO journal*, 16(1):83–97, January 1997.

[98] Josée Ash, Cunle Wu, Robert Larocque, Maleek Jamal, Willem Stevens, Mike Osborne, David Y Thomas, and Malcolm Whiteway. Genetic analysis of the interface between Cdc42p and the CRIB domain of Ste20p in Saccharomyces cerevisiae. *Genetics*, 163(1):9–20, January 2003.

[99] Philippe Wiget, Yukiko Shimada, Anne-Christine Butty, Efrei Bi, and Matthias Peter. Site-specific regulation of the GEF Cdc24p by the scaffold protein Far1p during yeast mating. *The EMBO journal*, 23(5):1063–74, March 2004.

[100] M Blondel, P M Alepuz, L S Huang, S Shaham, G Ammerer, and M Peter. Nuclear export of Far1p in response to pheromones requires the export receptor Msn5p/Ste21p. *Genes & development*, 13(17):2284–300, September 1999.

[101] A C Butty, P M Pryciak, L S Huang, I Herskowitz, and M Peter. The role of Far1p in linking the heterotrimeric G protein to polarity establishment proteins during yeast mating. *Science (New York, N.Y.)*, 282(5393):1511–6, November 1998.

[102] A Nern and R A Arkowitz. A Cdc24p-Far1p-Gbetagamma protein complex required for yeast orientation during mating. *The Journal of cell biology*, 144(6):1187–202, March 1999.

[103] T Leeuw, A Fourest-Lieuvin, C Wu, J Chenevert, K Clark, M Whiteway, D Y Thomas, and E Leberer. Pheromone response in yeast: association of Bem1p with proteins of the MAP kinase cascade and actin. *Science (New York, N.Y.)*, 270(5239):1210–3, November 1995.

[104] Anne-Christine Butty, Nathalie Perrinjaquet, Audrey Petit, Malika Jaquenoud, Jeffrey E Segall, Kay Hofmann, Catherine Zwahlen, and Matthias Peter. A positive feedback loop stabilizes the guanine-nucleotide exchange factor Cdc24 at sites of polarization. *The EMBO journal*, 21(7):1565–76, April 2002.

[105] Lukasz Kozubowski, Koji Saito, Jayme M Johnson, Audrey S Howell, Trevin R Zyla, and Daniel J Lew. Symmetry-breaking polarization driven by a Cdc42p GEF-PAK complex. *Current biology*, 18(22):1719–26, November 2008.

[106] M Evangelista, K Blundell, M S Longtine, C J Chow, N Adames, J R Pringle, M Peter, and C Boone. Bni1p, a yeast formin linking cdc42p and the actin cytoskeleton during polarized morphogenesis. *Science (New York, N.Y.)*, 276(5309):118–22, April 1997.

[107] N Valtz and I Herskowitz. Pea2 protein of yeast is localized to sites of polarized growth and is required for efficient mating and bipolar budding. *The Journal of cell biology*, 135(3):725–39, November 1996.

[108] Brian R Graziano, Amy Grace DuPage, Alphee Michelot, Dennis Breitsprecher, James B Moseley, Isabelle Sagot, Laurent Blanchoin, and Bruce L Goode. Mechanism and cellular function of Bud6 as an actin nucleation-promoting factor. *Molecular biology of the cell*, 22(21):4016–28, November 2011.

[109] R A Arkowitz and N Lowe. A small conserved domain in the yeast Spa2p is necessary and sufficient for its polarized localization. *The Journal of cell biology*, 138(1):17–36, July 1997.

[110] M Snyder. The SPA2 protein of yeast localizes to sites of cell growth. *The Journal of cell biology*, 108(4):1419–29, April 1989.

[111] Frank van Drogen and Matthias Peter. Spa2p functions as a scaffold-like protein to recruit the Mpk1p MAP kinase module to sites of polarized growth. *Current biology : CB*, 12(19):1698–703, October 2002.

[112] David E Levin. Regulation of cell wall biogenesis in Saccharomyces cerevisiae: the cell wall integrity signaling pathway. *Genetics*, 189(4):1145–75, December 2011.

[113] K Ozaki, K Tanaka, H Imamura, T Hihara, T Kameyama, H Nonaka, H Hirano, Y Matsuura, and Y Takai. Rom1p and Rom2p are GDP/GTP exchange proteins (GEPs) for the Rho1p small GTP binding protein in Saccharomyces cerevisiae. *The EMBO journal*, 15(9):2196–207, May 1996.

[114] T Wang and A Bretscher. The rho-GAP encoded by BEM2 regulates cytoskeletal structure in budding yeast. *Molecular biology of the cell*, 6(8):1011–24, August 1995.

[115] Sue Ann Krause, Michael J Cundell, Pak P Poon, Josephine McGhie, Gerry C Johnston, Clive Price, and Joseph V Gray. Functional specialization of the yeast Rho1 GTP exchange factors. *Journal of cell science*, February 2012.

[116] J Drgonová, T Drgon, K Tanaka, R Kollár, G C Chen, R A Ford, C S Chan, Y Takai, and E Cabib. Rho1p, a yeast protein at the interface between cell polarization and morphogenesis. *Science (New York, N.Y.)*, 272(5259):277–9, April 1996.

[117] H Qadota, C P Python, S B Inoue, M Arisawa, Y Anraku, Y Zheng, T Watanabe, D E Levin, and Y Ohya. Identification of yeast Rho1p GTPase as a regulatory subunit of 1,3-beta-glucan synthase. *Science (New York, N.Y.)*, 272(5259):279–81, April 1996.

[118] A Bender. Genetic evidence for the roles of the bud-site-selection genes BUD5 and BUD2 in control of the Rsr1p (Bud1p) GTPase in yeast. *Proceedings of the National Academy of Sciences of the United States of America*, 90(21):9926–9, November 1993.

[119] H O Park, E Bi, J R Pringle, and I Herskowitz. Two active states of the Ras-related Bud1/Rsr1 protein bind to different effectors to determine yeast cell polarity. *Proceedings of the National Academy of Sciences of the United States of America*, 94(9):4463–8, April 1997.

[120] K Madden and M Snyder. Specification of sites for polarized growth in Saccharomyces cerevisiae and the influence of external factors on site selection. *Molecular biology of the cell*, 3(9):1025–35, September 1992.

[121] R. Dorer, P M Pryciak, and L H Hartwell. Saccharomyces cerevisiae cells execute a default pathway to select a mate in the absence of pheromone gradients. *The Journal of Cell Biology*, 131(4):845–861, November 1995.

[122] D G Drubin and W J Nelson. Origins of cell polarity. *Cell*, 84(3):335–44, February 1996.

[123] W L Lingle, W H Lutz, J N Ingle, N J Maihle, and J L Salisbury. Centrosome hypertrophy in human breast tumors: implications for genomic stability and cell polarity. *Proceedings of the National Academy of Sciences of the United States of America*, 95(6):2950–5, March 1998.

[124] Marek Mlodzik. Planar cell polarization: do the same mechanisms regulate Drosophila tissue polarity and vertebrate gastrulation? *Trends Genet*, 18(11):564–571, November 2002.

[125] Steven X Hou, Zhiyu Zheng, Xiu Chen, and Norbert Perrimon. The Jak/STAT pathway in model organisms: emerging roles in cell movement. *Dev Cell*, 3(6):765–778, December 2002.

[126] Steven D Harris, Nick D Read, Robert W Roberson, Brian Shaw, Stephan Seiler, Mike Plamann, and Michelle Momany. Polarisome meets spitzenkörper: microscopy, genetics, and genomics converge. *Eukaryot Cell*, 4(2):225–229, February 2005.

[127] Ian C Schneider and Jason M Haugh. Mechanisms of gradient sensing and chemotaxis: conserved pathways, diverse regulation. *Cell Cycle*, 5(11):1130–1134, June 2006.

[128] Philippe Bastiaens, Maiwen Caudron, Philipp Niethammer, and Eric Karsenti. Gradients in the self-organization of the mitotic spindle. *Trends in cell biology*, 16(3):125–34, March 2006.

[129] Stephen C Bunnell, Andrew L Singer, David I Hong, Berri H Jacque, Martha S Jordan, Maria-Cristina Seminario, Valarie A Barr, Gary A Koretzky, and Lawrence E Samelson. Persistence of cooperatively stabilized signaling clusters drives T-cell activation. *Mol Cell Biol*, 26(19):7155–7166, October 2006.

[130] Nigel J Burroughs and P Anton van der Merwe. Stochasticity and spatial heterogeneity in T-cell activation. *Immunol Rev*, 216:69–80, April 2007.

[131] Tae Joo Park, Brian J Mitchell, Philip B Abitua, Chris Kintner, and John B Wallingford. Dishevelled controls apical docking and planar polarization of basal bodies in ciliated epithelial cells. *Nature genetics*, 40(7):871–9, July 2008.

[132] Fernando Martin-Belmonte and Mirna Perez-Moreno. Epithelial cell polarity, stem cells and cancer. *Nature reviews. Cancer*, 12(1):23–38, January 2012.

[133] K Shinjo, J G Koland, M J Hart, V Narasimhan, D I Johnson, T Evans, and R A Cerione. Molecular cloning of the gene for the human placental GTP-binding protein Gp (G25K): identification of this GTP-binding protein as the human homolog of the yeast cell-division-cycle protein CDC42. *Proceedings of the National Academy of Sciences of the United States of America*, 87(24):9853–7, December 1990.

[134] N Lamarche, N Tapon, L Stowers, P D Burbelo, P Aspenström, T Bridges, J Chant, and A Hall. Rac and Cdc42 induce actin polymerization and G1 cell cycle progression independently of p65PAK and the JNK/SAPK MAP kinase cascade. *Cell*, 87(3):519–29, November 1996.

[135] Sandrine Etienne-Manneville and Alan Hall. Cdc42 regulates GSK-3beta and adenomatous polyposis coli to control cell polarity. *Nature*, 421(6924):753–6, February 2003.

[136] R Kolluri, K F Tolias, C L Carpenter, F S Rosen, and T Kirchhausen. Direct interaction of the Wiskott-Aldrich syndrome protein with the GTPase Cdc42. *Proceedings of the National Academy of Sciences of the United States of America*, 93(11):5615–8, May 1996.

[137] J J Tyson. Modeling the cell division cycle: cdc2 and cyclin interactions. *Proceedings of the National Academy of Sciences of the United States of America*, 88(16):7328–32, August 1991.

[138] C Y Huang and J E Ferrell. Ultrasensitivity in the mitogen-activated protein kinase cascade. *Proceedings of the National Academy of Sciences of the United States of America*, 93(19):10078–83, September 1996.

[139] R Heinrich, F Montero, E Klipp, T G Waddell, and E Meléndez-Hevia. Theoretical approaches to the evolutionary optimization of glycolysis: thermodynamic and kinetic constraints. *European journal of biochemistry / FEBS*, 243(1-2):191–201, January 1997.

[140] Bente Kofahl and Edda Klipp. Modelling the dynamics of the yeast pheromone pathway. *Yeast*, 21(10):831–850, July 2004.

[141] Edda Klipp, Bodil Nordlander, Roland Krüger, Peter Gennemark, and Stefan Hohmann. Integrative model of the response of yeast to osmotic shock. *Nature biotechnology*, 23(8):975–82, August 2005.

[142] Nan Hao, Sujata Nayak, Marcelo Behar, Ryan H Shanks, Michal J Nagiec, Beverly Errede, Jeffrey Hasty, Timothy C Elston, and Henrik G Dohlman. Regulation of cell signaling dynamics by the protein kinase-scaffold Ste5. *Mol Cell*, 30(5):649–656, June 2008.

[143] Caleb J Bashor, Noah C Helman, Shude Yan, and Wendell A Lim. Using engineered scaffold interactions to reshape MAP kinase pathway signaling dynamics. *Science*, 319(5869):1539–1543, March 2008.

[144] A M Turing. The chemical basis of morphogenesis. *Philosophical Transactions of the Royal Society of London. Series B, Biological Sciences*, 237(641):37, 1952.

[145] Andrew B Goryachev and Alexandra V Pokhilko. Dynamics of Cdc42 network embodies a Turing-type mechanism of yeast cell polarity. *FEBS letters*, 582(10):1437–43, April 2008.

[146] G. G. Stokes. On the Change of Refrangibility of Light. *Philosophical Transactions of the Royal Society of London*, 142:463–562, January 1852.

[147] F. A. J. L. James. The Conservation of Energy, Theories of Absorption and Resonating Molecules, 1851-1854: G. G. Stokes, A. J. Angstrom and W. Thomson. *Notes and Records of the Royal Society*, 38(1):79–107, August 1983.

[148] Bernhard Valeur. *Molecular Fluorescence*. WILEY-VCH, Weinheim, Germany, 1 edition, 2007.

[149] Osamu Shimomura, Frank H. Johnson, and Yo Saiga. Extraction, Purification and Properties of Aequorin, a Bioluminescent Protein from the Luminous Hydromedusan,Aequorea. *Journal of Cellular and Comparative Physiology*, 59(3):223–239, June 1962.

[150] R Heim, A B Cubitt, and R Y Tsien. Improved green fluorescence. *Nature*, 373(6516):663–4, February 1995.

[151] M Chalfie, Y Tu, G Euskirchen, W. Ward, and D. Prasher. Green fluorescent protein as a marker for gene expression. *Science*, 263(5148):802–805, February 1994.

[152] Jeff W Lichtman and José-Angel Conchello. Fluorescence microscopy. *Nature methods*, 2(12):910–9, December 2005.

[153] Kenneth R. Spring. Fluorescence Microscopy. In Marcel Dekker, editor, *Encyclopedia of Optical Engineering*, pages 548–555. New York, NY, USA, 2003.

[154] Christian A Combs. Fluorescence microscopy: a concise guide to current imaging methods. *Current protocols in neuroscience*, Chapter 2:Unit2.1, January 2010.

[155] Howard R Petty. Fluorescence microscopy: established and emerging methods, experimental strategies, and applications in immunology. *Microscopy research and technique*, 70(8):687–709, August 2007.

[156] W Denk, J. Strickler, and W. Webb. Two-photon laser scanning fluorescence microscopy. *Science*, 248(4951):73–76, April 1990.

[157] E. Abbe. Beiträge zur Theorie des Mikroskops und der mikroskopischen Wahrnehmung. *Archiv für Mikroskopische Anatomie*, 9(1):413–418, December 1873.

[158] Marta Fernández-Suárez and Alice Y Ting. Fluorescent probes for super-resolution imaging in living cells. *Nature reviews. Molecular cell biology*, 9(12):929–43, December 2008.

[159] Stefan W. Hell and Jan Wichmann. Breaking the diffraction resolution limit by stimulated emission: stimulated-emission-depletion fluorescence microscopy. *Optics Letters*, 19(11):780, June 1994.

[160] Volker Westphal, Silvio O Rizzoli, Marcel A Lauterbach, Dirk Kamin, Reinhard Jahn, and Stefan W Hell. Video-rate far-field optical nanoscopy dissects synaptic vesicle movement. *Science (New York, N.Y.)*, 320(5873):246–9, April 2008.

[161] Stefan W Hell. Far-field optical nanoscopy. *Science (New York, N.Y.)*, 316(5828):1153–8, May 2007.

[162] Martin Andresen, Andre C Stiel, Jonas Fölling, Dirk Wenzel, Andreas Schönle, Alexander Egner, Christian Eggeling, Stefan W Hell, and Stefan Jakobs. Photoswitchable fluorescent proteins enable monochromatic multilabel imaging and dual color fluorescence nanoscopy. *Nature biotechnology*, 26(9):1035–40, September 2008.

[163] Eric Betzig, George H Patterson, Rachid Sougrat, O Wolf Lindwasser, Scott Olenych, Juan S Bonifacino, Michael W Davidson, Jennifer Lippincott-Schwartz, and Harald F Hess. Imaging intracellular fluorescent proteins at nanometer resolution. *Science (New York, N.Y.)*, 313(5793):1642–5, September 2006.

[164] Michael J Rust, Mark Bates, and Xiaowei Zhuang. Sub-diffraction-limit imaging by stochastic optical reconstruction microscopy (STORM). *Nature methods*, 3(10):793–5, October 2006.

[165] Tanja Brakemann, Gert Weber, Martin Andresen, Gerrit Groenhof, Andre C Stiel, Simon Trowitzsch, Christian Eggeling, Helmut Grubmüller, Stefan W Hell, Markus C Wahl, and Stefan Jakobs. Molecular basis of the light-driven switching of the photochromic fluorescent protein Padron. *The Journal of biological chemistry*, 285(19):14603–9, May 2010.

[166] Andre C Stiel, Martin Andresen, Hannes Bock, Michael Hilbert, Jessica Schilde, Andreas Schönle, Christian Eggeling, Alexander Egner, Stefan W Hell, and Stefan Jakobs. Generation of monomeric reversibly switchable red fluorescent proteins for far-field fluorescence nanoscopy. *Biophysical journal*, 95(6):2989–97, September 2008.

[167] H. R. Hulett, W. A. Bonner, J. Barrett, and L. A. Herzenberg. Cell Sorting: Automated Separation of Mammalian Cells as a Function of Intracellular Fluorescence. *Science*, 166(3906):747–749, November 1969.

[168] Amit Tzur, Jodene K Moore, Paul Jorgensen, Howard M Shapiro, and Marc W Kirschner. Optimizing optical flow cytometry for cell volume-based sorting and analysis. *PloS one*, 6(1):e16053, January 2011.

[169] W. A. Bonner. Fluorescence Activated Cell Sorting. *Review of Scientific Instruments*, 43(3):404, 1972.

[170] B Futcher. Cell cycle synchronization. *Methods in cell science : an official journal of the Society for In Vitro Biology*, 21(2-3):79–86, January 1999.

[171] Andrea K Bryan, Alexi Goranov, Angelika Amon, and Scott R Manalis. Measurement of mass, density, and volume during the cell cycle of yeast. *Proceedings of the National Academy of Sciences of the United States of America*, 107(3):999–1004, January 2010.

[172] L H Johnston and A L Johnson. Elutriation of budding yeast. *Methods in enzymology*, 283:342–50, January 1997.

[173] D C Amberg, D Burke, J N Strathern, and Cold Spring Harbor Laboratory. *Methods in yeast genetics: a Cold Spring Harbor Laboratory course manual*. Cold Spring. Cold Spring Harbor Laboratory Press, 2005.

[174] R D Gietz and R A Woods. Genetic transformation of yeast. *BioTechniques*, 30(4):816–20, 822–6, 828 passim, April 2001.

[175] R Daniel Gietz and Robert H Schiestl. Quick and easy yeast transformation using the LiAc/SS carrier DNA/PEG method. *Nature protocols*, 2(1):31–4, January 2007.

[176] Robert H. Schiestl and R. Daniel Gietz. High efficiency transformation of intact yeast cells using single stranded nucleic acids as a carrier. *Current Genetics*, 16(5-6):339–346, December 1989.

[177] Eleni P Mimitou and Lorraine S Symington. Nucleases and helicases take center stage in homologous recombination. *Trends in biochemical sciences*, 34(5):264–72, May 2009.

[178] M S Wold. Replication protein A: a heterotrimeric, single-stranded DNA-binding protein required for eukaryotic DNA metabolism. *Annual review of biochemistry*, 66:61–92, January 1997.

[179] Patrick Sung and Hannah Klein. Mechanism of homologous recombination: mediators and helicases take on regulatory functions. *Nature reviews. Molecular cell biology*, 7(10):739–50, October 2006.

[180] R K Saiki, S Scharf, F Faloona, K B Mullis, G T Horn, H A Erlich, and N Arnheim. Enzymatic amplification of beta-globin genomic sequences and restriction site analysis for diagnosis of sickle cell anemia. *Science (New York, N.Y.)*, 230(4732):1350–4, December 1985.

[181] R K Saiki, D H Gelfand, S Stoffel, S J Scharf, R Higuchi, G T Horn, K B Mullis, and H A Erlich. Primer-directed enzymatic amplification of DNA with a thermostable DNA polymerase. *Science (New York, N.Y.)*, 239(4839):487–91, January 1988.

[182] S Ho, H Hunt, R Horton, J Pullen, and L Pease. Site-directed mutagenesis by overlap extension using the polymerase chain reaction. *Gene*, 77(1):51–59, April 1989.

[183] Edyta Szewczyk, Tania Nayak, C Elizabeth Oakley, Heather Edgerton, Yi Xiong, Naimeh Taheri-Talesh, Stephen A Osmani, Berl R Oakley, and Berl Oakley. Fusion PCR and gene targeting in Aspergillus nidulans. *Nature protocols*, 1(6):3111–20, January 2006.

[184] Ana A Kitazono, Brian T D Tobe, Helen Kalton, Noam Diamant, and Stephen J Kron. Marker-fusion PCR for one-step mutagenesis of essential genes in yeast. *Yeast (Chichester, England)*, 19(2):141–9, January 2002.

[185] Simon Alberti, Aaron D Gitler, and Susan Lindquist. A suite of Gateway cloning vectors for high-throughput genetic analysis in Saccharomyces cerevisiae. *Yeast (Chichester, England)*, 24(10):913–9, October 2007.

[186] Daniel T Gillespie. Stochastic simulation of chemical kinetics. *Annu Rev Phys Chem*, 58:35–55, 2007.

[187] M A Gibson and J Bruck. Efficient Exact Stochastic Simulation of Chemical Systems with Many Species and Many Channels. *J. Phys. Chem. A*, 104(9):1876–1889, March 2000.

[188] Alexander Slepoy, Aidan P Thompson, and Steven J Plimpton. A constant-time kinetic Monte Carlo algorithm for simulation of large biochemical reaction networks. *The Journal of Chemical Physics*, 128(20):205101, 2008.

[189] Johan Elf, Andreas Doncic, and Mans Ehrenberg. Mesoscopic reaction-diffusion in intracellular signaling. In Sergey M Bezrukov, Hans Frauenfelder, and Frank Moss, editors, *Fluctuations and Noise in Biological, Biophysical, and Biomedical Systems*, volume 5110, pages 114–124. SPIE, 2003.

[190] J Elf and M Ehrenberg. Spontaneous separation of bi-stable biochemical systems into spatial domains of opposite phases. *Syst Biol (Stevenage)*, 1(2):230–236, December 2004.

[191] F Baras and M Malek Mansour. Reaction-diffusion master equation: A comparison with microscopic simulations. *Phys. Rev. E*, 54(6):6139–6148, December 1996.

[192] J Vidal Rodríguez, Jaap A Kaandorp, Maciej Dobrzyński, and Joke G Blom. Spatial stochastic modelling of the phosphoenolpyruvate-dependent phosphotransferase (PTS) pathway in Escherichia coli. *Bioinformatics (Oxford, England)*, 22(15):1895–901, August 2006.

[193] Matthias Vigelius, Aidan Lane, and Bernd Meyer. Accelerating Reaction-Diffusion Simulations with General-Purpose Graphics Processing Units. *Bioinformatics (Oxford, England)*, November 2010.

[194] Peter D Lax, P D Lax, and A N Milgram. Parabolic Equations. In Peter Sarnak and Andrew Majda, editors, *Selected Papers Volume I*, pages 8–31. Springer New York, 2005.

[195] P Deuflhard and A Hohmann. *Numerische Mathematik I: Eine algorithmisch orientierte Einführung*. De Gruyter Lehrbuch. De Gruyter, 2002.

[196] P Deuflhard. *Newton Methods for Nonlinear Problems: Affine Invariance and Adaptive Algorithms*. Springer Series in Computational Mathematics. Springer, 2005.

[197] X S Li. An overview of SuperLU: Algorithms, implementation, and user interface. *ACM Transactions on Mathematical Software (TOMS)*, 31(3):302–325, 2005.

[198] Timothy A. Davis. A column pre-ordering strategy for the unsymmetric-pattern multifrontal method. *ACM Transactions on Mathematical Software*, 30(2):165–195, June 2004.

[199] Wolfgang Giese. *Numerische Behandlung einer linearen Reaktions-Diffusions-Gleichung mit einer Anwendung in der interzellulären Kommunikation bei Hefezellen*. Diploma thesis, Humboldt-Universität zu Berlin, 2011.

[200] J Stoer and R Bulirsch. *Numerische Mathematik 2: Eine Einführung - unter Berücksichtigung von Vorlesungen von F.L.Bauer*. Springer-Lehrbuch. Springer, 2005.

[201] P Deuflhard and F Bornemann. *Numerische Mathematik. 2. Integration gewöhnlicher Differentialgleichungen*. Gruyter - de Gruyter Lehrb{ü}cher. De Gruyter, 1994.

[202] W Dahmen and A Reusken. *Numerik für Ingenieure und Naturwissenschaftler*. Springer-Lehrbuch. Springer, 2008.

[203] R Alexander. Diagonally implicit Runge-Kutta methods for stiff ODE's. *SIAM Journal on Numerical Analysis*, pages 1006–1021, 1977.

[204] C J P Bélisle. Convergence theorems for a class of simulated annealing algorithms on Rd. *Journal of Applied Probability*, pages 885–895, 1992.

[205] Robert G Endres and Ned S Wingreen. Accuracy of direct gradient sensing by single cells. *Proceedings of the National Academy of Sciences of the United States of America*, 105(41):15749–15754, October 2008.

[206] N Barkai, M D Rose, and N S Wingreen. Protease helps yeast find mating partners. *Nature*, 396(6710):422–3, December 1998.

[207] Steven S Andrews, Nathan J Addy, Roger Brent, and Adam P Arkin. Detailed simulations of cell biology with Smoldyn 2.1. *PLoS computational biology*, 6(3):e1000705, March 2010.

[208] M Jin, B Errede, M Behar, W Mather, S Nayak, J Hasty, H G Dohlman, and T C Elston. Yeast dynamically modify their environment to achieve better mating efficiency. *Sci Signal*, 4(186):ra54, 2011.

[209] Christopher M Waters and Bonnie L Bassler. Quorum sensing: cell-to-cell communication in bacteria. *Annual review of cell and developmental biology*, 21:319–46, January 2005.

[210] R Craig MacLean and Ivana Gudelj. Resource competition and social conflict in experimental populations of yeast. *Nature*, 441(7092):498–501, May 2006.

[211] Wenying Shou, Sri Ram, and Jose M G Vilar. Synthetic cooperation in engineered yeast populations. *Proceedings of the National Academy of Sciences of the United States of America*, 104(6):1877–82, February 2007.

[212] Scott Smukalla, Marina Caldara, Nathalie Pochet, Anne Beauvais, Stephanie Guadagnini, Chen Yan, Marcelo D Vinces, An Jansen, Marie Christine Prevost, Jean-Paul Latgé, Gerald R Fink, Kevin R Foster, and Kevin J Verstrepen. FLO1 is a variable green beard gene that drives biofilm-like cooperation in budding yeast. *Cell*, 135(4):726–37, November 2008.

[213] Lorenzo A Santorelli, Christopher R L Thompson, Elizabeth Villegas, Jessica Svetz, Christopher Dinh, Anup Parikh, Richard Sucgang, Adam Kuspa, Joan E Strassmann, David C Queller, and Gad Shaulsky. Facultative cheater mutants reveal the genetic complexity of cooperation in social amoebae. *Nature*, 451(7182):1107–10, February 2008.

[214] Jeff Gore, Hyun Youk, and Alexander van Oudenaarden. Snowdrift game dynamics and facultative cheating in yeast. *Nature*, 459(7244):253–6, May 2009.

[215] S Kondo and T Miura. Reaction-diffusion model as a framework for understanding biological pattern formation. *Science*, 329(5999):1616–1620, 2010.

[216] Hans Meinhardt. *Models of biological pattern formation*. Academic Press, London, 1982.

[217] W K Huh, J V Falvo, L C Gerke, A S Carroll, R W Howson, J S Weissman, E K O'Shea, and Others. Global analysis of protein localization in budding yeast. *Nature*, 425(6959):686–691, 2003.

[218] Alexander DeLuna, Michael Springer, Marc W Kirschner, and Roy Kishony. Need-based up-regulation of protein levels in response to deletion of their duplicate genes. *PLoS Biol*, 8(3):e1000347, March 2010.

[219] Ariel Chernomoretz, Alan Bush, Richard Yu, Andrew Gordon, and Alejandro Colman-Lerner. Using Cell-ID 1.4 with R for microscope-based cytometry. *Curr Protoc Mol Biol*, Chapter 14:Unit 14.18, October 2008.

[220] R Development Core Team. *R: A Language and Environment for Statistical Computing*. R Foundation for Statistical Computing, Vienna, Austria, 2012.

[221] Hannes Fischer, Igor Polikarpov, and Aldo F Craievich. Average protein density is a molecular-weight-dependent function. *Protein Sci*, 13(10):2825–2828, October 2004.

[222] Christophe Geuzaine and Jean-François Remacle. Gmsh: a three-dimensional finite element mesh generator with built-in pre- and post-processing facilities. *International Journal for Numerical Methods in Engineering*, 2008.

[223] C Geuzaine and J F Remacle. Gmsh: A 3-D finite element mesh generator with built-in pre- and post-processing facilities. *International Journal for Numerical Methods in Engineering*, 79(11):1309–1331, 2009.

[224] J.-D. Müller, P. L. Roe, and H. Deconinck. A frontal approach for internal node generation in Delaunay triangulations. *International Journal for Numerical Methods in Fluids*, 17(3):241–255, August 1993.

[225] P Bastian, K Birken, K Johannsen, S Lang, N Neuß, H Rentz-Reichert, and C Wieners. UG–a flexible software toolbox for solving partial differential equations. *Computing and Visualization in Science*, 1(1):27–40, 1997.

[226] P Bastian, M Blatt, A Dedner, C Engwer, R Klöfkorn, R Kornhuber, M Ohlberger, and O Sander. A Generic Grid Interface for Parallel and Adaptive Scientific Computing. Part II: Implementation and Tests in DUNE. *Computing*, 82(2–3):121–138, 2008.

[227] P Bastian, F Heimann, and S Marnach. Generic implementation of finite element methods in the Distributed and Unified Numerics Environment (DUNE). *Kybernetika*, 46(2):294–315, 2010.

[228] Peter Bastian and DUNE-Team. dune-pdelab Howto. www.dune-project.org, October 2010.

[229] Jean Hausser and Korbinian Strimmer. Entropy inference and the James-Stein estimator, with application to nonlinear gene association networks. *Journal of Machine Learning Research*, 10::1469–1484, November 2008.

[230] J Crank. *The mathematics of diffusion*. Oxford University Press, USA, 1979.

[231] Richard C Yu, C Gustavo Pesce, Alejandro Colman-Lerner, Larry Lok, David Pincus, Eduard Serra, Mark Holl, Kirsten Benjamin, Andrew Gordon, and Roger Brent. Negative feedback that improves information transmission in yeast signalling. *Nature*, 456(7223):755–761, December 2008.

[232] Javier Valdez-Taubas and Hugh R B Pelham. Slow diffusion of proteins in the yeast plasma membrane allows polarity to be maintained by endocytic cycling. *Curr Biol*, 13(18):1636–1640, September 2003.

[233] Karline Soetaert, Thomas Petzoldt, and R Woodrow Setzer. Solving Differential Equations in R: Package deSolve. *Journal of Statistical Software*, 33(9):1–25, 2010.

[234] C A Parent and P N Devreotes. Molecular genetics of signal transduction in Dictyostelium. *Annu Rev Biochem*, 65:411–440, 1996.

[235] E Palsson. A cAMP signaling model explains the benefit of maintaining two forms of phosphodiesterase in Dictyostelium. *Biophys J*, 97(9):2388–2398, 2009.

[236] Stephen P Diggle, Ashleigh S Griffin, Genevieve S Campbell, and Stuart A West. Cooperation and conflict in quorum-sensing bacterial populations. *Nature*, 450(7168):411–4, November 2007.

[237] Carey D Nadell, Kevin R Foster, and João B Xavier. Emergence of spatial structure in cell groups and the evolution of cooperation. *PLoS computational biology*, 6(3):e1000716, March 2010.

[238] Carey D Nadell, Joao B Xavier, and Kevin R Foster. The sociobiology of biofilms. *FEMS microbiology reviews*, 33(1):206–24, January 2009.

[239] R Nath. Properties of Barrier, a novel Saccharomyces cerevisiae acid protease. *Biochimie*, 75(6):467–72, January 1993.

[240] Jirí Dostál, Helena Dlouhá, Petr Malon, Iva Pichová, and Olga Hrusková-Heidingsfeldová. The precursor of secreted aspartic proteinase Sapp1p from Candida parapsilosis can be activated both autocatalytically and by a membrane-bound processing proteinase. *Biological chemistry*, 386(8):791–9, August 2005.

[241] S K Raths, F Naider, and J M Becker. Peptide analogues compete with the binding of alpha-factor to its receptor in Saccharomyces cerevisiae. *The Journal of biological chemistry*, 263(33):17333–41, November 1988.

[242] D D Jenness, A C Burkholder, and L H Hartwell. Binding of alpha-factor pheromone to yeast a cells: chemical and genetic evidence for an alpha-factor receptor. *Cell*, 35(2 Pt 1):521–9, December 1983.

[243] K J Blumer, J E Reneke, and J Thorner. The STE2 gene product is the ligand-binding component of the alpha-factor receptor of Saccharomyces cerevisiae. *The Journal of biological chemistry*, 263(22):10836–42, August 1988.

[244] P Dube and J B Konopka. Identification of a polar region in transmembrane domain 6 that regulates the function of the G protein-coupled alpha-factor receptor. *Molecular and cellular biology*, 18(12):7205–15, December 1998.

[245] N E David, M Gee, B Andersen, F Naider, J Thorner, and R C Stevens. Expression and purification of the Saccharomyces cerevisiae alpha-factor receptor (Ste2p), a 7-transmembrane-segment G protein-coupled receptor. *The Journal of biological chemistry*, 272(24):15553–61, June 1997.

[246] Q Chen and J B Konopka. Regulation of the G-protein-coupled alpha-factor pheromone receptor by phosphorylation. *Molecular and cellular biology*, 16(1):247–57, January 1996.

[247] B K Lee, S Khare, F Naider, and J M Becker. Identification of residues of the Saccharomyces cerevisiae G protein-coupled receptor contributing to alpha-factor pheromone binding. *The Journal of biological chemistry*, 276(41):37950–61, October 2001.

[248] J L Weiner, C Guttierez-Steil, and K J Blumer. Disruption of receptor-G protein coupling in yeast promotes the function of an SST2-dependent adaptation pathway. *The Journal of biological chemistry*, 268(11):8070–7, April 1993.

[249] D M Apanovitch, K C Slep, P B Sigler, and H G Dohlman. Sst2 is a GTPase-activating protein for Gpa1: purification and characterization of a cognate RGS-Galpha protein pair in yeast. *Biochemistry*, 37(14):4815–22, April 1998.

[250] M E Linder, D A Ewald, R J Miller, and A G Gilman. Purification and characterization of Go alpha and three types of Gi alpha after expression in Escherichia coli. *The Journal of biological chemistry*, 265(14):8243–51, May 1990.

[251] G H Biddlecome, G Berstein, and E M Ross. Regulation of phospholipase C-beta1 by Gq and m1 muscarinic cholinergic receptor. Steady-state balance of receptor-mediated activation and GTPase-activating protein-promoted deactivation. *The Journal of biological chemistry*, 271(14):7999–8007, April 1996.

[252] Tau-Mu Yi, Hiroaki Kitano, and Melvin I Simon. A quantitative characterization of the yeast heterotrimeric G protein cycle. *Proc Natl Acad Sci U S A*, 100(19):10764–10769, September 2003.

[253] Danying Shao, Wen Zheng, Wenjun Qiu, Qi Ouyang, and Chao Tang. Dynamic studies of scaffold-dependent mating pathway in yeast. *Biophysical journal*, 91(11):3986–4001, December 2006.

[254] F van Drogen, V M Stucke, G Jorritsma, and M Peter. MAP kinase dynamics in response to pheromones in budding yeast. *Nat Cell Biol*, 3(12):1051–1059, December 2001.

[255] Brian D Slaughter, Joel W Schwartz, and Rong Li. Mapping dynamic protein interactions in MAP kinase signaling using live-cell fluorescence fluctuation spectroscopy and imaging. *Proc Natl Acad Sci U S A*, 104(51):20320–20325, December 2007.

[256] Sina Ghaemmaghami, Won-Ki Huh, Kiowa Bower, Russell W Howson, Archana Belle, Noah Dephoure, Erin K O'Shea, and Jonathan S Weissman. Global analysis of protein expression in yeast. *Nature*, 425(6959):737–41, October 2003.

[257] H G Dohlman, P Goldsmith, A M Spiegel, and J Thorner. Pheromone action regulates G-protein alpha-subunit myristoylation in the yeast Saccharomyces cerevisiae. *Proceedings of the National Academy of Sciences of the United States of America*, 90(20):9688–92, October 1993.

[258] C D Clark, T Palzkill, and D Botstein. Systematic mutagenesis of the yeast mating pheromone receptor third intracellular loop. *The Journal of biological chemistry*, 269(12):8831–41, March 1994.

[259] Y Chvatchko, I Howald, and H Riezman. Two yeast mutants defective in endocytosis are defective in pheromone response. *Cell*, 46(3):355–64, August 1986.

6 Appendix

6.1 Derivations

Gillespie Method

We will first compute the probability that no reaction takes place in a time interval $(t, t+\tau]$. For that we assume that we already know the probability for no reaction happening in the τ-interval, $\mathbb{P}_0(\tau)$, and now want to know what the probability is that there is also no reaction happening in the extended interval $(t, t+\tau+d\tau]$, where $d\tau$ is an infitesimal time-interval in which only a single reaction can happen. So we want to know the probability that no reaction happened after τ *and* no reaction happens in the next $d\tau$. The probability that no reaction happens is the opposite of the probability that *any* reaction happens in $d\tau$. This translates into

$$\mathbb{P}(\tau + d\tau, 0) = \mathbb{P}_0(\tau) \cdot (1 - r_0(\mathbf{S}, \tau)d\tau). \tag{6.1}$$

Here $r_0(\mathbf{S}, t)d\tau$ is the probability that any reaction happens in $d\tau$, so r_0 is given by

$$r_0(\mathbf{S}, t)d\tau = \sum_{j=1}^{n} r_j(\mathbf{S}, t)d\tau. \tag{6.2}$$

. We now rearrange $\mathbb{P}_0(\tau)$ the same way we have done it with the master equation and get

$$\frac{\mathbb{P}_0(\tau + d\tau) - \mathbb{P}_0(\tau}{d\tau} = -r_0(\mathbf{S}, t)\,\mathbb{P}_0(\tau). \tag{6.3}$$

Letting again $d\tau \to 0$ gives us an ordinary differential equation for $\mathbb{P}_0(\tau)$:

$$\frac{\mathbb{P}_0(\tau}{d\tau} = -r_0(\mathbf{S}, t)\,\mathbb{P}_0(\tau), \tag{6.4}$$

which now has the solution

$$\mathbb{P}_0(\tau) = \exp(-r_0(\mathbf{S}, t)\tau). \tag{6.5}$$

How long do we have to wait and which reaction will happen after we are done waiting? In order to respond to this, we need the probability of first waiting some time τ and than having the reaction j happening in an infitesimal $d\tau$, which we will call $\mathbb{P}(\tau, j|\mathbf{S}, t)d\tau$. So using the same trick as before this is again the probability of first having no reaction happening in τ and than having reaction j happening:

$$\mathbb{P}(\tau, j|\mathbf{S}, t) = \mathbb{P}_0(\tau) \cdot r_j(\mathbf{S}, t)d\tau. \tag{6.6}$$

Plugging in our solution from before we immediately get

$$\mathbb{P}(\tau, j|\mathbf{S}, t) = r_j(\mathbf{S}, t) \cdot \exp(-r_0(\mathbf{S}, t)\tau). \tag{6.7}$$

Multiplying the solution by $(r_0/r_0 = 1)$ yields

$$\mathbb{P}(\tau, j|\mathbf{S}, t) = \frac{r_j(\mathbf{S}, t)}{r_0(\mathbf{S}, t)} \cdot r_0(\mathbf{S}, t) \exp(-r_0(\mathbf{S}, t)\tau) \tag{6.8}$$

$$= \mathbb{P}(j|\tau) \cdot \mathbb{P}(\tau, 0), \tag{6.9}$$

where $\mathbb{P}(\tau, 0)$ is the probability that we have to wait a time τ until any next reaction happens and which is uniquely defined by an exponential distribution with rate parameter $r_0(\mathbf{S}, t)$. $\mathbb{P}(\tau, j)$ now is the probability that the next reaction will be reaction j.

Tau-leap step size

The change of reaction rates in some time interval $(t, t+\tau]$ is given by

$$\Delta r_j(\mathbf{S}, \tau) = r_j(\mathbf{S}, t+\tau) - r_j(\mathbf{S}, t). \tag{6.10}$$

This leads to the following first order Taylor expansion in $\mathbf{S}$:

$$\Delta r_j(\mathbf{S}, \tau) \approx 0 + \sum_k \frac{\partial r_j(\mathbf{S}, t)}{\partial S_k} \left(\mathbf{S}(t+\tau) - \mathbf{S}(t)\right). \tag{6.11}$$

Applying the update rule for our state ($S_k(t+\tau) = S_k(t) + \sum_l \rho_l \cdot \phi_{kl}$) to the equation than yields

$$\Delta r_j(\mathbf{S}, \tau) \approx \sum_k \frac{\partial r_j(\mathbf{S}, t)}{\partial S_k} \sum_l \rho_l \cdot \phi_{kl}. \tag{6.12}$$

Here ϕ_{kl} is again the stoichiometry. So it describes how the substance S_k changes when reaction l is executed. Applying the expectation and using the fact that $\langle \rho_l \rangle = r_l(\mathbf{S}, t)\tau$ finally gives us the mean change in the reaction rate

$$\langle \Delta r_j(\mathbf{S}, \tau) \rangle \approx \langle \sum_k \frac{\partial r_j(\mathbf{S}, t)}{\partial S_k} \sum_l \rho_l \cdot \phi_{kl} \rangle \tag{6.13}$$

$$\approx \sum_k \frac{\partial r_j(\mathbf{S}, t)}{\partial S_k} \sum_l \langle \rho_l \rangle \cdot \phi_{kl} \tag{6.14}$$

$$\approx \sum_k \frac{\partial r_j(\mathbf{S}, t)}{\partial S_k} \sum_l r_l(\mathbf{S}, t)\tau \cdot \phi_{kl} \tag{6.15}$$

$$\langle \Delta r_j(\mathbf{S}, \tau) \rangle \approx \sum_l \mathcal{D}_{jl} \cdot r_l(\mathbf{S}, t)\tau, \quad \text{with } \mathcal{D}_{jl} = \sum_k \frac{\partial r_j(\mathbf{S}, t)}{\partial S_k} \cdot \phi_{kl} \tag{6.16}$$

We repeat the same procedure for the variance of $\Delta r_j(\mathbf{S}, \tau)$:

$$\mathbf{Var}(\Delta r_j(\mathbf{S}, \tau)) \approx \mathbf{Var}(\sum_k \frac{\partial r_j(\mathbf{S}, t)}{\partial S_k} \sum_l \rho_l \cdot \phi_{kl}) \tag{6.17}$$

$$\approx \sum_k \frac{\partial r_j(\mathbf{S}, t)}{\partial S_k} \sum_l \mathbf{Var}(\rho_l) \cdot \phi_{kl} \tag{6.18}$$

$$\approx \sum_l \left(\sum_k \frac{\partial r_j(\mathbf{S}, t)}{\partial S_k} \cdot \phi_{kl} \right)^2 \cdot r_l(\mathbf{S}, t)\tau \tag{6.19}$$

$$\mathbf{Var}(\Delta r_j(\mathbf{S}, \tau)) \approx \sum_l \mathcal{D}_{jl}^2 \cdot r_l(\mathbf{S}, t)\tau, \quad \text{with } \mathcal{D}_{jl} = \sum_k \frac{\partial r_j(\mathbf{S}, t)}{\partial S_k} \cdot \phi_{kl} \tag{6.20}$$

Additional derivations for section 3.4

Derivation of the steady states

Enforcing the steady state condition on the reaction-diffusion equations (equations 1 – 5 in the main text) leads to the following equation system

$$0 = k_2 A^{on}(x,t) - k_1 A(x,t) S(x) + D_A^* \Delta A(x,t) \tag{6.21}$$

$$0 = k_1 A(x,t) S(x) + k_6 A B^{on}(x,t) - k_2 A^{on}(x,t) - k_5 A^{on}(x,t) B^{on}(x,t) + D_A \Delta A^{on}(x,t) \tag{6.22}$$

$$0 = k_4 B^{on}(x,t) - k_3 B(x,t) S(x) + D_B^* \Delta B(x,t) \tag{6.23}$$

$$0 = k_3 B(x,t) S(x) + k_6 A B^{on}(x,t) - k_4 B^{on}(x,t) - k_5 A^{on}(x,t) B^{on}(x,t) + D_B \Delta B^{on}(x,t) \tag{6.24}$$

$$0 = k_5 A^{on}(x,t) B^{on}(x,t) - k_6 A B^{on}(x,t) + D_{AB} \Delta A B^{on}(x,t) \tag{6.25}$$

with identical boundary conditions as for the original reaction-diffusion equations. Here, D_A^* and D_B^* can either be the diffusion rates for membrane-bound proteins (with $D_A^* \approx D_A$ and $D_B^* \approx D_B$) or the cytosolic diffusion rates (where $D_A^* \gg D_A$ and $D_B^* \gg D_B$). Furthermore, from now on if a function is written without its arguments this will denote its steady state value, thus $Y := Y(x,t)|_{t\to\infty} = Y(x)$.

Rearranging the system leads to an intermediate steady state description with

$$A = \frac{k_2}{k_1 S} A^{on} + \frac{D_A^*}{k_1 S}\Delta A \tag{6.26}$$

$$A^{on} = \frac{k_1}{k_2} A \cdot S + \frac{1}{k_2}\left(k_6 AB^{on} - k_5 A^{on} B^{on}\right) + \frac{D_A}{k_2}\Delta A^{on} \tag{6.27}$$

$$B = \frac{k_3}{k_4 S} B^{on} + \frac{D_B^*}{k_3 S}\Delta B \tag{6.28}$$

$$B^{on} = \frac{k_3}{k_4} B \cdot S + \frac{1}{k_4}\left(k_6 AB^{on} - k_5 A^{on} B^{on}\right) + \frac{D_B}{k_4}\Delta B^{on} \tag{6.29}$$

$$AB^{on} = \frac{k_5}{k_6} A^{on} B^{on} + \frac{D_{AB}}{k_6}\Delta AB^{on} \tag{6.30}$$

Combining equation 6.26 and 6.27 immediately leads to

$$A = \frac{k_2}{k_1 S}\left(\frac{k_1}{k_2} A \cdot S + \frac{D_{AB}}{k_2}\Delta AB^{on} + \frac{D_A}{k_2}\Delta A^{on}\right) + \frac{D_A^*}{k_1 S}\Delta A \tag{6.31}$$

$$\to A = A + \frac{D_{AB}}{k_1 S}\Delta AB^{on} + \frac{D_A}{k_1 S}\Delta A^{on} + \frac{D_A^*}{k_1 S}\Delta A \tag{6.32}$$

$$\to \Delta A = -\frac{D_{AB}}{D_A^*}\Delta AB^{on} - \frac{D_A}{D_A^*}\Delta A^{on}. \tag{6.33}$$

This is now a simple second order differential equation and can be solved directly by applying the fundamental theorem of calculus.

$$\int_0^x \int_0^x A(s)ds^2 = -\frac{D_{AB}}{D_A^*}\int_0^x \int_0^x \Delta AB^{on}(s)ds^2 - \frac{D_A}{D_A^*}\int_0^x \int_0^x \Delta A^{on}(s)ds^2 + \alpha \cdot x + \beta, \quad \alpha, \beta \in \mathbb{R} \tag{6.34}$$

$$\to A(x) = \alpha \cdot x + \beta - \frac{D_{AB}}{D_A^*} AB^{on}(x) - \frac{D_A}{D_A^*} A^{on}(x) \tag{6.35}$$

Due to the boundary condition $A(-\pi r, t) = A(\pi r, t)$ it immediately follows that $\alpha = 0$. From the equation it also follows that $A = \beta$ if $AB^{on} = A^{on} = 0$. However in that case, where no A is used in other complexes it must hold that $A = A_0$, thus $\beta = A_0$ and equation 6.35 resolves to

$$\boxed{A(x) = A_0 - \frac{D_{AB}}{D_A^*} AB^{on}(x) - \frac{D_A}{D_A^*} A^{on}(x)} \tag{6.36}$$

Combining equations 6.27, 6.30, 6.35 and using the property that membrane diffusion rates will be much smaller than average reaction rates yields

$$A^{on} = \frac{k_1}{k_2}\left(A_0 - \frac{D_{AB}}{D_A^*} AB^{on} - \frac{D_A}{D_A^*} A^{on}\right) S + \frac{D_{AB}}{k_2}\Delta AB^{on} + \frac{D_A}{k_2}\Delta A^{on} \tag{6.37}$$

$$\to \left(k_2 + \frac{k_1 D_A}{D_A^*} S\right) A^{on} = k_1 A_0 S - \frac{k_1 D_{AB}}{D_A^*} AB^{on} S + D_{AB}\Delta AB^{on} + D_A \Delta A^{on} \tag{6.38}$$

$$\to A^{on} = \frac{k_1 A_0 S}{k_2 + \frac{k_1 D_A}{D^* A} S} - \frac{k_1 \frac{D_{AB}}{D_A^*} AB^{on} S}{k_2 + k_1 \frac{D_A}{D_A^*} S} + D_{AB}\Delta AB^{on} + D_A \Delta A^{on} \tag{6.39}$$

Fully solving this equation would require integration of the original function $S(x)$ which can not be done for arbitrary functions S. However, since D_A and D_{AB} denote diffusion rates in the membrane,

which are small, the last two terms will be vanishing for most biologically relevant systems, which yields the approximation

$$\boxed{A^{on} \approx \frac{k_1 A_0 S}{k_2 + \frac{k_1 D_A}{D^* A} S} - \frac{k_1 \frac{D_{AB}}{D_A^*} AB^{on} S}{k_2 + k_1 \frac{D_A}{D_A^*} S}} \tag{6.40}$$

In case the signal is only transferred via the monomers ($AB^{on} = 0$), the monomers $\tilde{A}^{on}$ take a hyperbolic form with

$$\boxed{\tilde{A}^{on} \approx \frac{k_1 A_0 S}{k_2 + \frac{k_1 D_A}{D^* A} S}} \tag{6.41}$$

Similar results can be obtained for B, B^{on} and $\tilde{B}^{on}$ when combining equations 6.28 – 6.30:

$$\boxed{B(x) = B_0 - \frac{D_{AB}}{D_B^*} AB^{on}(x) - \frac{D_B}{D_B^*} B^{on}(x)} \tag{6.42}$$

$$\boxed{B^{on} \approx \frac{k_3 B_0 S}{k_4 + k_3 \frac{D_B}{D_B^*} S} - \frac{k_3 \frac{D_{AB}}{D_B^*} AB^{on} S}{k_4 + k_3 \frac{D_B}{D_B^*} S}} \tag{6.43}$$

$$\boxed{\tilde{B}^{on} \approx \frac{k_3 B_0 S}{k_4 + k_3 \frac{D_B}{D_B^*} S}} \tag{6.44}$$

Substituting equations 6.40 and 6.43 into equation 6.30 yields a quadratic algebraic equation for non-zero S[1]

$$0 = (AB^{on})^2 - p(x) \cdot AB^{on} + q, \text{ with} \tag{6.45}$$

$$p(x) := \left(\frac{A_0 D_A^* + B_0 D_B^*}{D_{AB}} + \frac{k_6 (k_2 + k_1 \frac{D_A}{D_A^*} S)(k_4 + k_3 \frac{D_B}{D_B^*} S) D_A^* D_B^*}{D_{AB}^2 k_1 k_3 k_5 S^2} \right) \text{ and} \tag{6.46}$$

$$q := \frac{A_0 B_0 D_A^* D_B^*}{D_{AB}^2}. \tag{6.47}$$

This equations may have two real solutions, however only one of them fullfills the property that no AB^{on} complexes can be formed when the signal approaches zero S

$$\lim_{S(x) \to 0} AB^{on}(x) = 0. \tag{6.48}$$

The remaining solution is given by

$$\boxed{AB^{on}(x) \approx \frac{1}{2} p(x) - \sqrt{\frac{1}{4} p(x)^2 - q}} \tag{6.49}$$

Interpretation

All of the derived solutions become constant if $S \to \infty$, which would correspond to a saturation of the signaling molecules which results in a homogeneous distribution at the cell membrane. When complexes are formed at the membrane directly, by activated membrane-bound proteins, the diffusion rates within the model will be in the same order of magnitude which results in $D_A^* = D_B^* = D_A = D_B = D_{AB}$. Therefore, the system may operate in a non-saturated state, if S and AB^{on} are low, or

[1] Note that $p(x)$ and $q(x)$ are both approaching infinity if D_A^* and D_B^* are high compared to the remaining diffusion rates. This may lead to numerical problems when evaluating the formula (especially for small $S(x)$).

in a saturated state, if S and AB^{on} are high.
In the non-saturated state the expressions for A^{on} and B^{on} simplify to

$$A^{on} \approx \frac{k_1}{k_2} A_0 S \tag{6.50}$$

$$B^{on} \approx \frac{k_3}{k_4} B_0 S. \tag{6.51}$$

This directly implies a non-saturated steady state for the complexes AB^{on} as well, with

$$AB^{on} \approx \frac{k_1 k_3 k_5}{k_2 k_4 k_6} A_0 B_0 \cdot S^2. \tag{6.52}$$

However this is only valid for relatively low activation levels of AB^{on}, thus, if only few complexes are formed.

If the complexes, however, are formed from cytosolic proteins which are recruited to the membrane this results in fast diffusion of the free proteins A and B. Due to that the diffusive ratios become close to zero:

$$\frac{D_A}{D_A^c} \approx \frac{D_B}{D_B^c} \approx \frac{D_{AB}}{D_A^c} \approx 0. \tag{6.53}$$

Applying this to the equations 6.40, 6.43 and 6.30 also directly leads to the linear and quadratic forms

$$A^m \approx \frac{k_1}{k_2} A_0 S \tag{6.54}$$

$$B^m \approx \frac{k_3}{k_4} B_0 S \tag{6.55}$$

$$AB^m \approx \frac{k_1 k_3 k_5}{k_2 k_4 k_6} A_0 B_0 \cdot S^2. \tag{6.56}$$

This however does not require S or AB^m to be low. As a direct consequence, in the case of recruited cytosolic proteins, saturation is diminished by the ratio of the cytosolic to membrane diffusion rates.

Response behavior for different signals

Using the response behavior derived from the steady states, we can analyze the shape and overall response of several types of signals. We repeat the analysis for three different kinds of signal: a linear (triangle) signal, a quadratic signal and a Gaussian shape. The signals may all have different widths but will all have the same overall abundance S_{tot}. Without loss of generality we assume that the space variable x is given in angular coordinates (radians). For each signal we then calculate the resulting response as well as the overall response. Following from that, all signals fulfill the property

$$\int_{-\pi}^{\pi} S(x, w) dx = S_{tot} \quad \forall w \leq \pi \tag{6.57}$$

Linear signal (triangle)

The linear signal with width w is given by

$$S(x, w) := \begin{cases} \frac{S_{tot}}{w^2}(x + w) & \text{if } -w \leq x \leq 0 \\ \frac{S_{tot}}{w^2}(w - x) & \text{if } 0 < x \leq w \\ 0 & \text{else} \end{cases}. \tag{6.58}$$

If the signal is not saturated this results in the response

$$\mathcal{R}(x, w) = \begin{cases} \alpha \frac{S_{tot}}{w^4}(x + w)^2 & \text{if } -w \leq x \leq 0 \\ \alpha \frac{S_{tot}}{w^4}(w - x)^2 & \text{if } 0 < x \leq w \\ 0 & \text{else} \end{cases} \tag{6.59}$$

with the overall response

$$\int_{-\pi}^{\pi} \mathcal{R}(x,w)dx = 0 + \frac{\alpha S_{tot}}{w^4} \int_{-w}^{0} (x+w)^2 dx + \frac{\alpha S_{tot}}{w^4} \int_{0}^{w} (w-x)^2 dx \tag{6.60}$$

$$= \frac{2}{3} \cdot \frac{\alpha S_{tot}}{w} \tag{6.61}$$

Quadratic Signal

The quadratic signal with width w is given by

$$S(x,w) := \begin{cases} \frac{3S_{tot}}{4w}\left(1 - \frac{x^2}{w^2}\right) & \text{if } |x| \leq w \\ 0 & \text{else} \end{cases}. \tag{6.62}$$

The non-saturated response is given by

$$\mathcal{R}(x,w) = \begin{cases} \frac{9\alpha S_{tot}}{16w^2}\left(1 - \frac{x^2}{w^2}\right)^2 & \text{if } |x| \leq w \\ 0 & \text{else} \end{cases} \tag{6.63}$$

with the overall response

$$\int_{-\pi}^{\pi} \mathcal{R}(x,w)dx = 0 + \frac{9\alpha S_{tot}}{16w^2} \int_{-w}^{w} \left(1 - \frac{x^2}{w^2}\right)^2 dx \tag{6.64}$$

$$= \frac{3}{5} \cdot \frac{\alpha S_{tot}}{w} \tag{6.65}$$

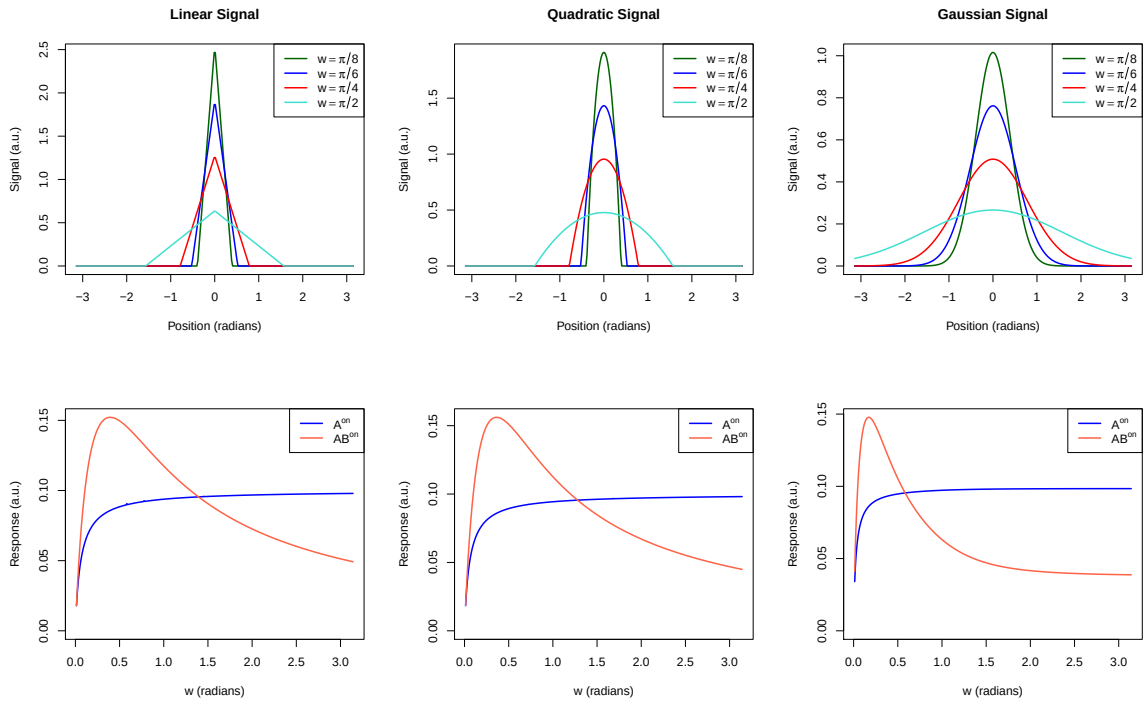

Figure 6.1: Considered signal shapes and gradient-response encoding in the presence of local depletion.

Gaussian Signal

The gaussian signal with width w is given by

$$S(x,w) := S_{tot}\frac{\exp\left(\frac{x^2}{2w^2}\right)}{\int_{-\pi}^{\pi}\exp\left(\frac{x^2}{2w^2}\right)dx} \tag{6.66}$$

and has the response function

$$\mathcal{R}(x,w) = \frac{\alpha S_{tot}\exp\left(\frac{x^2}{w^2}\right)}{\left(\int_{-\pi}^{\pi}\exp\left(\frac{x^2}{2w^2}\right)dx\right)^2}. \tag{6.67}$$

There is no analytic formula for the overall response produced by arbitrary gaussian signals, but there is one if the signal width is well below the perimeter of the cell, such that $\int_{-\pi}^{\pi}\exp\left(\frac{x^2}{2w^2}\right)dx \approx \sqrt{2\pi w^2}$. In this case the overall response is given by

$$\int_{-\pi}^{\pi} S(x,w)dx \approx \frac{1}{2\pi w^2}\int_{-\pi}^{\pi}\exp\left(\frac{x^2}{w^2}\right)dx \tag{6.68}$$

$$\approx \frac{1}{2\sqrt{\pi}}\cdot\frac{\alpha S_{tot}}{w}, \tag{6.69}$$

because $\exp(-x^2/w^2)$ is a Gaussian with parameter $\hat{w} := w/\sqrt{2} < w$.

6.2 Additional Data

Reactions and rates used in 3-D stochastic model

This list includes the kinetic rates used in the large stochastic model presented in section 3.3.

Kdis
Reaction: alpha $\rightarrow \varnothing$
Value: $25\,s^{-1}$ Derivation: Chosen to reproduce the original $\boldsymbol{\alpha}$-factor profile from the analytical solution.
Sources: [230]

Ksec
Reaction: $\varnothing \rightarrow$ alpha
Value: $4000\,s^{-1}$
Derivation: Chosen as a $MAT\boldsymbol{\alpha}$ with low secretion of $\boldsymbol{\alpha}$-factor.
Sources: [20]

Kdeg_alpha
Reaction: Bar1 + alpha $\rightarrow$ Bar1
Value: $0.93\,l\,\mu mol^{-1}s^{-1}$
Derivation: The Km for Bar1 is 0.03 mmol/l. Since our local pheromone concentration is always far below this Km (pheromone is about 10nM whereas the Km is in the range of 30000 nM). Therefore, from $S < Km$ it follows that $\frac{Vmax\cdot S}{Km+S} = \frac{Vmax}{Km}\cdot S = \frac{k_{cat}}{Km}\cdot E\cdot S$.
Sources: For the kcat we take the mean of two secreted aspartyl proteases from *Candida parapsilosis* which yields a kcat of 28 $s^{-}1$. Km has been measured [239, 240].

Kdis_Bar1
Reaction: Bar1 $\rightarrow \varnothing$
Value: $10s^{-1}$
Derivation: Chosen to reproduce analytical solution.

Sources: [230]

Ksynth_Bar1
Reaction: $\varnothing \rightarrow$ Bar1
Value: $1000 s^{-1}$
Derivation: The actual value does not really matter here. Together with the secretion rate the equilibrium will be the measured Bar1 abundance of 672 molecs/cell.
Sources: See Bar1 abundance.

Kon_alpha
Reaction: Ste2 + alpha $\rightarrow$ Ste2:alpha
Value: $0.185\, l\, \mu mol^{-1} s^{-1}$
Derivation: Calculated rom the Kd and Koff rate by kon=koff/Kd.

Koff_alpha
Reaction: Ste2:alpha $\rightarrow$ Ste2 + alpha
Value: $1.0 \pm 0.1 \cdot 10^{-3}\, s^{-1}$
Derivation: Average of 3 experiments.
Sources: [241, 242, 37]

Kd_alpha
Reaction: none
Value: $5.4 \pm 2.5\, nM$
Derivation: Average from 9 experiments. Internal parameter to calculate the on- and off-rates.
Sources: [243, 41, 244, 245, 46, 246–248, 37]

Kp_alpha
Reaction: Ste2 + Yck1/2$\rightarrow$ Ste2.P + Yck1/2
Value: $0.6668\, l\, mmol^{-1} s^{-1}$
Derivation: Approximated by fitting to a small ODE model with the data from Hicke.
Sources: Data from the Hicke Paper, Molecular abundances [42].

Kp_Ste2alpha
Reaction: Ste2:alpha + Yck1/2 $\rightarrow$ Ste2.P:alpha + Yck1/2
Value: $0.01713\, l\, \mu mol^{-1} s^{-1}$
Derivation: Approximated by fitting to a small ODE model with the data from Hicke.
Sources: Data from the Hicke Paper, Molecular abundances.

Kdeg_Ste2
Reaction: Ste2.P:* $\rightarrow \varnothing$
Value: $0.00561 s^{-1}$
Derivation: Approximated by fitting to a small ODE model with the data from Hicke and the constraint that the degradation should be slower than the phosphorylation rate of the pheromone-bound form.
Sources: Data from the Hicke Paper, Molecular abundances.

Kon_G_spont
Reaction: Gpa1.Ste4.Ste18 $\rightarrow$ Gp1.GTP + Ste4.Ste18
Value: $6.17 \cdot 10^{-4} s^{-1}$
Derivation: measured
Sources: [249]

Kon_G_rec
Reaction: Gpa1.Ste4.Ste18 +Ste2.*:alpha $\rightarrow$ Gpa1.GTP + Ste4.Ste18 + Ste2.*:alpha
Value: $74.353\, l\, \mu mol^{-1} s^{-1}$
Derivation: We ignored the value measured by Yi since it is impossible given the diffusion limit. Following Linder the rate-limiting step is the disassociation oft GDP which happens with a rate of $0.19 min^{-}1$ at 30 °C. We assume that is for one GAP protein and recalculate the second-order con-

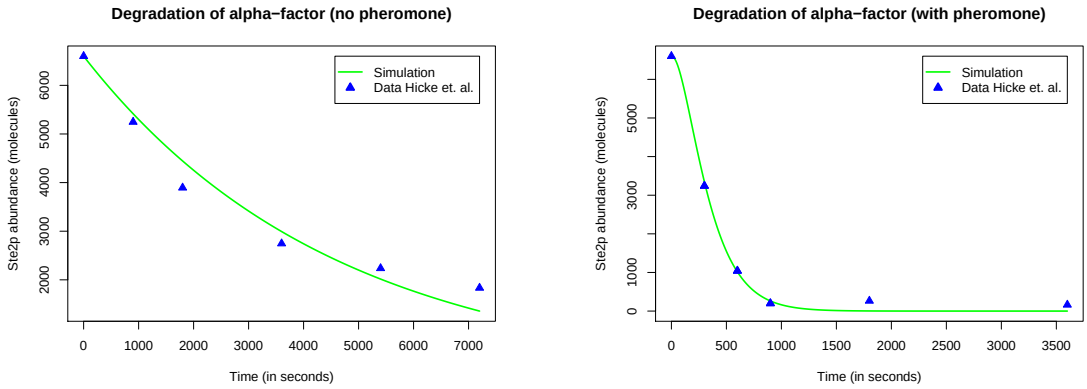

Figure 6.2: Fit of a simple ODE model to the data generated by Hicke et. al. in order to approximate the phosphorylation and degradation rate of Ste2. Significance was assessed using the F-test resulting in a p-value smaller 0.01.

stant by multiplying the amount of 1 nm molecules in our cell which yields the given rate.
Sources: Rate taken from the paper. Molecule number for 1nm in the our cell (23.49 molecules) [250].

Khyd_spont
Reaction: Gpa1.GTP → Gpa1.GDP
Value: $0.0045\,s^{-1}$
Derivation: Again we rather take values measured experimentally then fitted to data. Thus we take values for the rat Galpha again which is $0.27min^{-}1$.
Sources: [250]

Khyd_Sst2
Reaction: Gpa1.GTP + Sst2:* → Gpa1.GDP + Sst2:*
Value: $0.1031\,l\,\mu mol^{-1}s^{-1}$
Derivation: We assume that presence of the RGS protein globally increases the rate of hydrolysis 600-fold, as is has been shown for other G proteins. However since we assume that this is a cumulative effect of the all Sst2 molecules in the vicinity of the membrane this rate is further divided by the abundance of Sst2 bound to Ste2 or at the membrane in steady state. Thus the final rate is given by $Khyd\_spont \cdot 600 \cdot Sst2[nm]^{-1}_{mem}$.
Sources: [251]

Ktrim_G
Reaction: Gpa1.GDP + Ste4.Ste18 → Gpa1.Ste4.Ste18
Value: $23.486\,l\,\mu mol^{-1}s^{-1}$
Derivation: We calculate that from the rate of 1 $(molecspercell)^{-}1$ as from the Yi paper and use the equivalence from our model that 1nM = 23.486 molecules.
Sources: They did fit his to data, but it is quite clear that due to the low diffusion rate in the membrane this reaction is diffusion limited anyways [252].

Kon_Sst2
Reaction: Ste2:* + Sst2 → Ste2:*:Sst2
Value: $1\,l\,\mu mol^{-1}s^{-1}$
Derivation: Chosen to be in the range of other binding constants and Kds in the model.

Koff_Sst2
Reaction: Ste2:*:Sst2 → Ste2:* + Sst2
Value: $1s^{-1}$
Derivation: Arbitrarily chosen to be in the range of other binding constants and Kds in the model.

Kon_Ste5
Reaction: Ste4.Ste18 + Ste5 → Ste5:Ste4.Ste18
Value: $0.83\,l\,\mu mol^{-1}s^{-1}$
Derivation: [253]

Koff_Ste5
Reaction: Ste5:Ste4.Ste18 → Ste5 + Ste4.Ste18
Value: $0.084\,s^{-1}$
Derivation: Derived from the FRAP recovery of membrane-localized Ste5 as $ln(2)/t_{0.5}$ [254].

Kdim_Ste5
Reaction: Ste5:* + Ste5:* → Ste5:*:Ste5:*
Value: $10\,l\,\mu mol^{-1}s^{-1}$
Derivation: Since Ste5 dimers are hard to be detected we assume that they have a fast binding an disociation rate. Furthermore we observed that a Kd of about $0.1\mu M$ nicely reproduced the fraction of 10% dimers as observed by Slaughter et. al. [255].

Kdimoff_Ste5
Reaction: Ste5:*:Ste5:* → Ste5:* + Ste5:*
Value: $1s^{-1}$
Derivation: See previous comments.

Kdeg_Sst2
Reaction: Sst2 → ∅
Value: $3.85 \cdot 10^{-4}s^{-1}$
Derivation: Taken from a half life time of 30 min [48].

Ksynth_Ste2
Reaction: ∅ → Ste2
Value: $0.79095s^{-1}$
Derivation: Chosen to reproduce the steady state amount of Ste2 in the cell.

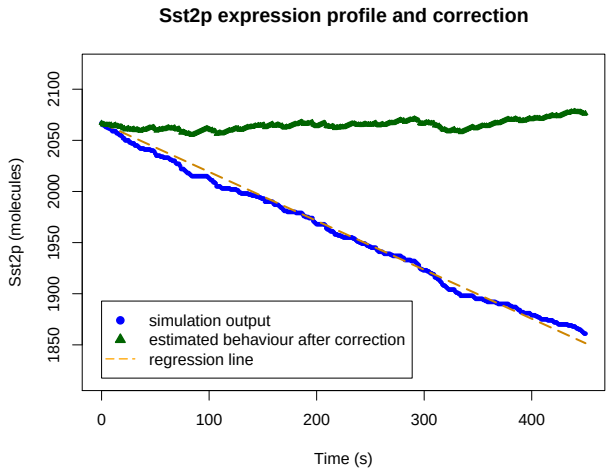

Figure 6.3: Approximation of the synthesis rates for Sst2 and Ste2 was performed by first simulating the model without synthesis and using a linear regression to approximate the rate required to counteract the molecule loss.

Ksynth_Sst2
Reaction: ∅ → Sst2

Value: $0.47864 s^{-1}$
Derivation: Chosen to reproduce the steady state amount of Sst2 in the cell.

Molecular abundances for various components of the yeast pheromone response

protein	molecules per cell (mean)	sources
Fus3	4250	[256, 75, 255]
Gpa1	5584	only myristoilated,[256, 252, 257, 49]
Ste4	820	[256, 252, 51]
Ste2	6600	[41, 245, 46, 24, 248, 243, 241, 258, 259]
Kss1	3205	[256, 255]
Msg5	829	[256, 255]
Sst2	2000	[49]
Ste5	600	[75, 255]
Ste7	985	[75, 255]
Ste11	658	[75, 255]
Ste20	259	[256]
Ptp2/3	917	[256]
Yck1/2	7790	[256]

Diffusion rates for different proteins in the yeast pheromone response

All values assume room temperature (25 °C). We used measured viscosities for different parts of the yeast cell [232, 255]. Diffusion rates are given in $\mu m^2/s$.

protein	cytosol/nucleus	membrane
Bar1	8.2285	$1.4539 \cdot 10^{-3}$
Ste2	9.0589	$1.6064 \cdot 10^{-3}$
α-factor	28.427	$5.0229 \cdot 10^{-3}$
Yck1/2	8.3	$1.46 \cdot 10^{-3}$
Gpa1	8.6941	$1.5362 \cdot 10^{-3}$
Ste4	9.1412	$1.6152 \cdot 10^{-3}$
Ste18	14.292	$2.5254 \cdot 10^{-3}$
Sst2	7.6356	$1.3492 \cdot 10^{-3}$
Ste20	7.0246	$1.2412 \cdot 10^{-3}$
Msg5	8.6865	$1.5348 \cdot 10^{-3}$
Ptp2/3	7.2	$1.27 \cdot 10^{-3}$
Ste5	7.0162	$1.2397 \cdot 10^{-3}$
Ste11	7.6038	$1.3435 \cdot 10^{-3}$
Ste7	8.5066	$1.5031 \cdot 10^{-3}$
Fus3	9.5613	$1.6894 \cdot 10^{-3}$
Kss1	9.4139	$1.6634 \cdot 10^{-3}$

6.3 Additional figures

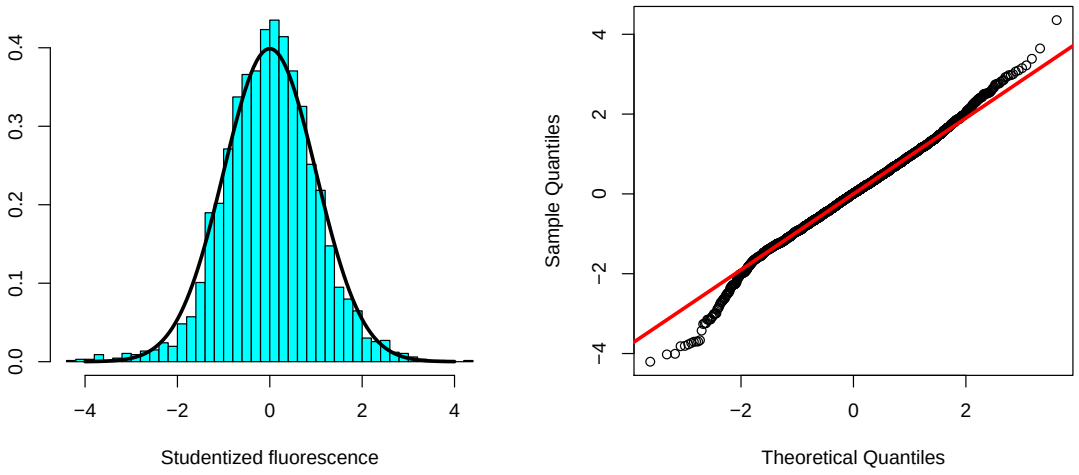

Figure 6.4: Histogram and QQ-Plot for studentized Fus1-GFP fluorescence. For each α-factor distribution the GFP fluorescence was centered by its mean and scaled by its standard deviation to yield the studentized measurements. Both plots show that the fluorescence values are Normal distributed (n=3320).

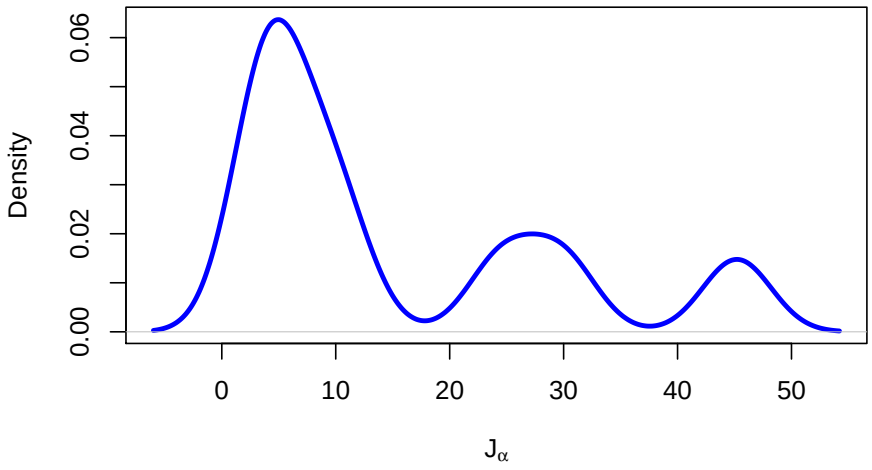

Figure 6.5: Distribution of obtained α-factor fluxes. A flux of 1 nM roughly corresponds to 450 molecules per cell and second. Thus, the peak in the first component corresponds to roughly 2300 molecules per cell and second.

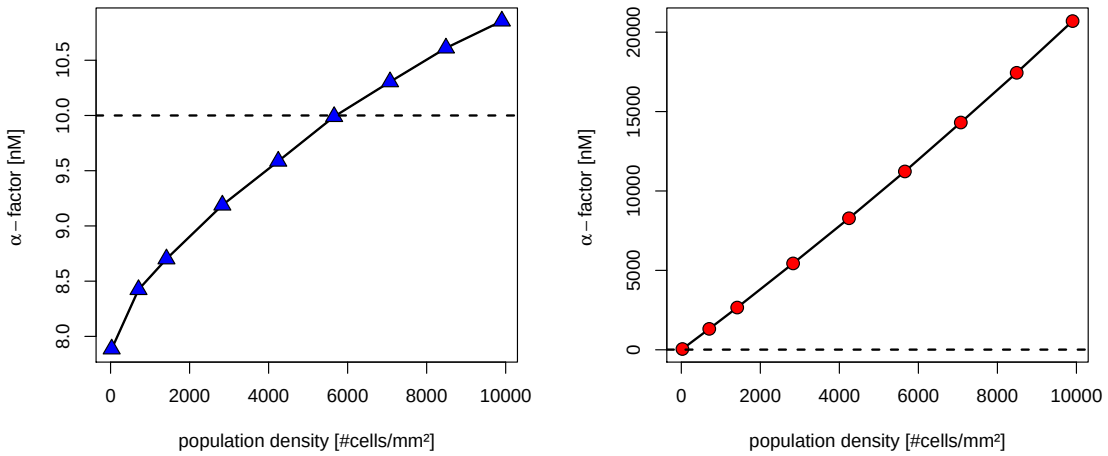

Figure 6.6: The average $\boldsymbol{\alpha}$-factor concentration observed in *in silico* populations of yeast in wild type (left) and $BAR1\Delta$ conditions (right). The dashed line denotes the concentration of $\boldsymbol{\alpha}$-factor which is usually sufficient to induce mating.

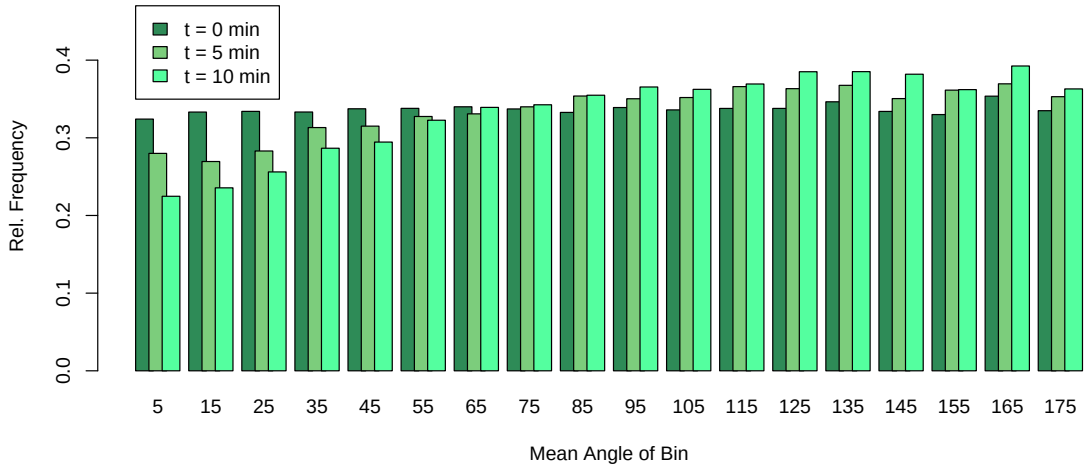

Figure 6.7: Local depletion of non-active Ste2 receptors.

List of Figures

1.1 The life cycle of Systems Biology. Repeated modification and probing of the biological systems is used to unravel an abstract functional description of the system, the model, that is used in turn to generate hypotheses which are validated or falsified by experiments. 4
1.2 The life cycle of *Saccharomyces cerevisiae*. Haploid yeast cells can either reproduce asexually by budding or recombine into a new diploid cell by mating. Diploid cells can produce spores which again yield haploid cells. The transition of a haploid into a diploid population likely takes place in a newly awaken culture. 6
1.3 The barrier experiment performed by Hicks and Herskowitz demonstrating the presence of a $\boldsymbol{\alpha}$-factor-inhibiting protein in *MAT***a** and the presence of this protein in the extracellular medium. 9
1.4 Overview of the pheromone response pathway in *MAT***a** cells of *Saccharomyces cerevisiae*. 11
1.5 The activation of Fus3 on Ste5 and its effect on the gene expression. Fus3 blocks activation of the filamentous growth response by inducing the degradation of Tec1, a component of the filamentous transcription factor complex. The small P indicates phosphorylation events. 14
1.6 Components involved in the formation of the polarisome and budding of *Saccharomyces cerevisiae*. 16

2.1 Structure of green fluorescent protein (GFP). GFP shows a barrel-like protein structure with an active core consisting of the amino acids Ser65–Tyr66–Gly67 which form the active chromophore by a stacking of the two aromatic rings. 24
2.2 Schematic view of the main components of an epifluorescence microscope. 25
2.3 Schematic view of a confocal microscope and the obstruction of light from outside the focal point. 26
2.4 Super-resolution can either be achieved by (A) the RESOLFT principle (e.g. STED) or by (B) PALM/STORM. 28
2.5 Example of the resolution gain using PALM. Shown are cryosections of *E. coli* stained with two membrane-anchored reversibly switchable fluorophores. The resolution of using conventional confocal imaging (upper) shows much less details than the PALM images (lower). Scale bars 500 nm, figure adapted from Andresen et. al [162]. 29
2.6 Structure of the reversibly switchable fluorescent protein Padron with its cis-trans chromophore center. Adapted from Brakemann et. al. [165]. 30
2.7 Components of a FACS system, including the liquid chamber generating the laminar flow, the acquisition unit and the optional cell sorting unit. 31
2.8 Examples for constructs achieving different kinds of mutations during a homologous recombination event. 34
2.9 Comparison of the original Gillespie algorithm (a) to the Tau-leaping algorithms (b). . 42
2.10 The next subvolume method as derived by Elf. 48
2.11 The shapes of the finite elements and their standardized mapping into a new coordinate system. Control points for the linear basis functions are shown as dark blue dots. The additional control points for the cubic basis functions are shown as red diamonds. . . . 57
2.12 Allowing for discontinuities in space of the approximated solution u may sometimes be advantageous to a completely continuous solution as in FEM methods. Thus, the discontinuous Galerkin (dG) method may allow for discontinuities which improve the approximation even if the real solution u^* is continuous. 60

3.1 Confocal microscopy images of mixed cell populations with different fluorescent markers in (A) Bar1 wild type and (B) *BAR1*Δ. 79

3.2 The calibration curve obtained from Fus1-GFP-*BAR1*Δ strains. The confidence for each data set is shown in green. Tick marks at the upper border indicate the **α**-factor concentrations used for the experiments. The fitted hill curve is shown in black along with parameter values and statistics. 80
3.3 The subdivision and boundaries of the space Ω used for the model. 82
3.4 Results of the parameter optimization for the degradation activity by Bar1. Shown are the mean values of the fluorescence measurements and the resulting parameters. . . . 85
3.5 Meshes generated from microscope images with different degrees of coarseness. 87
3.6 (A) The full assay to quantify the extracellular signaling environment. (B) Obtained **α**-factor distributions for the wild type and *BAR1*Δ. 89
3.7 Time course data of mixed haploid yeast populations consisting of wild type *MAT***a**-Fus1-GFP and *MAT***α**-mCherry and the resulting pheromone gradients. 90
3.8 (A) Maximum information content and (B) relative front-back ratios (gradients) produced by the **α**-factor distribution in wild type and *BAR1*Δ conditions. The theoretical maximum information content of any distribution with the same binning is given as a dashed line. 91
3.9 In the presence of Bar1 activity high **α**-factor concentrations are kept within high density mating sub-populations. This creates hot-spots of **α**-factor activity. This effect is absent in *BAR1*Δ conditions. 92
3.10 Flourescence obtained by flow cytometry of mixed haploid cultures in wild type (A,B) and *BAR1*Δ conditions (C,D). Points are colored by local density from blue to red. . 93
3.11 (A-B) Results of the FACS experiment. Each point denotes fractions obtained from 2×10.000 living cells. Error bars denote differences of the two biological samples in order indicate reproducibility of the experiment. (C-D) Cell numbers and and sizes (error bars denote standard deviation, n=6). The box indicates phenotypes in mixed cultures. 94
3.12 The presence of Bar1 also induces higher noise levels in the response. Compare to figure 3.2. 95
3.13 The geometry of the used model. The *MAT***a** cell is shown in green with blue nucleus and the *MAT***α** cell in blue with red nucleus. The outer boundary of the simulated volume is indicated with the lightgreen ellipsis. 96
3.14 The approximation of the analytical solution by the outer boundary condition. 97
3.15 Validation of the model simulations using and independent data set from Yu et. al. (triangles, [231]). The dynamics and noise levels are correctly predicted by the model. 98
3.16 Activation profiles of key components in the pheromone detection. The six curves correspond to increasing cell distances from bottom (0.5 μm) to top (3 μm). Means and quartiles were smoothed by a sliding mean approach over the 10 replicates. 99
3.17 The distance is linearly encoded in the molecule abundances as shown by the regression lines. However, good separation is only achieved on the level of receptors and G proteins, whereas **α**-factor itself and G proteins show very high noise levels. 100
3.18 Three dimensional rendering of simulation output. Setup shown here is for a cell distance of 0.5 μm, but the spatial distribution varied only little with distance. The illustration in the lower right shows the calculation of angles used to quantify the gradients. 101
3.19 Angular distributions of key components in the pheromone detection system at a cell-to-cell distance of 0.5 μm. 102
3.20 Local noise levels for the key components of the pheromone detection. 103
3.21 (A) Wild type *MAT***a** carrying a Fus1-GFP marker. Fus1 is recruited to the polarisome before conjugation. The cells were subjected to a uniform concentration of 25 μM of **α**-factor for 1 hour. (B) The basic processes governing the construction of the polarisome. 104
3.22 The simplifications applied to reduce the dimensionality of the space. 104
3.23 Simulation of the reaction-diffusion systems. The steady state approximation is shown in triangles. Chosen parameters: $r = 2.5\mu m, w = \pi r/3, A(x,0) = B(x,0) = 1, A^{on}(x,0) = B^{on}(x,0) = AB^{on}(x,0) = 0, k_1 = 8, k_2 = 1, k_3 = 0.5, k_4 = 1, k_5 = 10, k_6 = 1, k_7 = 1, k_8 = 1$. Diffusion rates are $0.05\mu m^2 s^{-1}$ in the direct model and $5\mu m^2 s^{-1}$ for cytosolic proteins in the recruited model. 107

3.24 The relation between signal widths and the amount of formed complexes. Numbers represent the fraction of of initial A and B molecules bound in complexes. 108
3.25 (A) the considered mechanisms of motif combination. (B) The resulting amplified polarization, due to the exponential dependence on the signal S, here exemplified for a Gaussian signal. 109

4.1 The functional interpretation of different parts of the pheromone response as obtained in this thesis. 112

6.1 Considered signal shapes and gradient-response encoding in the presence of local depletion. 138
6.2 Fit of a simple ODE model to the data generated by Hicke et. al. in order to approximate the phosphorylation and degradation rate of Ste2. Significance was assessed using the F-test resulting in a p-value smaller 0.01. 141
6.3 Approximation of the synthesis rates for Sst2 and Ste2 was performed by first simulating the model without synthesis and using a linear regression to approximate the rate required to counteract the molecule loss. 142
6.4 Histogram and QQ-Plot for studentized Fus1-GFP fluorescence. For each $\boldsymbol{\alpha}$-factor distribution the GFP fluorescence was centered by its mean and scaled by its standard deviation to yield the studentized measurements. Both plots show that the fluorescence values are Normal distributed (n=3320). 144
6.5 Distribution of obtained $\boldsymbol{\alpha}$-factor fluxes. A flux of 1 nM roughly corresponds to 450 molecules per cell and second. Thus, the peak in the first component corresponds to roughly 2300 molecules per cell and second. 144
6.6 The average $\boldsymbol{\alpha}$-factor concentration observed in *in silico* populations of yeast in wild type (left) and *BAR1*Δ conditions (right). The dashed line denotes the concentration of $\boldsymbol{\alpha}$-factor which is usually sufficient to induce mating. 145
6.7 Local depletion of non-active Ste2 receptors. 145

Curriculum vitae

For reasons of data protection, the Curriculum vitae is not published in the online version.

For reasons of data protection, the Curriculum vitae is not published in the online version.

For reasons of data protection, the Curriculum vitae is not published in the online version

Ehrenwörtliche Erklärung

Hiermit erkläre ich, die vorliegende Arbeit selbstständig ohne fremde Hilfe verfasst und nur die angegebene Literatur und Hilfsmittel verwendet zu haben.

Christian Diener (Verfasser)
Mexiko-Stadt, den 31. August 2012